T-3265

FORWARD MODELING AND INVERSION OF RESPONSES FOR BOREHOLE NORMAL AND LATERAL ELECTRODE ARRANGEMENTS

by

Jin-Hoo Kim

ProQuest Number: 10796292

All rights reserved

INFORMATION TO ALL USERS
The quality of this reproduction is dependent upon the quality of the copy submitted.

In the unlikely event that the author did not send a complete manuscript
and there are missing pages, these will be noted. Also, if material had to be removed,
a note will indicate the deletion.

ProQuest 10796292

Published by ProQuest LLC (2019). Copyright of the Dissertation is held by the Author.

All rights reserved.
This work is protected against unauthorized copying under Title 17, United States Code
Microform Edition © ProQuest LLC.

ProQuest LLC.
789 East Eisenhower Parkway
P.O. Box 1346
Ann Arbor, MI 48106 – 1346

T-3265

A thesis submitted to the Faculty and the Board of Trustees of the Colorado School of Mines in partial fulfillment of the requirements for the degree of Doctor of Philosophy(Geophysics)

Golden, Colorado

Date Nov. 4, 1986

Signed: _____
Jin-Hoo Kim

Approved: _____
Dr. Guy H. Towle
Thesis Advisor

Golden, Colorado

Date 6 Nov 86

Signed: _____
Dr. Phillip R. Romig
Professor, Head of
Geophysics Department

ABSTRACT

The finite difference method is used to solve the forward problems which simulate the borehole normal and lateral electrode arrangements for the combined boundary (2-D) earth model which has both horizontal and cylindrical boundaries.

The ridge regression estimator is then applied to solve the inverse problems which determine the earth parameters such as bed boundaries, extent of invaded zones, and vertical and horizontal resistivity profiles from the borehole normal and lateral resistivity logs.

The apparent resistivity values in the presence of borehole mud, invaded zone, and horizontal bed boundaries can be obtained from an earth geometry provided that the model is symmetric around the borehole axis. The quick and accurate forward calculations are achieved by using a gradually expanding grid system and a terminal resistance type boundary condition, and by using a two-dimensional average resistivity scheme in a grid block. The finite difference solutions are verified against analytical solutions for limiting cases, and excellent agreement is obtained. The finite difference forward modeling also can be used for investigation into the effects of the earth parameter variations on the apparent resistivities.

Inverse modeling is tested on synthetic and field data. The field data are inverted to a horizontally layered (1-D) model, and the theoretical data are inverted to a 2-D model. The test results indicate that the thickness and the resistivity of each layer can be determined simultaneously. For the practical inversion of field data, the 1-D model inversion results can be used as a first try model of the 2-D inversion. Interactive inverse modeling can be used for an automatic interpretation of the resistivity logs, with models constrained by logging and geologic information.

TABLE OF CONTENTS

LIST OF FIGURES

LIST OF TABLES

ACKNOWLEDGEMENTS

The author would like to express the deepest gratitude to Professor Guy H. Towle for suggesting this thesis topic and for continuing guidance and encouragement.

The author also would like to thank Professor Walter W. Whitman for the extensive suggestions and corrections.

The author is grateful to Professors William A. Schneider, Frank Hagin, and Donald I. Dickinson for their suggestions and observations.

The author also wishes to express his gratitude to Professor James E. White, Head of Borehole Geophysics Project, and to the Tenneco Oil Co. for their finantial supports for this research.

The author also would like to express the deepest gratitude to his mother, Mrs. Jie-Sung Chung, for giving him a good educational opportunity and devoting herself making him an effective scholar.

The author also thanks his wife, Mrs. Moon-Kyung Kim, for her support and for encouraging him to complete his study successfully.

The author also wishes to express his gratitude to Professors Min-Sung Lee and Kie-Hwa Lee of Seoul National University, Korea, for giving him the opportunity of studying at the Colorado School of Mines.

INTRODUCTION

The borehole resistivity forward modeling can be accomplished with three different earth models. The first model consists of an arbitrary number of horizontal layers with a current electrode located in a horizontally stratified medium without a borehole (1-D model). In this model the borehole diameter and the radius of invasion into the layer are assumed to be negligibly small, so that the borehole environment effects can be ignored. The second model consists of a number of cylindrical boundaries in a medium of infinite thickness with a current electrode located in the coaxial cylindrical region representing the borehole (1-D model). The first model is useful for the investigation of the vertical resistivity profile without borehole effects, while the second one is useful for the investigation of the radial resistivity profile without bed boundary effects. For both models each layer is assumed to be homogeneous and has isotropic specific resistivity. The analytical solutions for 1-D models were investigated by Dakhnov (1962) and Van Nostrand and Cook (1966), and the recursive algorithms were developed by Daniels (1978), Yang and Ward (1984), and Drahos (1984). A simple finite difference algorithm for a horizontally layered earth model was investigated by Mufti (1978, 1980).

The third model consists of an arbitrary number of horizontal and cylindrical layers (2-D model), which represent the practical well logging environment very well. Use of this model allows analyses of the effects caused by the two dimensional variations in earth parameters, i.e., the variations in the bed thickness and the formation resistivity, and the variations in the extent and the nature of the invasion. In order to estimate the borehole resistivity readings, Guyod (1955), and Dakhnov (1962) constructed a resistor network model, in which a great number of resistors were used. A few numerical solutions for this model were investigated and developed by Gianzero and Anderson (1982), Zhang and Shen (1984), and Tshang (1984). They showed numerical evaluations of an integral equation solution and an integral transform solution. These algorithms are accurate but are difficult in use.

In this study the finite difference algorithm with non-uniform grid spacings is developed to simulate the borehole normal and lateral electrode arrangements in a 2-D model. A large, sparse, linear system generated by the finite difference approximation is solved by the adaptive accelerated iterative algorithms developed by Kincaid et al (1982). Feasibility and efficiency of this approach for the 16" normal and the 18′ lateral electrode arrangements are demonstrated by comparing the test results with those

obtained by an analytical method and those obtained by an integral equation method.

In the inverse modeling, the earth parameters can be determined from the resistivity data. The important earth parameters which should be obtained correctly from the resistivity logs are the thickness and the true resistivity of the target stratum. These parameters as well as the invasion diameter and the resistivity of the invaded zone play a great role in the formation evaluation. Inversion of the borehole normal resistivity logs was introduced by Yang and Ward (1984). The horizontally layered earth model with a correction program for compensating borehole effects was used in their work.

In this investigation, a weighted least-squares inversion scheme with ridge regression estimator is used for the direct interpretation of the borehole normal and lateral resistivity logs. This scheme minimizes the root-mean-squares error between observed data and calculated data from the estimated earth model. Since the solutions to the inverse problem are generally non-unique, it is important that the meaningful earth parameters can be obtained by restricting the complexity of the earth model or reducing the size of the problem. Both theoretical data and field data are tested with a 1-D model and a 2-D model. For the practical inversion of field data, each resistivity log is

inverted to a 1-D model first. Once the best fit 1-D models are found, the borehole and the invasion effects can be considered with a 2-D model which best fits the normal and the lateral resistivity logs simultaneously. A set of synthetic resistivity logs for the 16" normal and the 18′ lateral with 3′ span is illustrated in Appendix A, where the resistive and the conductive beds which have the different bed thicknesses with the variations in the earth parameters are considered.

CHAPTER 1

FORWARD MODELING

Response of resistivity tools in a combined boundary earth model which has horizontal and radial boundaries is considered with a finite difference method. Figure 1.1 shows a two-dimensional logging environment which has axial symmetry around the borehole and has horizontal layers,

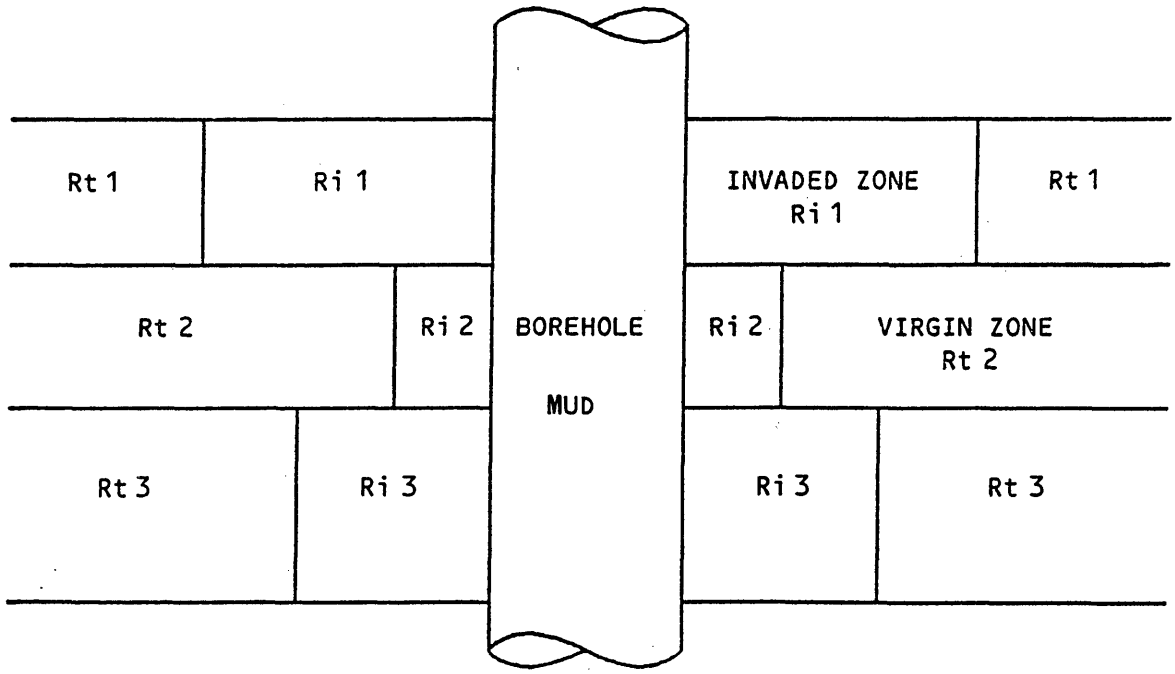

Figure 1.1 An axially symmetrical logging environment

borehole, invaded zones, and virgin zones. Invaded zones may have different resistivities and diameters.

This model is more practical than any of the other one-dimensional earth models, which are rarely encountered in nature. The one-dimensional earth model includes the horizontally layered medium without a borehole and the cylindrically layered medium of infinite thickness.

A Cylindrical coordinates system is used and the bed boundaries are all perpendicular to the borehole. The current electrode is centered in the borehole and the potentials are measured along the borehole axis.

1.1 Finite Difference Equation

The flow of steady state electric current in an inhomogeneous medium is governed by the equation

$$\nabla\cdot(\frac{1}{\rho}\nabla U) + q = 0, \qquad (1.1)$$

where ρ is the resistivity of the medium, U the potential, and q the strength of the current source. In cylindrical coordinates, assuming axial symmetry, equation (1.1) is expressed as

$$\frac{\partial}{\partial r}(\frac{1}{\rho}\frac{\partial U}{\partial r}) + \frac{\partial}{\partial z}(\frac{1}{\rho}\frac{\partial U}{\partial z}) + \frac{1}{r\rho}\frac{\partial U}{\partial r} + q = 0, \qquad (1.2)$$

where $\rho = \rho(r,z)$ and $U = U(r,z)$. This equation defines the

electric potential due to a system of current sources in an extended medium.

The potential function obtained by solving equation (1.2) must satisfy the following boundary conditions. The axial symmetry around the z-axis yields the boundary condition

$$\left.\frac{\partial U}{\partial r}\right|_{r=0} = 0. \tag{1.3}$$

At large distances from the current source, the potential should approach zero:

$$\lim_{r\to\infty, z\to\pm\infty} U = 0. \tag{1.4}$$

Figure 1.2 represents the vertical section of the medium. Only the finite portion of the medium is considered and is divided into a number of rectangular grids. Since the model is symmetrical around the z-axis, only one-half of the vertical section, $r \geq 0$, must be discretized.

It is necessary that the grids be very finely spaced in the area near the current source in order that the current spreads evenly and uniformly as it does in the earth (Dakhnov, 1962). At points far from the current source, the grids may be much coarser than the grids near the current source area. In general, the grid system is designed to fit the shape of the potential, which varies rapidly near the borehole and becomes smaller with slower variation away

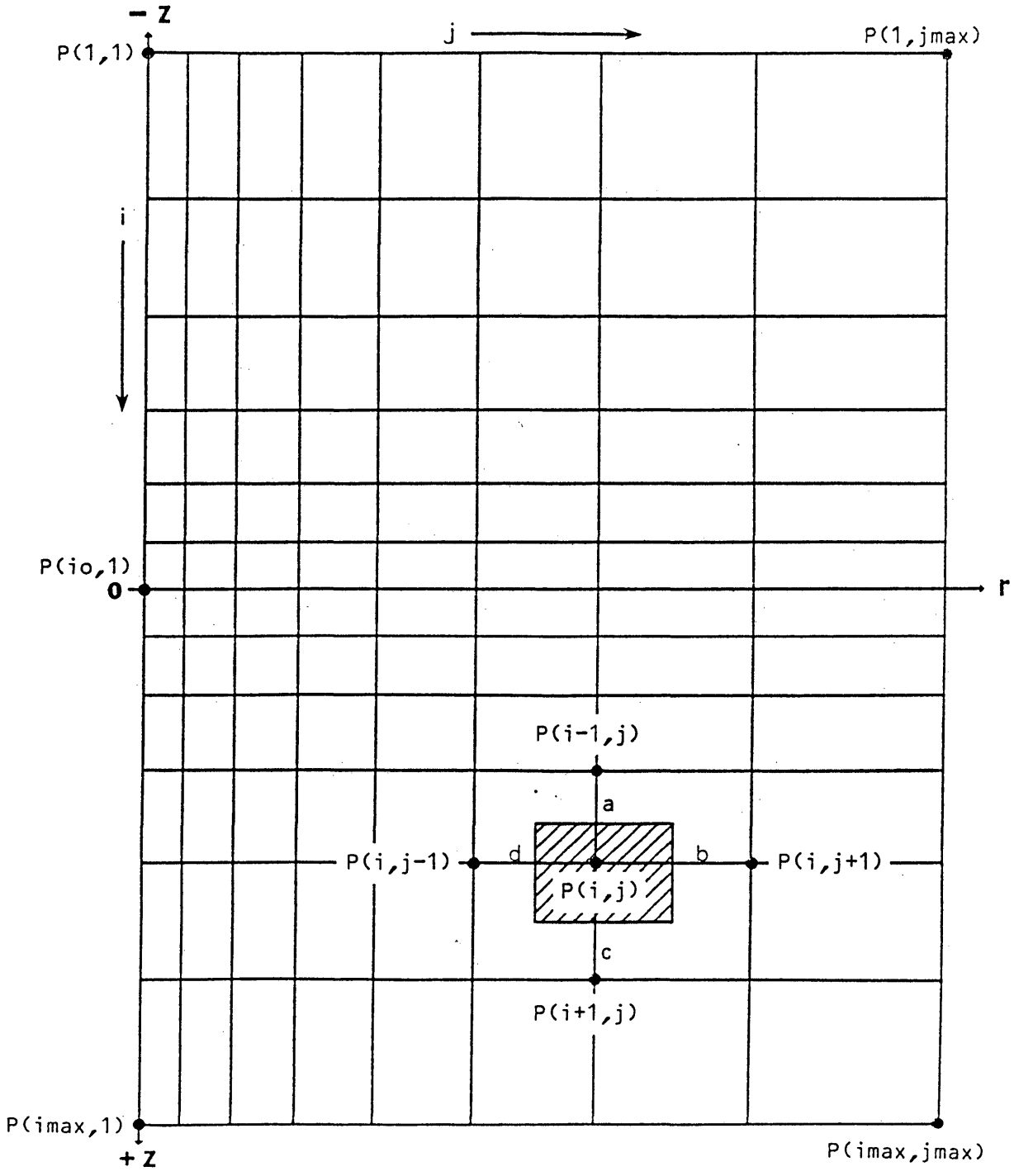

Figure 1.2 An exponentially expanding rectangular grid system in the cylindrical coordinates

from the wellbore and from the source. It is convenient and systematic to increase the grid spacings exponentially as distance from the current source increases.

The node corresponding to the ith row and the jth column is denoted by P(i,j) and its immediate four neighbors are denoted by P(i-1,j), P(i,j+1), P(i+1,j), and P(i,j-1). The distances of P(i,j) from the nodes P(i-1,j), P(i,j+1), P(i+1,n), and P(i,j-1) are assigned by a, b, c, and d, respectively. j=1 corresponds to the borehole axis (r=0). i=1 and i=imax correspond to the upper and the lower boundaries, respectively, and the j=jmax corresponds to the radial boundary of the finite difference model. The point source is denoted by P(io,1).

The location of P(i,j) in an exponentially expanding grid system can be expressed by

$$r(i,j) = \frac{\Delta r(1)(\alpha^{j-1}-1)}{\alpha-1}, \text{ for } j=1,jmax;$$

and (1.5)

$$z(i,j) = \pm\frac{\Delta z(io)(\beta^{|io-i|}-1)}{\beta-1}, \text{ for } i=1,imax;$$

where α and β denote the expanding ratio for the radial direction and axial direction, respectively. $\Delta r(1)$ represents the smallest radial spacing corresponding to the distance of P(i,2) from the axis of symmetry, and $\Delta z(io)$ represents the smallest spacing corresponding to the

vertical distance of P(io-1,j) or P(io+1,j) from P(io,j). The element associated with P(i,j) represents the rectangular area bounded by r(i,j-d/2), r(i,j+b/2), z(i-a/2,j), and z(i+c/2,j) in the vertical cross-section.

By using the grid system and the notations as described in Figure 1.2, the finite difference equivalence of equation (1.2) can be obtained as

$$\frac{2}{b+d}\left[\frac{U(i,j+1)-U(i,j)}{\rho(i,j+b/2)\ b} - \frac{U(i,j)-U(i,j-1)}{\rho(i,j-d/2)\ d}\right] +$$

$$\frac{2}{a+c}\left[\frac{U(i+1,j)-U(i,j)}{\rho(i+c/2,j)\ c} - \frac{U(i,j)-U(i-1,j)}{\rho(i-a/2,j)\ a}\right] + \qquad (1.6)$$

$$\frac{U(i,j+1)-U(i,j-1)}{r(i,j)\rho(i,j)\ (b+d)} + q_{ij} = 0,$$

where $\rho(i-a/2,j)$, $\rho(i,j+b/2)$, $\rho(i+c/2,j)$, and $\rho(i,j-d/2)$

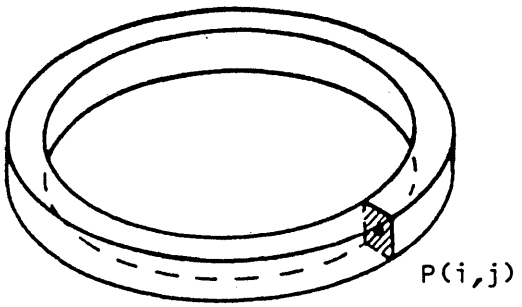

Figure 1.3 A ring disc volume element associated with P(i,j)

denotes the average resistivities between the point P(i,j) and its four neighbors P(i-1,j), P(i,j+1), P(i+1,j), and P(i,j-1), respectively.

If the rectangular area which represents the point P(i,j) is rotated through an angle of 2π around the axis of the symmetry, assuming b ≈ d, a ring disc volume element can be obtained (Figure 1.3) and its linearized volume is

$$V(i,j) = 2\pi r(i,j)\left(\frac{a+c}{2}\right)\left(\frac{b+d}{2}\right). \tag{1.7}$$

Multiplying the equation (1.6) throughout by equation (1.7), we have

$$\frac{U(i-1,j)-U(i,j)}{Ca} + \frac{U(i,j+1)-U(i,j)}{Cb} + \frac{U(i+1,j)-U(i,j)}{Cc} +$$

$$\frac{U(i,j-1)-U(i,j)}{Cd} + I(i,j) = 0, \tag{1.8}$$

where
$$Ca = \frac{\rho(i-a/2,j)}{\pi r(i,j)}\,\frac{a}{b+d},$$

$$Cb = \frac{\rho(i,j+b/2)}{\pi}\left(\frac{r(i,j)}{b}+0.5\right)^{-1}\frac{1}{a+c},$$

$$Cc = \frac{\rho(i+c/2,j)}{\pi r(i,j)}\,\frac{c}{b+d}, \tag{1.9}$$

$$Cd = \frac{\rho(i-d/2,j)}{\pi}\left(\frac{r(i,j)}{d}-0.5\right)^{-1}\frac{1}{a+c},$$

and

$$I_{ij} = 2\pi r(i,j)q(i,j)\left(\frac{a+c}{2}\right)\left(\frac{b+d}{2}\right).$$

Ca, Cb, Cc, and Cd are referred to as resistivity coefficients. Since q(i,j) represents the current density of element P(i,j), I(i,j) denotes the total amount of current entering the element P(i,j). If the point P(i,j) corresponds to a current source, I(i,j) will be positive, and if it corresponds to a sink, I(i,j) will be negative. When the point P(i,j) corresponds to a potential electrode, I(i,j) equals zero. Equation (1.8) is the same as the difference form of Kirchhoff's first law. The units of the potential, the resistivity coefficients, and the current are [Volt], [Ω], and [Amp], respectively.

1.2 Resistivity Coefficients

1.2.1 Resistivity Coefficient and Resistance

The resistivity of the medium is related to the electrical resistance as

$$R = \frac{\rho \cdot L}{A}, \qquad (1.10)$$

where R is the resistance of the conductor, A the cross-sectional area, and L the length of conductor. Figure 1.4 depicts the cross-section of the ring disc volume elements associated with the nodes P(i,j) and P(i,j+1). The average

resistivity and the distance between two nodes are denoted by

$$\rho = \rho(i,j+b/2), \tag{1.11a}$$

and $L = b$. (1.11b)

The height of the element is $(a+c)/2$ and the radial distance of the point $P(i,j+b/2)$ is $r(i,j)+b/2$. Consequently, the area open to the flow of current from the volume element associated with $P(i,j)$ to the volume element associated with $P(i,j+1)$ is expressed as

$$A = 2\pi[r(i,j)+b/2]\,\frac{a+c}{2}. \tag{1.11c}$$

If the current is flowing between two nodes $P(i,j)$ and

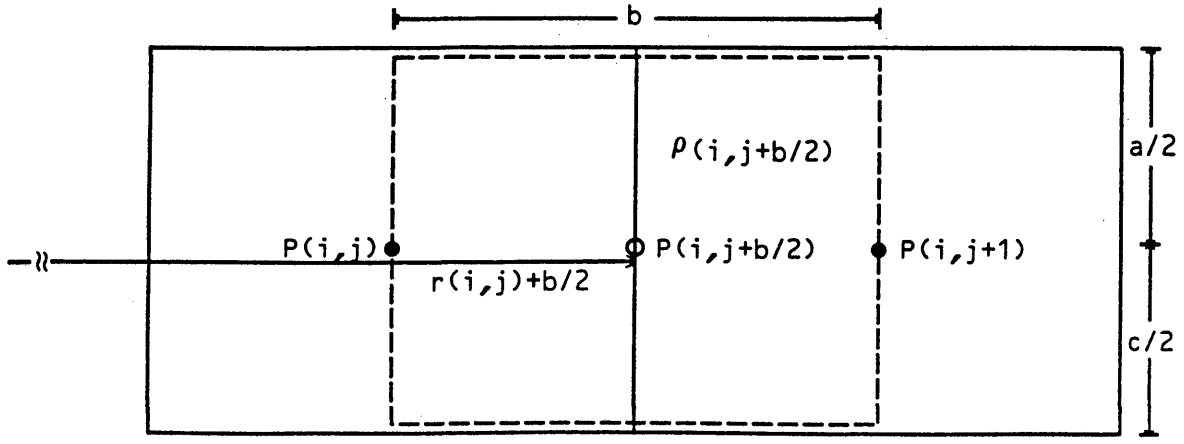

Figure 1.4 Cross-section of ring disc volume elements associated with $P(i,j)$ and $P(i,j+1)$

P(i,j+1), the volume element associated with the passage of current will be a ring disc conductor associated with the fictitious node P(i,j+b/2). The cross-section of the volume element associated with P(i,j+b/2) is denoted by a dashed rectangle. Substituting equations (1,11a), (1,11b), and (1,11c) into equation (1.10) yields

$$Rb = \frac{\rho(i,j+b/2)\ b}{2\pi[r(i,j)+b/2](a+c)/2}$$

$$= \frac{\rho(i,j+b/2)}{\pi}\left[\frac{r(i,j)}{b}+0.5\right]^{-1}\frac{1}{a+c} \qquad (1.12)$$

$$= Cb.$$

Thus, the resistivity coefficients can be replaced by the resistances which are associated with P(i,j) and its four neighbors.

The resistivity and the dimension of the volume element associated with P(i,j) and P(i-1,j) are

$$\rho = \rho(i-a/2,j),$$

$$L = a, \qquad (1.13)$$

and $A = 2\pi r(i,j-d/2)\frac{b+d}{2}$.

Substituting equation (1,13) into equation (1.10) yields Ra = Ca. In a similar manner, the relations Rc = Cc and Rd = Cd can be found.

1.2.2 Evaluation of Generalized Resistivity Coefficients

The primary task in evaluation of the resistivity coefficient is determination of the average resistivity correctly. If there is no resistivity variations in the element associated with P(i,j), the resistivity associated with P(i,j) can be assigned to ρ(i,j). Likewise, the resistivity associated with P(i,j+1) can be assigned to ρ(i,j+1). In this case, the resistivity coefficient Cb′ associated with P(i,j) and P(i,j+b/2), and the resistivity coefficient Cb" associated with P(i,j+b/2) and P(i,j+1) can be obtained. On account of equation (1.11), we have

$$Cb' = \frac{\rho(i,j)\quad b/2}{2\pi[r(i,j)+b/4](a+c)/2},$$

$$Cb'' = \frac{\rho(i,j+1)\quad b/2}{2\pi[r(i,j)+3b/4](a+c)/2}, \tag{1.14}$$

By taking an average cross-sectional area open to the flow of current across P(i,j) and P(i,j+1), we have modified coefficients

$$Cb' = \frac{\rho(i,j)\quad b/2}{2\pi[r(i,j)+b/2](a+c)/2},$$

$$Cb'' = \frac{\rho(i,j+1)\quad b/2}{2\pi[r(i,j)+b/2](a+c)/2}, \tag{1.15}$$

Finally, the resistivity coefficient associated with P(i,j)

and P(i,j+1) can be expressed by adding two coefficients Cb′ and Cb":

$$Cb = Cb' + Cb''$$

$$= \left[\frac{\rho(i,j)+\rho(i,j+1)}{2\pi}\right]\left[\frac{r(i,j)}{b}+0.5\right]^{-1}\frac{1}{a+c}. \qquad (1.16)$$

Equation (1.16) implies that the average resistivity of the volume element associated with P(i,j) and P(i,j+1) is

$$\rho(i,j+b/2) = [\rho(i,j)+\rho(i,j+1)]/2. \qquad (1.17)$$

The average resistivity expressed in this equation is valid if the resistivity varies at most from one element to the next, i.e., no boundaries exist within an element.

In the case where a large number of thin parallel layers or cylindrical boundaries exist, the average resistiviy expression must be modified. Otherwise, the detailed variations in resistivity will not influence the results. By taking the advantage of the relationship between resistivity coefficient and the resistance the generalized average resistivity can be visualized.

Figure 1.5 shows the variations of the resistivity in the volume element associated with P(i,j) and P(i,j+1), and the corresponding resistance network model. If the volume element associated with P(i,j) and P(i,j+1) has radial variations in resistivity as shown in Figure 1.5a, the resistivity coefficient expressed in equation (1.16) can be modified to the general formula in the terms of series

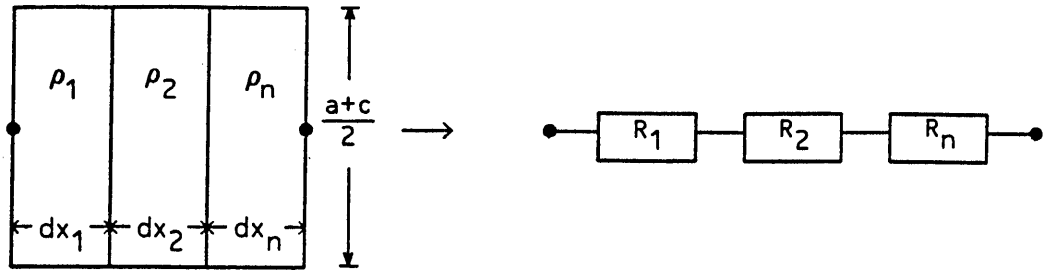

(a) Series Connection

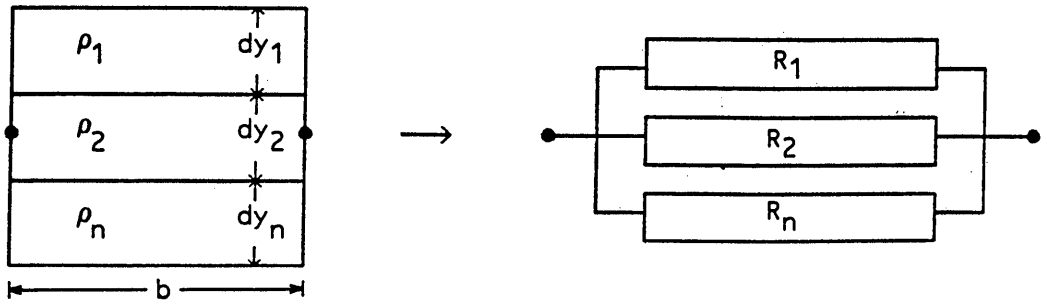

(b) Parallel Connection

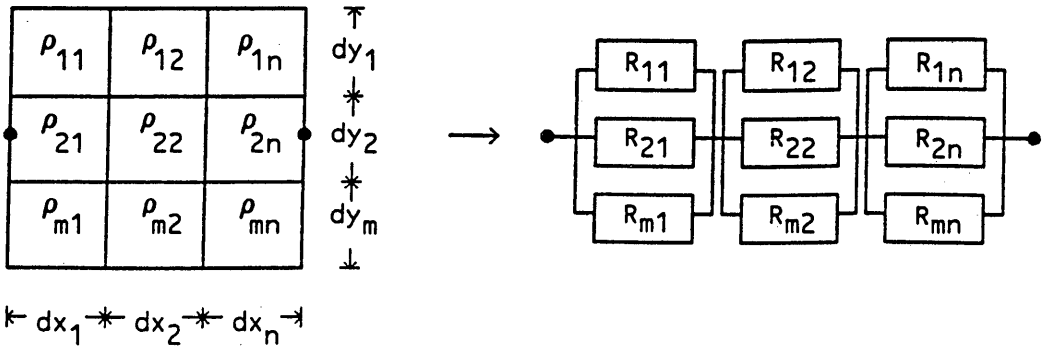

(c) Combined Connection

Figure 1.5 The volume elements associated with P(i,j) and P(i,j+1), and the corresponding resistance network model

connection of the resistances:

$$C_b = \frac{1}{2\pi}(r(i,j)+\frac{b}{2})^{-1}\frac{2}{a+c}\{\sum_{k=1}^{n}(\rho_k dx_k)\}. \qquad (1.18)$$

In the case when $\rho_1 = \rho(i,j)$, $\rho_2 = \rho(i,j+1)$, $dx_1 = b/2$, and $dx_2 = b/2$, the coefficient Cb equals the one previously obtained in equation (1.16).

If the volume element associated with P(i,j) and P(i,j+1) has a number of horizontal layers as shown in Figure 1.5b, the resistivity coefficient can be expressed in terms of parallel connection of the resistances:

$$C_b = \frac{1}{2\pi}(r(i,j)+\frac{b}{2})^{-1}/\{\sum_{k=1}^{n}(dy_k/\rho_k)\}. \qquad (1.19)$$

If the volume element associated with P(i,j) and P(i,j+1) has a number of horizontal layers and has a number of cylindrical boundaries as shown in Figure 1.5c, the generalized resistivity coefficient Cb becomes

$$C_b = \frac{1}{2\pi}(r(i,j)+\frac{b}{2})^{-1}\{\sum_{l=1}^{n}(dx_l/\sum_{k=1}^{m}(dy_k/\rho_{kl}))\}. \qquad (1.20)$$

Similarly,

$$C_d = \frac{1}{2\pi}(r(i,j)-\frac{d}{2})^{-1}\{\sum_{l=1}^{n}(dx_l/\sum_{k=1}^{m}(dy_k/\rho_{kl}))\}. \qquad (1.21)$$

Similar argument can be applied to the coefficients Ca and Cc. Since the cross-sectional area for the flow of current in the element associated with P(i,j) and P(i-1,j) equals the area associated with P(i,j) and P(i+1,j), the

generalized resistivity coefficients Ca and Cc are the same:

$$C_a = C_c = \frac{1}{2\pi r(i,j)}\{\sum_{k=1}^{m} (dy_k / \sum_{l=1}^{n} (dx_l/\rho_{lk}))\}. \qquad (1.22)$$

1.2.3 Resistivity Coefficients at the Boundary

Refering to Figure 1.2, the resistivity coefficients for the set of elements {P(i,j)| i=1,imax, j=1} must be computed subject to boundary condition of equation (1.3). This can be done by introducing a fictitious column of elements {P(i,j)| i=1,imax, j=0}. On account of axial symmetry and the fact that the current source is located on the axis of symmetry, the current always flows in the positive r-direction. Consequently, the boundary condition at the axis of symmetry leads to

$$U(i,0) = U(i,1), \quad \text{for } i=1,imax. \qquad (1.23)$$

By substituting equation (1.23) into (1.8) for j=1, the ~~third~~ fourth term in equation (1.8) is dropped out and the equation is modified as

$$\frac{U(i-1,1)-U(i,1)}{Ca} + \frac{U(i,2)-U(i,1)}{Cb} + \frac{U(i+1,1)-U(i,1)}{Cc}$$

$$+ I(i,1) = 0. \qquad (1.24)$$

The coefficient Cb can be obtained by substituting r(i,1)=0 into equation (1.20). This leads to

$$C_b = \frac{1}{\pi b}\{\sum_{l=1}^{n} (dx_l / \sum_{k=1}^{m} (dy_k/\rho_{kl}))\}, \text{ for } i=1,imax. \qquad (1.25)$$

The resistivity coefficients Ca and Cc at the axis of symmetry can be obtained by considering a volume element shown in Figure 1.6. The cross-sectional area associated with P(i,1) and P(i-1,1) is $\pi(b/2)^2$ and the distance of P(i,1) from P(i-1,1) equals a. As mentioned earlier, the coefficient Ca can be replaced by the resistance associated with P(i,1) and P(i-1,1), we have

$$Ca = \frac{\rho(i-a/2,1)\ a}{\pi(b/2)^2}, \quad \text{for } i=2,imax. \qquad (1.26)$$

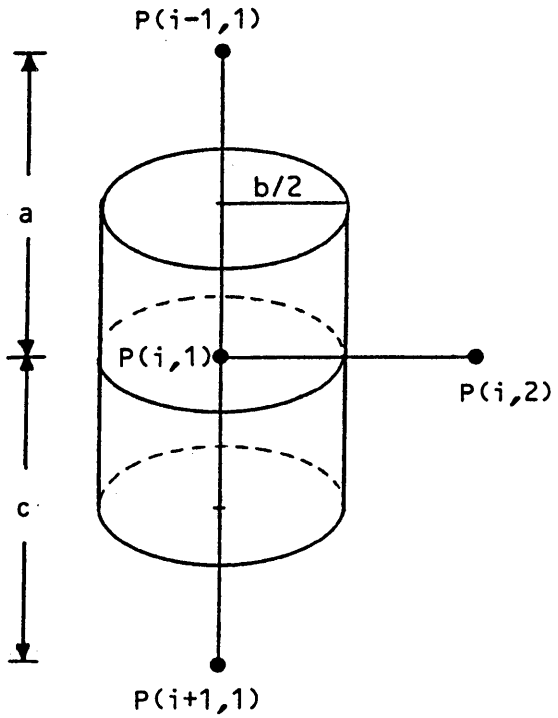

Figure 1.6 A volume element associated with P(i,1) at the axis of symmetry

In the same manner, the resistivity coefficient Cc is given as

$$Cc = \frac{\rho(i-c/2,1)\ c}{\Pi(b/2)^2}, \text{ for } i=1,imax-1. \qquad (1.27)$$

The electrical potential for the set of remaining boundary elements {P(i,j)| i=1, j=1,jmax}, {P(i,j)| i=imax, j=1,jmax}, and {P(i,j)| i=1,imax, j=jmax} can be specified as U = Uo, if the potential function be can defined at the boundaries. If the distance of boundaries is very large such that the condition of equation (1.4) is satisfied, the boundary potential approaches zero. But those conditions

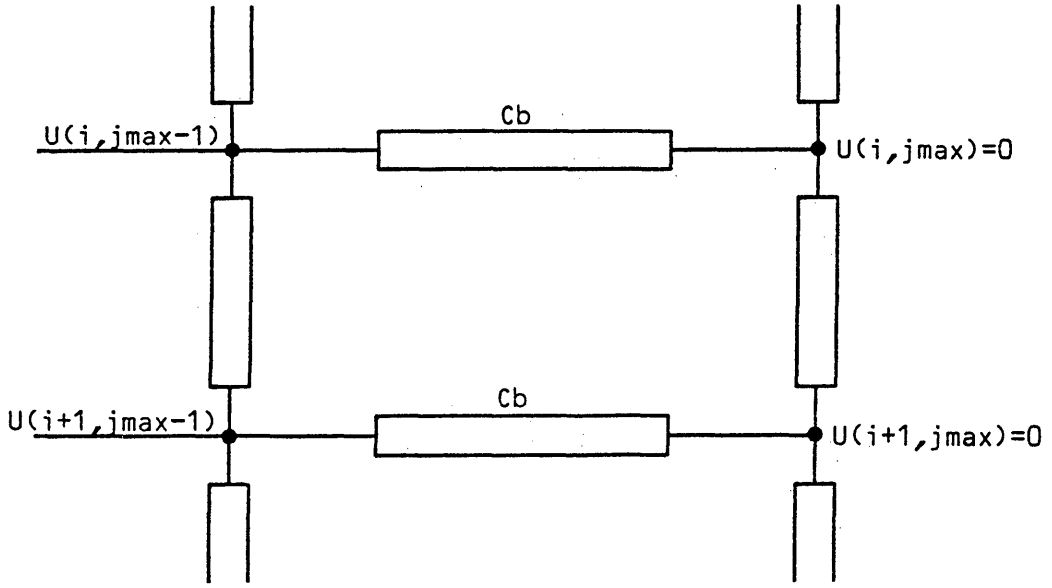

Figure 1.7 A portion of boundary elements

become impractical if the dimensions of the model are small, or if the medium is inhomogeneous.

The boundary condition that would be considered for the heterogeneous medium and/or relatively small grid system, where the boundary potential cannot be placed zero, is the terminal resistance type boundary condition (Stoyer, 1985). Figure 1.7 depicts a portion of boundary elements {P(i,j)| i=1,imax, j=jmax}. The boundary potentials {U(i,j)| i=1,imax, j=jmax} are placed at zero. The resistivity coefficient Cb associated with P(i,jmax-1) and P(i,jmax) is determined by using equation (1.20). The boundary potentials can be placed zero by replacing the resistances (resistivity coefficients) associated with P(i,jmax-1) and P(i,jamx) with larger ones. The terminal resistance factor (TRF) is defined as the ratio of the new coefficient to the old one such that

$$TRF = \frac{Cb(new)}{Cb} \qquad (1.28)$$

or $Cb(new) = TRF \times Cb$.

For the upper boundary of the model, the resistivity coefficient Ca associated with {P(i,j)| i=2, j=1,jmax-1} is replaced by

$$Ca(new) = TRF \times Ca, \qquad (1.29)$$

and the boundary potential is

$$\{U(i,j)|\ i=1,\ j=1,jmax-1\} = 0.$$

Similarly the resistivity coefficient Cc associated with the elements {P(i,j)| i=imax, j=1,imax-1} is replaced by

$$Cc(new) = TRF \times Cc, \qquad (1.30)$$

and the boundary potential is

$$\{U(i,j)|\ i=imax,\ j=1,jmax-1\} = 0.$$

The main advantage of the terminal resistance boundary condition is that the boundary potentials, which are usually unknown in the inhomogeneous medium, need not be determined in advance.

An example of selecting a terminal resistor factor is shown in Figure 1.8, in which a homogeneous medium which has 100 ohm-m resistivity is used. In the homogeneous medium the apparent resistivity is supposed to be constant and equals the true resistivity throughout the whole range of electrode spacings. If the terminal resistance factor is chosen too high or too low, the apparent resistivities as a function of electrode spacing diverges. It implies that the terminal resistance factor would be chosen so that the deviation of the apparent resistivity from the true resistivity curve is minimum. If the outer boundaries are placed at zero potential without the terminal resistances, (TRF = 1), the electrical potential approaches zero with increasing spacing ratio. As the terminal resistance factor increases, the tail of the apparent resistivity curve

arises. A value of 6.5 would be the appropriate size of the terminal resistance factor for the grid system used. Figure 1.8 also shows that the accuracy of the forward calculation for the short electrode spacings can be increased by using the terminal resistance type boundary condition.

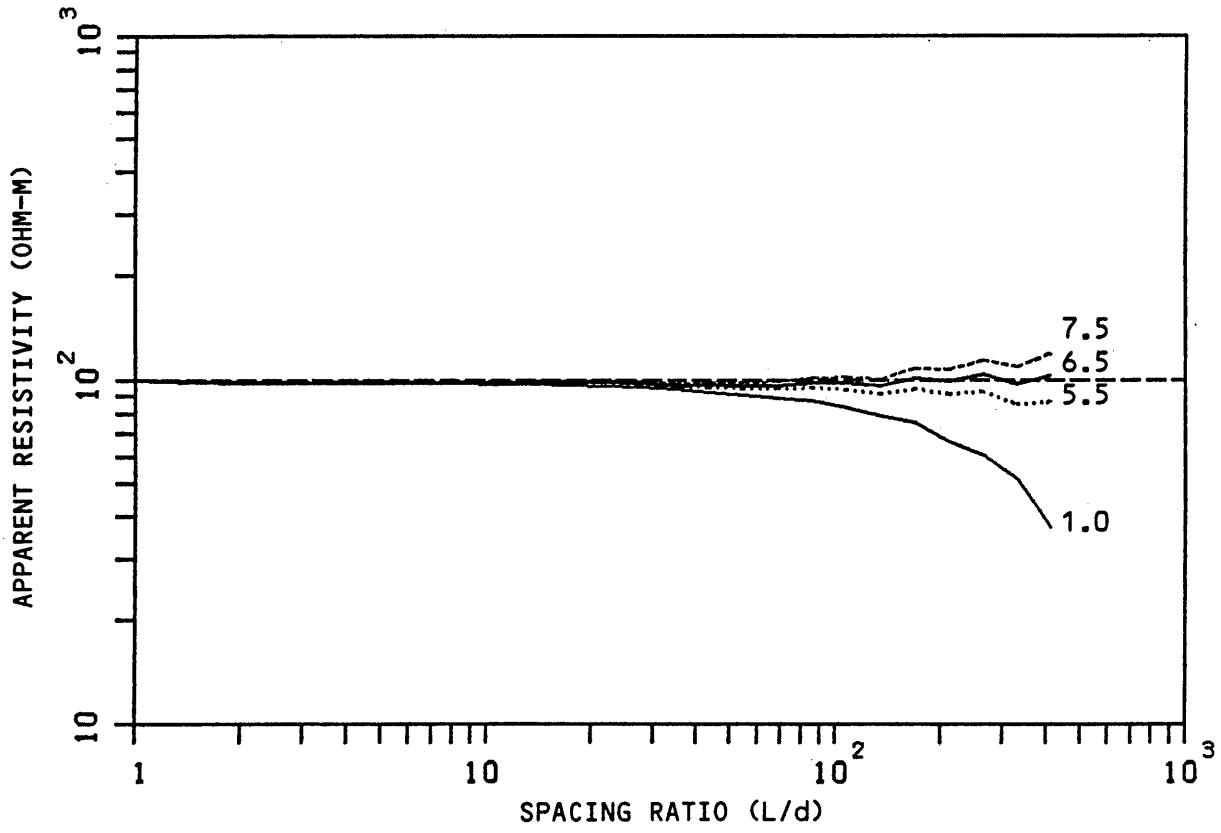

Figure 1.8 Apparent resistivity curves for different terminal resistance factors

By specifying zero potential at the boundary, the finite difference equation for the set of elements {P(i,j)| i=2, j=2,jmax-2} is

$$\frac{-U(2,j)}{Ca(new)} + \frac{U(2,j+1)-U(2,j)}{Cb} + \frac{U(3,j)-U(2,j)}{Cc} +$$

$$\frac{U(2,j-1)-U(2,j)}{Cd} + I(2,j) = 0. \qquad (1.31a)$$

On account of (1.24), the finite difference equation for the element associated with P(2,1) is

$$\frac{-U(2,1)}{Ca(new)} + \frac{U(2,2)-U(2,1)}{Cb} + \frac{U(3,1)-U(2,1)}{Cc}$$

$$+ I(2,1) = 0. \qquad (1.31b)$$

The finite difference equation for the set of elements associated with {P(i,j)| i=2, j=jmax-1} becomes

$$\frac{-U(2,jmax-1)}{Ca(new)} + \frac{-U(2,jmax-1)}{Cb(new)} + \frac{U(3,jmax-1)-U(2,jmax-1)}{Cc}$$

$$+ \frac{U(2,jmax-2)-U(2,jmax-1)}{Cd} + I(2,jmax-1) = 0. \qquad (1.31c)$$

The same argument can be applied for the lower and the radial boundaries of the model and the corresponding finite difference equation is straightforward.

1.3 Evaluation of Apparent Resistivity

1.3.1 Evaluation of Potential Distribution

The finite difference equation (1.7) constructs a linear system

$$\mathbf{A}\,\mathbf{x} = \mathbf{b}, \tag{1.31}$$

where **A** is the coefficient matrix, **x** the unknown vector, and **b** the known right hand side vector. Refering to Figure 1.2, the size of the problem is product of imax and jmax. For the elements associated with P(i,j), the matrix equation equivalence of equation (1.7) can be expressed as equation (1.33).

$$\begin{bmatrix} \cdots & -1/Ca & \cdots & -1/Cd & 1/C & -1/Cb & \cdots & -1/Cc & \cdots \end{bmatrix} \begin{bmatrix} \vdots \\ U(i-1,j) \\ \vdots \\ U(i,j-1) \\ U(i,j) \\ U(i,j+1) \\ \vdots \\ U(i+1,j) \\ \vdots \end{bmatrix} = \begin{bmatrix} \\ I(i,j) \\ \\ \end{bmatrix}$$

where $1/C = 1/Ca + 1/Cb + 1/Cc + 1/Cd$. (1.33)

The coefficient matrix **A** has a penta-diagonal structure, where four off-diagonal entries and the main diagonal entries have non-zero values, while the remaining entries are all zeros. On account of (1.20) and (1.21), the coefficient Cb associated with P(i,j) equals the coefficient

Cd associated with P(i,j+1), that is

$$Cb(i,j) = Cd(i,j+1). \tag{1.34}$$

Similarly, equation (1.22) leads to

$$Cc(i,j) = Ca(i+1,j). \tag{1.35}$$

Equations (1.34) and (1.35) imply that the matrix A is symmetric:

$$a_{ij} = a_{ji}, \tag{1.36}$$

where a_{ij} represents the entry corresponding to ith row and jth column of the matrix **A**.

Equation (1.33) shows that the matrix **A** has positive diagonal entries

$$a_{ii} > 0, \tag{1.37}$$

and has a diagonal dominance

$$a_{ii} \geq \sum_{i \neq j} |a_{ij}|. \tag{1.38}$$

For the solution vector $\mathbf{x} \neq 0$, it can be found that the coefficient matrix **A** is positive definite such that

$$\mathbf{x}^T \mathbf{A}\, \mathbf{x} > 0, \tag{1.39}$$

where $\mathbf{x}^T$ is a transpose of the vector **x**.

The matrix equation (1.33) can be solved for the unknown vector **x** which defines the potential distribution in the simulation model. Many techniques have been developed to solve such a linear system. Elimination methods can be used for relatively small problems. For large problems, the iterative method will be superior to the elimination method,

because the iterative method can reduce the large rounding-off errors and voluminous arithmetic operations.

The practical method found very effective is the adaptive accelerated iterative algorithms, ITPACK 2C (Kincaid et al., 1982), which are a collection of seven FORTRAN subroutines and are suitable for solving large sparse linear systems. Basic iterative procedures, such as the Jacobi method, the successive overrelaxation method, the symmetric successive overrelaxation method, and the RS method for the reduced system are combined, where possible, with acceleration procedures, such as Chebyshev (semi-iteration) and conjugate gradient, for rapid convergence. Automatic selection of the acceleration parameter and the use of accurate stopping criteria are major features of this software package.

The ITPACK 2C uses a sparse storage scheme in which only the non-zero entries are stored in the array. Since the coefficient matrix A is symmetric, as shown in (1.36), computer memory would be saved by storing only non-zero entries in each row on and above the main diagonal. The conditions (1.37), (1.38), and (1.39) provide the necessary conditions for the succesful convergence of the iterative methods.

The choice of the grid system is the main factor which affects the finite difference results. The rate of

expansion can be determined by the compensating factors of accuracy and computational efficiency. The accuracy would deteriorate if the grid size expanded too rapidly. On the other hand, Excessive computer time would be required if the grid size expanded too slowly. The expanding ratio of 1.25 to 1.4 would provide sufficiently fine grid spacings near the current source. The ratio should be determined by taking into account the size and the complexity of the earth model. In the case where the earth model is small and complex, the small expanding ratio should be used. The expanding ratios of the radial direction (α) and the axial direction (β) may be different from each other, according to the earth model.

Also, the smallest grid spacings, $\Delta r(1)$ and $\Delta z(io)$, should be determined by taking into account the earth model, especially location of the borehole wall and the thickness of the layer. $\Delta z(io)$ must be smaller than the thickness of the thinnest layer, and $\Delta r(1)$ must be smaller than the radius of the borehole. The small values of $\Delta r(1)$ and $\Delta z(io)$ provide the even and uniform distribution of the current near the source.

In order to provide a theoretically noise-free result, the size of the grid system, usually expressed by imax by jmax, must be greater than 39 by 20. This size of grid system provides sufficient accuracy for the short normal

arrangement, and it takes about 4~5 seconds of computational time. Evaluation of the apparent resistivity for the lateral arrangement requires a large grid system such as 59 by 30, and it takes about 15~20 seconds of computational time with the Gould 9600 computer. The size of the grid system depends on required accuracy and the actual size of the simulation model.

1.3.2 Apparent Resistivity from Potential Distribution

The apparent resistivity for the normal and the lateral electrode arrangements can be evaluated from the potential distribution in the simulation model. The schematic diagram of the normal and the lateral arrangements are shown in Figure 1.9. For both arrangements, the current return B is placed at the ground surface and is infinitely far from the current source.

For the normal arrangement, the reference potential electrode N is located at infinity and the measuring electrode M is located at a distance AM from the current source A. In that case the apparent resistivity is given by

$$Ra = 4\Pi\ AM\ \frac{U(M)}{I}. \qquad (1.40)$$

The value of Ra obtained by this equation represents the apparent resistivity corresponding to the depth point O. Since the current source and the potential electrodes are

located at the borehole axis, a set of elements associated with {P(i,j)| i=1,imax, j=1} is used to evaluate the apparent resistivities.

If the potential electrode M lies on the point P(i,1), the apparent resistivity can be expressed by

$$Ra = 4\pi\ AM\ \frac{U(i,1)}{I}. \qquad (1.41)$$

If the potential electrode is located in between P(i-1,1) and P(i,1), the potential at M can be obtained by the linear interpolation of U(i-1,1) and U(i,1). The accuracy of the

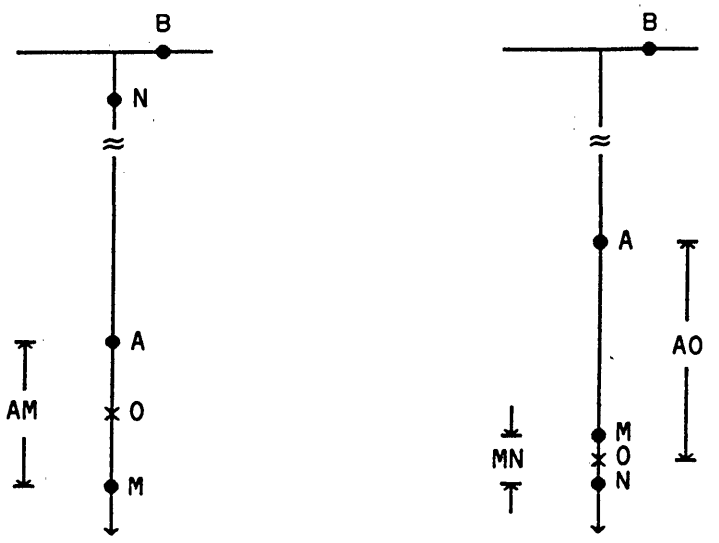

(a) Normal Arrangement (b) Lateral Arrangement

Figure 1.9 Schematic diagram of (a) the normal and (b) the lateral arrangements

results would be increased and the need for interpolation can be eliminated by inserting a horizontal grid line which represents the vertical position of the potential electrode M, and by reconstructing a grid system (Figure 1.10). The element which was associated with P(i,j) is assigned to P(i+1,1), and the element associated with M is assigned to P(i,1).

For the lateral arrangement the potentials are measured at M and N, which are separated by the span MN. In that case the apparent resistivity is given by

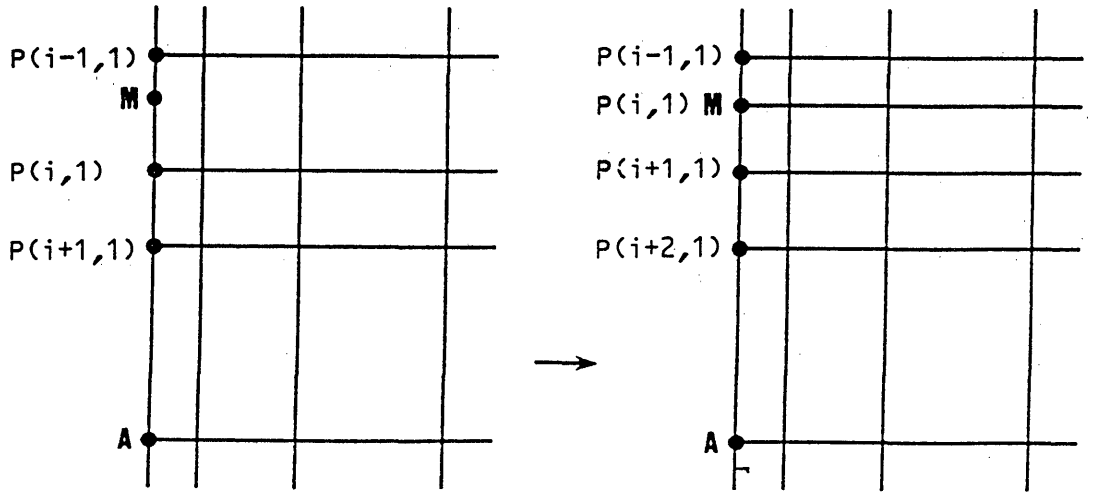

(a) M lies in between nodal points

(b) Reconstructed grid system

Figure 1.10 Reconstruction of the grid system for the normal arrangement

$$Ra = 4\pi \frac{AM \cdot AN}{MN} \cdot \frac{U(M)-U(N)}{I}. \qquad (1.42)$$

The Ra represents the resistivity corresponding to the depth point O. If the potential electrodes M and N lie on the points P(i,1), P(i+1,1), the apparent resistivity can be obtained by

$$Ra = 4\pi \frac{AM \cdot AN}{MN} \cdot \frac{U(i,1)-U(i+1,1)}{I}. \qquad (1.43)$$

Also, the accuracy of the result would be much increased by inserting two horizontal grid lines which represent the vertical positions of the potential electrodes M and N, and

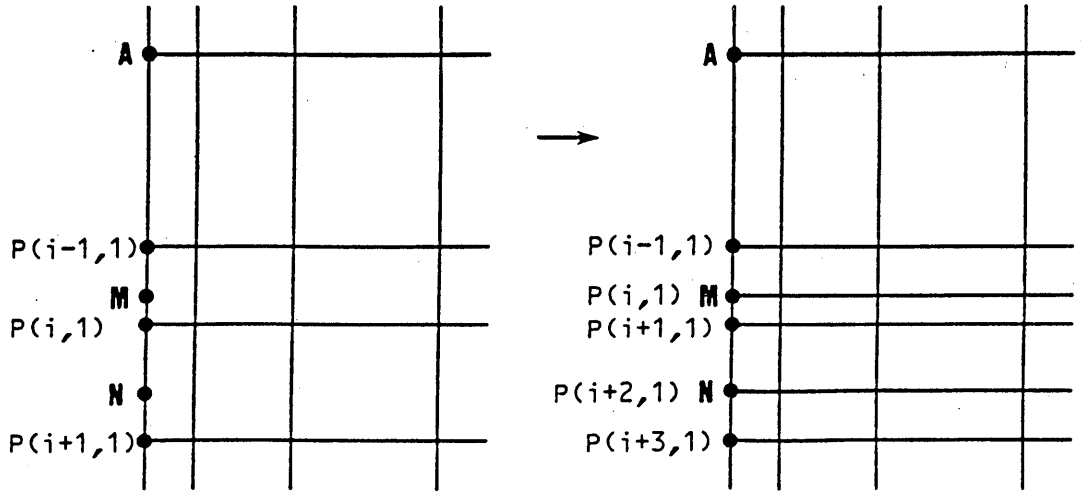

(a) M and N lie in between nodal points

(b) Reconstructed grid system

Figure 1.11 Reconstruction of the grid system for the lateral arrangement

by reconstructing a grid system (Figure 1.11). The elements which were associated with P(i,1) and P(i+1,1) are assigned to P(i+1,1) and P(i+3,1), respectively. The element associated with M is assigned to P(i,1) and the element associated with N is assigned to P(i+2,1).

1.4 Verification of the Results

The numerical results obtained from the finite difference method have been checked against other available solutions in limiting cases. These include the analytic solutions for the horizontally layered earth model and for the cylindrically layered earth model, and the integral equation solution. All tests have indicated that the finite difference (FD) method is accurate, computationally efficient, and versatile.

1.4.1 Comparison with the Analytical Solutions

The first test case involves horizontally layered model in the absence of a borehole. In this case the medium is divided into a number of layers. Each layer is bounded by plane-parallel boundaries and has specific resistivity and thickness. Determination of the potential field in the medium is developed by Van Nostrand and Cook (1966) and the recursive expressions for the evaluation of apparent

resistivities are obtained by Daniels (1978) and Yang and Ward (1984). The Romberg integration method (Carnahan et al, 1969) is used to perform the numerical integration.

A synthetic log for the 16" short normal tool in the multiple beds is presented in Figure 1.12 in which the resistivities of the beds are 10, 100, 5, and 20 ohm-m from the top to bottom. The thicknesses of the second and the third bed are 100" each, and the top and the bottom beds have infinite thicknesses. The departure of the FD method from the analytical solution is vanishingly small. The relative error involved in the FD method with 39 by 20 grid system is less than 1 percent. Excellent agreement was also obtained for a wide variety of resistivity and bed thickness combinations. If increased accuracy is required, such as in the high resistivity contrast case, a finer grid system must be generated. Due to the adaptability of the grid generation scheme, it can be easily performed by specifying smaller numbers of $\Delta r(1)$, $\Delta z(io)$, and grid expanding ratios.

A synthetic log for the 18′ lateral device in the multibeds is shown in Figure 1.13 in which the resistivities of the beds are 10, 100, 5, and 20 ohm-m from the top to bottom. The thicknesses of the second and the third bed are 100′ each, and the top and bottom bed also have infinite thicknesses. The departure of the solution from the

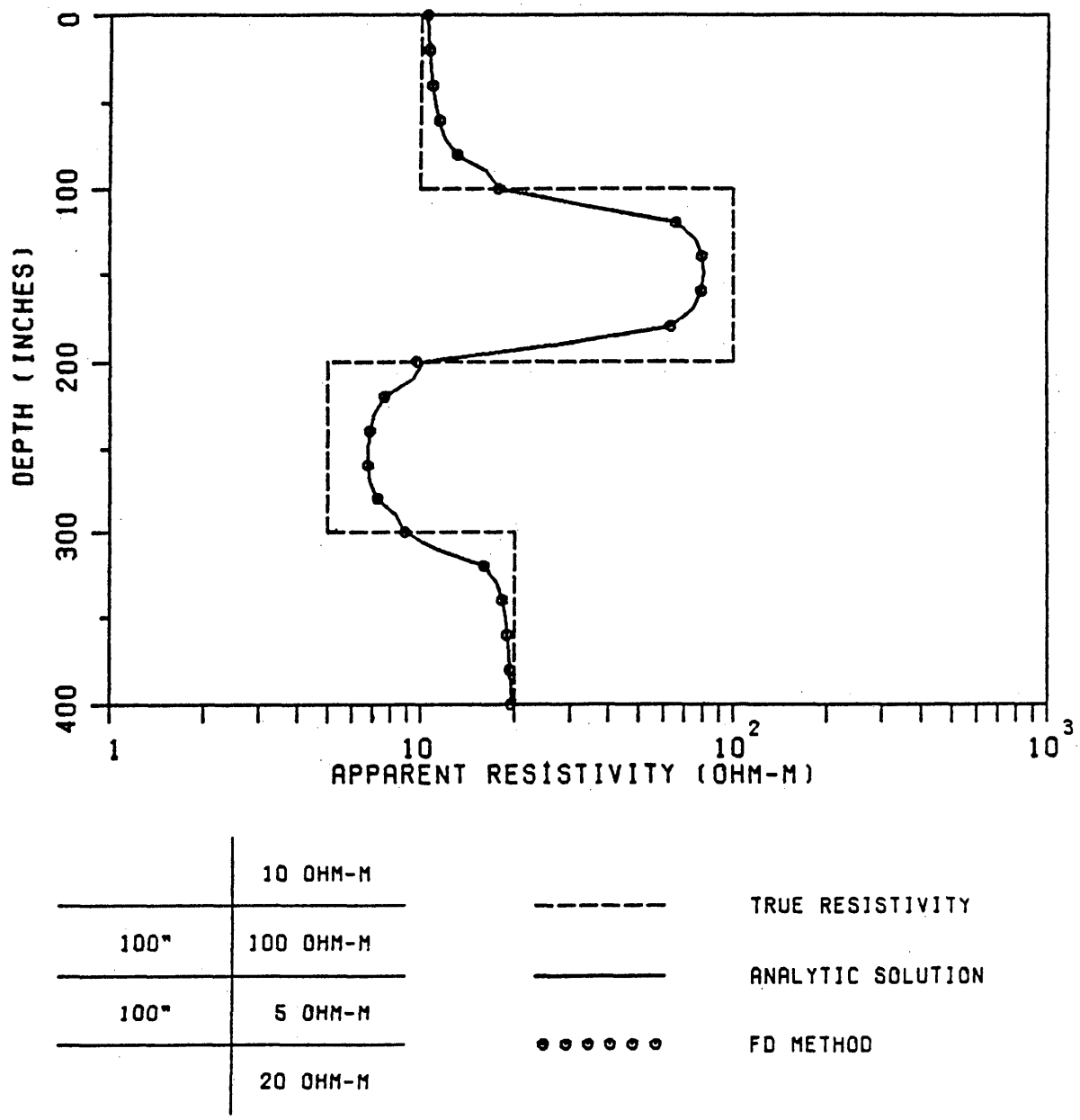

Figure 1.12 Comaparison of the FD method with analytical solution for the 16" normal arrangement (horizontal lyers)

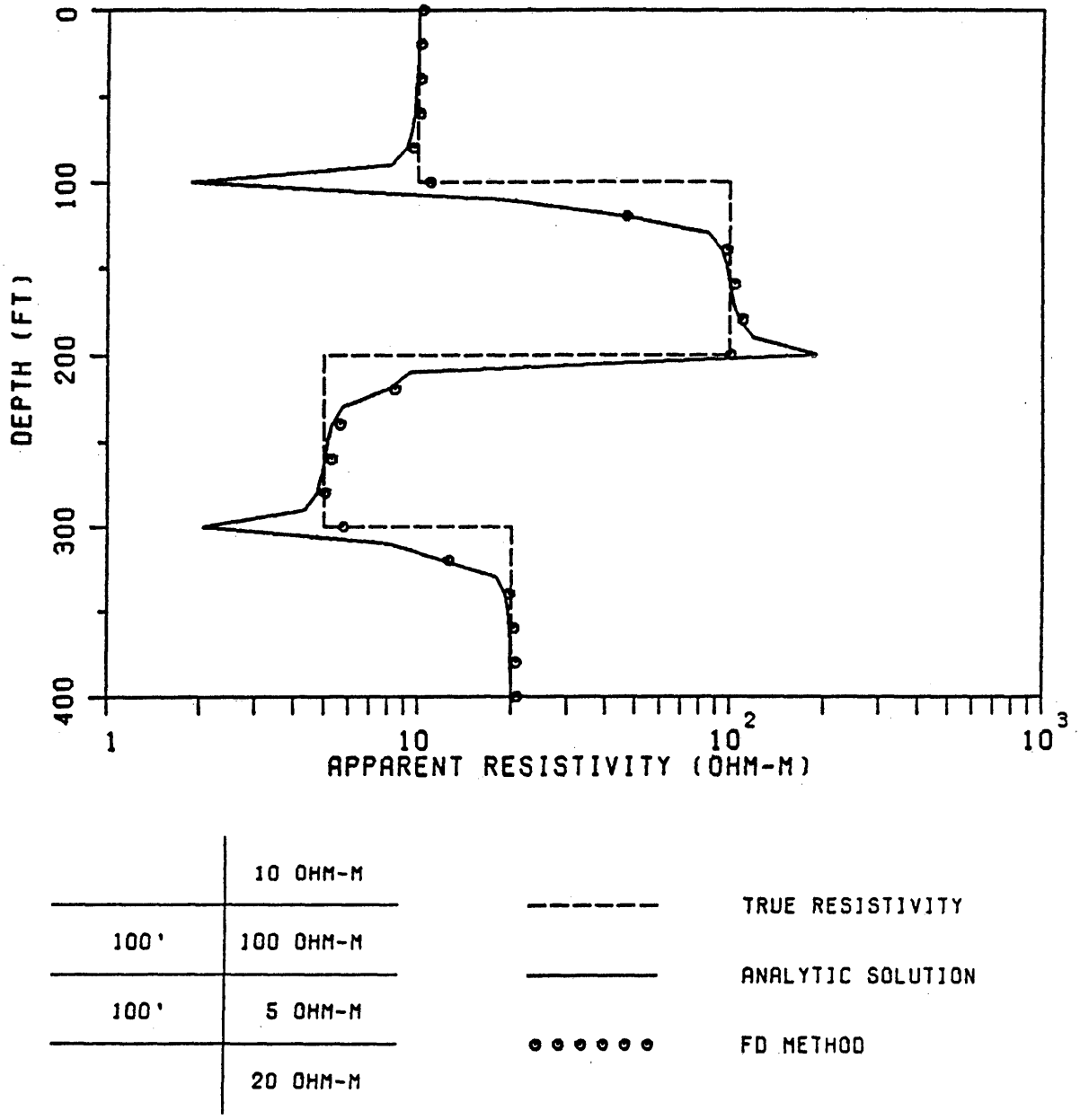

Figure 1.13 Comparison of the FD method with analytical solution for the 18' lateral arrangement (horizontal layers)

analytical solution is larger than that of short normal case due to the potential electrode span effect and the errors involved in calculating potential gradient at the logging point. In the FD method the potential gradient is obtained by calculating the slope of potential distribution at the measuring point, while in the analytic soution potential gradient is directly calculated from taking a derivative of potential function with respect to the electrode spacing. Therefore, in the analytical solution the potential electrode span, MN, is considered as infinitesimally small, while in the FD method the electrode span is always involved and is not small. Another important feature to be noted is that the sharp apparent resistivity discontinuities near the boundaries are smeared out in the finite difference method. The smearing is due to the discretization and the electrode span effects.

The second test case considered here is the cylindrically layered medium which has infinite thickness. The borehole and the invaded zone would be considered in this model. A recursive formula to evaluate the apparent resistivity for this case is developed by Drahos (1984). By using the recursive technique, it becomes possible to solve the problem for an arbitrary number of layers cases. A special lagged convolution technique (Anderson, 1975) is used to perform the numerical integration.

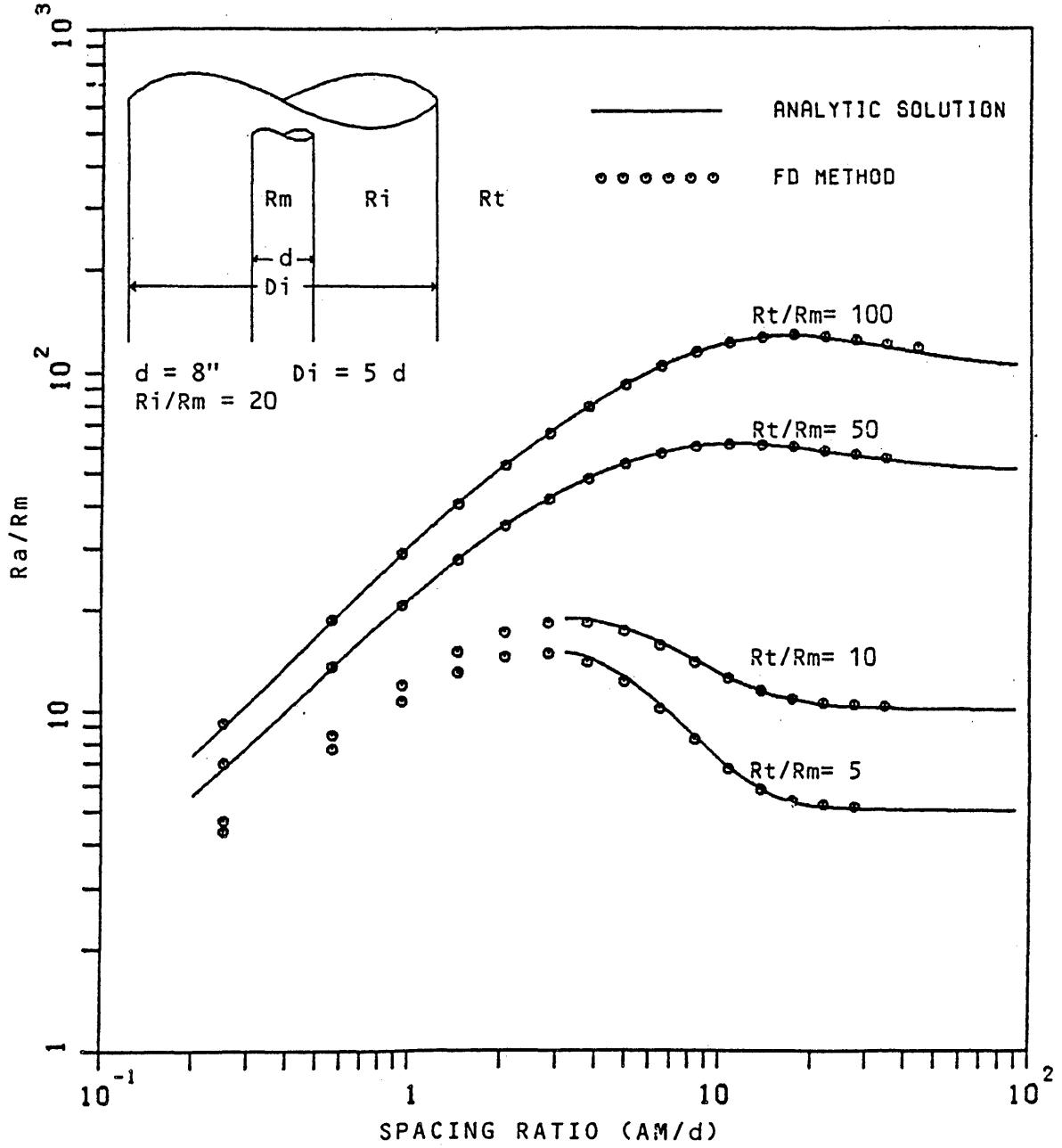

Figure 1.14 Comparison of the FD method with analytical solution for the normal arrangement (cylindrical layers)

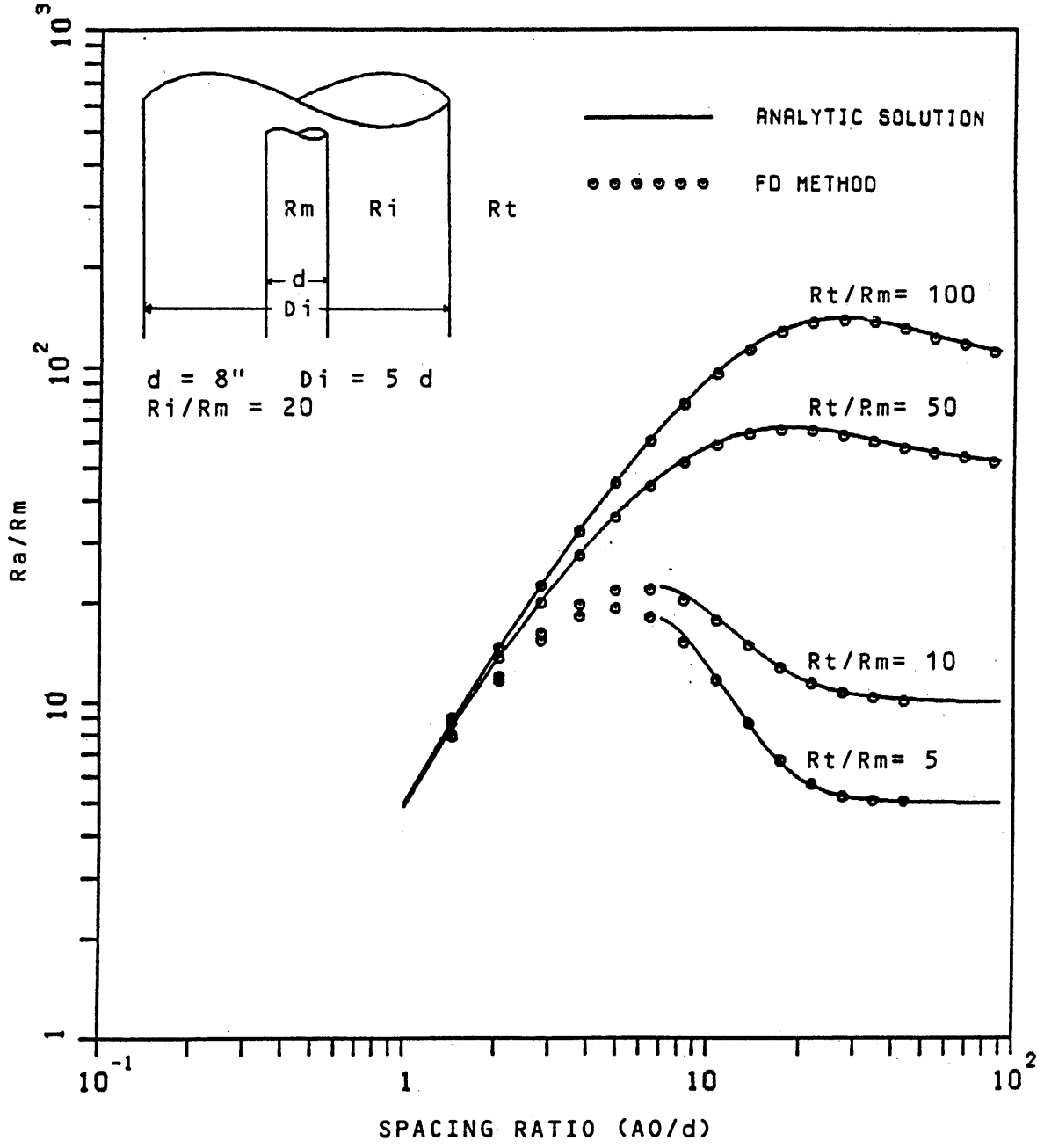

Figure 1.15 Comparison of the FD method with analytical solution for the lateral arrangement (cylindrical layers)

As an example of the cylindrically layered earth model, the departure curves for the three-layer case are generated. The resistivities in the borehole and invaded zone are 1 and 20 ohm-m, respectively. The borehole diameter is 8 inches and the diameter of invasion is 40 inches. True resistivities of 5, 10, 50, and 100 ohm-m are considered. Figure 1.14 shows the departure curves for the normal device. The finite difference method agrees very well with the analytical solution for all of the cases shown. Figure 1.15 shows the departure curves for the lateral device for the same configuration. The slight discrepancy between the FD method and the analytic solution can be improved by reducing the grid sizes.

One of the advantages of the finite difference method is that it can provide apparent resistivities which are extremely difficult to compute by the analytical method. The main limitation of the analytical method is that the numerical integration sometimes diverges, so that the apparent resistivities for the short electrode spacing ratio may not be evaluated accurately. For that reason, the departure curves for Rt/Rm = 10 and Rt/Rm = 5 start from the spacing ratio of 3 in Figure 1.14 and from the spacing ratio of 7 in Figure 1.15.

1.4.2 Comparison with the Integral Equation Solution

To verify the finite difference method in the presence of combined cylindrical and horizontal boundaries, a boundary value problem in which a single horizontal bed boundary and a wellbore are involved is considered and the results are compared with the integral equation solution obtained by Zhang and Shen (1984). Figure 1.16 shows the response of the 16" tool in a borehole crossing a bed boundary. An 8" borehole is filled with mud of 1 ohm-m resistivity and the resistivities of the upper layer and the lower layer are 10 and 100 ohm-m, respectively. Apparent resistivities obtained from the finite difference method coincide with those of the integral equation method.

From the test results it is found that the finite difference method consistently agrees well with either the analytical solution or the integral equation method, whenever these methods can be applied in a simple model. The confidence established in the test results enables us to proceed to forward modeling of complex geometries.

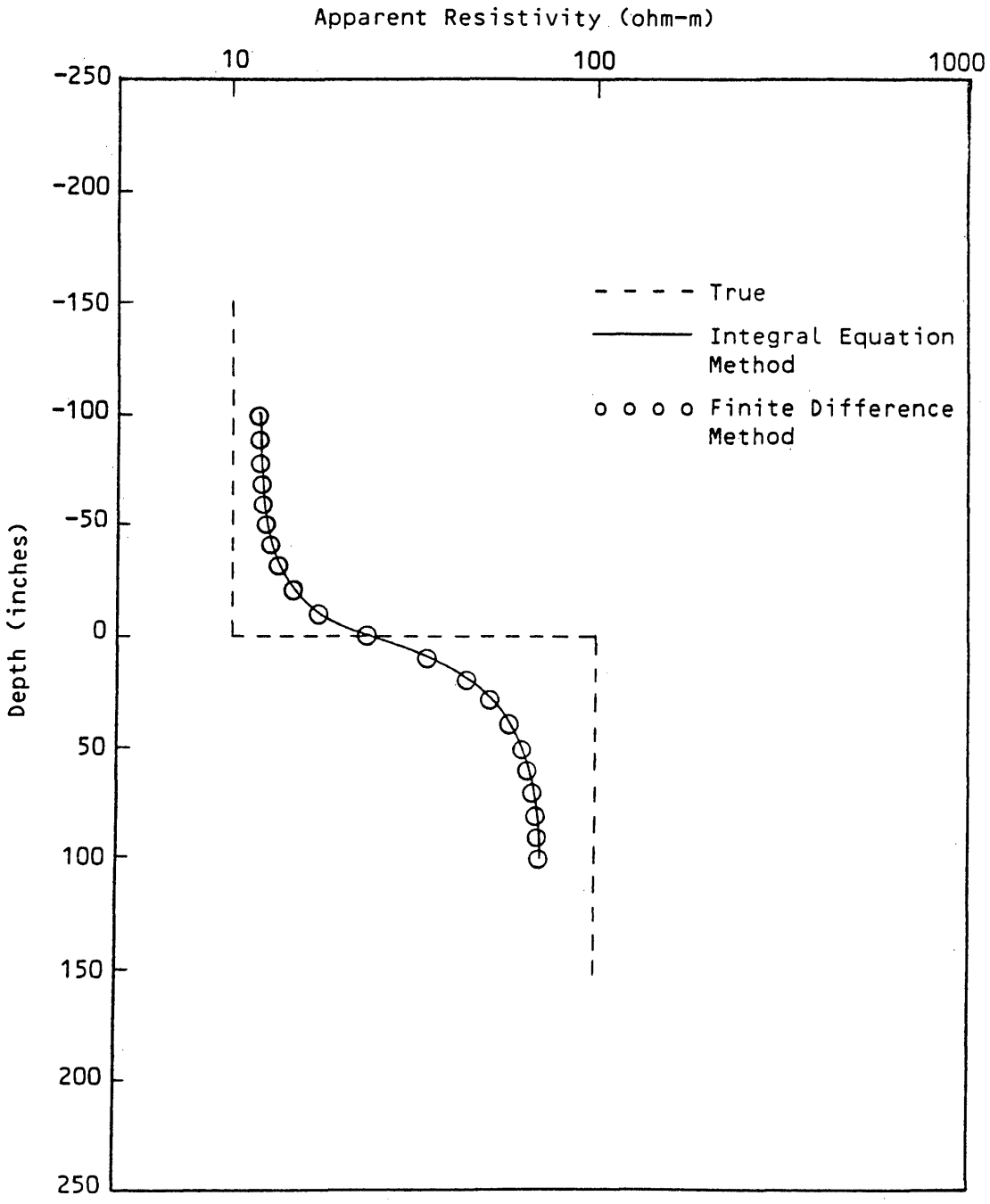

Figure 1.16 Comparison of the FD method with the integral equation solution (Combined boundary model)

1.5 The Analysis of Synthetic Resistivity Logs

The finite difference method is now applied to the combined boundary earth model for which the analytical solutions no longer exist. Both 16" short normal and 18′ lateral arrangements are considered. The electrode span used for the lateral arrangement is 3′. The apparent resistivities for the conductive bed and those for the resistive bed are obtained, and the responses for the thick, critical, and thin bed models are compared each other. The critical bed thickness is the thickness which equals the electrode spacing. The effects due to the variations in earth parameters are also considered. The earth parameters include mud resistivity (Rm), borehole diameter (d), resistivity of invaded zone (Ri), invasion diameter (Di), and true resistivity of the formation (Rt). The complete set of synthetic resistivity logs is included in Appendix A.

1.5.1 Normal Arrangement in a Conductive Bed

Figure 1.17a (or Figure A-1.1) shows the apparent resistivity curves for the 16" normal arrangement in a thick conductive layer model. The resistivities of the shoulder and the target layer are 100 and 10 ohm-m, respectively, and the borehole diameter is 8 inches. Mud

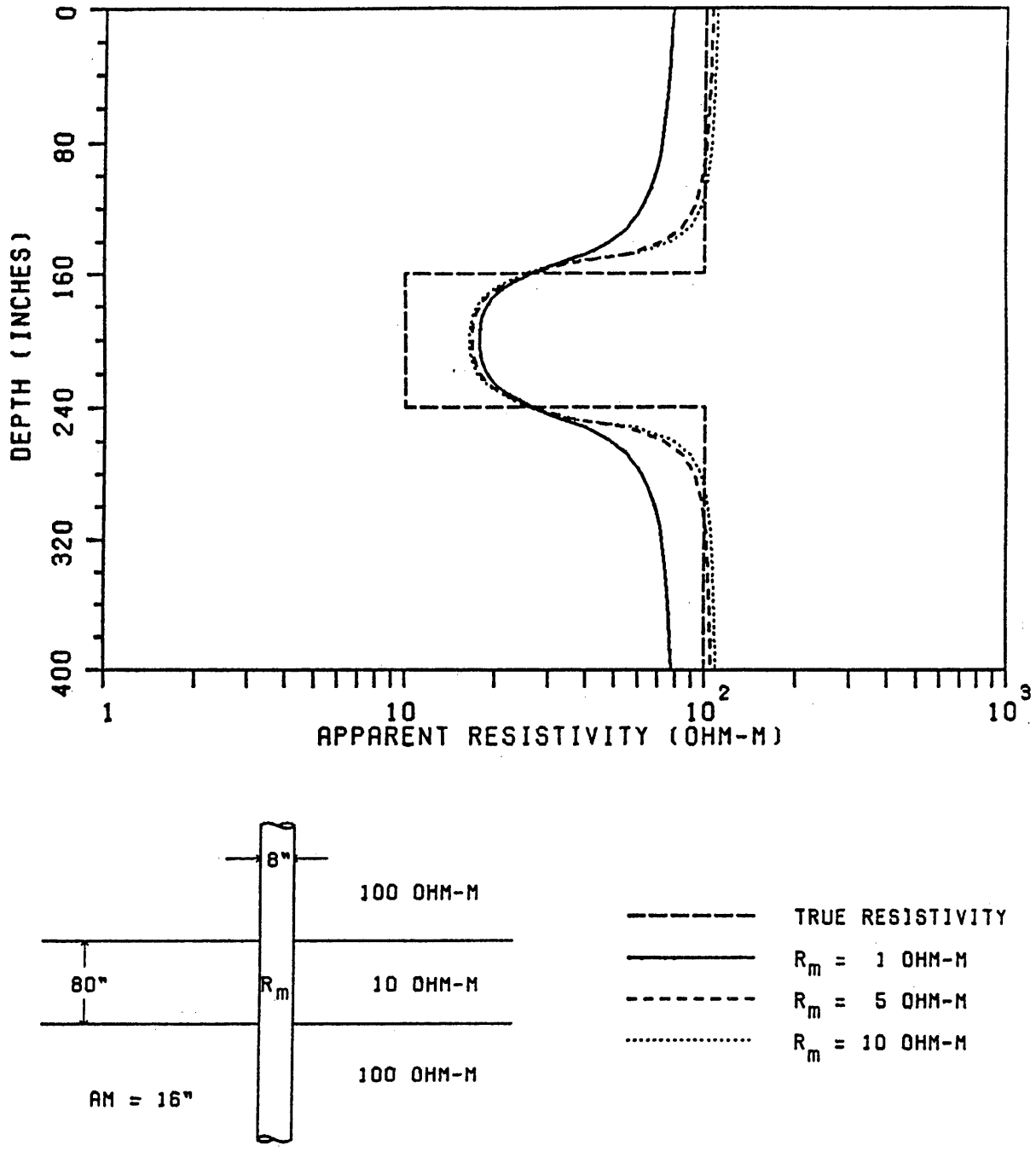

Figure 1.17a Variations in Rm (Normal-Thick-Conductive)

resistivities of 1, 5, and 10 ohm-m are considered. The thickness of the target layer is 80 inches and corresponds to 5 times the electrode spacing. The responses show that there are no appreciable differences between curves, and that the minimum values of the apparent resistivity curves are greater than the true resistivity. When the mud resistivity is low, the resistivity in the shoulder layer has a large departure from the shoulder resistivity. It is also found that the departure from the true resistivity in the conductive layer increases, as the bed thickness decreases (Figure A-1.2, Figure A-1,3).

Figure 1.17b (or Figure A-1.4) shows the apparent resistivity curves for the 16" normal arrangement crossing a thick conductive bed. The mud resistivity is 1 ohm-m, and borehold diameters of 8, 10, and 12 inches are considered. The responses indicate that the departures from the true resistivity in the conductive layer are about the same despite the variations in borehold diameter, and that the minimum values of apparent resistivity curves are greater than the true resistivity.

As the bed thickness becomes smaller (Figure A-1.5, Figure A-1.6), the differences between curves in the conductive layer become larger, and in the shoulder layer the differences become smaller.

Figure 1.17c (or Figure A-1.7) shows the apparent

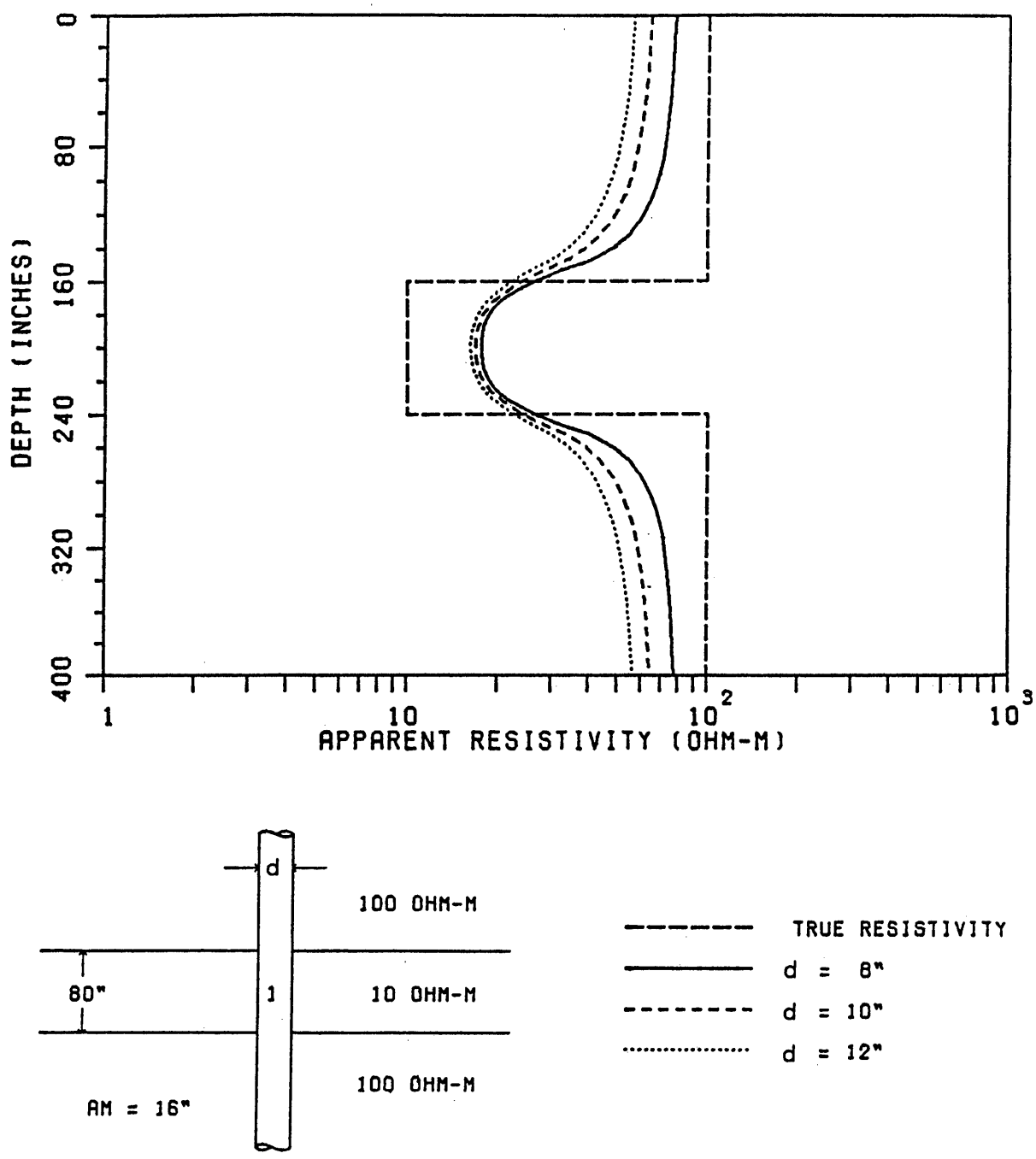

Figure 1.17b Variations in d (Normal-Thick-Conductive)

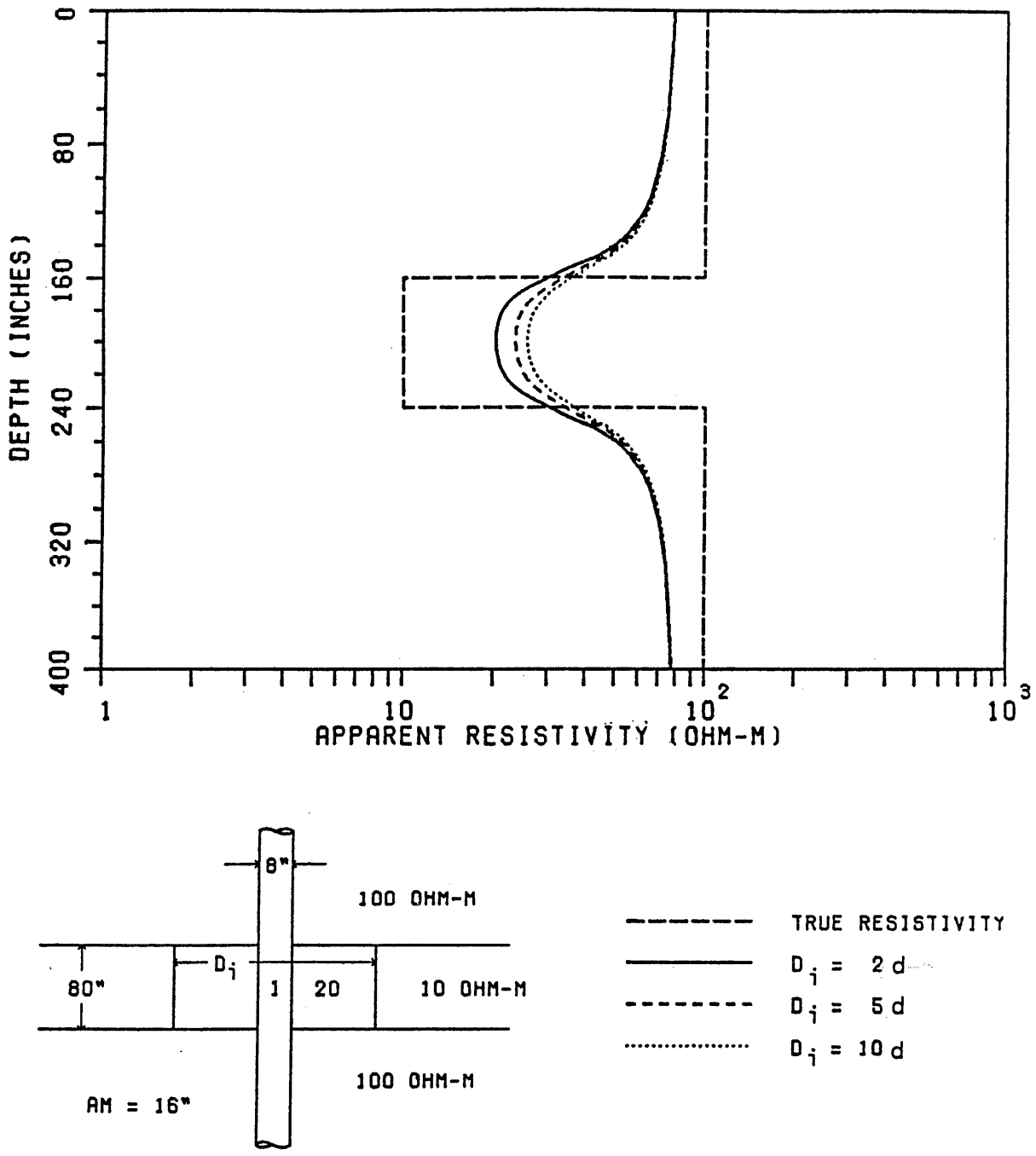

Figure 1.17c Variations in Di (Normal-Thick-Conductive)

resistivity curves for the 16" normal arrangement in a thick conductive bed which has a certain extent of invasion. The resistivity of the invaded zone is 20 ohm-m. Invasion diameters of 2d, 5d, and 10d are considered, where d is the borehole diameter. The responses indicate that the apparent resistivity in the conductive bed is greatly affected by the extent of invasion. The responses also show that as the invasion diameter increases, the departure from the true resistivity increases. The apparent resistivities in the shoulder layer are not appreciably affected by the invasion. Hence, the tails of the curves are merged into one at top and bottom of the figure, and conform with the apparent resistivity curve which is obtained without a consideration of the invasion.

As the bed thickness becomes smaller (Figure A-1.8, Figure A-1.9), the differences between curves in the conductive bed become smaller, and in the shoulder layer the differences become larger.

Figure 1.17d (or Figure A-1,10) shows the apparent resistivity curves for the 16" normal arrangement crossing a conductive thick bed which has an invaded zone. The invasion diameter is 40 inches (5d). The invaded zone resistivities of 20, 50, and 100 ohm-m are considered. The responses indicate that the apparent resistivity in the conductive layer is considerably affected by the variations

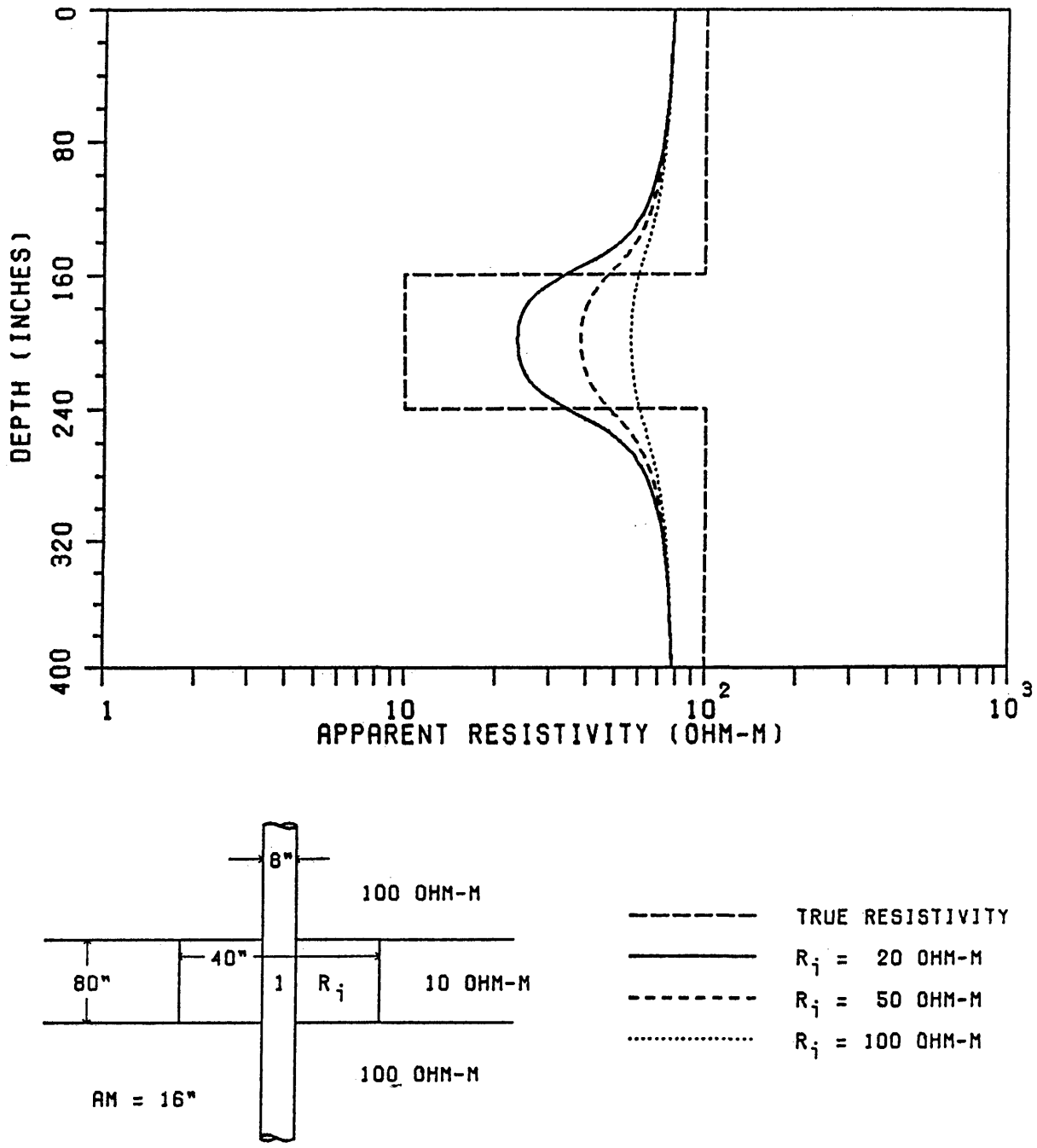

Figure 1.17d Variations in Ri (Normal-Thick-Conductive)

in invaded zone resistivities: The apparent resistivity increases, as the resistivity of the invaded zone increases. The apparent resistivities in the shoulder layer show that there are no appreciable differences between curves due to the variations in invaded zone resistivity.

As the bed thickness decreases (Figure A-1.11, Figure A-1.12), the differences between curves decrease and the departure from the true resistivity increases.

Figure 1.17e (or Figre A-1.13) depicts the apparent resistivity curves for the 16" normal arrangement in a thick conductive bed which has an invaded zone. True resistivities of 1, 2, 5, and 10 ohm-m are considered. The mud resistivity and the resistivity of invaded zone are 1 and 10 ohm-m, respectively. This model can be encountered in nature when the borehole is filled with fresh mud and the formation is saturated with the formation water of low resistivity. The responses show that the apparent resistivity increases with the increase of the true resistivity.

As the bed thickness decreases, the departure from the true resistivity increases (Figure A-1.14, Figure A-1.15).

From the analysis of the apparent resistivity curves for the 16" normal arrangement in conductive beds, it can be concluded that the apparent resistivities are greatly affected by the variations in invaded zone resistivity and diameter. It would be very difficult to identify the true

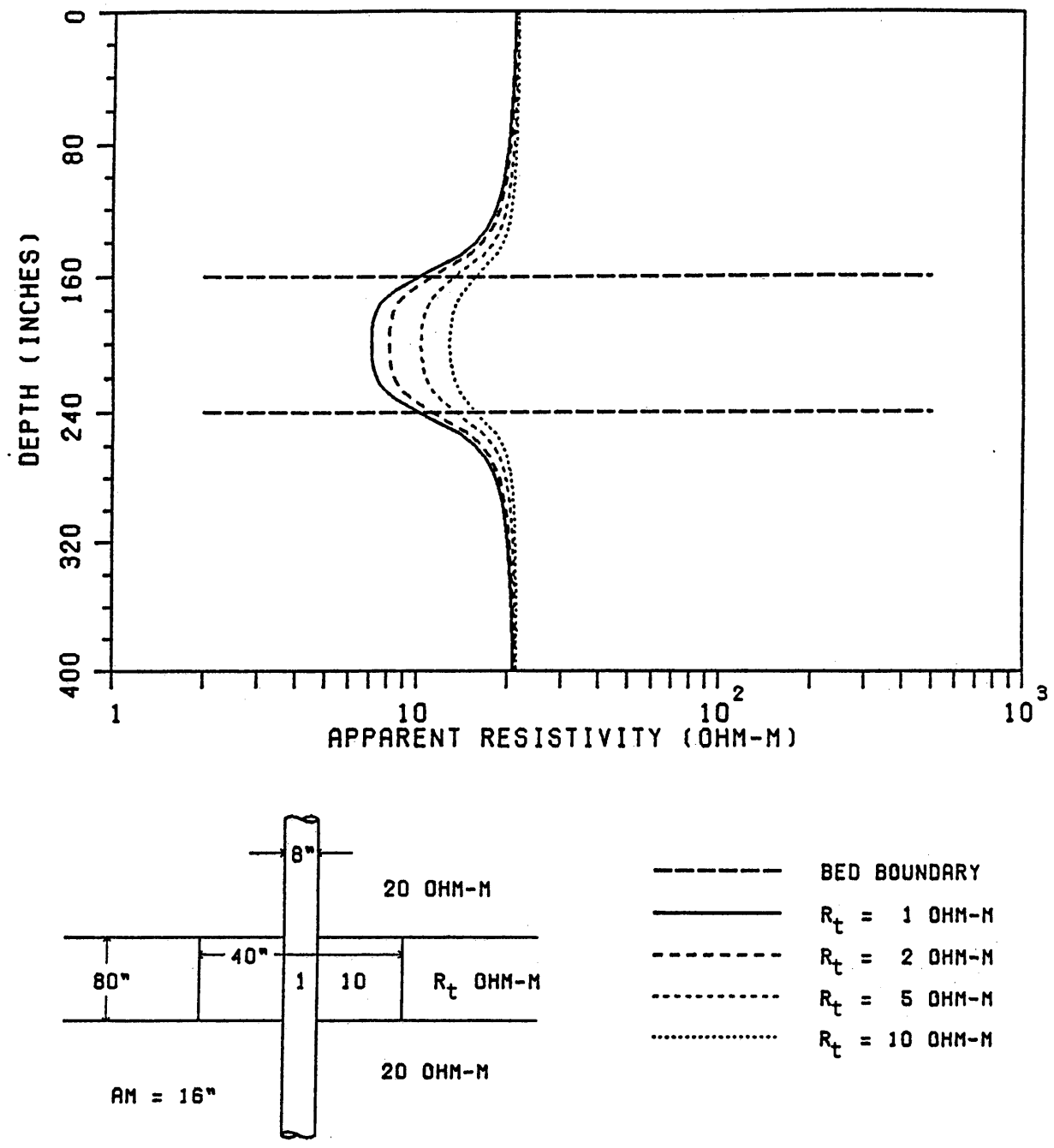

Figure 1.17e Variations in Rt (Normal-Thick-Conductive)

resistivity and the boundaries of a conductive layer, if its thickness is less than the electrode spacing. The large diameter hole and the low-resistivity borehole mud adversely affect the apparent resistivity responses in conductive beds.

1.5.2 Normal Arrangement in a Resistive Bed

Figure 1.18a (or Figure A-1.1) shows the apparent resistivity curves for the 16" normal arrangement in a thick resistive layer model. The resistivities of the shoulder and the target layer are 10 and 100 ohm-m, respectively. The borehole diameter is 8 inches, and mud resistivities of 1, 5, and 10 ohm-m are considered. The thickness of the resistive bed is 80 inches, which corresponds to 5 times the electrode spacing. When the mud resistivity is low, the departure from the true resistivity is large. On the other hand, when the mud resistivity approaches shoulder resistivity, the departure becomes smaller. The responses also show that the maximum values of the apparent resistivity curves are less than the true resistivity.

The departure from the true resistivity in the resistive layer increases, as the bed thickness decreases (Figure A-2.2, Figure A-2.3). If the bed thickness is smaller than the electrode spacing, the apparent resistivity

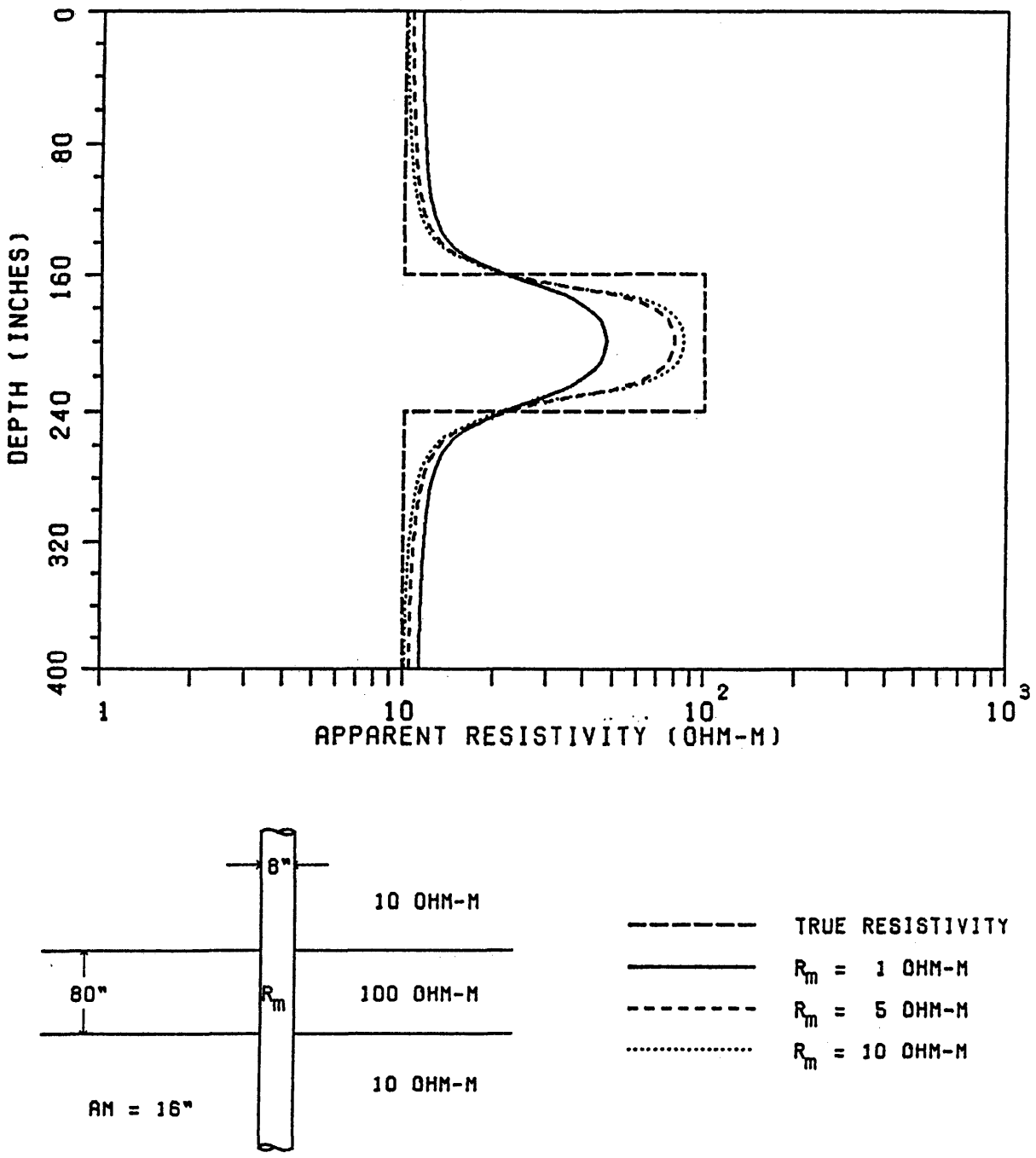

Figure 1.18a Variations in Rm (Normal-Thick-Resisitive)

curves have lower resistivity readings in the resistive bed than those in the shoulder layers. It may lead to the misinterpretation of a resistive thin bed as a conductive thin bed.

Figure 1.18b (or Figure A-2.4) depicts the apparent resistivity curves for the 16" normal arrangement crossing a thick resistive bed. The mud resistivity is 1 ohm-m, and borehole diameters of 8, 10, 12 inches are considered. Unlike the responses for the conductive bed, the apparent resistivity in the resistive bed is affected by the variations in borehole diameter. As the borehole diameter increases, the departure from the true resistivity increases. The peak values of the apparent resistivity curves in the resistive bed is less than the true resistivity of the bed.

As the bed thickness becomes smaller (Figure A-2.5, Figure A-2.6), the differences between curves in the resistive layer become smaller and the departure from the true resistivity becomes larger.

Figure 1.18c (or Figure A-2.7) shows the apparent resistivity curves for the 16" normal arrangement in a thick conductive bed which has a certain extent of invasion. The resistivity of the invaded zone is 20 ohm-m, and invasion diameters of 2d, 5d, and 10d are considered. The responses indicate that the apparent resistivity in the

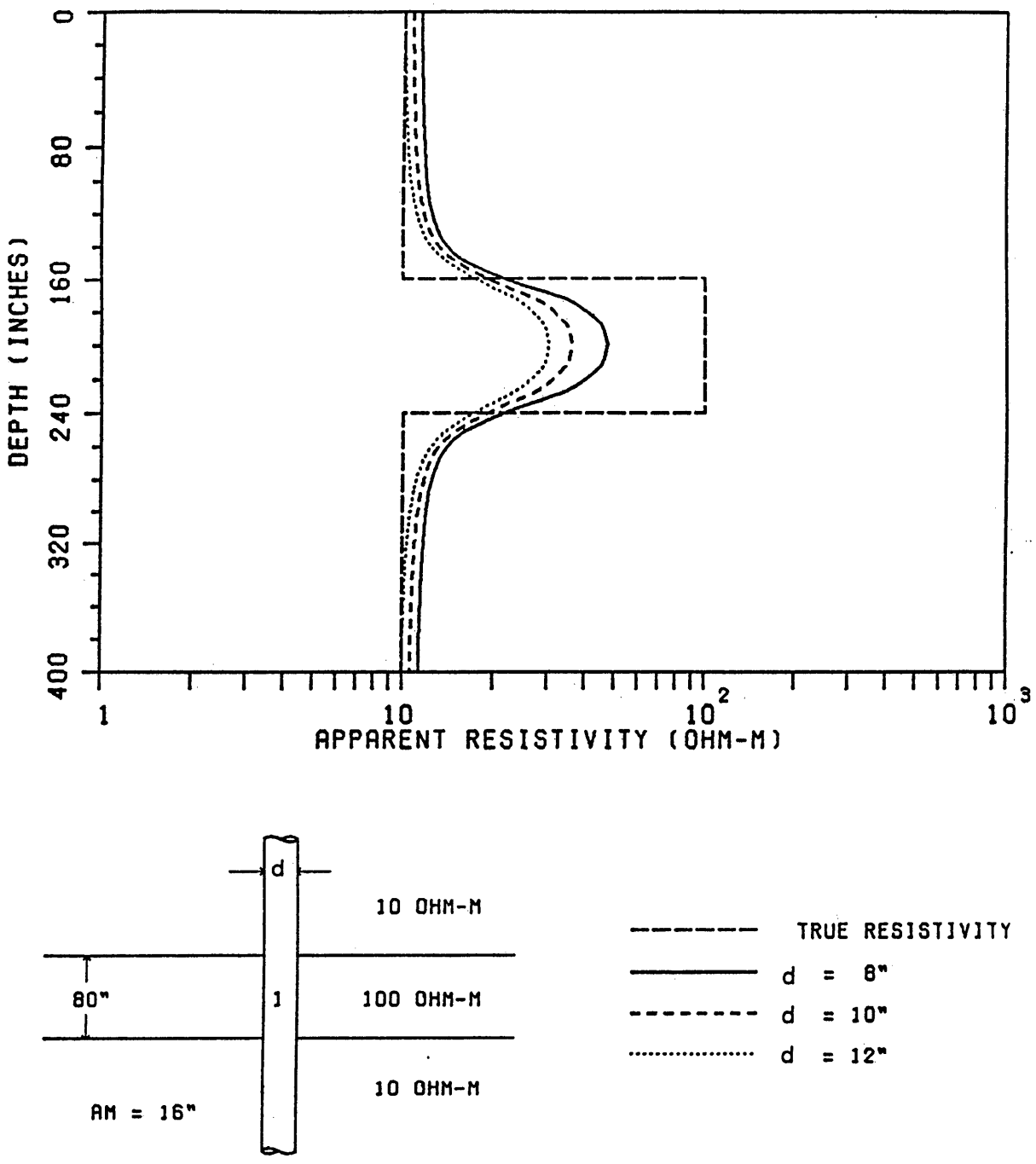

Figure 1.18b Variations in d (Normal-Thick-Resistive)

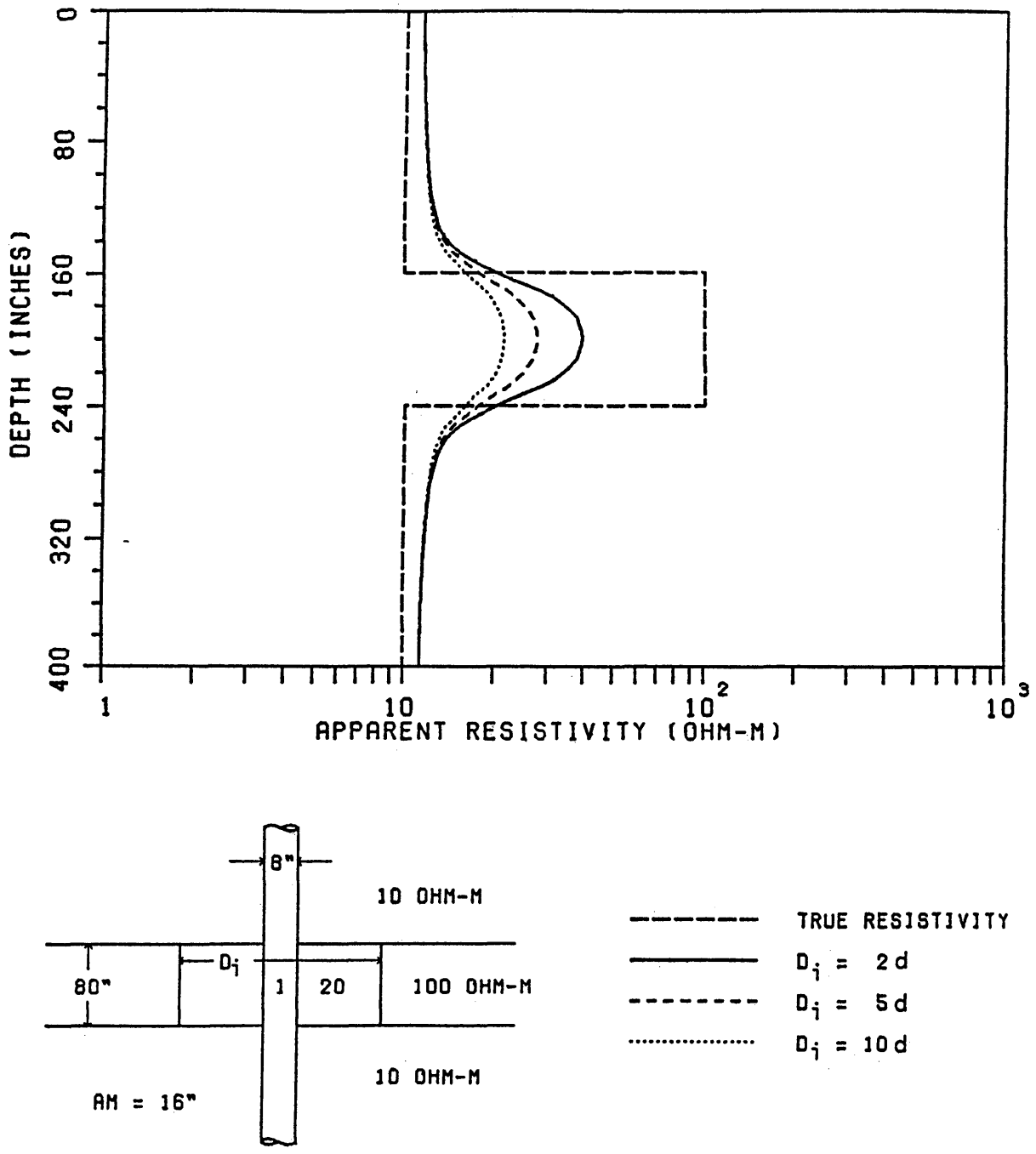

Figure 1.18c Variations in Di (Normal-Thick-Resistive)

resistive bed is greatly affected by the extent of invasion. The departure from the true resistivity is large for the deep invasion, and is small for the shallow invasion. The apparent resistivities in the shoulder layer are not appreciably affected by the invasion except in the vicinities at the bed boundaries. Hence, the tails of the curves are merged into one at the top and bottom of the figure, and conform with the apparent resistivity curve which is obtained without a consideration of the invasion.

As the bed thickness decreases (Figure A-2.8, Figure A-2.9), the differences between curves in the resistive bed decrease, and in the shoulder layer the differences increase.

Figure 1.18d (or Figure A-1.10) depicts the apparent resistivity curves for the 16" normal arrangement crossing a thick resistive bed which has an invaded zone. Invasion diameter is 40 inches (5d), and the invaded zone resistivities of 10, 20, and 50 ohm-m are considered. The responses indicate that the apparent resistivity in the resistive bed is considerably affected by the variations in resistivities of the invaded zone. The departure from the true resistivity decreases, as the invaded zone resistivity increases. The apparent resistivities in the shoulder layer show that there are no appreciable differences between curves except those near the bed boundaries.

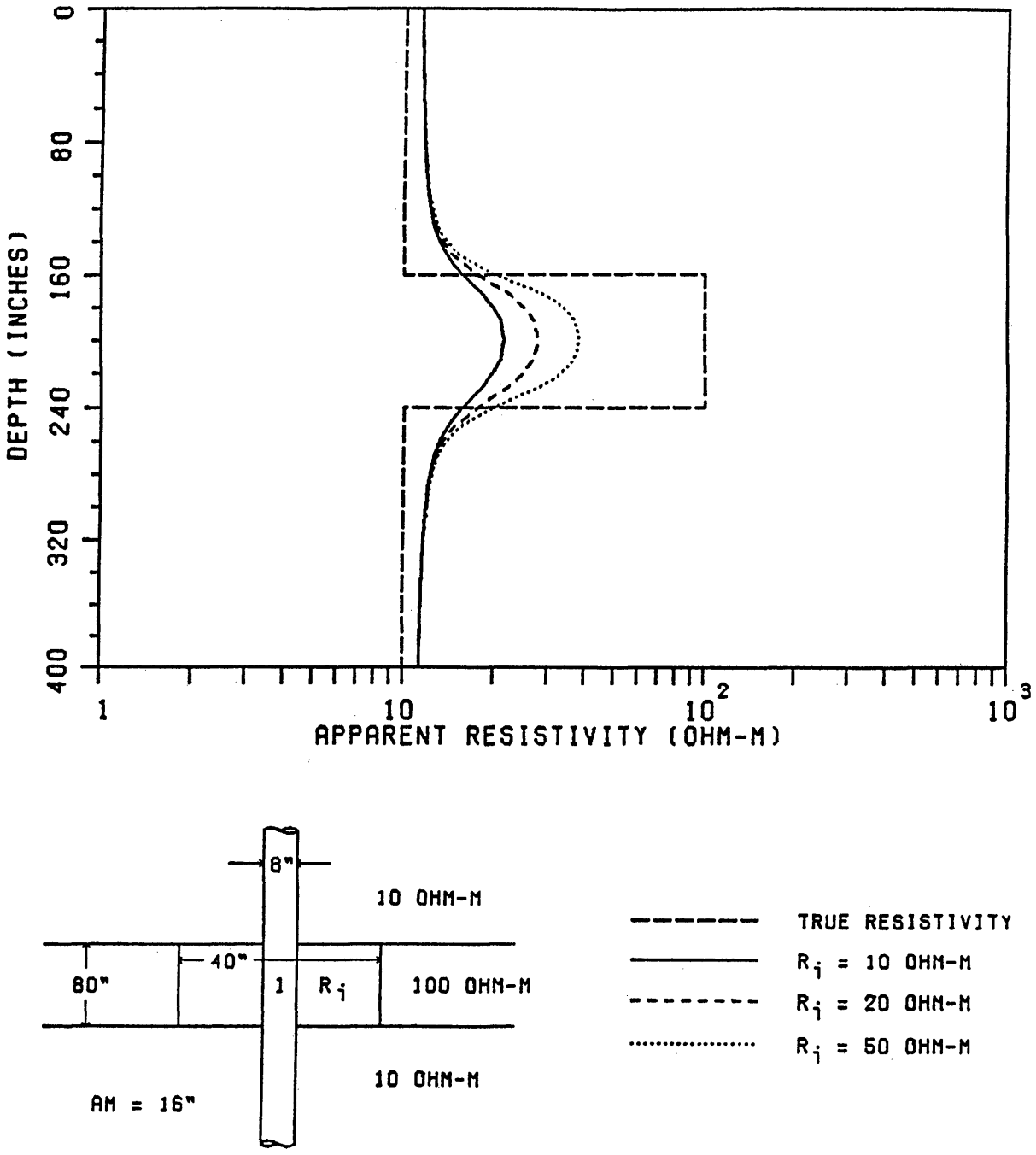

Figure 1.18d Variations in Ri (Normal-Thick-Resistive)

As the bed thickness decreases (Figure A-2.11, Figure A-2.12), the differences between curves decrease and the departure from the true resistivity increases.

Figure 1.18e (or Figure A-2.13) shows the apparent resistivity curves for the 16" normal arrangement in a thick resistive bed which has an invaded zone. True resistivities of 10, 20, 50, and 100 ohm-m are considered. The mud resistivity and the resistivity of invaded zone are 1 and 10 ohm-m, respectively. This model can be obtained by considering an oil bearing zone. For example, in the case where the formation resistivity factor (F) of the target layer is 20, and the resistivity index (I) is 25, and the resistivity of the formation water is 0.1 ohm-m, the true resistivity of the formation will be 50 ohm-m. Also, the resistivity of the invaded zone will be 10 ohm-m, if the invaded zone is filled with the 0.5 ohm-m mud filtrate. The responses show that the apparent resistivity increases with the increase of the true resistivity.

As the bed thickness decreases, the departure from the true resistivity increases (Figure A-2.14, Figure A-2.15). For the resistive thin layer model, there are no appreciable differences between curves, and the bed boundaries are not distinguishable.

From the analysis of the apparent resistivity curves for the 16" normal arrangement in the resistive bed, it can be

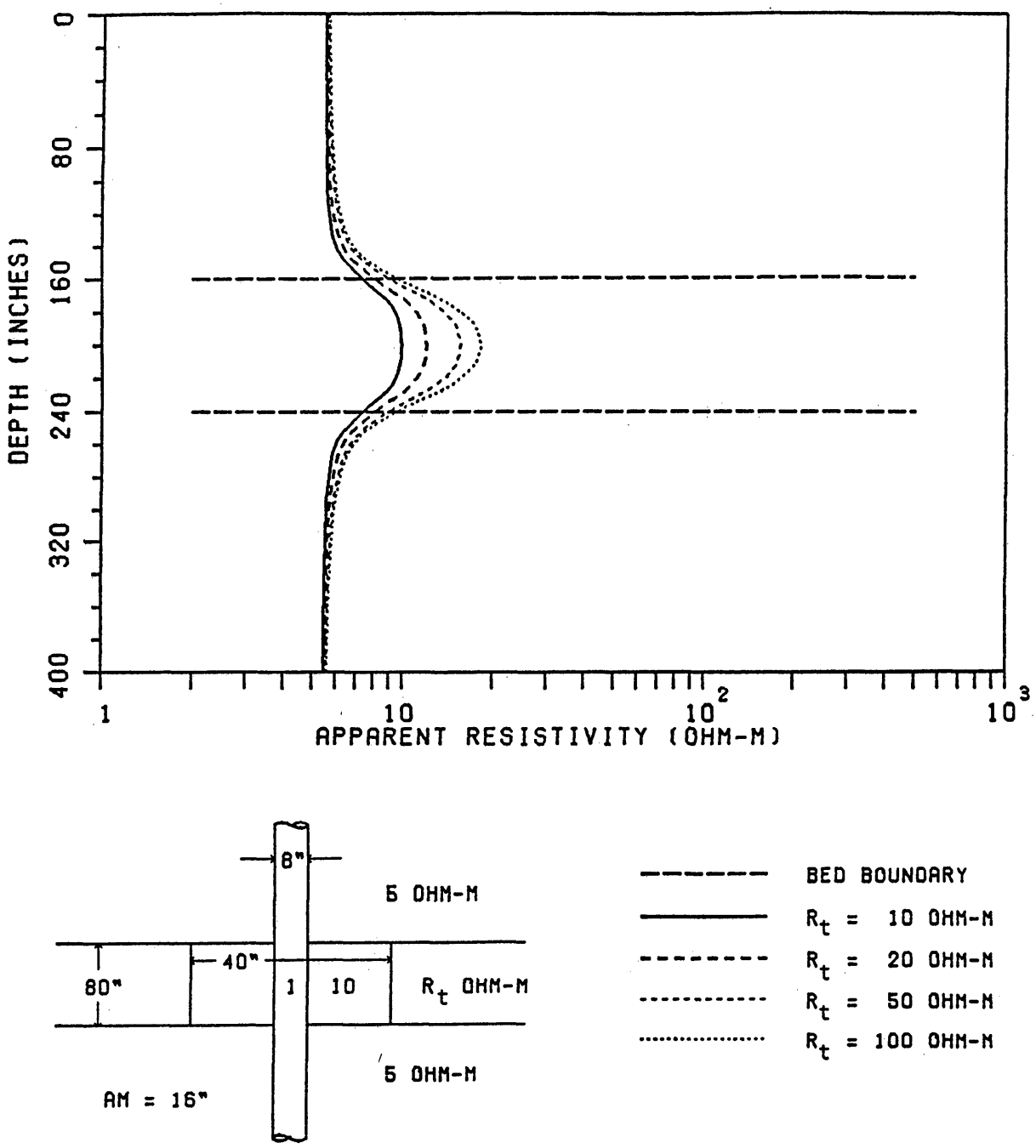

Figure 1.18e Variations in Rt (Normal-thick-Resistive)

concluded that the apparent resistivity in thick resistive beds is greatly affected by the extent and the nature of the invasion. It would be very difficult to discriminate the boundaries and the true resistivity of the formation if the bed thickness is less than the electrode spacing. The large diameter hole and the low-resistivity borehole mud adversely affect the apparent resistivity responses in resistive beds.

In general, the logging environment which affects the response of the normal electrode arrangement can be summarized as follows.

1. Borehole effects: The large diameter hole and the low-resistivity mud increase the departure from the true resistivity.
2. Invasion effects: Since the radius of investigation of the 16" normal arrangement is small, the apparent resistivity is greatly affected by the invasion diameter and the invaded zone resistivity.
3. Bed thickness effects: The bed thickness effects become significant when the thickness is less than 5 times the electrode spacing. If the bed thickness is less than or equal to the electrode spacing, this bed cannot be discriminated by the normal arrangement devices.

1.5.3 Lateral Arrangement in a Conductive Bed

Figure 1.19a (or Figure A-3.1) shows the apparent resistivity curves for the 18′ lateral arrangement in a thick conductive layer model. The resistivities of the shoulder and the target layer are 100 and 10 ohm-m, respectively. The borehole diameter is 8 inches, and mud resistivities of 1,5, and 10 ohm-m are considered. The thickness of the conductive bed is 90 feet, which corresponds to 5 times the electrode spacing. The responses indicate that there are no appreciable differences between curves in the conductive bed, while the differences are large in the shoulder layer. The apparent resistivity readings at the flat portion of the curve near the middle of the layer provide the true resistivity estimation of the formation. If the mud resistivity is low, the departure from the shoulder resistivity becomes larges.

As the bed thickness decreases (Figure A-3.1, Figure A-3.2), the departure from the true resistivity increases and the flat portion of the curve in the conductive layer disappears. It is also found that low-resistivity borehole mud affects the apparent resistivity readings in a conductive bed.

Figure 1.19b (or Figure A-3.4) depicts the apparent resistivity curves for the 18′ lateral arrangement crossing a thick conductive bed. The mud resistivity is 1 ohm-m, and

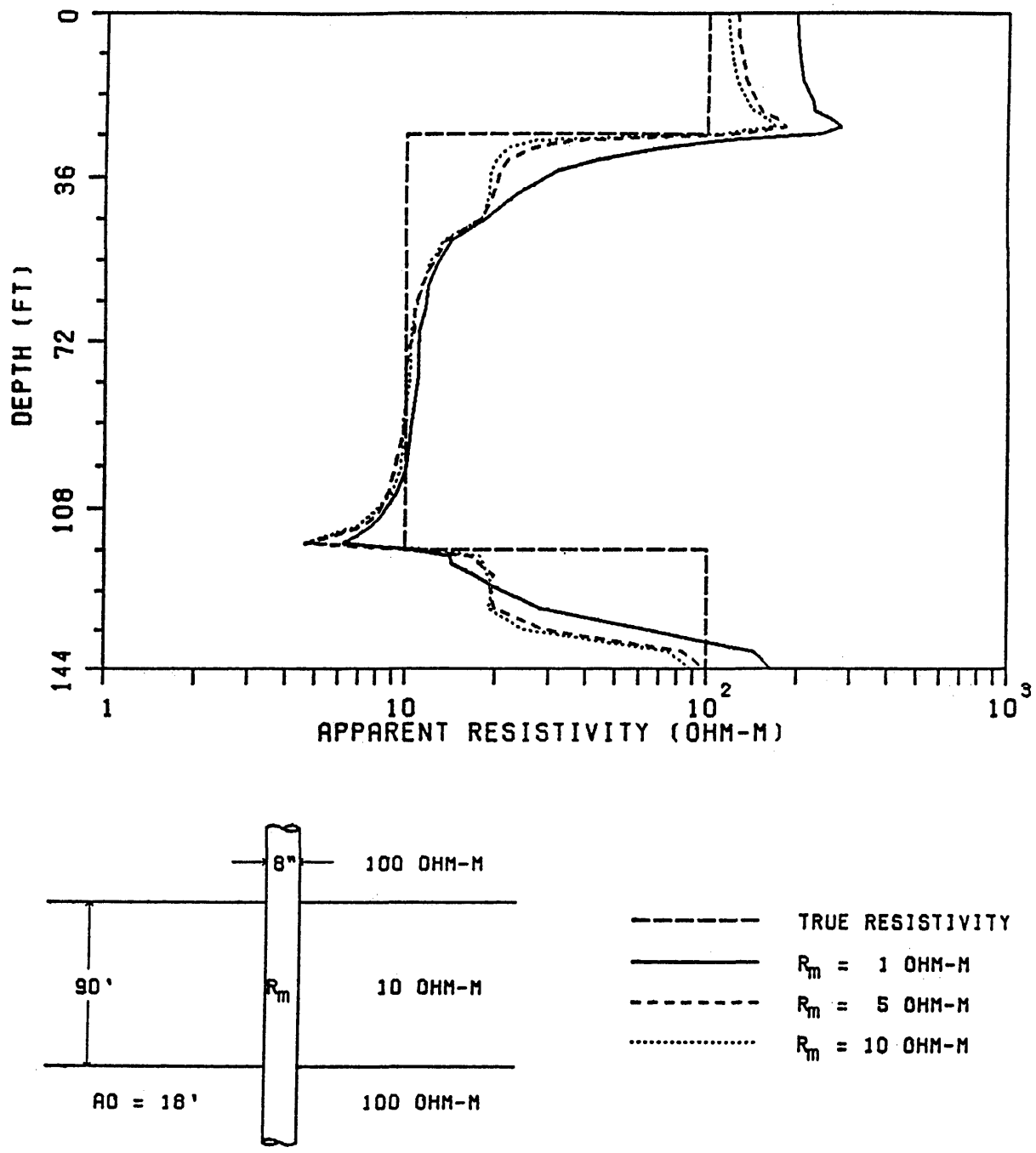

Figure 1.19a Variations in Rm (Lateral-Thick-Conductive)

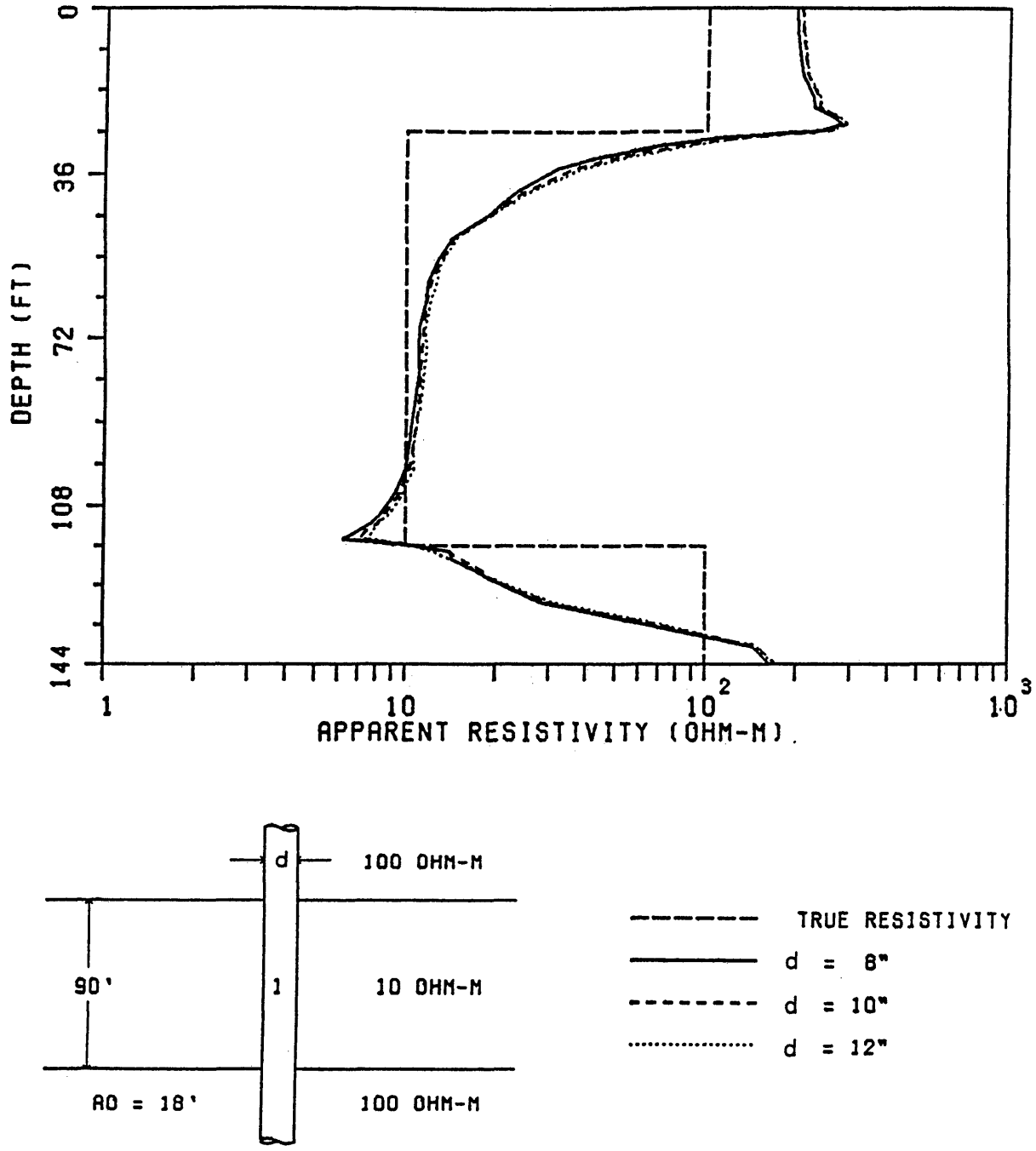

Figure 1.19b Variations in d (Lateral-Thick-Conductive)

borehole diameters of 8, 10, and 12 inches are considered. The responses indicate that there are no appreciable differences between curves in the conductive layer or in the shoulder layer due to the variations in borehole diameter. The apparent resistivity values in the conductive layer yield a good approximation of the true resistivity.

As the bed thickness decreases (Figure A-3.5, Figure A-3.6), the departure from the true resistivity increases, and the flat portion of the curve in the conductive layer disappears.

Figure 1.19c (or Figure A-3.7) shows the apparent resistivity curves for the 18′ lateral arrangement in a thick conductive bed which has a certain extents of invasion. The resistivity of the invaded zone is 20 ohm-m, and invasion diameters of 2d, 5d, and 10d are considered. Since the maximum invasion diameter is only 80", which is relatively small compared to the electrode spacing, the variations in invasion diameter does not appreciably affect the response of the lateral arrangement devices. The departure from the true resistivity slightly increases with the increase of invasion diameter. The true resistivity can be estimated by taking the apparent resistivity at the flat portion of the curve in the conductive layer.

As the bed thickness decreases (Figure A-3.8, Figure A-3.9), the departure from the true resistivity increases,

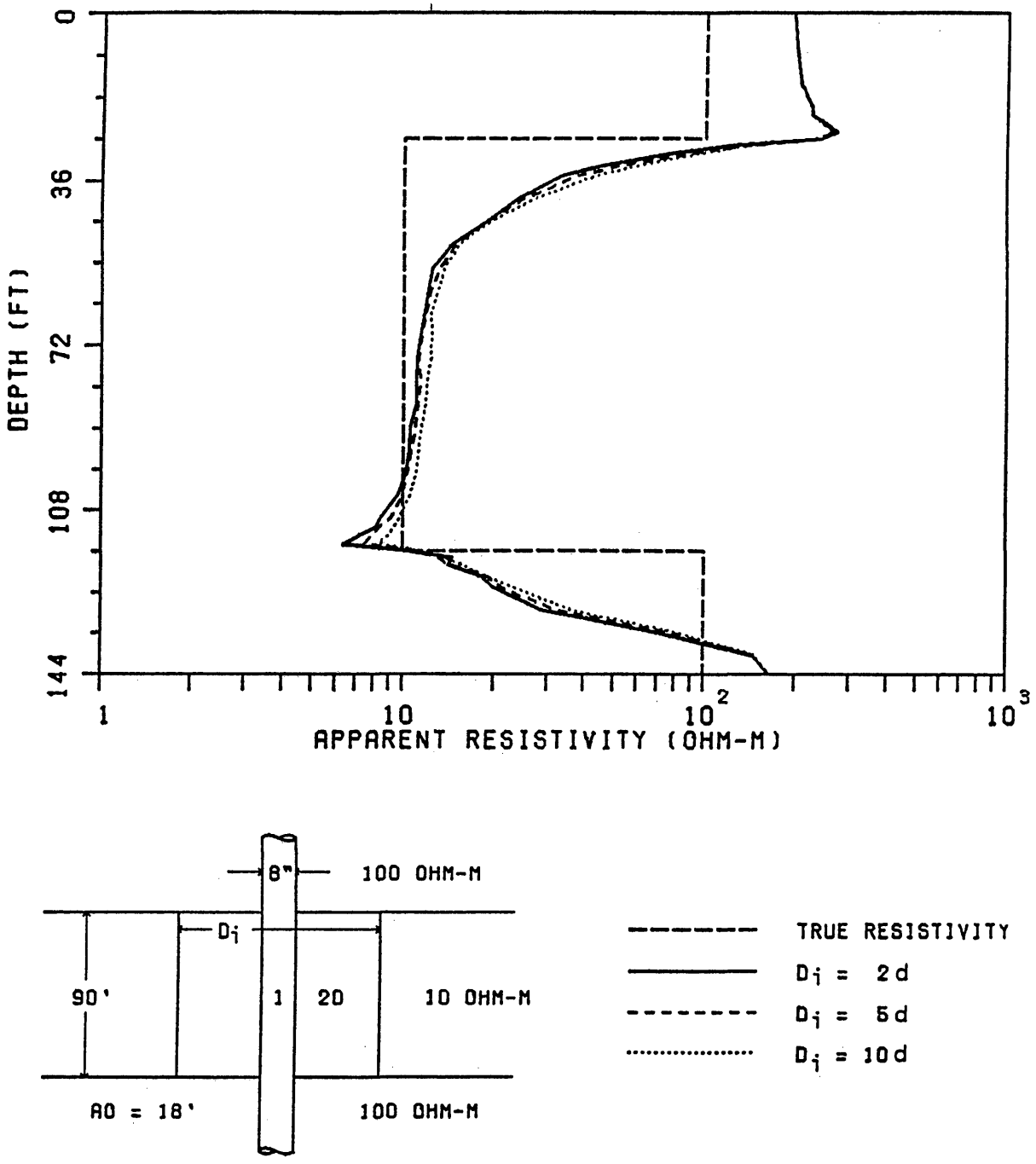

Figure 1.19c Variations in Di (Lateral-Thick-Conductive)

and the flat portion of the curve in the conductive layer disappears.

Figure 1.19d (or Figure A-3.10) depicts the apparent resistivity curves for the 18′ lateral arrangement crossing a thick conductive bed which has an invaded zone. The invasion diameter is 40 inches, which corresponds to 5/27 of the electrode spacing. Invaded zone resistivities of 20, 50, and 100 ohm-m are considered. When the invaded zone resistivity is 20 ohm-m, which equals two times the true resistivity, the apparent resistivity curve is very similar to the one obtained without a consideration of invasion. Hence, the apparent resistivity curve yields a good approximation of the true resistivity of the formation. If the invaded zone resistivity is high, the potential distribution between the current source and the measuring electrodes is distorted by the high-resistivity invaded zone. Consequently, the invasion effects become significant. As a result, the departure from the true resistivity increases with the increase of invaded zone resistivity. The same argument can be applied to the conductive thin layer models (Figure A-3.11, Figure A-3.12).

Figure 1.19e (or Figure A-3.13) shows the apparent resistivity curves for the 18′ lateral arrangement in a thick conductive bed which has an invaded zone. The mud resistivity and the resistivity of the invaded zone are 1

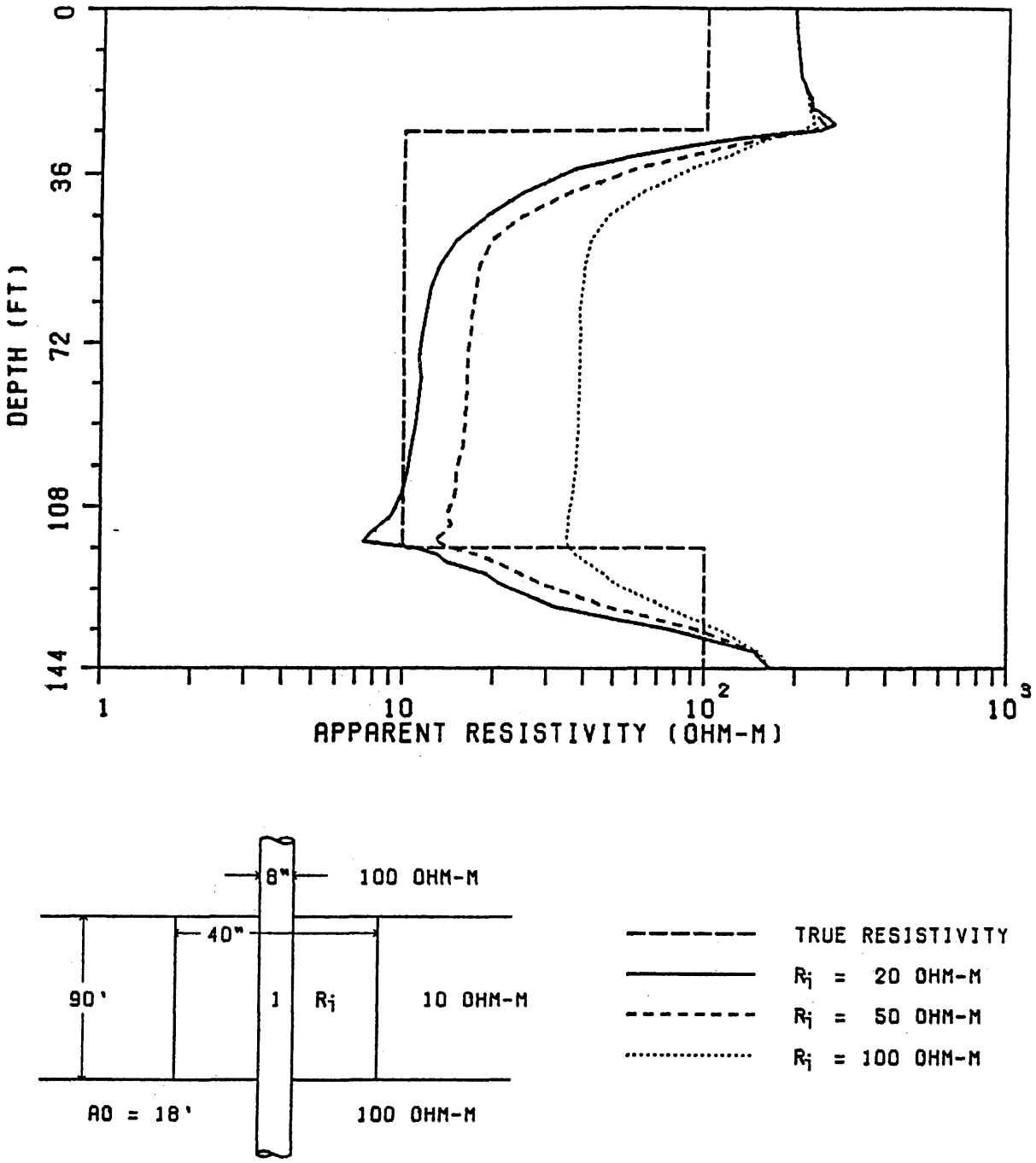

Figure 1.19d Variations in Ri (Lateral-Thick-Conductive)

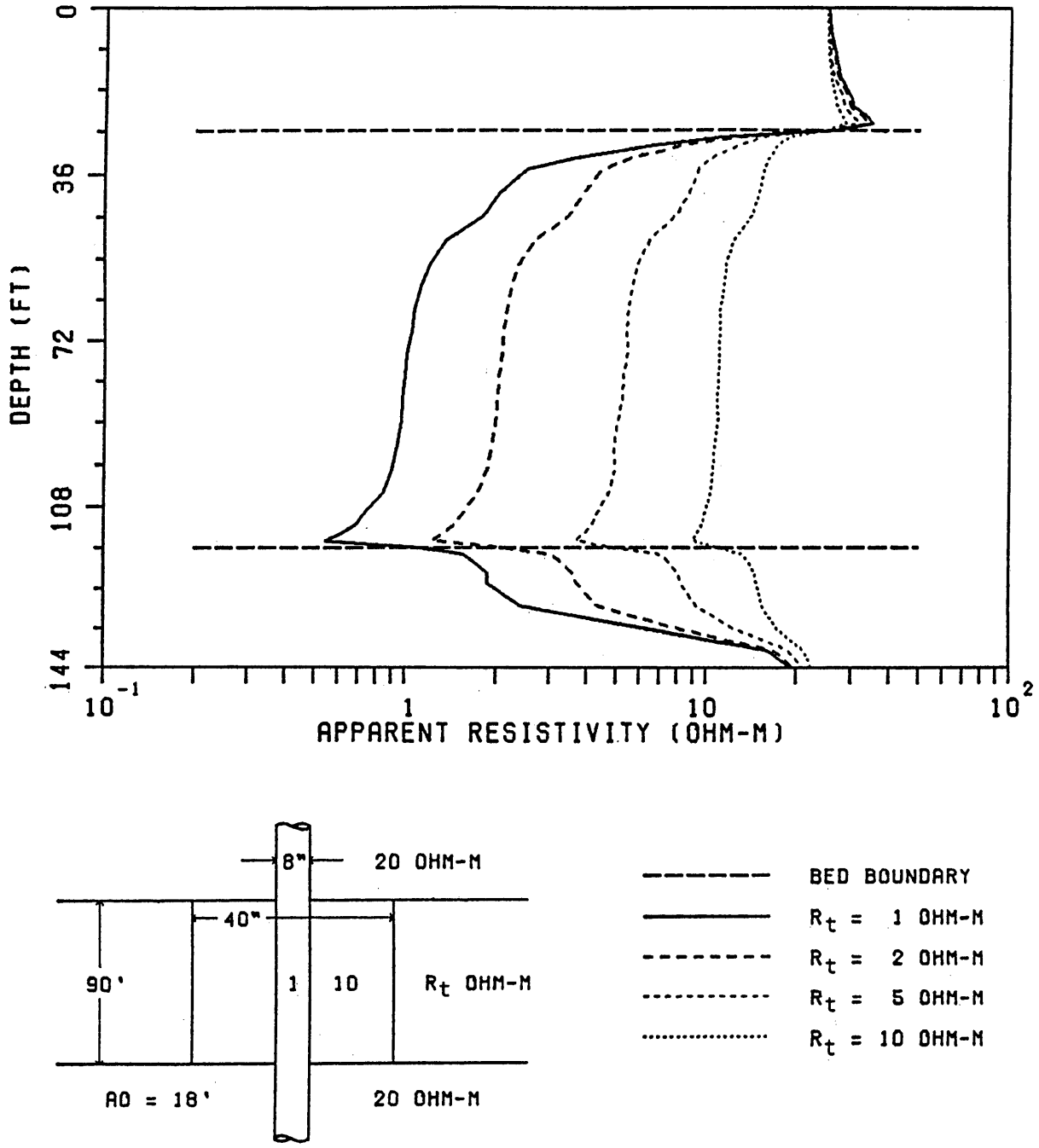

Figure 1.19e Variations in Rt (Lateral-Thick-Conductive)

and 10 ohm-m, respectively. True resistivities of 1, 2, 5, and 10 ohm-m are considered. Since the resistivity of the invaded zone is not too high compared to the mud resistivity, the apparent resistivity curves reflect the true resistivities of the layer very well.

As the bed thickness decreases, the departure from the true resistivity increases (Figure A-3.14, Figure A-3.15). Even though it is difficult to estimate true resistivity from the apparent resistivity curve in the conductive thin layer, it is still possible to identify the bed boundaries.

From the analysis of the apparent resistivity curves for the 18′ lateral arrangement in conductive beds, it can be concluded that the apparent resistivity is not appreciably affected by the extent and the resistivity of the invaded zone unless the invaded zone resistivity is too high compared to the true resistivity. Since the apparent resistivity curves are asymmetry and have sharp discontinuities near the bed boundaries, the bed boundaries of the formation can be easily identified . The true resistivity of the formation can be obtained by reading the apparent resistivity value at the flat portion of the curve in the conductive medium. The dimension of the borehole does not appreciably affect the apparent resistivity readings, while low-resistivity borehole mud adversely affects the responses in conductive bed.

1.5.4 Lateral Arrangement in a Resistive Bed

Figure 1.20a (or Figure A-4.1) shows the apparent resistivity curves for the 18′ lateral arrangement in a thick resistive layer model. The resistivities of the shoulder and the target layer are 10 and 100 ohm-m, respectively. The borehole diameter is 8 inches, and mud resistivities of 1, 5, and 10 ohm-m are considered. The thickness of the resistive bed is 90 feet. The responses indicate that the low-resistivity borehole mud adversely affects the responses for the lateral arrangement device in the resistive bed. The apparent resistivity readings at the flat portion of the curve in the resistive bed yield an overestimation of the true resistivity. The responses also show that the difference between curves in the shoulder layer are small and the departure from the shoulder resistivity is also small.

As the bed thickness decreases (Figure A-4.1, Figure A-4.2), the departure from the true resistivity increases and the flat portion of the curve in the resistive layer disappears. If the bed thickness is smaller than the electrode spacing, the apparent resistivity curves have big notches just beneath the lower boundary of the layer (shadow zone). The apparent resistivities in the shadow zone is even lower than the shoulder resistivity.

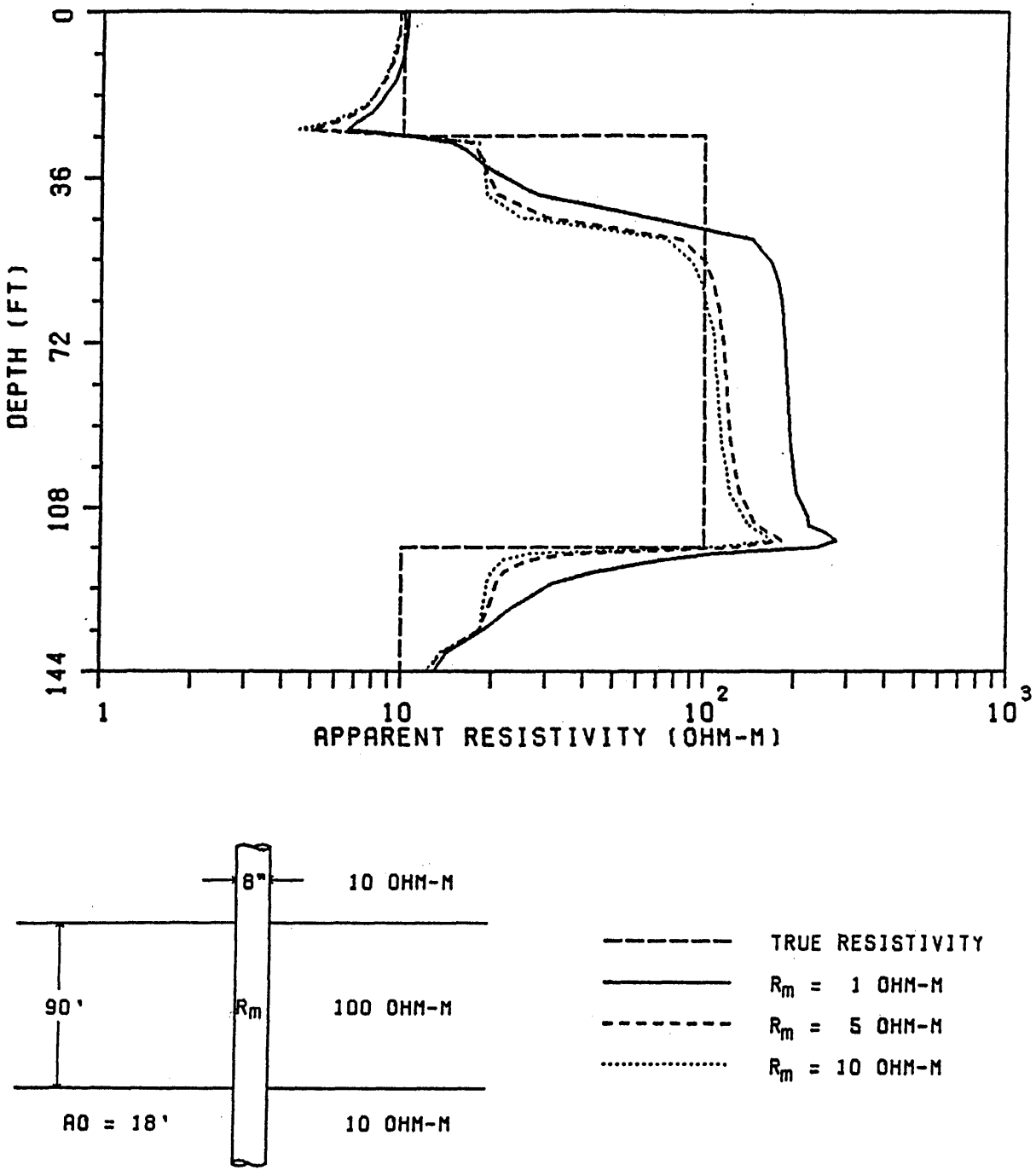

Figure 1.20a Variations in Rm (Lateral-Thick-Resistive)

Figure 1.20b (or Figure A-4.4) depicts the apparent resistivity curves for the 18′ lateral arrangement crossing a thick resistive bed. The mud resistivity is 1 ohm-m, and borehole diameters of 8, 10, and 12 inches are considered. The responses indicate that there are no appreciable differences between curves in the resistive layer or in the shoulder layer due to the variations in borehole diameter. The apparent resistivity values in the resistive layer provide an overestimation of the true resistivity.

As the bed thickness decreases (Figure A-4.5, Figure A-4.6), the departure from the true resistivity increases, and the flat portion of the curve in the resistive layer disappears. The shadow zone also occurs when the bed thickness is less than the electrode spacing.

Figure 1.20c (or Figure A-4.7) shows that the apparent resistivity curves for the 18′ lateral arrangement in a thick resistive bed which has a certain extent of invasion. The resistivity of the invaded zone is 20 ohm-m, and invasion diameters of 2d, 5d, and 10d are considered. Even though the invasion diameter is relatively small compared to the electrode spacing, the apparent resistivities in the resistive bed are somewhat affected by the extent of the invasion. On the other hand, the apparent resistivities in the shoulder layer are not appreciably affected by the invasion of the target layer. The true resistivity will be

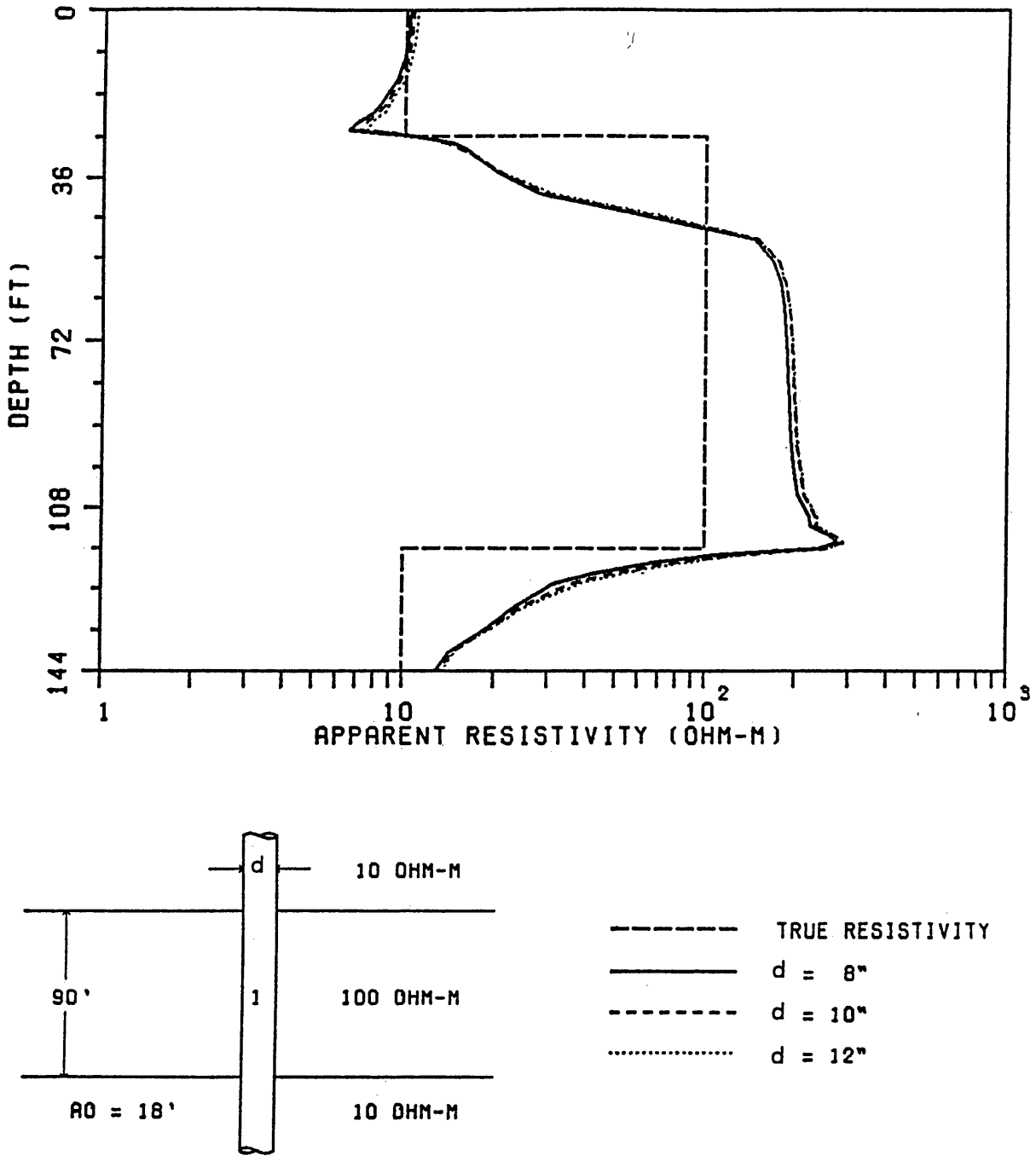

Figure 1.20b Variations in d (Lateral-Thick-Resistive)

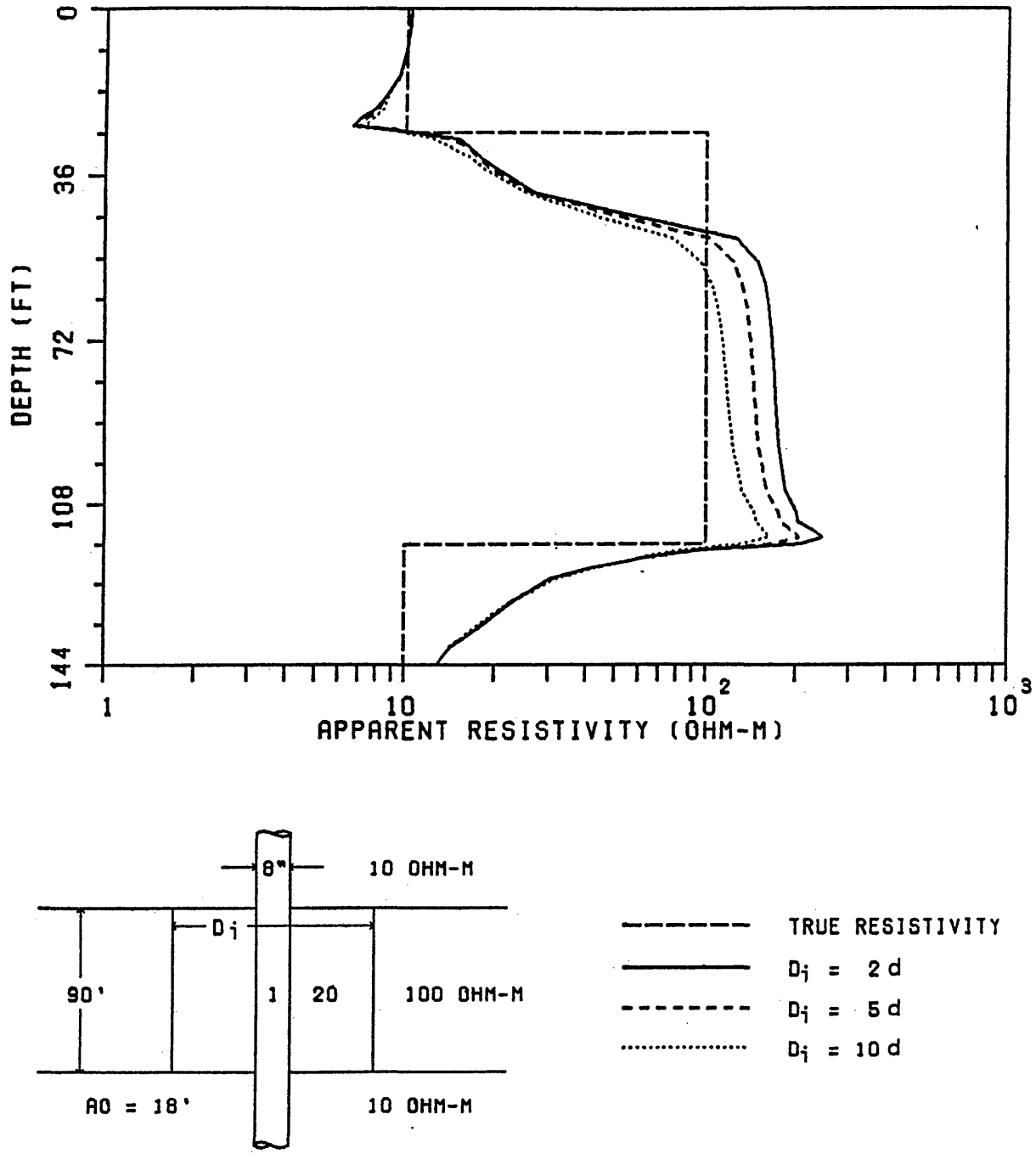

Figure 1.20c Variations in Di (Lateral-Thick-Resistive)

overestimated, if the flat portion of the apparent resistivity curves in the resistive layer is taken for the estimation of the formation resistivity.

As the bed thickness decreases (Figure A-4.8, Figure A-4.9), the differences between curves decrease and the departure from the true resistivity increases. The shadow zone occurs beneath the thin resistive layer model.

Figure 1.20d (of Figure A-4.10) depicts the apparent resistivity curves for the 18′ lateral arrangement crossing a thick resistive bed which has an invaded zone. The invasion diameter is 40 inches, and invaded zone resistivities of 10, 20, and 50 ohm-m are considered. The responses indicate that there are no appreciable differences between curves due to the variations in invaded zone resistivity. The apparent resistivity readings in the resistive bed also yield an overestimation of the true resistivity. The departure from the true resistivity increases with the decrease of the bed thickness (Figure A-4.11, Figure A-4.12). The shadow zone occurs when the bed thickness is less than the electrode spacing.

Figure 1.20e (or Figure A-4.13) shows the apparent resistivity curves for the 18′ lateral arrangement in a thick resistive bed which has an invaded zone. The mud resistivity and the resistivity of the invaded zone are 1 and 10 ohm-m, respectively. True resistivities of 10, 20,

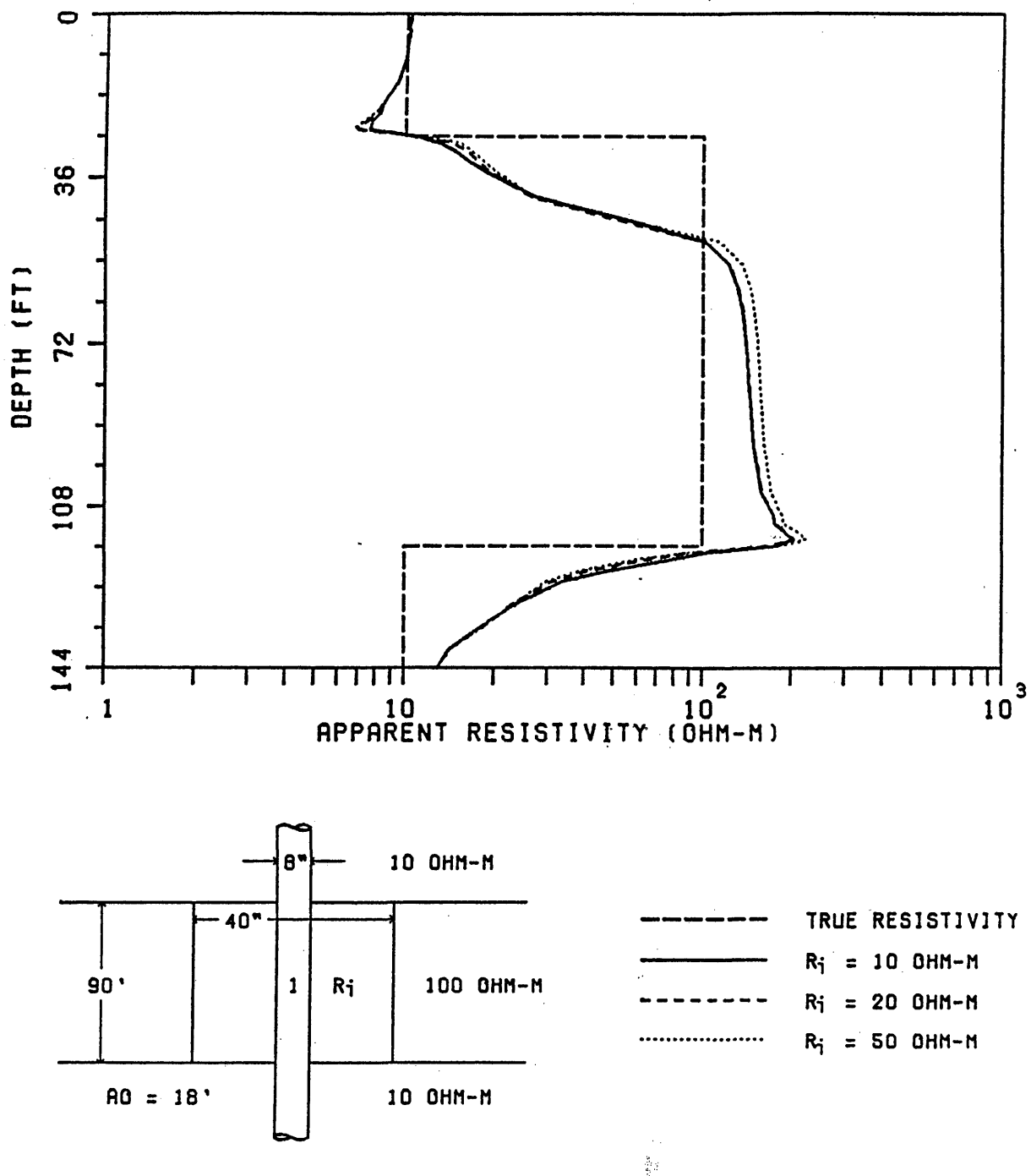

Figure 1.20d Variations in Ri (Lateral-Thick-Resistive)

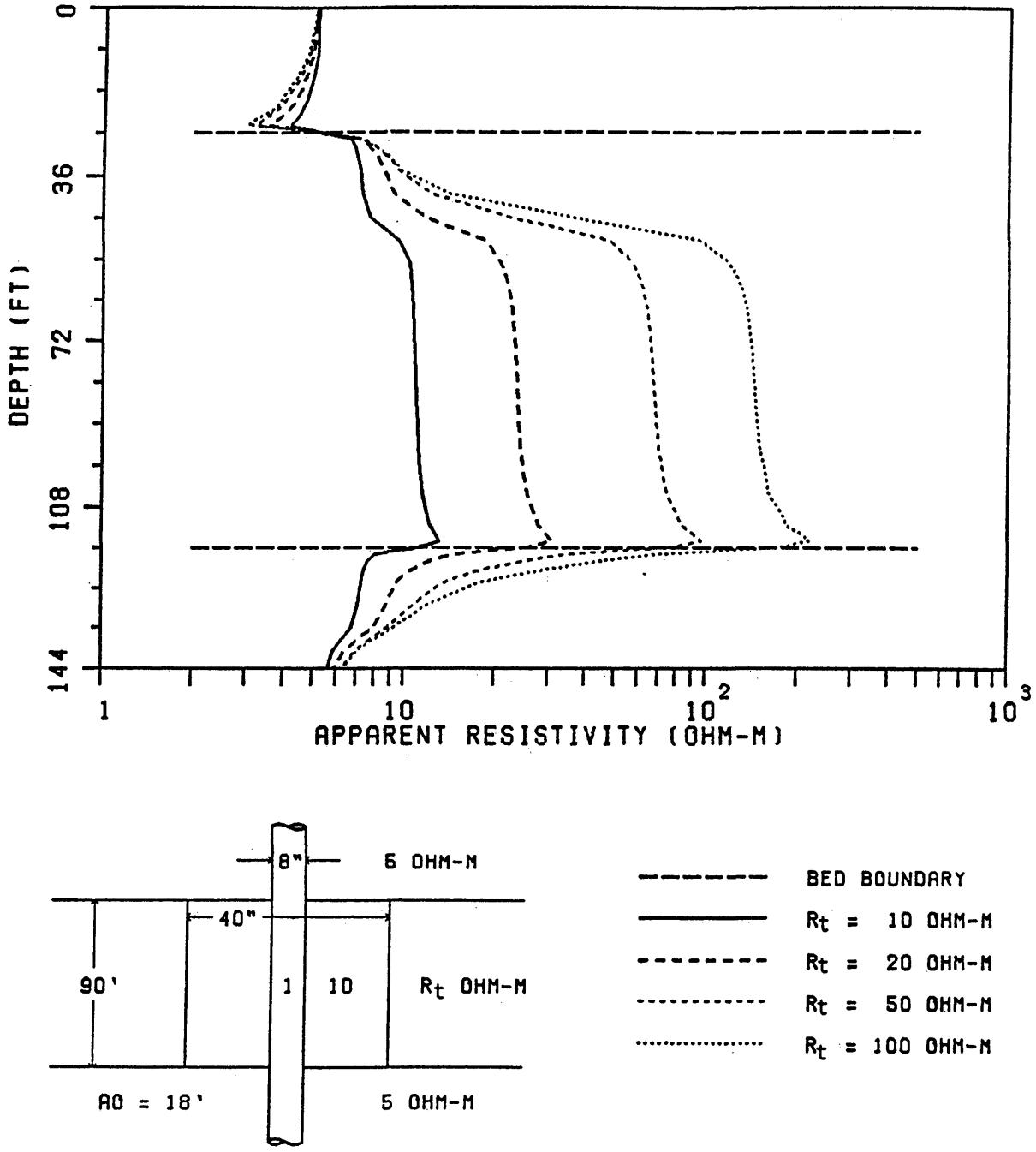

Figrue 1.20e Variations in Rt (Lateral-Thick-Resistive)

50, and 100 ohm-m are considered. Due to the borehole effect the apparent resistivities are slightly greater than the true resistivities.

As the bed thickness decreases, the departure from the true resistivity increases and the shadow zone becomes dominant (Figure A-4.14, Figure A-4.15). The bed boundaries are still distinguishable even though the bed thickness is less than the electrode spacing.

From the analysis of the apparent resistivity curves for the 18′ lateral arrangement in resistive beds, it can be concluded that the apparent resistivity is not appreciably affected by the invasion resistivity, but large-diameter invasion adversely affects the apparent resistivity readings in resistive beds. The bed boundaires can be easily identified, and the apparent resistivities in the resistive medium are mainly governed by the ratio of true resistivity to the mud resistivity (Rt/Rm). The dimension of the borehole does not appreciably affect the apparent resistivity readings, while the low-resistivity borehole mud adversely affects the responses in resistive beds.

In general, the logging environment which affects the response of the 18′ lateral electrode arrangement can be summarized as follows.

1. Borehole effects: When Rt/Rm is large, the borehole effects are significant, and the apparent resistivity is

greater than the true resistivity. For common borehole sizes, the variations in borehole diameter do not appreciably affect the the apparent resistivity.

2. Invasion effects: The invasion effects are significant when the invaded zone resistivity is greater than the true resistivity.
3. Bed thickness effect: the bed thickness effects become significant when the thickness is less than at least two times the electrode spacing. If the bed thickness is less than electrode spacing, the shadow zone occurs beneath a thin resistive bed.

1.5.5 Mutiple Invaded Layers

Finally the multiple invaded layer model is considered to investigate the responses of the 16" normal and the 18' lateral electrode arrangements. Figure 1.21a shows the apparent resistivity curve for the 16" normal arrangement crossing multiple invaded layers. The resistivity of the shoulder layer is 10 ohm-m, and the resistivities of the thin layers are 50, 100, and 30 ohm-m from the top to bottom. The mud resistivity is 1 ohm-m and the borehole diameter is 8 inches. The invaded zone resistivities are 20, 30, and 15 ohm-m and the invasion diameters are 32, 48, and 16 inches from the top to bottom, respectively. the bed thicknesses are 80, 24, and 56 inches from top to bottom of

the model. For the 18′ lateral arrangement different bed thickness are considered. As shown in Figure 1.21b, the bed thicknesses are 18, 6, and 12 feet from top to bottom of the model. Figure 1.21a and Figure 1.21b indicate that the finite difference method is so versatile that the apparent resistivities for the normal and the lateral electrode arrangements can be accurately obtained provided that the earth model has an axial symmetry.

The forward modeling for the combined boundary earth model, especially for the complicated axisymmetrical logging environment, has many possible applications. These include: the design of new electrode resistivity tools, the calibration of the existing tools, and the prediction of the apparent resistivity for a given geometry to improve interpretation of the resistivity logs.

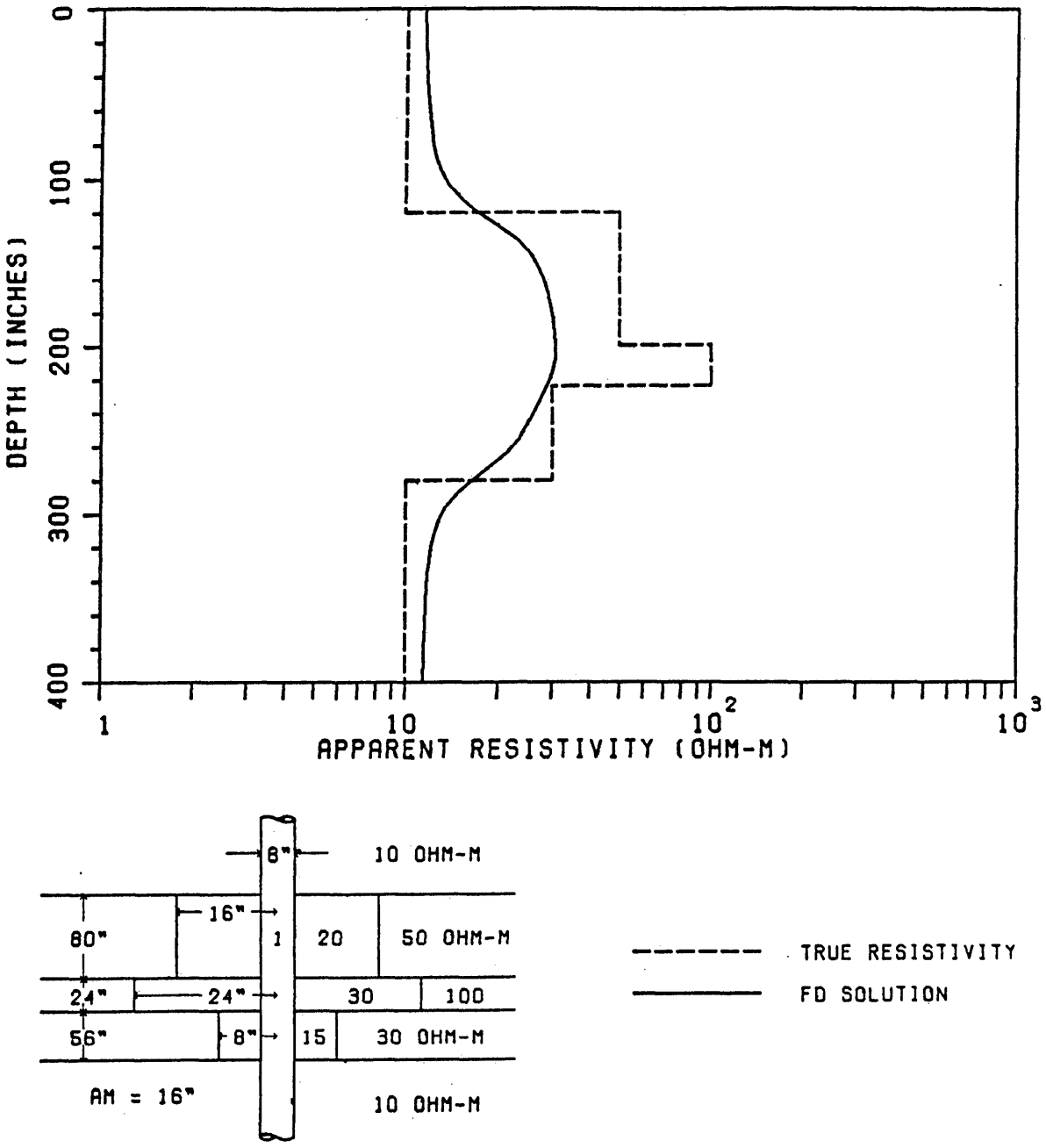

Figure 1.21a A synthetic 16" normal log in multiple layers

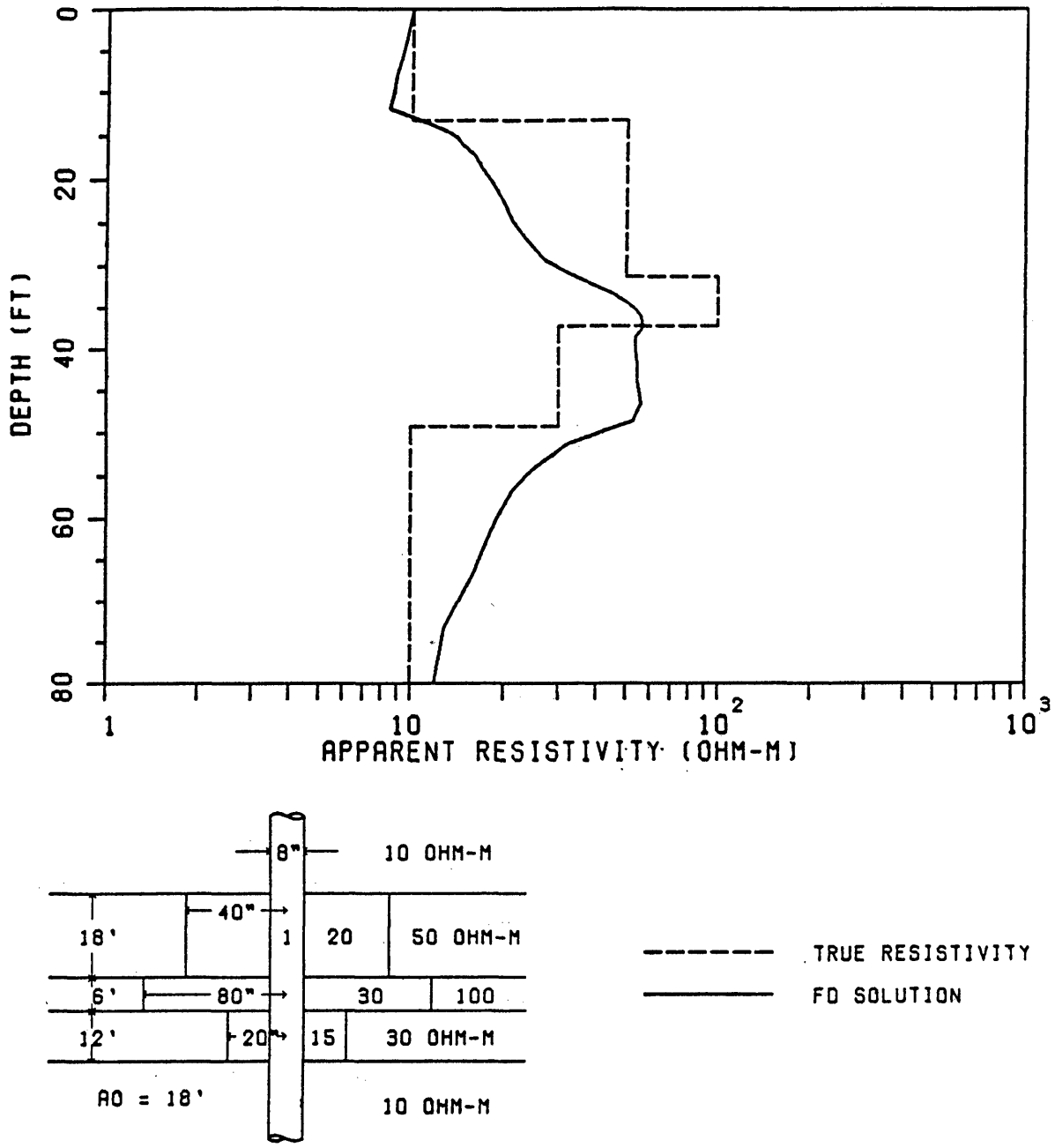

Figure 1.21b A synthetic 18' lateral log in multiple layers

CHAPTER 2

INVERSION OF RESISTIVITY LOGS

The purpose of the borehole resistivity data inversion is to determine earth parameters, such as resistivity and thickness of the layer, and resistivity and diameter of the invaded zone, from a set of normal and lateral resistivity logs or from a single resistivity log.

The borehole resistivity data inversion can be accomplished with two different earth models. The first model consists of layers separated by plane-parallel boundaries, and the layers have various thickness and resistivities. This one-dimensional (1-D), horizontally layered earth model can be applied to the case where a drill-hole penetrates beds of finite thicknesses, but the electrode spacing is large enough that the resistivity of the drilling mud and the invaded zone may be neglected. The second model consists of horizontal layers with a borehole and/or invaded zones. This two-dimensional (2-D), combined boundary earth model can be applied to the case where a drill-hole penetrates beds of finite thicknesses and the existence of the invaded zone is known.

Once the model is chosen and the earth geometry is defined, the apparent resistivities are calculated and compared to the observed data. The root-mean-squares (rms)

error between calculated data and the observed data is then found. The earth parameters are changed to minimize the error and new apparent resistivities are calculated and compared to the observed data. This procedure will be repeated for a number of iterations until the desired accuracy is obtained. Inman et al. (1973) discussed a problem of direct interpretation of surface resistivity sounding curves from horizontally layered models by using the generalized linear inverse theory. They also discussed the resolution of the model parameters to be determined. Then Inman (1975) applied a ridge regression estimator to the resistivity inversion problem, and discussed a statistical analysis for the estimated parameters. Hoversten et al. (1982) compared five least-squares inversion techniques in resistivity sounding and found that the ridge regression algorithm required the fewest numbers of forward calculations to reach a desired convergence criteria. Moreover, Inman (1975) pointed out that the ridge regression estimator is more stable than the generalized linear inverse estimator.

In this study, the ridge regression estimator is used for the borehole resistivity data inversion, and the resolution and the statistical analysis for the estimated earth parameters follow. Two types of resistivity logs are chosen to test the inversion scheme. One of them is the

field data ,and is inverted to a 1-D earth model. The other one is the theoretical data, and is inverted to a 2-D earth model.

Finally, a set of field data obtained from the 16" normal, the 64" normal, and the 18'8" lateral logs is inverted to the 1-D earth models, and is inverted to the 2-D earth models. The earth parameters obtained from the 1-D and the 2-D inversion are then compared.

2.1 Ridge Regression Estimator

As shown in the previous chapter, the apparent resistivity in the borehole can be evaluated from a given earth model. With mathematical notations it can be stated that the M unknown earth parameters **P** are related to the measurable quantity C by a nonlinear functional F as presented by the following:

$$C = F(\mathbf{P}, \mathbf{X}), \qquad (2.1)$$

where the known model parameters are contained in the vector **X**. The vector **X** contains the N depth reference points at which the apparent resistivity are measured.

The apparent resistivity calculated from equation (2.1) is tried to fit to the observed data O. The fitting is usually carried out in a least-squares sense. The least-squares fitting is in turn performed on a linearized version

of the governing equation.

The nonlinear apparent resistivity equation (2.1) is linearized by expansion in Taylor's series about an initial estimate $\mathbf{P}^0$ in the parameter space at each depth point. The series, neglecting second and higher order terms, is

$$O(\mathbf{X},\mathbf{P})_i = C(\mathbf{X},\mathbf{P}^0)_i + \sum_{j=1}^{N} \frac{\partial}{\partial P_j}[C(\mathbf{X},\mathbf{P}^0)_i](P_j - P^0{}_j), \qquad (2.2)$$

with

$j=1,M$ and $i=1,N$,

where $O(\mathbf{X},\mathbf{P})_i$ is the ith observation, $C(\mathbf{X},\mathbf{P}^0)_i$ is the ith calculated value for the current estimate of the unknown parameter set $\mathbf{P}$, and $(P_j - P^0{}_j)$ is the linear estimate of the correction needed in the jth unknown parameter. Rewriting equation (2.2) in matrix notation, we have

$$\Delta\mathbf{G} = \mathbf{A}\,\Delta\mathbf{P}, \qquad (2.3)$$

where

$$\Delta G_i = O(\mathbf{X},\mathbf{P})_i - C(\mathbf{X},\mathbf{P}^0)_i,$$

$$A_{ij} = \left.\frac{\partial C(\mathbf{X},\mathbf{P})_i}{\partial P_j}\right|_{\substack{\mathbf{x}=\mathbf{x}_i \\ \mathbf{p}=\mathbf{p}^0}},$$

and $\Delta P_j = P_j - P^0{}_j$.

Equation (2.3) represents a system of N linear equations in M unknown. The $\mathbf{A}$ in equation (2.3) is called the system matrix and it represents the sensitivities of the calculated values with respect to the small changes in the current estimate of the parameters. In the borehole resistivity

problem, the system matrix **A** is comprised of partial derivatives of the apparent resistivity with respect to the resistivity and thickness of each layer in the current model.

Since the problem is nonlinear and is linearized by expansion in Taylor's series, the solution of equation (2.3) provides only a linear estimate of $\Delta\mathbf{P}$ and equation (2.2) is strictly true for small values of $\Delta\mathbf{P}$.

The ridge regression estimator, $\Delta\mathbf{P}'$, of $\Delta\mathbf{P}$ is

$$\Delta\mathbf{P}' = (\mathbf{A}^T\mathbf{A} + k\mathbf{I})^{-1}\,\mathbf{A}^T\,\Delta\mathbf{G}, \qquad (2.4)$$

where **I** is the identity matrix and $k \geq 0$ (Marquardt, 1970). Equation (2.4) represents that the eigenvalues of $\mathbf{A}^T\mathbf{A}$ is increased in the ridge regression estimator by the factor of k. Hence, the inversion of the matrix $(\mathbf{A}^T\mathbf{A} + k\mathbf{I})$ becomes more stable than the inversion of matrix $(\mathbf{A}^T\mathbf{A})$ which is used in the generalized linear inversion (Inman, 1975).

The underlying concept of the ridge regression estimator is that the $\Delta\mathbf{P}'$ minimizes the sum of squares of residuals

$$\Phi(\Delta\mathbf{P}') = (\Delta\mathbf{G} - \mathbf{A}\,\Delta\mathbf{P}')^T(\Delta\mathbf{G} - \mathbf{A}\,\Delta\mathbf{P}') \qquad (2.5)$$

on the sphere whose squared radius is $(\Delta\mathbf{P}'^T\Delta\mathbf{P}')$, and that the best direction for finding a minimum residual sum of squares lies somewhere between the direction given by the Taylor's series increment (k=0) and the direction of the steepest descent ($k=\infty$).

An important consideration in the ridge regression estimator is the choice of a suitable values of k so that the residual sum of squares is minimized. The damping factor k can be obtained by inserting various values of k into equation (2.4) and finding the minimum residual sum of squares. Once the minimum error is found, the current earth parameters are replaced by the new parameters corresponding to the value of k which yields a minimum error between the observed and the caluclated data. The new parameter set **P** can be obtained from the relation.

$$\mathbf{P} = \mathbf{P} + \Delta\mathbf{P}. \qquad (2.6)$$

In this way, the new earth parameter **P** yields a new apparent resistivity curve that better fits the field data. The parameter **P** obtained in equation (2.6) now replaces the old parameter $\mathbf{P}^0$ and the procedure continues until a solution is obtained. In each iteration a different value of k may be used. At the initial stage of the inversion process a large value of k is used to fit the broad aspects of the data, and as the iteration goes on, the smaller value of k is used to provide the finer fit.

2.2 Parameter Resolution and Statistics

The ridge regression estimator of the unknown parameter changes ΔP is obtained from equation (2.4), and the new parameter estimates are calculated by using equation (2.6). Once the final estimates are obtained, the confidence level of the earth parameter can be analyzed qualitatively through the resolution matrix (Inman et al, 1973), and the accuracy of the estimates can be analyzed by using parameter statistics.

Substituting equation (2.3) in equation (2.4), we have

$$\Delta P' = (A^T A + kI)^{-1} A^T A \, \Delta P, \qquad (2.7)$$

$$= R \, \Delta P,$$

where the matrix R is referred as the resolution matrix. Equation (2.7) shows that the estimated parameter changes $\Delta P_j'$ are linearly related to the unkown parameter changes ΔP_j. If the model is overconstrained ($N > M$) and the rank of the system matrix A is equal to the number of unknown parameters, then the resolution matrix will be the identity matrix (Inman et al., 1973). Thus the parameter differences ΔP_j can be uniquely resolved for a single iteration, and the estimated parameter changes $\Delta P_j'$ will be equal to the unknown parameter changes ΔP. If the noise-free observation data are used, and if the initial model is close to the true model, the identity resolution matrix, $R = I$, can be

obtained in a few iterations depending upon the complexity of the problem. Due to the nonuniqueness of the inverse problems, the estimated earth model may be different from the true model. The estimated earth model depends on the initial guess model.

In the overconstrained case when the rank of the system matrix is less than the number of unknown parameters the resolution matrix is no longer the identity matrix, and the estimated parameter changes $\Delta P'$ is a weighted average of the unknown parameter changes used to describe the earth model (Inman et al., 1973). In the case where the diagonal element of the resolution matrix is much smaller than one, the parameter difference ΔP_j will be poorly resolved and the final model would be removed from the true model.

In the problem of borehole resistivity data inversion, a weighted least-squares scheme is used. In order to find a model that uniformly fits the resistivity log when the percentage data error is equal for all data, a logarithmic weighting (Rijo et al., 1977) is used. In this weighting scheme, the function to be minimized in the least-squares sense is

$$(\Delta G)^2 = \sum_{i=1}^{N} [\log O_i - \log C_i]^2. \qquad (2.8)$$

This scheme weights the data equally in the logarithmic scale (Hoversten et al., 1982).

The system matrix **A** and the perturbing equation (2.6) are then replaced by

$$A_{ij} = \left.\frac{\partial \log C(\mathbf{X},\mathbf{P})_i}{\partial \log P_j}\right|_{\substack{\mathbf{X}=\mathbf{X}_i \\ \mathbf{P}=\mathbf{P}^0}},$$

and $\mathbf{P} = \mathbf{P}^0 \times 10^{(\Delta P')}$.

The rms-log error is derived from

$$E(\text{rms log}) = \{(\Delta G)^2/N\}^{1/2},$$

and the percent error can be calculated by using the relation

$$E(\%) = 100 \times 10^{(E(\text{rms log})-1)}.$$

The estimate of data variance for the logarithmically weighted least-squares fit can be obtained from the reduced chi square (Hoversten et al,. 1982; Yang and Ward, 1984)

$$\chi^2 = \frac{\Delta G^T \mathbf{W}^T \mathbf{W} \Delta G}{N - M}, \qquad (2.9)$$

where

$$W_{ij} = \begin{cases} \log O_i - \log C_i & \text{for } i=j, \\ 0 & \text{for } i \neq j, \end{cases}$$

and (N - M) represents the degrees of freedom.

The inversion process will be repeated for a number of iterations until a predetermined number of iterations is exhausted or the difference between the minimum error of the two successive iterations is less than a desired value, or the new error is less than a predetermined error allowance.

2.3 Test Results

The inversion scheme is tested with the consideration of two different models: (1) horizontally layered earth model, and (2) combined boundary earth model.

As a 1-D inversion test, the 16" short normal field data are inverted to a horizontally layered earth model. As a 2-D inversion the 16" short normal synthetic resistivity data are inverted to a combined boundary earth model, and the estimated earth parameters are compared to those of the given model.

In each test, the confidence level of the estimated earth parameters is discussed by using a parameter resolution matrix, and the data variance is calculated.

2.3.1 One-Dimensional Inversion

As shown in Figure 2.1, a segment of the 16" short normal resistivity log is chosen from the depth of 5370 ft to 5420 ft, and is inverted to a horizontally layered earth model. A seven-layer initial guess model is considered and the inversion is initiated. Figure 2.2a shows the observed data which are digitized from the original log for every 2 ft, the initial guess model, and the synthetic resistivity log calculated from the initial guess model. The rms error between observed data and the initial guess log is about 25

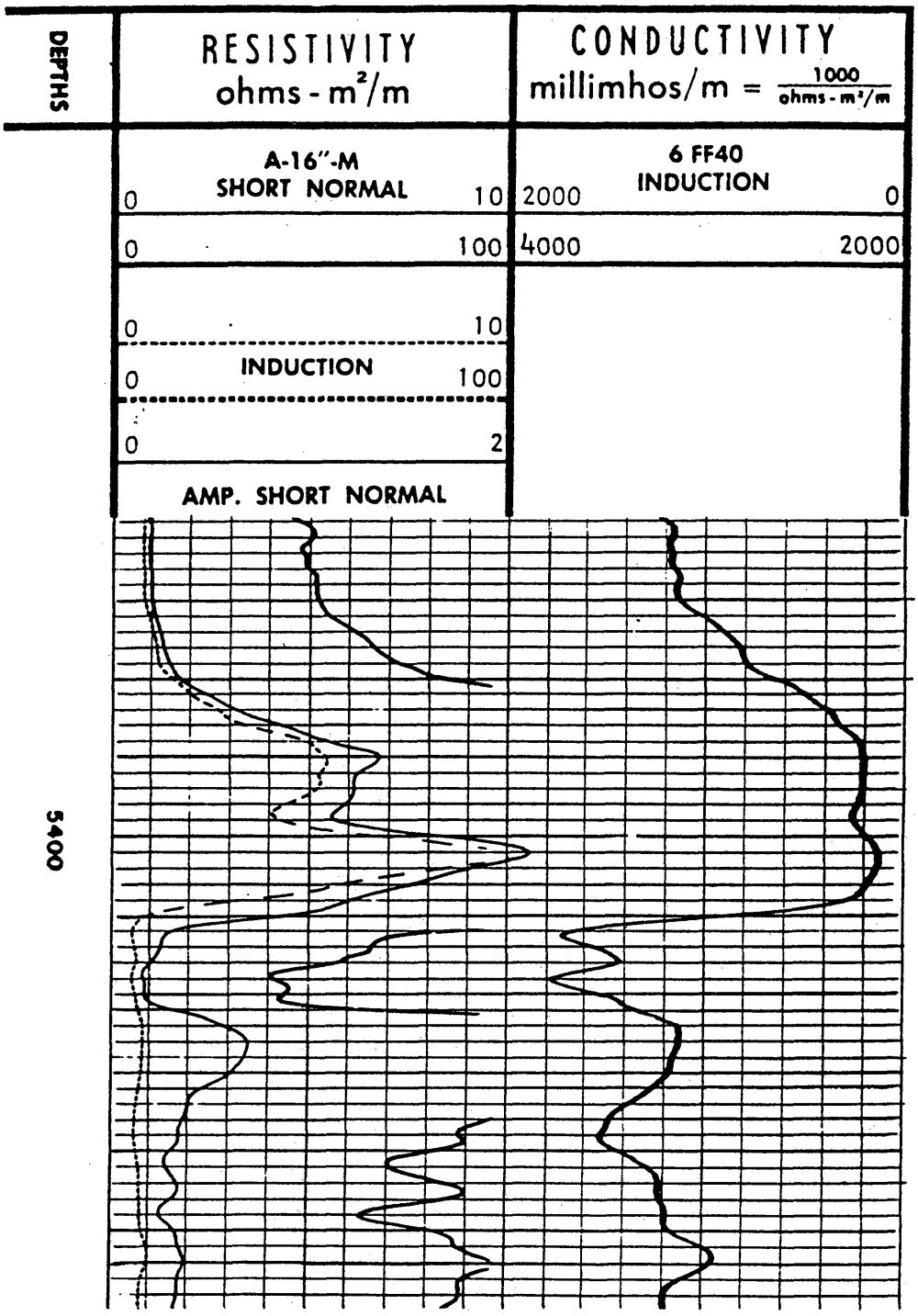

Figure 2.1 A segment of the 16" short normal resistivity log to be inverted to a 1-D model (after Hilchie, 1978)

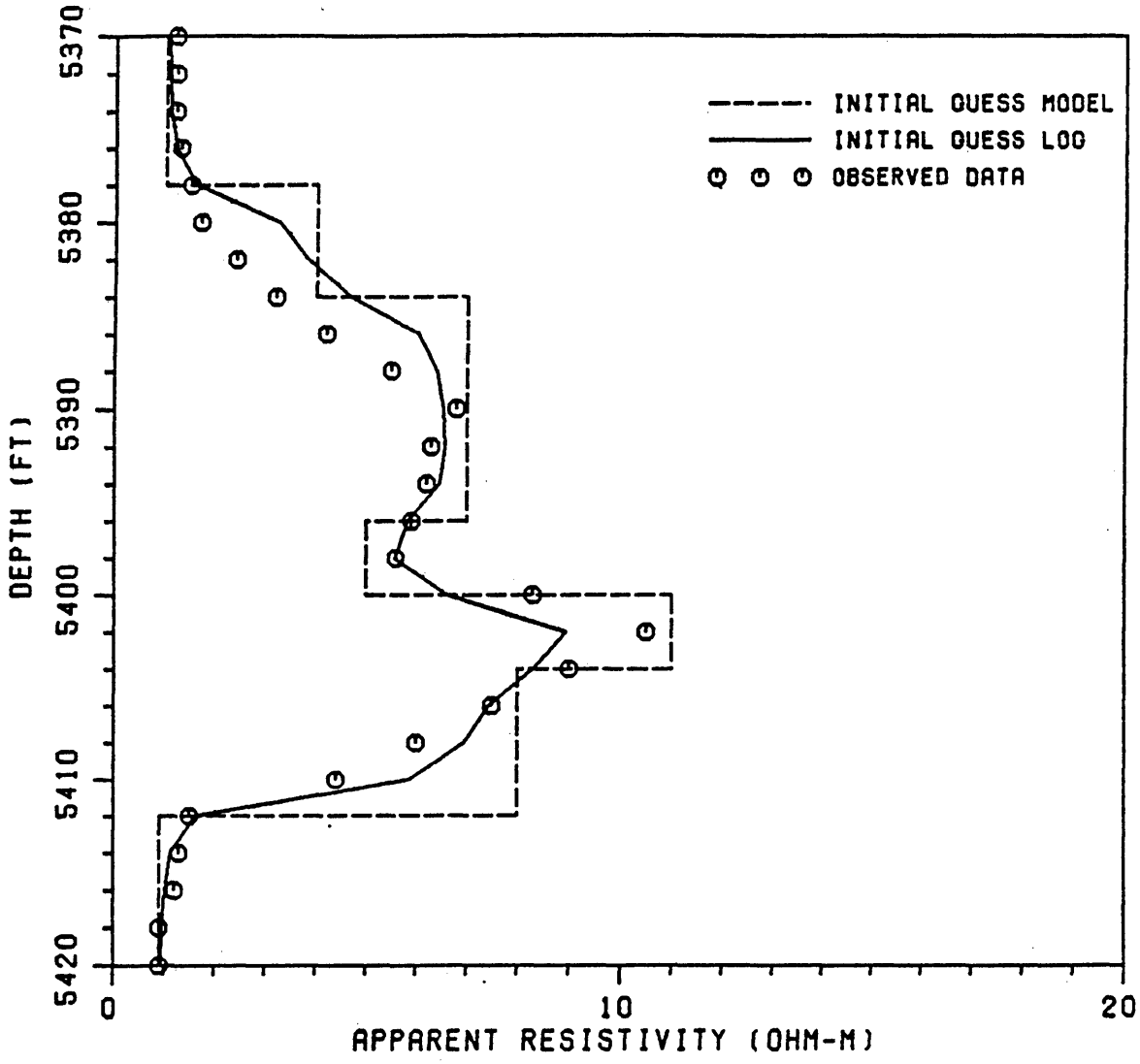

Figure 2.2a Comparison between observed data and the initial guess log for a 1-D model fit (25% rms error)

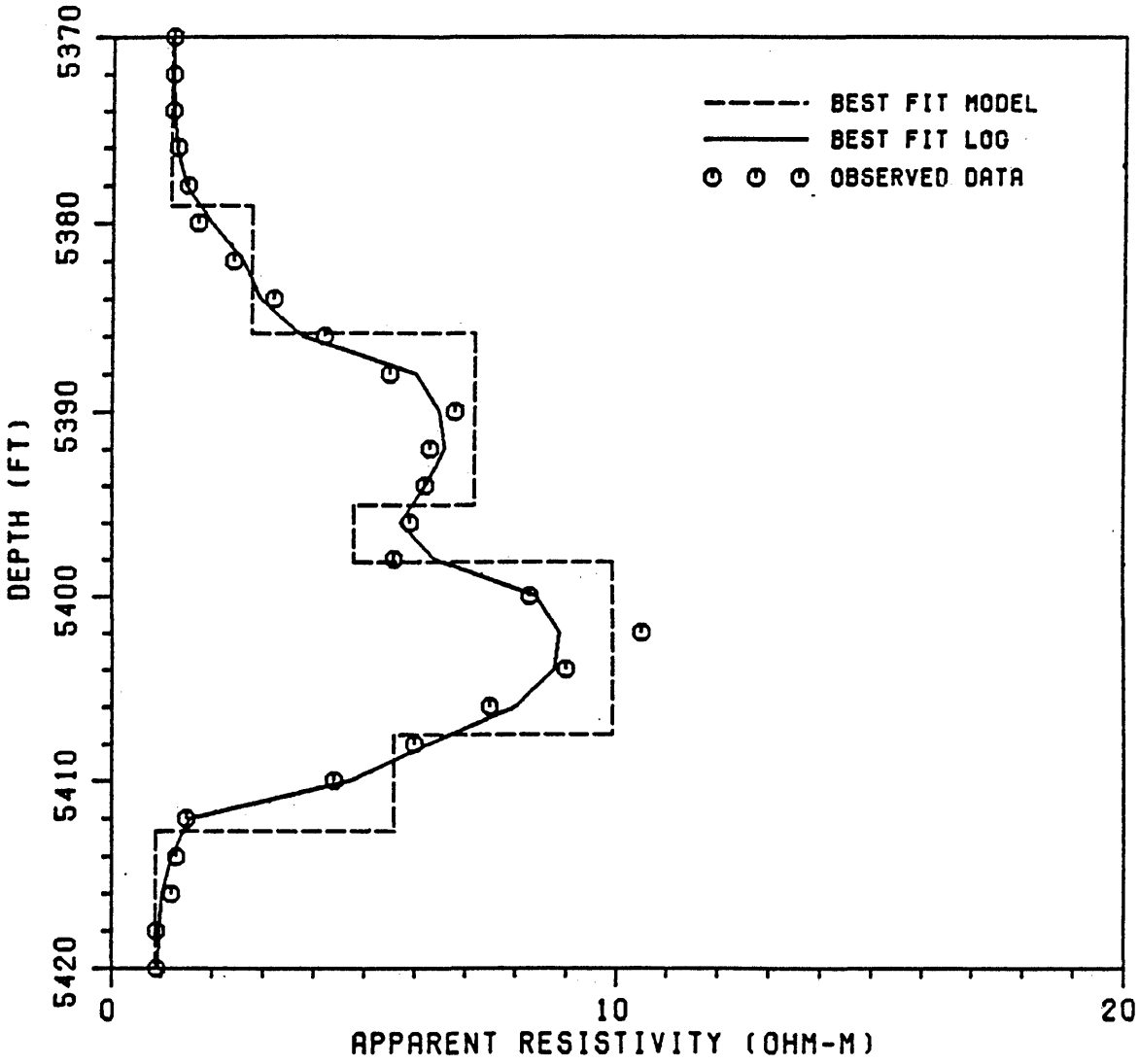

Figure 2.2b Comparison between observed data and the best fit log obtained from a best fit 1-D model (8% rms error)

percent.

The inversion result for a seven-layer fit is shown in Figure 2.2b. The readings of field resistivity log, the best fit model, and the resistivity log calculated from the best fit model are shown in the figure. The best fit log obtained from the best fit model agrees well with the field data except a few data points. The rms error between observed data and the resistivity log calculated from the best fit model is 8 percent, and the data variance estimated by using equation (2.9) is 5.55E-5. These statistics indicate that there is a very small error in the final fit. The inversion results for each layer are listed in Table 2.1a where the depth to the top of the first layer is 5370 ft.

Table 2.1a Estimated parameters derived from an 1-D inversion of field data shown in Figure 2.1

Layer	Resistivity	Thickness
1	1.2 ohm-m	9.1 ft
2	2.8 ohm-m	6.7 ft
3	7.2 ohm-m	9.2 ft
4	4.8 ohm-m	3.1 ft
5	9.9 ohm-m	9.4 ft
6	5.6 ohm-m	5.1 ft
7	0.9 ohm-m	-------

The symmetrical parameter resolution matrix is obtained by using equation (2.7), and the main diagonal elements are listed in Table 2.1b. It can be said that the parameter changes are well resolved if the resolution coefficients are close to 1.0 and the parameter change are poorly resolved if the coefficients are much less than 1.0. Table 2.1b indicates that the parameter resolutions for the layer 3 are relatively poor. The analysis of parameter resolution matrix indicates that the estimated earth parameters listed in Table 2.1a would be very close to the true parameters, and that the bed boundaries can be precisely determined rather than resistivities. The rms error between observed data and the best fit resistivity log can be reduced by

Table 2.1b The main diagonal elements of the parameter resolution matrix obtained from the 1-D inversion of the field data shown in Figure 2.1

Layer	Resistivity Resolution Coefficient	Thickness Resolution Coefficient
1	0.98	0.99
2	0.98	0.99
3	0.42	0.62
4	0.97	0.99
5	0.78	0.99
6	0.92	1.00
7	0.97	----

adjusting the number of layers in the initial guess model and/or eliminating noisy data from the field resistivity log.

The test results of the 1-D inversion indicate that the resistivity log can be inverted to identify the bed boundaries and to estimate the true resistivities of each layer if the borehole and the invasion effects can be neglected.

2.3.2 Two-Dimensional Inversion

A thin invaded layer model is then considered to test the two-dimensional borehole resistivity inversion. The observed data are obtained from the synthetic resistivity log calculated from the given model and those data are inverted to get the radial as well as the vertical resistivity profiles. The finite difference method is now used for the forward calculations. Resistivities of mud, invaded zone and virgin zone of the model are 1, 20, and 50 ohm-m. The upper and the lower shoulder resistivities, Rsh1 and Rsh2, are 10 and 5 ohm-m. The borehole and the invasion diameters are 8 and 16 inches. The bed thickness is 80 inches, and the distance to the upper bed boundary, Z1, is 160 inches and the distance to the lower bed boundary, Z2, is 240 inches, respectively. The inversion is initiated by disturbing these known earth parameters and by providing

disturbed parameters as an initial guess to the ridge regression eatimator.

A three-layer initial guess model, which has an invaded zone at the center layer, is considered. The observed data, the initial guess model, and the synthetic resistivity log calculated from the initial guess model are shown in Figure 2.3a. The rms error between observed data and the initial guess log is 80 percent.

The inversion result for a three-layer fit is shown in Figure 2.3b. The observed data, the best fit model, and the resistivity log calculated from the best fit model are shown in the figure. Figure 2.3b also indicates that the best fit log and the observed data have an excellent agreement. The rms error between observed data and the best fit log is 3

Table 2.2a Comparison between true, initial guess, and best fit model for a 2-D inversion of the theoretical data

Parameters	True Model	Initial guess	Best fit model
Rm	1.0 ohm-m	1.0 ohm-m	1.0 ohm-m
Ri	20.0 ohm-m	10.0 ohm-m	11.9 ohm-m
Rt	50.0 ohm-m	60.0 ohm-m	57.4 ohm-m
Rsh1	10.0 ohm-m	11.0 ohm-m	10.3 ohm-m
Rsh2	5.0 ohm-m	6.0 ohm-m	5.0 ohm-m
d	8.0 inches	8.0 inches	8.0 inches
Di	16.0 inches	24.0 inches	17.5 inches
Z1	160.0 inches	128.0 inches	157.7 inches
Z2	240.0 inches	192.0 inches	239.7 inches
h	80.0 inches	64.0 inches	81.9 inches

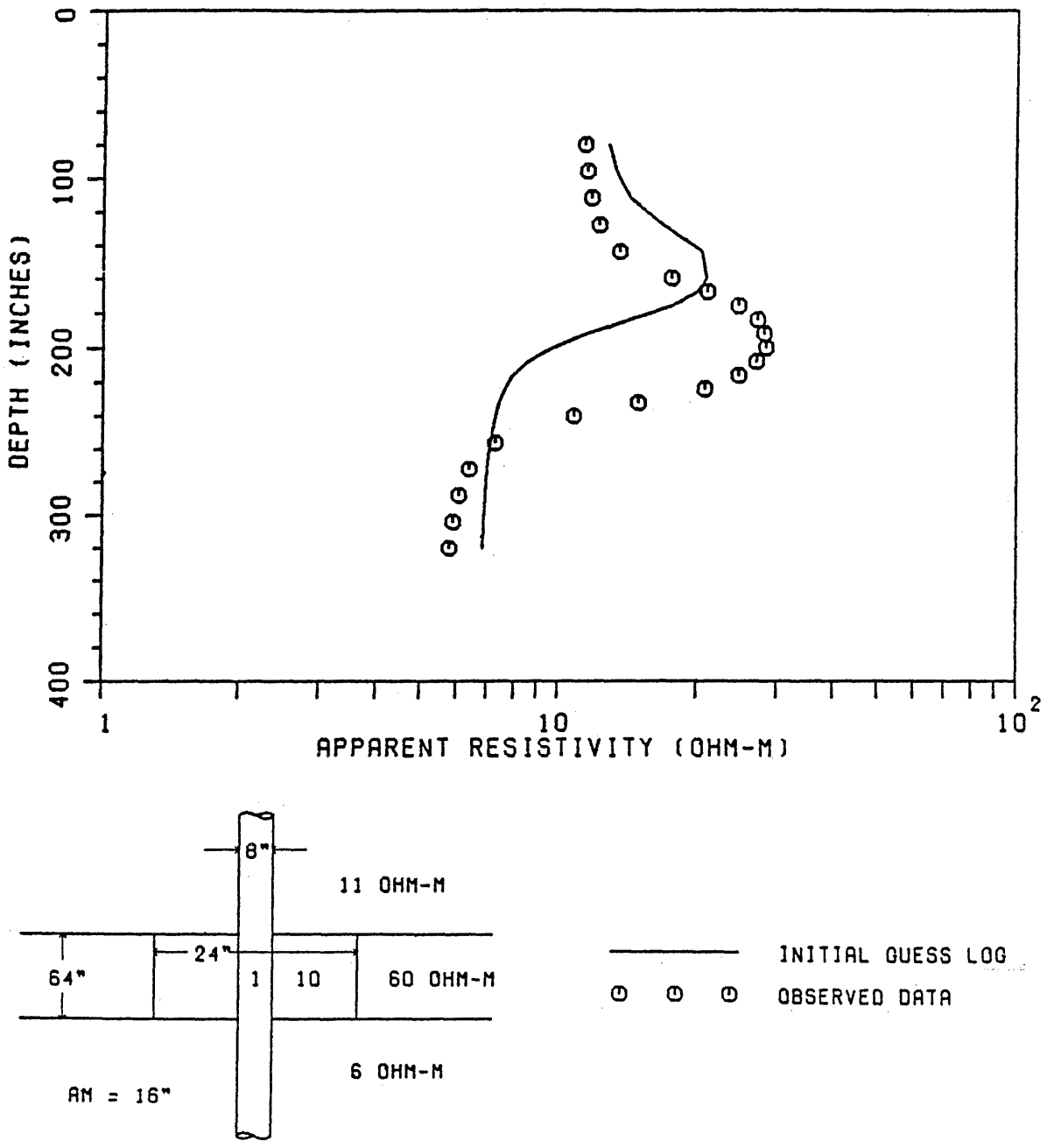

Figure 2.3a Comparison between observed data and the initial guess log for a 2-D model fit (80% rms error)

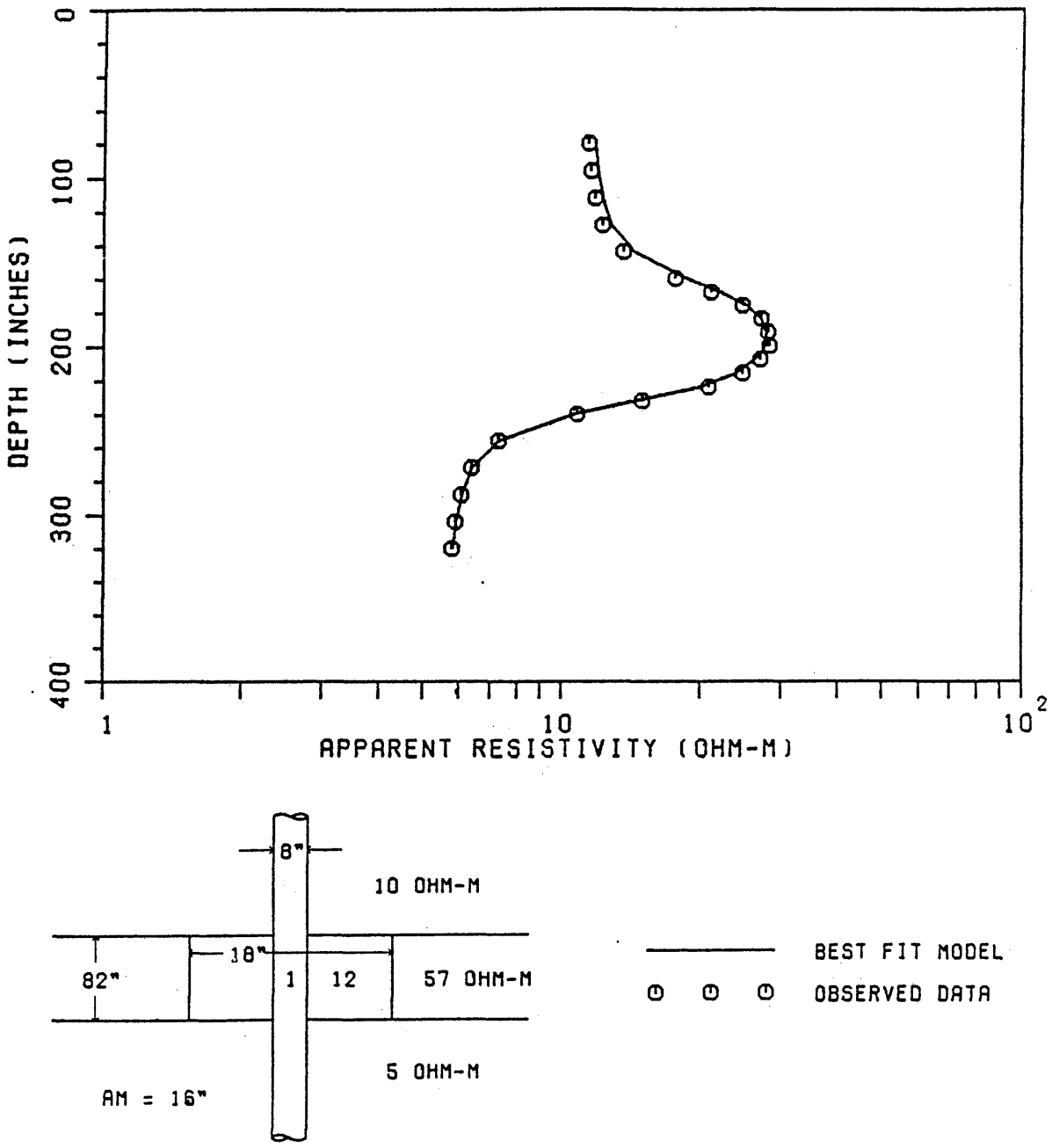

Figure 2.3b Comparison between observed data and the best fit log obtained from a best fit 2-D model (3% rms error)

Table 2.2b The main diagonal elements of the parameter resolution matrix obtained from the 2-D inversion of the theoretical data

Parameters	Resolution Coefficients
Rm	0.00 (fixed)
Ri	0.02
Rt	0.49
d	0.00 (fixed)
Di	0.60
Z1	1.00
Z2	1.00
Rsh1	0.99
Rsh2	0.99

percent, and the estimate of the data variance is 1.08E-6.

The inversion results and the parameters of true and initial guess model are listed in Table 2.2a. The borehole diameter and the mud resistivity are fixed during the inversion process.

The main diagonal elements of the parameter resolution matrix are listed in Table 2.2b. The analysis of parameter resolution matrix indicates that the shoulder resistivities and horizontal boundaries can be precisely determined, while the determination of the extent and the resistivity of the invaded zone has an uncertainty due to the nature of the downhole resistivity profiling.

The accuracy of the 2-D inversion can be increased by considering a set of resistivity logs of various electrode arrangements and spacings simultaneously.

2.4 Inversion of the Field Data

Finally the actual resistivity data run in the East Salt Creek well, Natrona, Wyoming, have been inverted by using a 1-D and a 2-D inversion schemes. Three types of resistivity logs, the 16" short normal, the 64" long normal, and the 18'8" lateral logs, are considered as shown in Figure 2.4. The apparent resistivity values are picked up from the curves for every foot from 5916 ft to 5950 ft. The borehole diameter is 9" and the mud resistivity in the logging depth is 0.8 ohm-m from the logging informations in the heading.

The resistivity data are first inverted by using an 1-D earth model, and then the data are inverted to a simple 2-D earth model which has a borehole and does not have an invasion. The earth parameters obtained from the 1-D inversion are used as an initial guess model for the 2-D inversion. The existence of invasion can be identified by comparing the 1-D or the 2-D inversion results. Once the invaded zone is found, with geologic and other informations, a composite 2-D earth model which best fits the normal and the lateral logs simultaneously can be found.

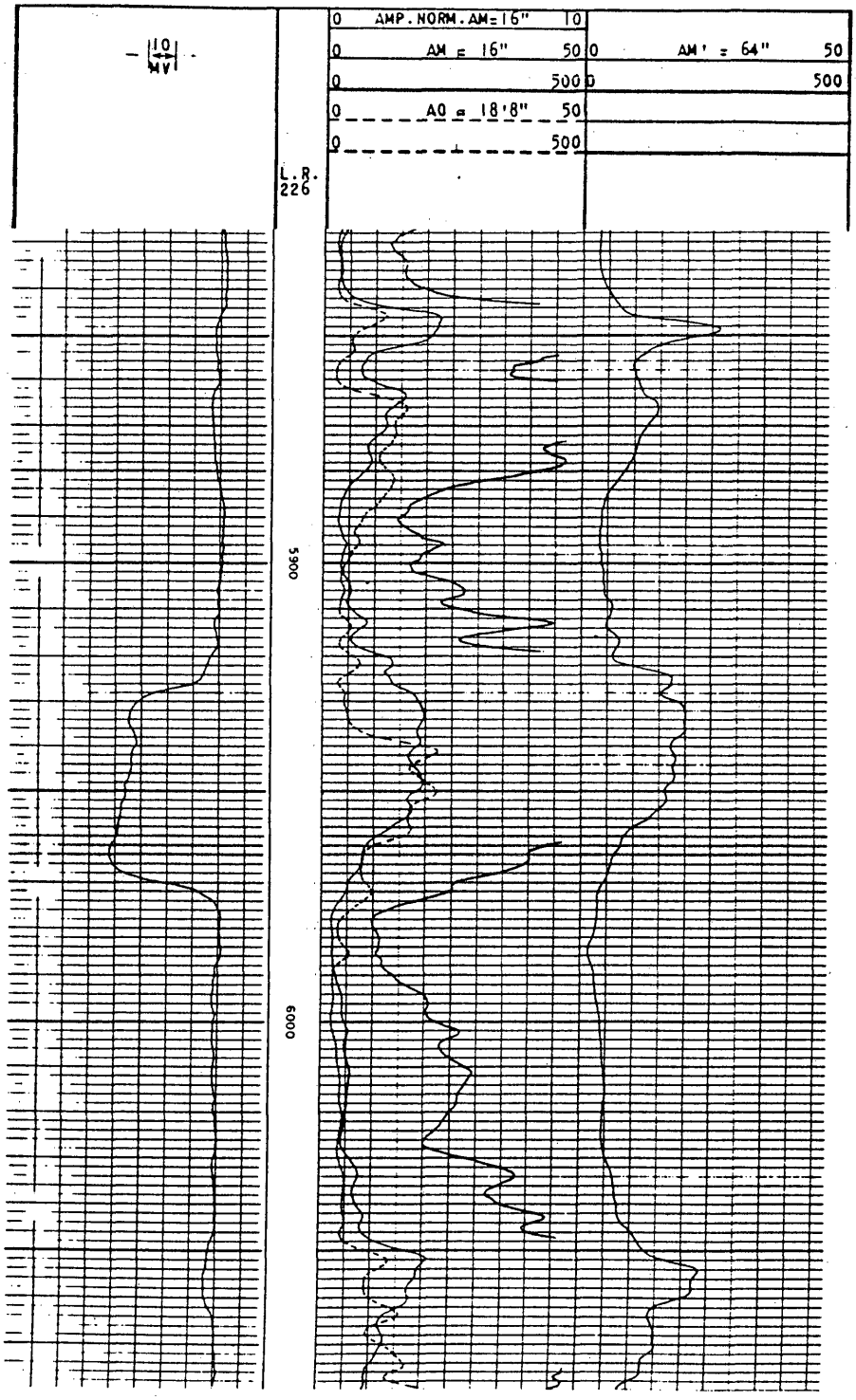

Figure 2.4 A segment of normal and lateral resistivitiy logs to be inverted

2.4.1 Inversion of the 16" Normal Data

The 16" short normal resistivity data are inverted to a horizontally layered earth model. The inversion results for an eight-layer fit are shown in Figure 2.5, which shows the observed data from the 16" normal resistivity log, the best fit model, and the resistivity log calculated from the best fit model. The rms error between observed data and the resistivity log calculated from the best fit model is 4 percent, and the estimate of the data variance is 6.24E-4. The earth parameters for each layer are listed in Table 2.3, where the depth to the top of the first layer is 5910 ft.

The 16" short normal data are then inverted to a 2-D earth model which has a borehole. The inversion results are shown in Figure 2.6, and the earth parameters for each layer are listed in in Table 2.3.

Table 2.3 Earth parameters determined from the inversion of the 16" normal resistivity data

Layer	Resistivity (ohm-m)		Thickness (ft)	
	1-D Model	2-D Model	1-D Model	2-D Model
1	4.8	4.2	8.8	8.7
2	16.1	17.3	4.1	3.8
3	13.0	10.6	3.3	3.8
4	19.3	20.0	3.9	3.8
5	20.4	20.5	7.0	6.5
6	18.3	18.4	3.8	4.2
7	16.4	15.2	4.0	3.8
8	19.6	19.3	---	---

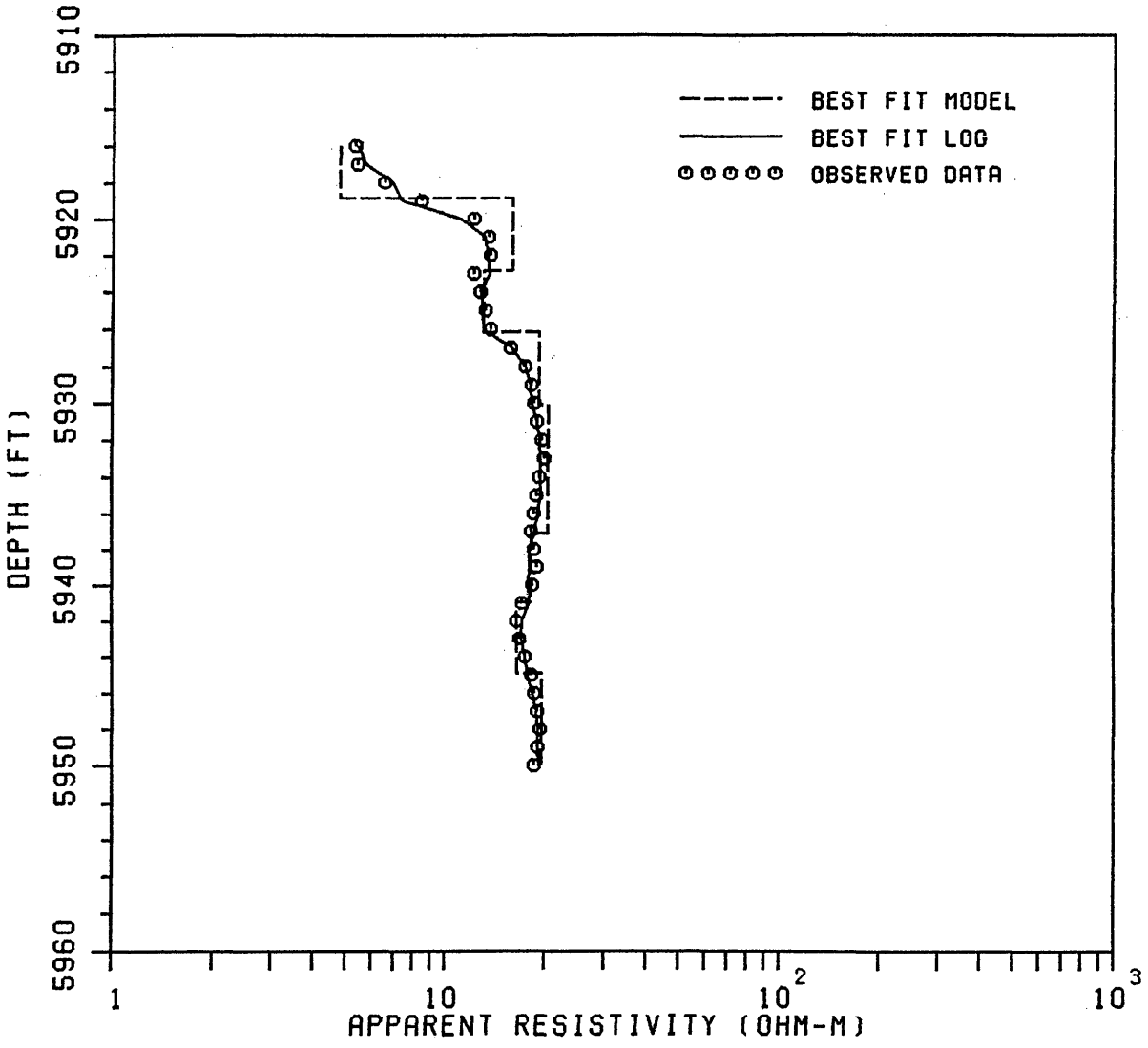

Figure 2.5 Comparison between observed data and the best fit log obtained from an 1-D inversion of the 16" normal resistivity data (4% rms error)

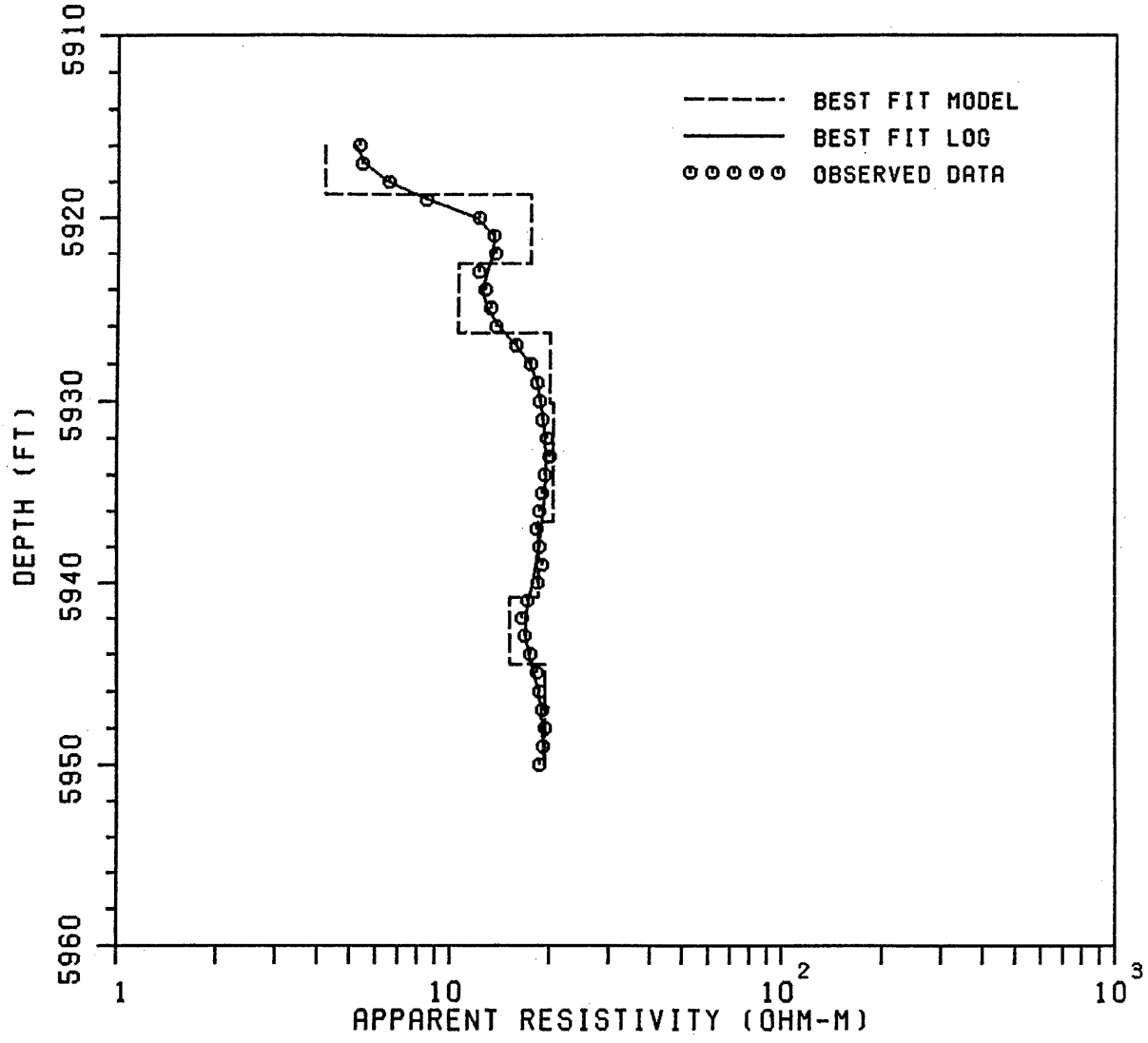

Figure 2.6 Comparison between observed data and the best fit log obtained from a 2-D inversion of the 16" normal resistivity data (2% rms error)

The rms error between observed data and the resistivity log calculated from the best fit model is 2 percent, and the data variance is 5.31E-5. The 16" normal resistivity data inversion results indicate that the rms error can be reduced by considering a 2-D model.

The parameter changes are very well resolved for the all layers except for the bed thickness of the layer 7 for the 1-D inversion. For the 2-D inversion, bed thickness resolutions are relatively poor in layers 3, 4, 6, and 7.

2.4.2 Inversion of the 64" Normal Data

The 64" long normal resistivity data are then inverted to a horizontally layered earth model. The inversion result for an eight-layer fit is shown in Figure 2.7, which shows the observed data from the 64" resistivity log, the best fit model, and the resistivity log calculated from the best fit model. The rms error between observed data and the resistivity log calculated from the best fit model is 3 percent, and the estimate of the data variance is 2.47E-4. The earth parameters for each layer are listed in Table 2.4, where the depth to the top of the first layer is 5910 ft.

The 64" long normal resistivity data are inverted to a 2-D model which has a borehole. The inversion results are shown in Figure 2.8, and the earth parameters for each layer are compared to the 1-D inversion results in Table 2.4.

Table 2.4 Earth parameters determined from the inversion of the 64" normal resistivity data

Layer	Resistivity (ohm-m)		Thickness (ft)	
	1-D Model	2-D Model	1-D Model	2-D Model
1	4.1	4.2	8.7	9.1
2	29.9	134.7	3.7	2.9
3	18.3	7.5	4.2	5.2
4	28.8	56.2	3.9	2.7
5	21.1	13.6	6.9	9.0
6	24.2	20.4	4.0	2.9
7	18.2	12.6	4.0	4.4
8	16.2	13.2	---	---

The rms error between observed data and the resistivity log calculated from the best fit model is 3 percent, and the estimate of the data variance is 2.64E-4. The 64" normal data inversion results indicate that the parameter estimate is not improved by considering a 2-D model.

The comparison of the 1-D and the 2-D inversion results shows that there are big differences between estimated earth parameters.

The parameter changes for the resistivities are very well resolved, while the resolutions for the bed thicknesses are moderate.

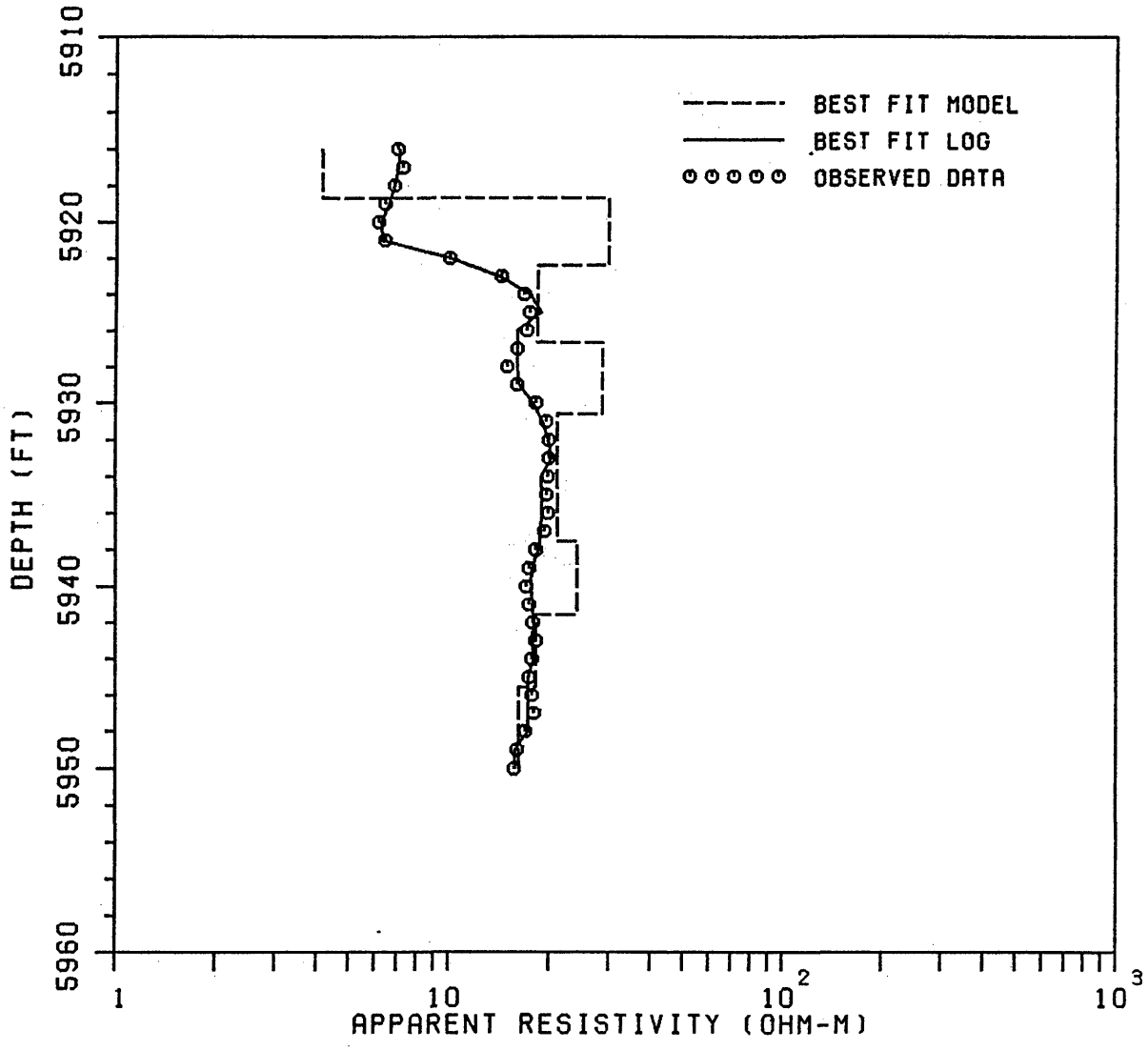

Figure 2.7 Comparison between observed data and the best fit log obtained from an 1-D inversion of the 64" normal resistivity data (3% rms error)

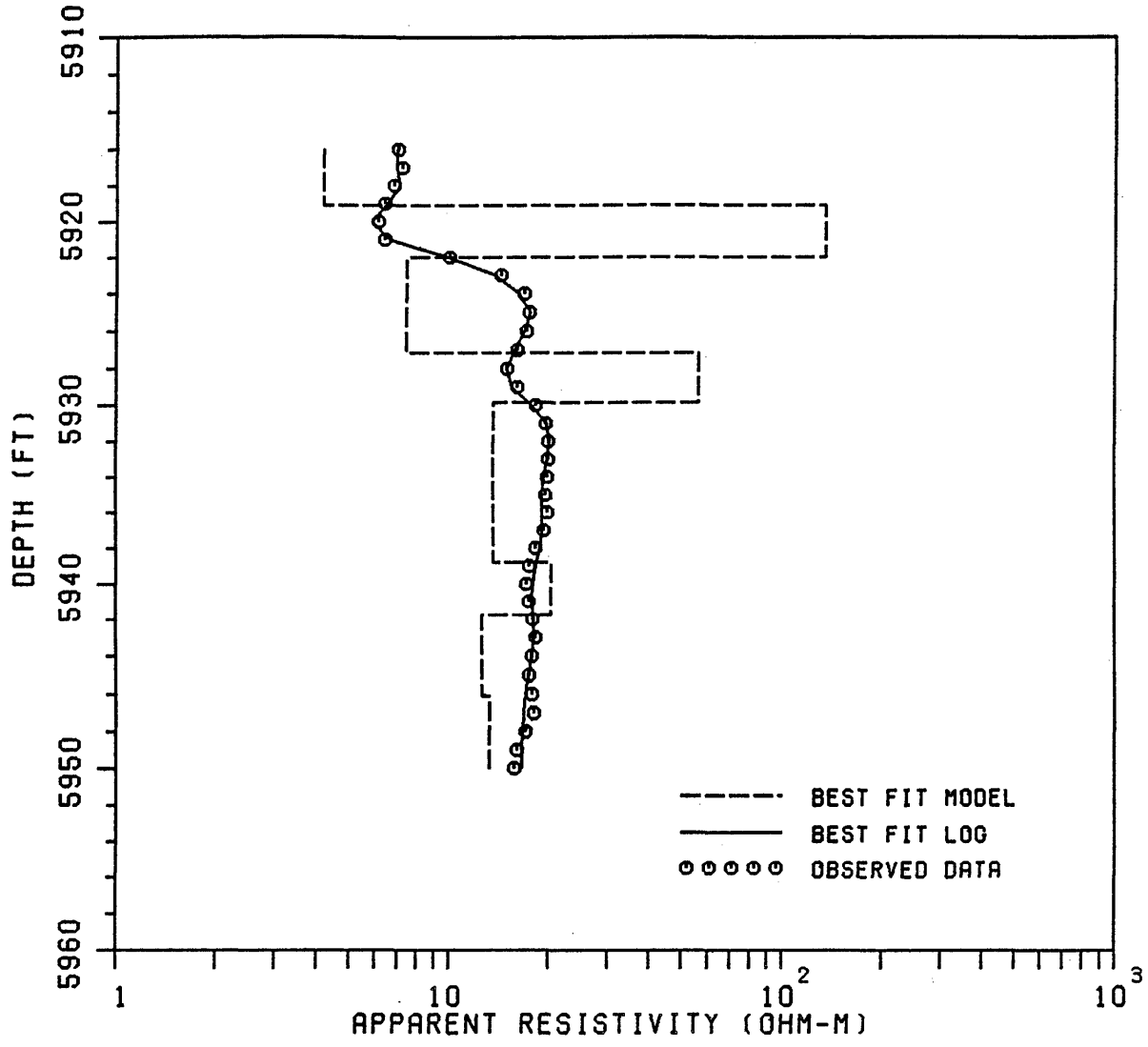

Figure 2.8. Comparison between observed data and the best fit log obtained from a 2-D inversion of the 64" normal resistivity data (3% rms error)

2.4.3 Inversion of the 18'8" Lateral Data

The 18'8" lateral resistivity data are finally inverted with horizontally layered earth model. The inversion result for an eight-layer fit is shown in Figure 2.9, which shows the observed data from the 18'8" lateral log, the best fit model, and the synthetic resistivity log calculated from the best fit model. The rms error between observed data and the resistivity log calculated from the best fit model is 27 percent, and the estimate of the data variance is 1.68E-1. This large error and data variance can be reduced by considering a more detailed earth model. Despite the large rms error, it was found that the resolutions for the earth parameters are very good. The earth parameters for each layer are listed in Table 2.5, where the depth to the top of the first layer is 5910 ft.

The 18'8" lateral resistivity data are then inverted to a 2-D earth model which has a borehole. The inversion results are shown in Figure 2.10, and the earth parameters for each layer are compared to the 1-D inversion results in Table 2.5.

The rms error between observed data and the resistivity log calculated from the best fit model is 10 percent, and the data variance is 4.11E-3. The 18'8" lateral data inversion results indicate that the parameter estimate is much improved by considering a 2-D model.

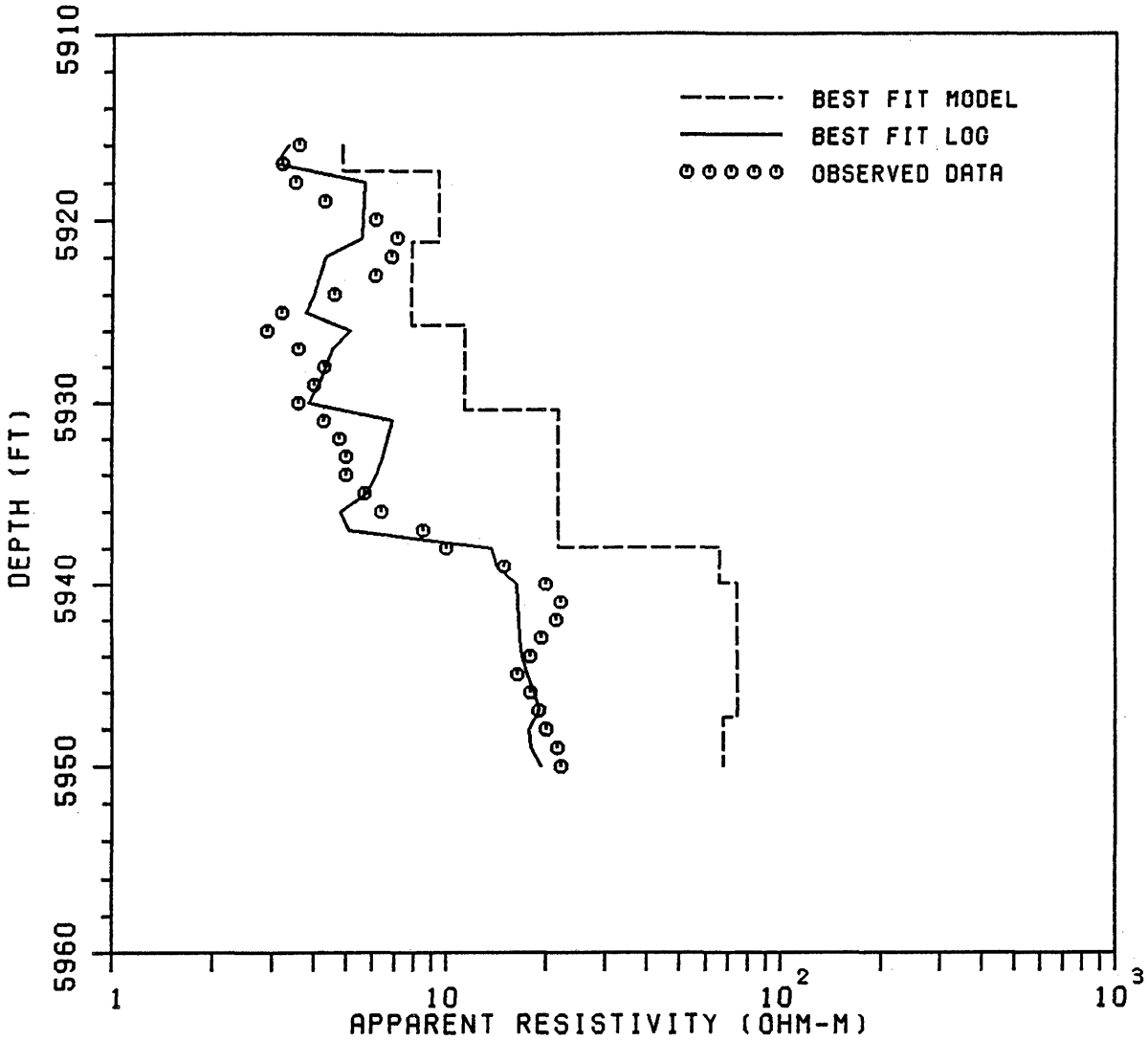

Figure 2.9 Comparison between observed data and the best fit log obtained from an 1-D inversion of the 18'8" lateral resistivity data (27% rms error)

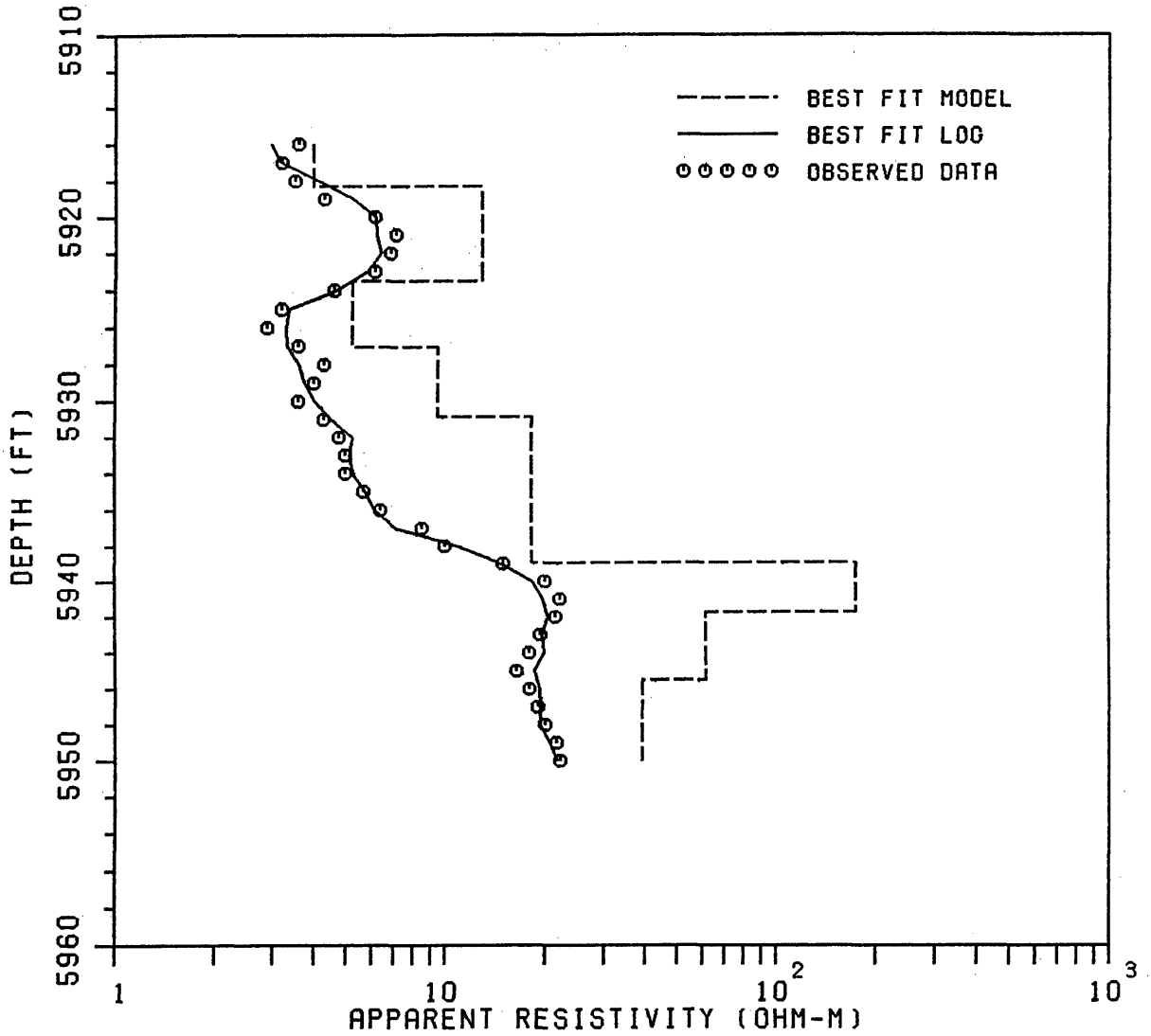

Figure 2.10 Comparison between observed data and the best fit log obtained from a 2-D inversion of the 18'8" lateral resistivity data (10% rms error)

Table 2.5 Earth parameters determined from the inversion of the 18'8" lateral resistivity data

Layer	Resistivity (ohm-m)		Thickness (ft)	
	1-D Model	2-D Model	1-D Model	2-D Model
1	4.7	4.0	7.3	8.3
2	10.0	12.8	4.0	5.2
3	9.0	5.2	4.7	3.6
4	10.6	9.5	4.2	3.8
5	22.2	18.3	8.6	8.1
6	66.3	174.6	1.9	2.8
7	78.0	61.5	7.4	3.8
8	70.5	39.3	---	---

The comparison of the 1-D and the 2-D inversion results shows that there are big differences in parameter estimates of layers 6, 7, and 8. The parameter changes for the resistivities and the bed thicknesses are very well resolved for all the layers except layers 6 and 7.

2.4.4 Comparison of the Inversion Results

The earth parameters obtained from the 1-D inversion of three different resistivity data are compared in Figure 2.11. True resistivities for layers 1 and 5 show an excellent agreement between them, while those for the other layers show big differences. True resistivities obtained from the inversion of the 18'8" lateral resistivity data have the lowest values in layers 2, 3, and 4, and those

obtained from the inversion of the 64" normal resistivity data have the highest values in corresponding layers. This suggests that there are resistive invaded zones in layers 2, 3, and 4. True resistivities obtained from the inversion of the 18'8" lateral resistivity data are high in layers 6, 7, and 8, and those obtained from the inversion of the 16" and the 64" normal data are low in corresponding layers. This suggests that there are conductive deep invaded zones in layers 6, 7, and 8.

Inversion results for bed thicknesses show that the bed boundaries between layers 3 and 4, layers 4 and 5 , and layers 6 and 7 are very well determined.

The earth parameters obtained from the 2-D inversion of three different resistivity data are compared in Figure 2.12. the figure also suggests that there are resistive invaded zones in layers 2, 3, and 4, and that there are conductive deep invaded zones in layers 6, 7, and 8.

The bed boundaries between layers 1 and 2, layers 3 and 4, and layers 6 and 7 are very well determined.

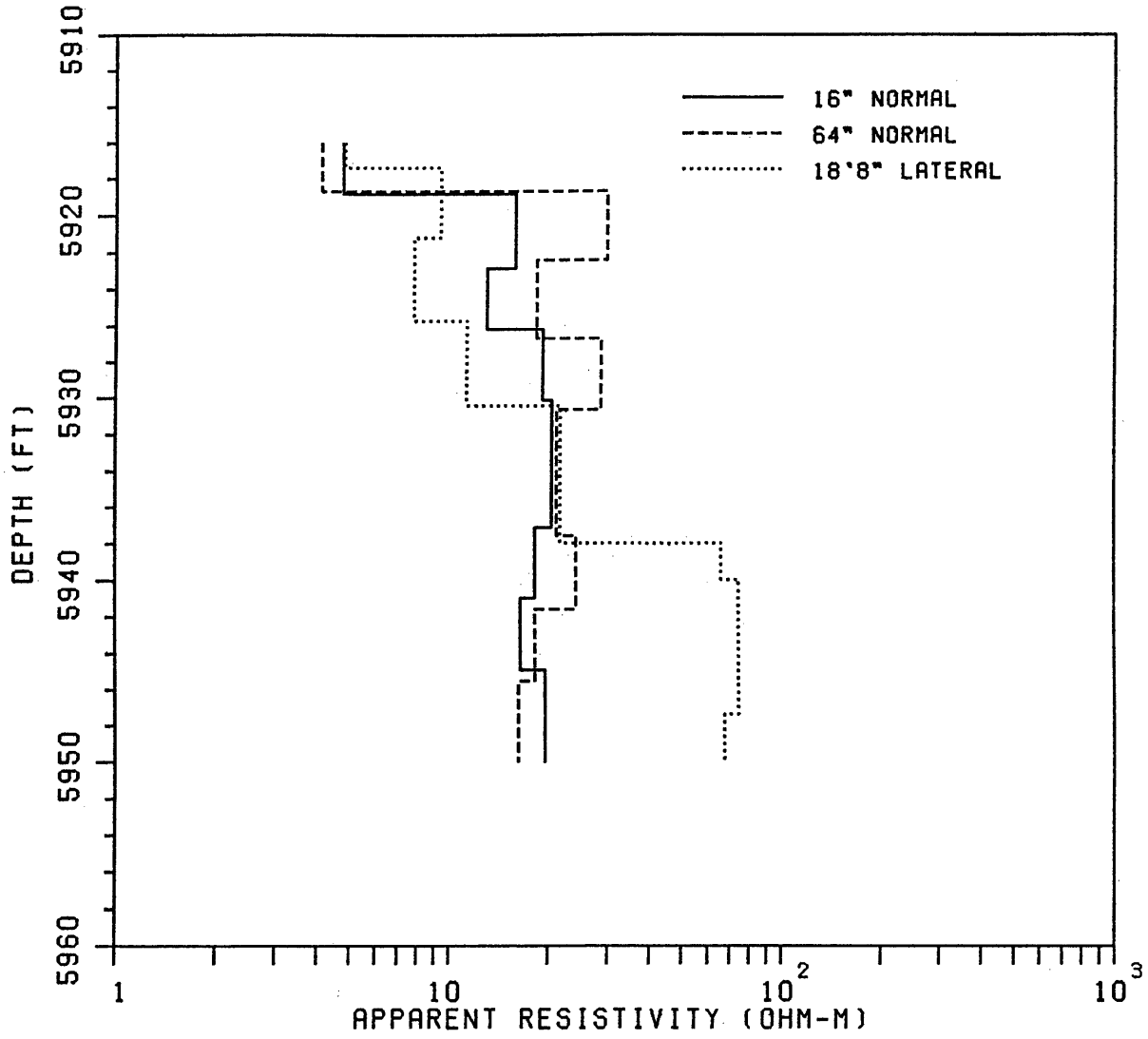

Figure 2.11 Comparison of 1-D inversion results of three different resistivity logs.

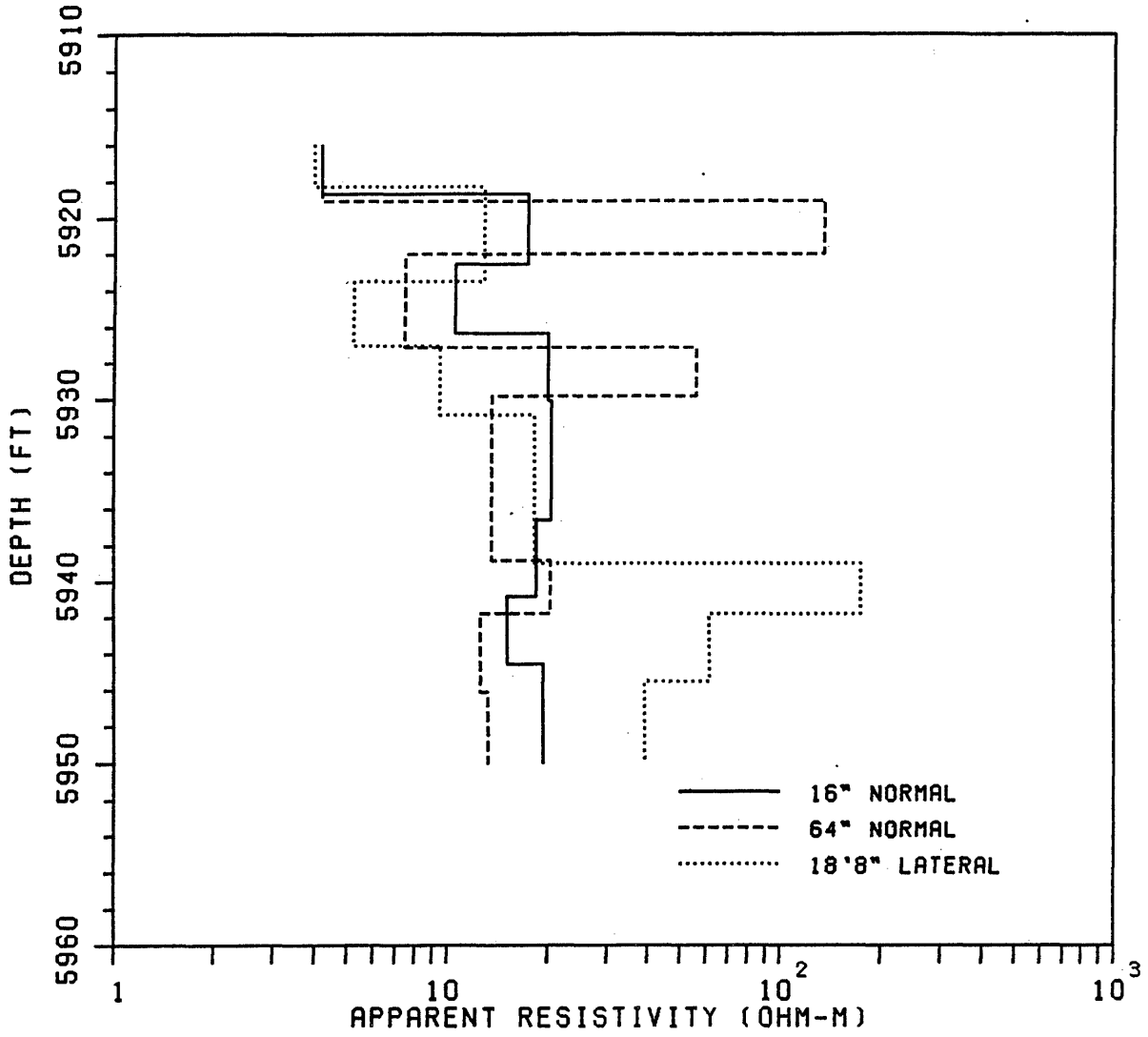

Figure 2.12 Comparison of 2-D inversion results of three different resistivity logs.

CONCLUSIONS

The finite difference method was used to simulate normal and lateral resistivity logs in a combined boundary earth model. The apparent resistivities in the presence of borehole mud, invaded zone, and horizontal bed boundaries can be obtained provided that the model has an axial symmetry.

An exponentially expanding grid system was introduced to reduce the size of the problem dramatically. The accuracy of the forward calculation was improved by considering a terminal resistance type boundary condition and a two-dimensional average resistivity calculation. Estimation of the electrical potentials at the exact positions of the the measuring electrodes also improved an accuracy of the results and eliminated a need for interpolation.

Comparison with analytical solutions for horizontally layered earth model and cylindrically layered earth model have shown that the finite difference method is a very accurate, fast, and flexible method to compute the apparent resistivities. The flexibility of the finite difference method was demonstrated in the numerical results, showing the synthetic resistivity logs calculated from muliple, invaded layers. The excellent agreement was also

obtained between the finite difference solution and the integral equation solution represented by Zhang and Shen (1984).

A comprehensive study of the effects on the earth parameter variations has been accomplished with various 2-D models. The results are:

(1) A large-diameter hole and low-resistivity mud increase the departure of apparent resistivity from the true resistivity,

(2) Short spacing tools are very sensitive to the borehole and invasion effects,

(3) If the bed thickness is less than the electrode spacing, it is very difficult to identify the bed boundaries and the true resistivities.

The forward modeling of the 2-D earth model has many possible applications. These include a better interpretation of the resistivity logs, a study of the invaded zone, a calibration of resistivity tools, a basis of resistivity inversion, a correction for the borehole environment, a development of new electrical logging tools, and so forth.

A ridge regression inversion technique was used to invert resistivity data. The test results indicate that the thickness and the resistivity of each layer can be determined simultaneously. For the 2-D model inversion the

finite difference algorithm was also used in the forward calculations. It has been demonstrated that the 1-D inversion results of field data can be used as a basis of the 2-D inversion. The existence of invasion can be identified by comparing the 1-D inversion results. Once the invaded zone is found, with the consideration of borehole effects, the 2-D model which best fits the normal and the lateral logs simultaneously can be found.

The current study has been restricted to the borehole normal and lateral resistivity data interpretations in an axially symmetrical earth model. Further study in this area might include: (1) Resistivity data interpretation in a 3-D model, (2) Forward and inverse modeling for the focused resistivity logging tools, and (3) development of approximate forward solutions for the fast inversions.

REFERENCES

Anderson, W.L., 1975, Improved Digital Filters for Evaluating Fourier and Hankel Transform Integrals. NTIS report, PB-242-800, USGS, Sprinfield, VA.

Carnahan, B. et al., 1969, Applied Numerical Methods, John Wiley & Sons, Inc., 604p.

Dakhnov, V.N., 1962, Quarterly of the Colorado School of Mines, translated by G.V. Keller, 445p.

Daniels, J.J., 1978, Interpretation of Buried Electrode Resistivity Data Using a Layered Earth Model, Geophysics, **43**, 988-1001.

Drahos, D., 1984, Electrical Modeling of the Inhomogeneous Invaded Zone, Geophysics, **49**, 1580-1585.

Gianzero, C., and Anderson, B., 1982, An integral transform solution to the fundamental problem in resistivity logging, Geophysics, **47**, 946-956.

Guyod, Hubert, 1955, Electrical analogue of Resistivity Logging, Geophysics, **20**, 615-629.

Hilchie, D.W., 1978, Applied Openhole Log Interpretation, Douglas W. Hilchie Inc., Golden, Co.

Hoversten, G.M. et al., 1982, Comparison of Five Least-Squares Inversion Techniques in Resistivity Sounding, Geophysical Prospecting, **30**, 688-715.

Inman, J.R. et al, 1973, Resistivity Inversion,

Geophysics, **38**, 1088-1108.

Inman, J.R., 1975, Resistivity Inversion with Ridge Regression, Geophysics, **40**, 798-817.

Kincaid et al., 1982, ITPACK 2C: A Fortran Package for solving Large Sparse Linear Systems by Adaptive Accelerated Iterative Methods, ACM Trans. on Math. Software, **8**, 302-322.

Marquardt, D.W., 1970, Generalized Inverse, Ridge Regression, Biased Linear Estimation, and Nonlinear Estimation, Technometrics, **12**, 592-612.

Mufti, I.R., 1978, A practical Approach to Finite-Difference Resistivity Modeling, Geophysics, **43**, 930-942.

Mufti, I.R., 1980, Finite-Difference Evaluation of Apparent Resistivity Curves, Geophysical Prospecting, **28**, 146-166.

Rijo, L. et al., 1977, Interpretation of Apparent resistivity data from Apodi Valley, Rio Grande de Norte, Brasil, Geophysics, **42**, 811-822.

Stoyer, C., 1985, Personal Communications.

Tsang, L. et al, 1984, Solution of the Fundamental Problem in Resistivity Logging with a Hybrid Method, Geophysics **49**, 1596-1604.

Van Nostrand, D.D., and Cook, K.L., 1966, Interpretation of Resistivity Data, USGS Prof. Paper 499, 310p.

Yang, F.W., and Ward, S.H., 1984, Inversion of Borehole Normal Resistivity Logs, Gepophysics, **49**, 1541-1548.

Yuratich, M.A., and Meger, W.J., 1984, The Application of Finite Difference Methods to Normal Resistivity Logs, SPWLA 25th Annual Logging Symposium Trans., V.

Zhang, G.Z., and Shen, L.C., 1984, Response of a Normal Resistivity Tool in a Borehole Crossing a Bed Boundary, Geophysics, **49**, 142-149.

APPENDIX A

SYNTHETIC RESISTIVITY LOGS

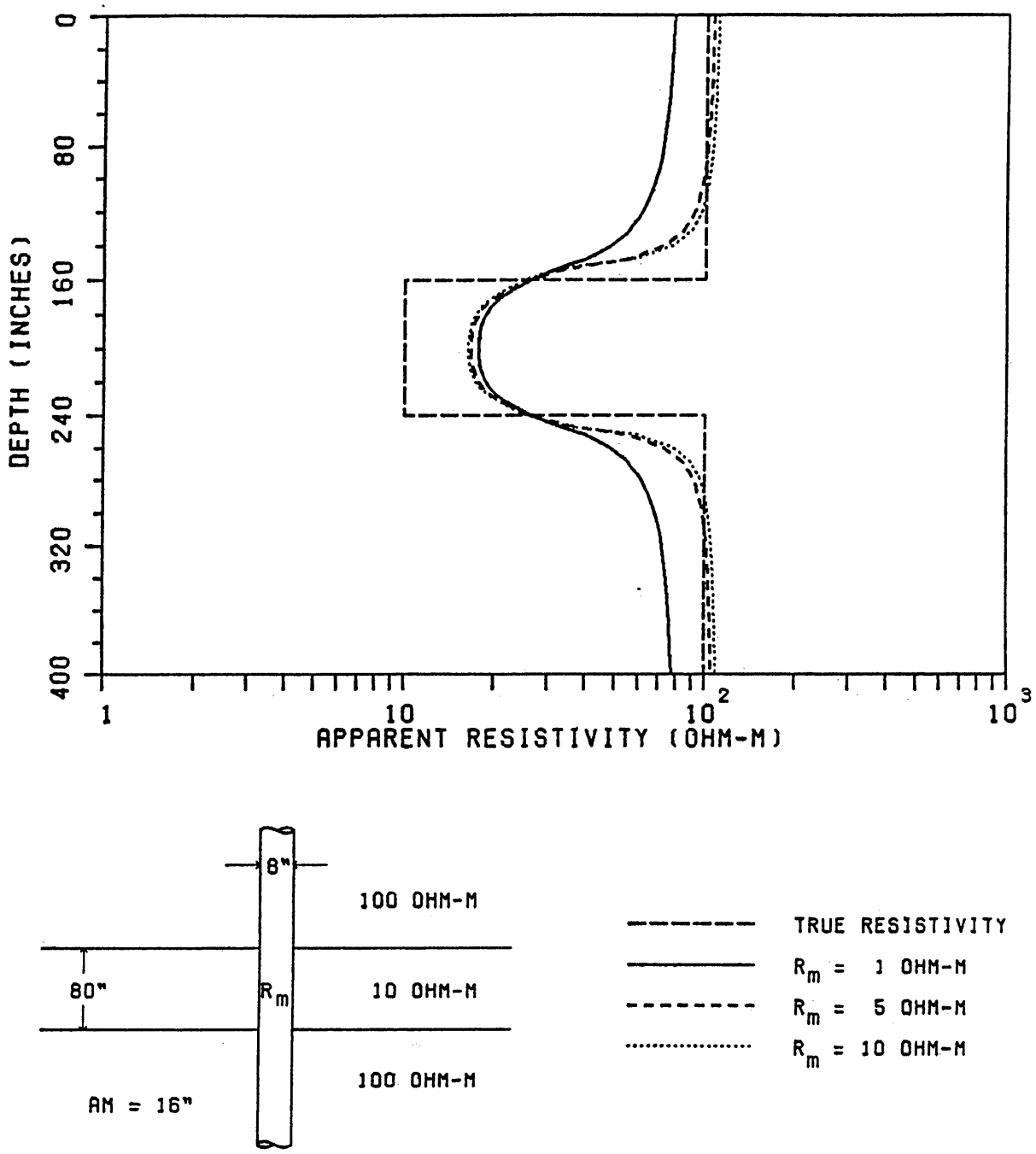

A-1.1 Variations in Rm (Normal-Thick-Conductive)

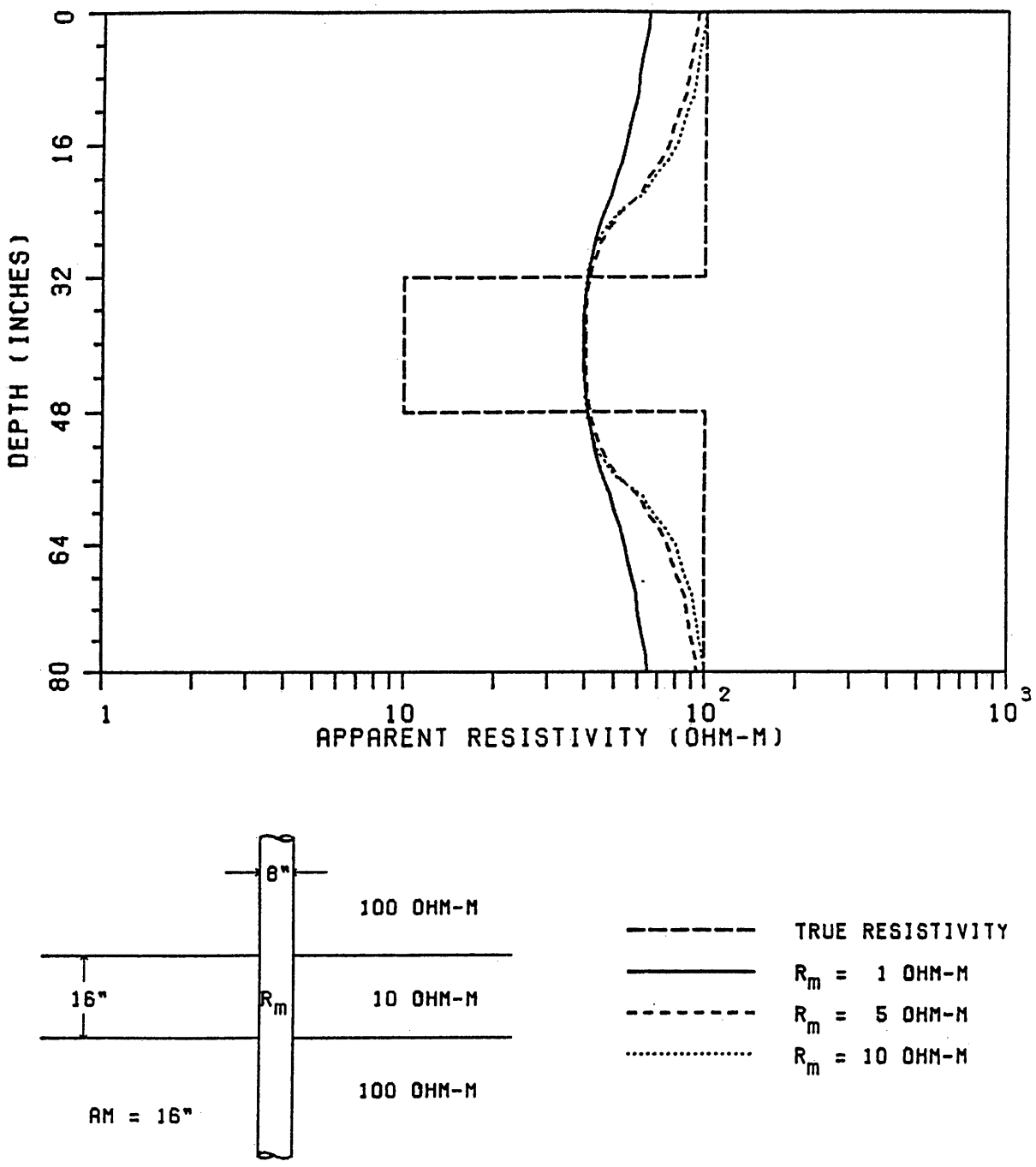

A-1.2 Variations in Rm (Normal-Critical-Conductive)

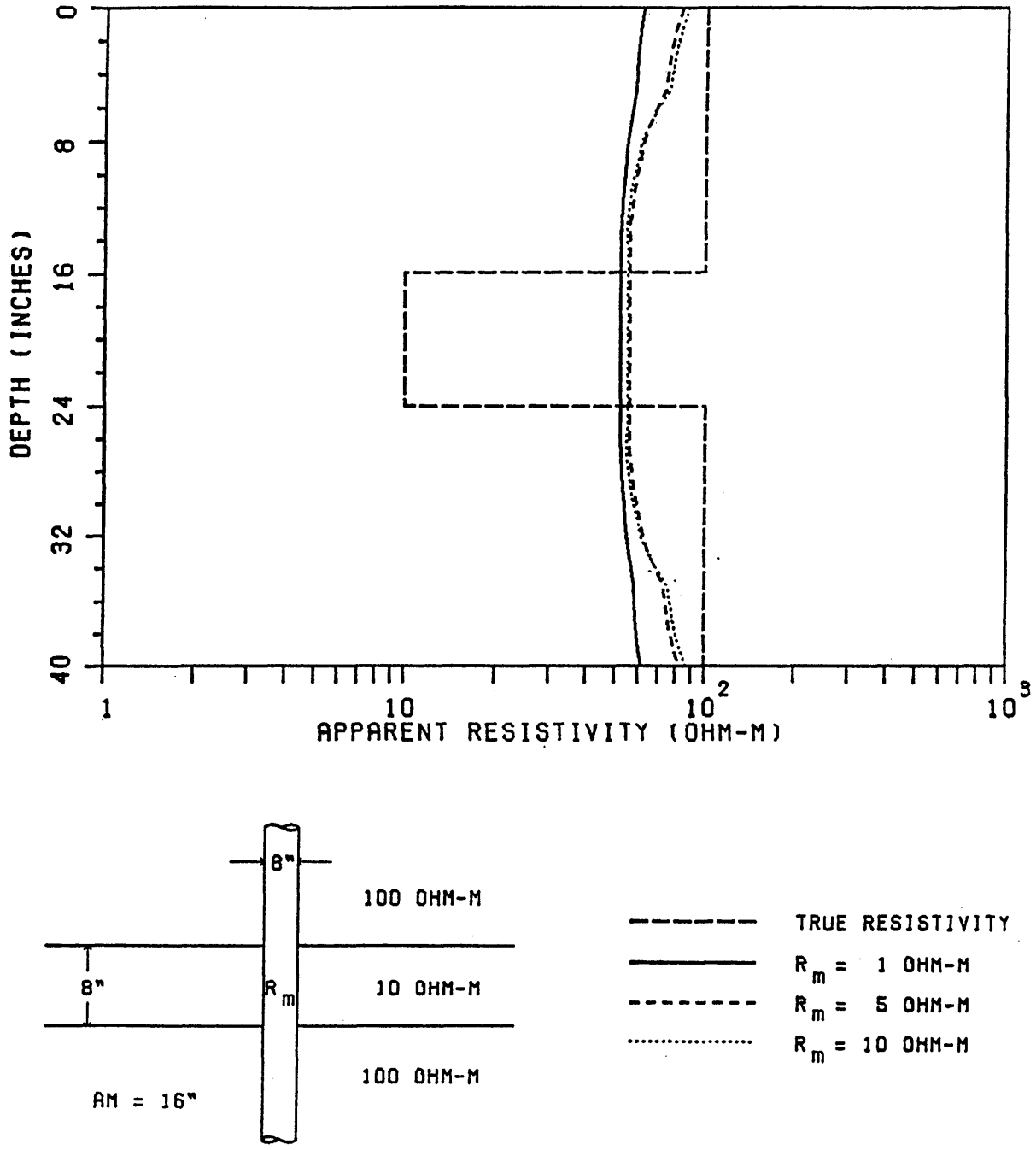

A-1.3 Variations in Rm (Normal-Thin-Conductive)

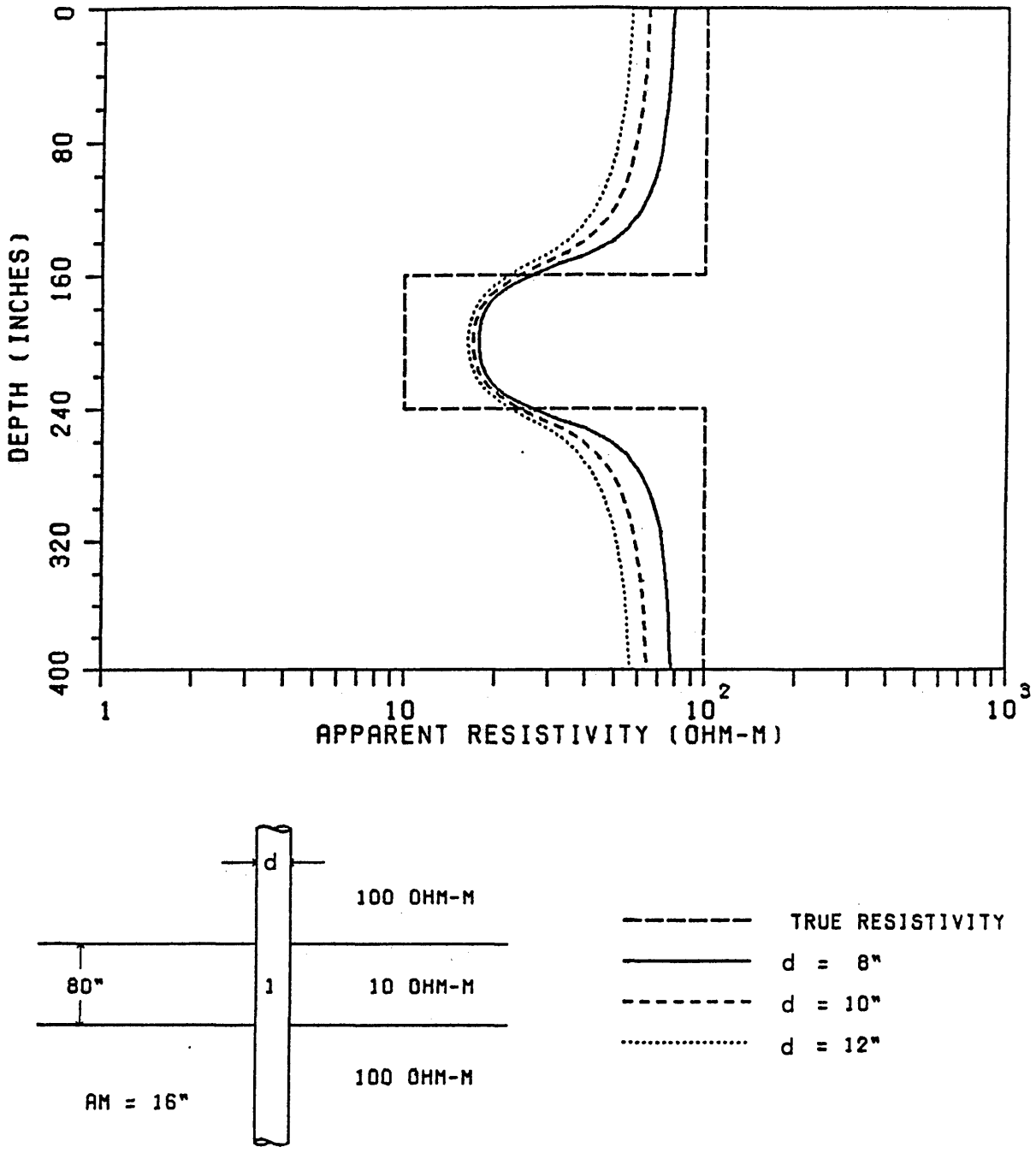

A-1.4 Variations in d (Normal-Thick-Conductive)

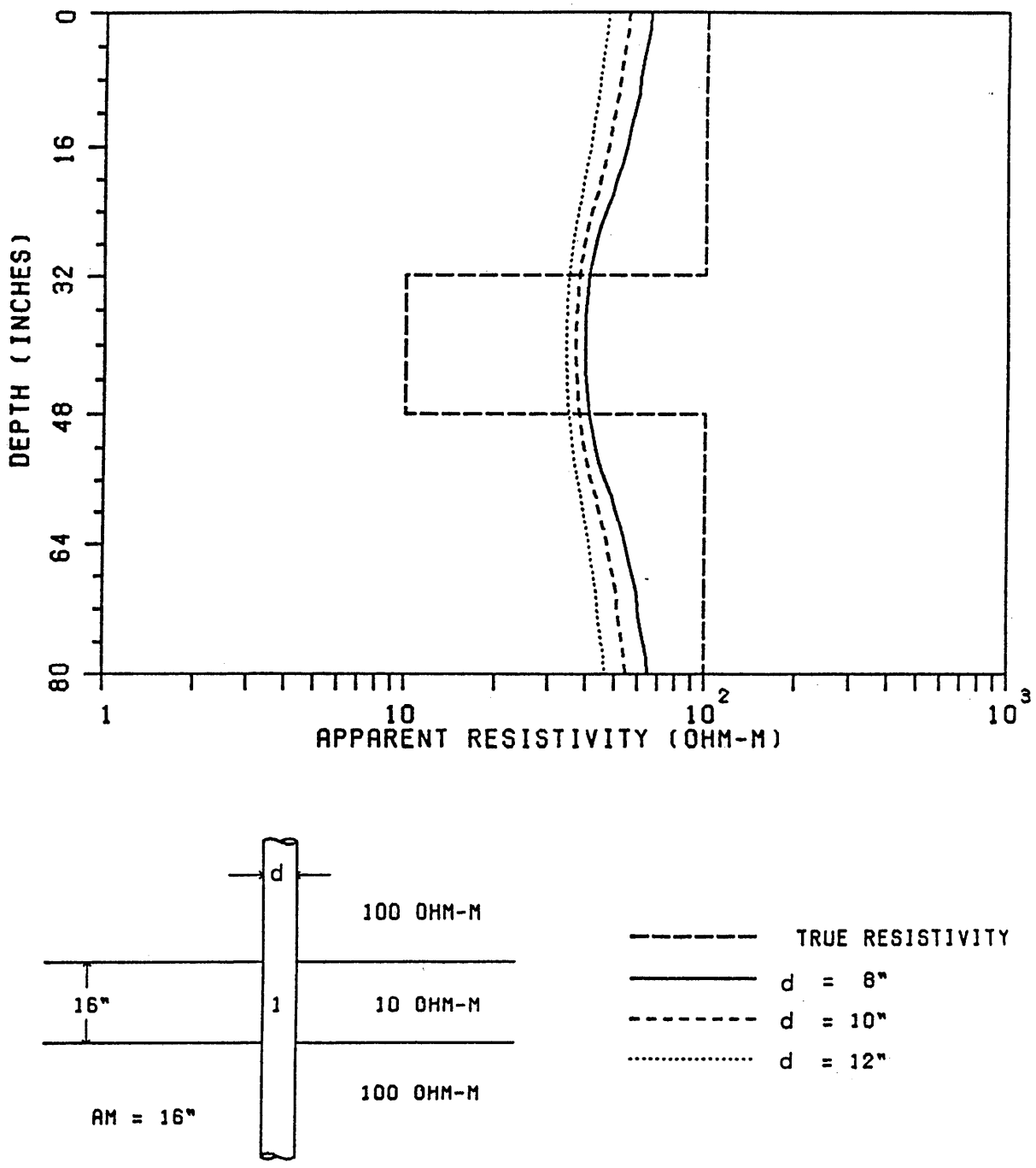

A-1.5 Variations in d (Normal-Critical-Conductive)

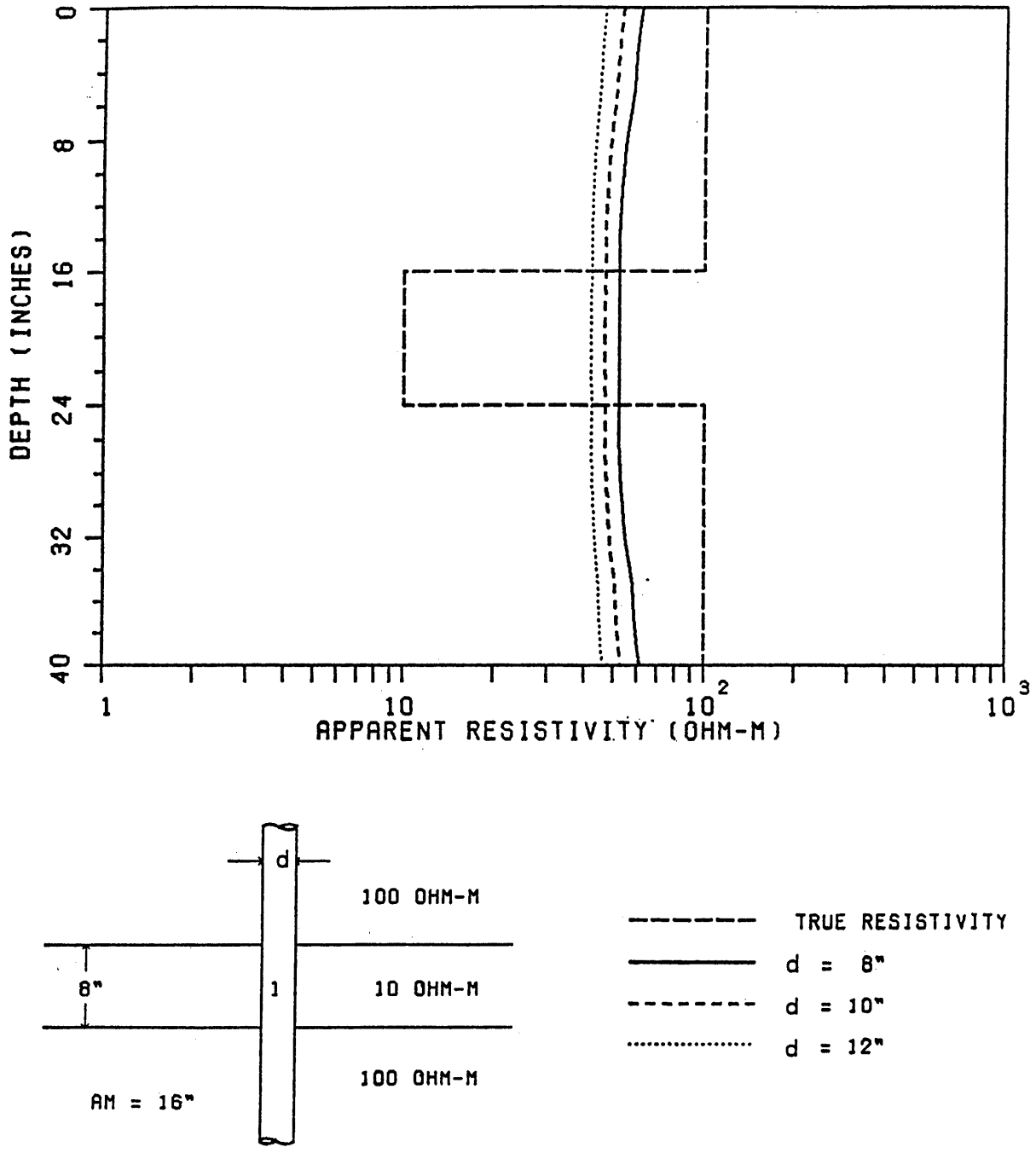

A-1.6 Variations in d (Normal-Thin-Conductive)

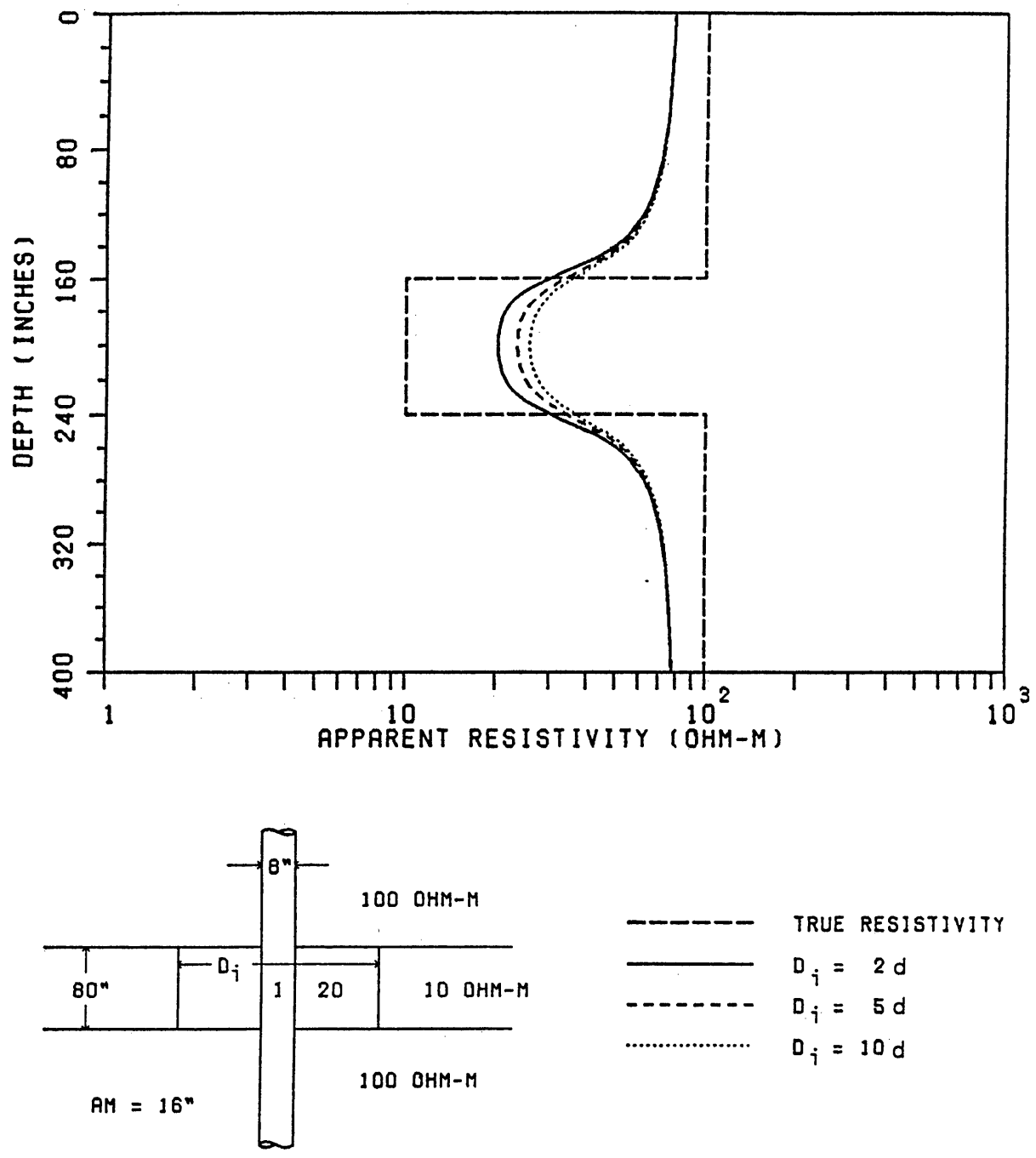

A-1.7 Variations in Di (Normal-Thick-Conductive)

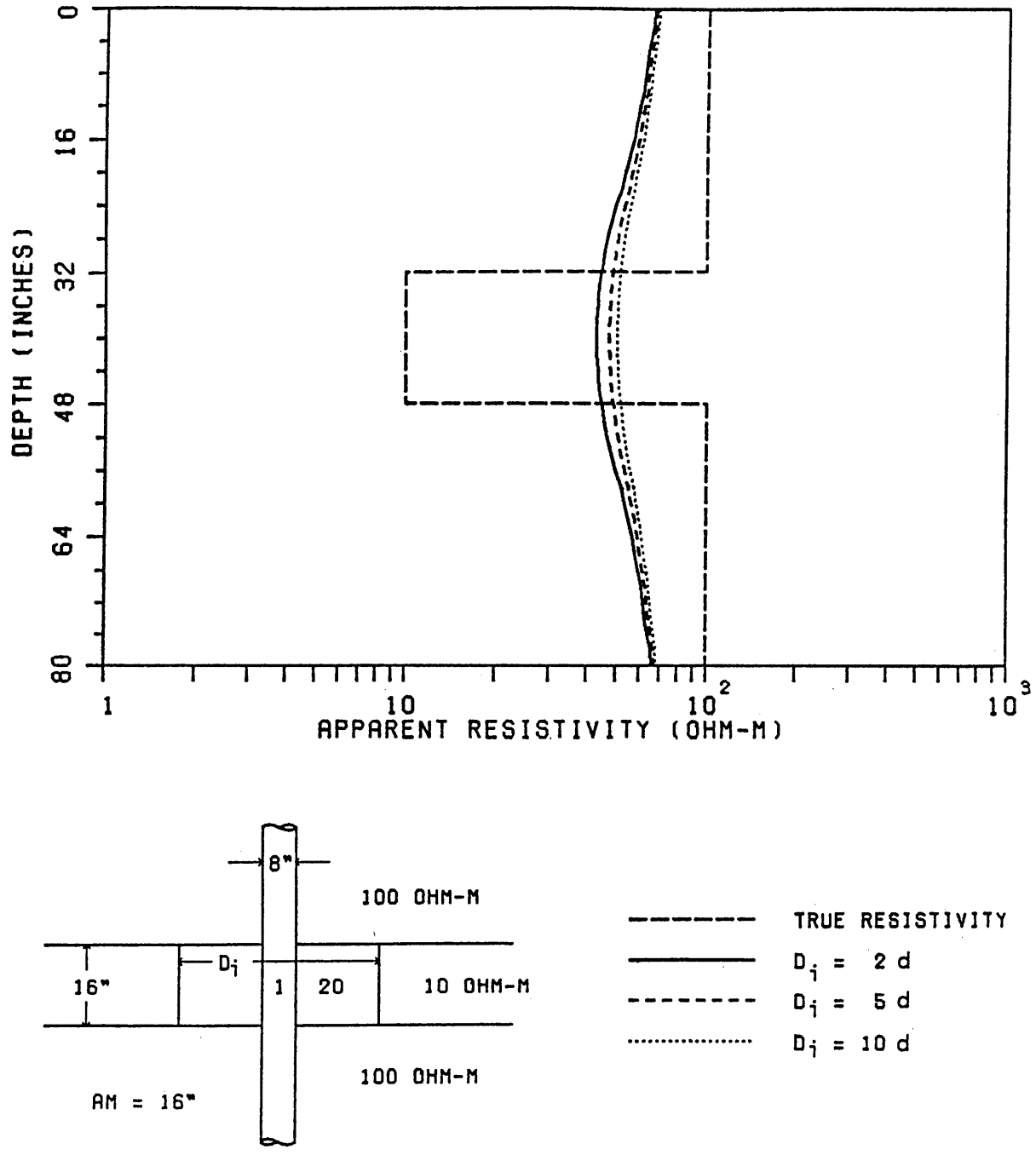

A-1.8 Variations in Di (Normal-Critical-Conductive)

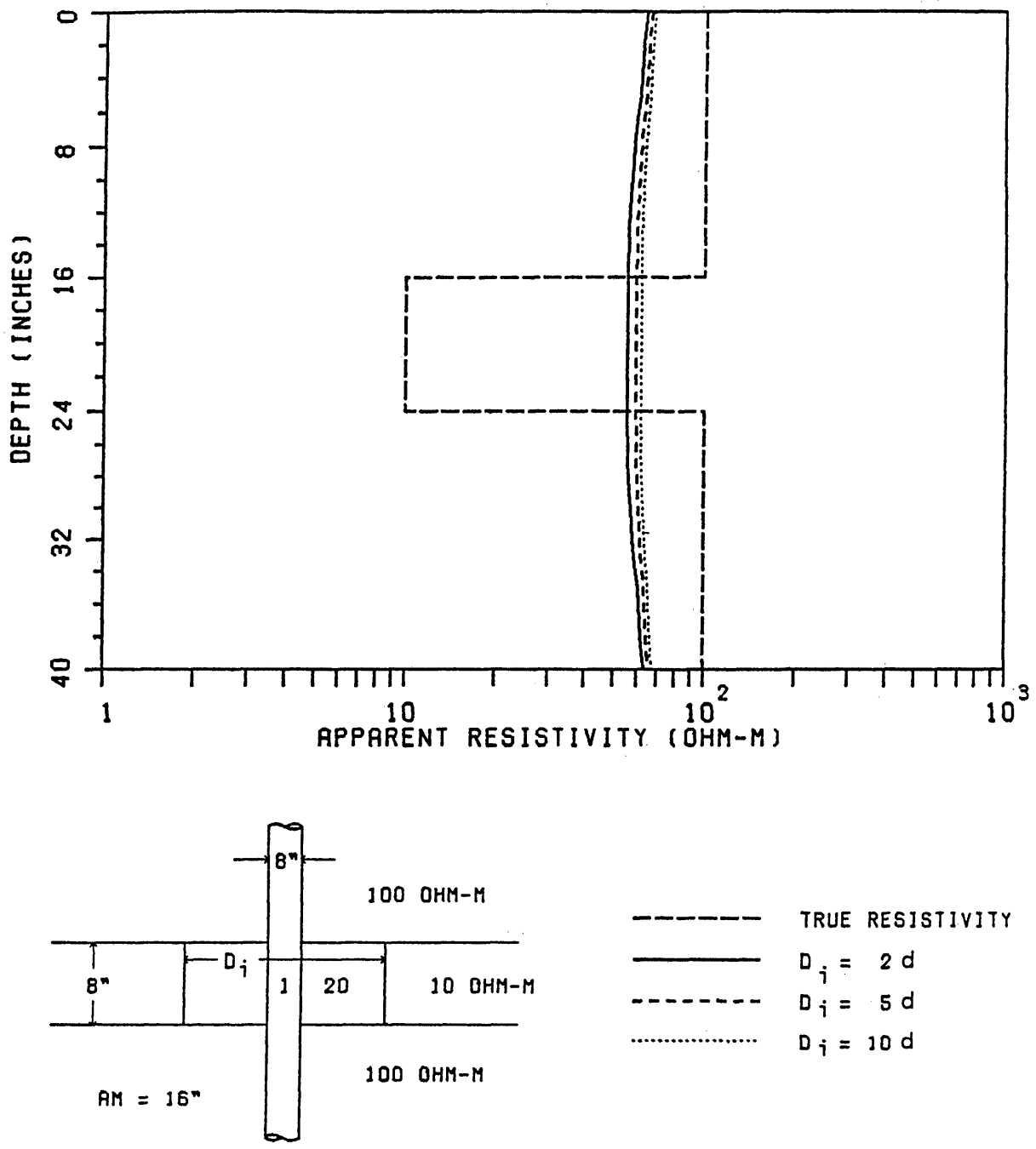

A-1.9 Variations in Di (Normal-Thin-Conductive)

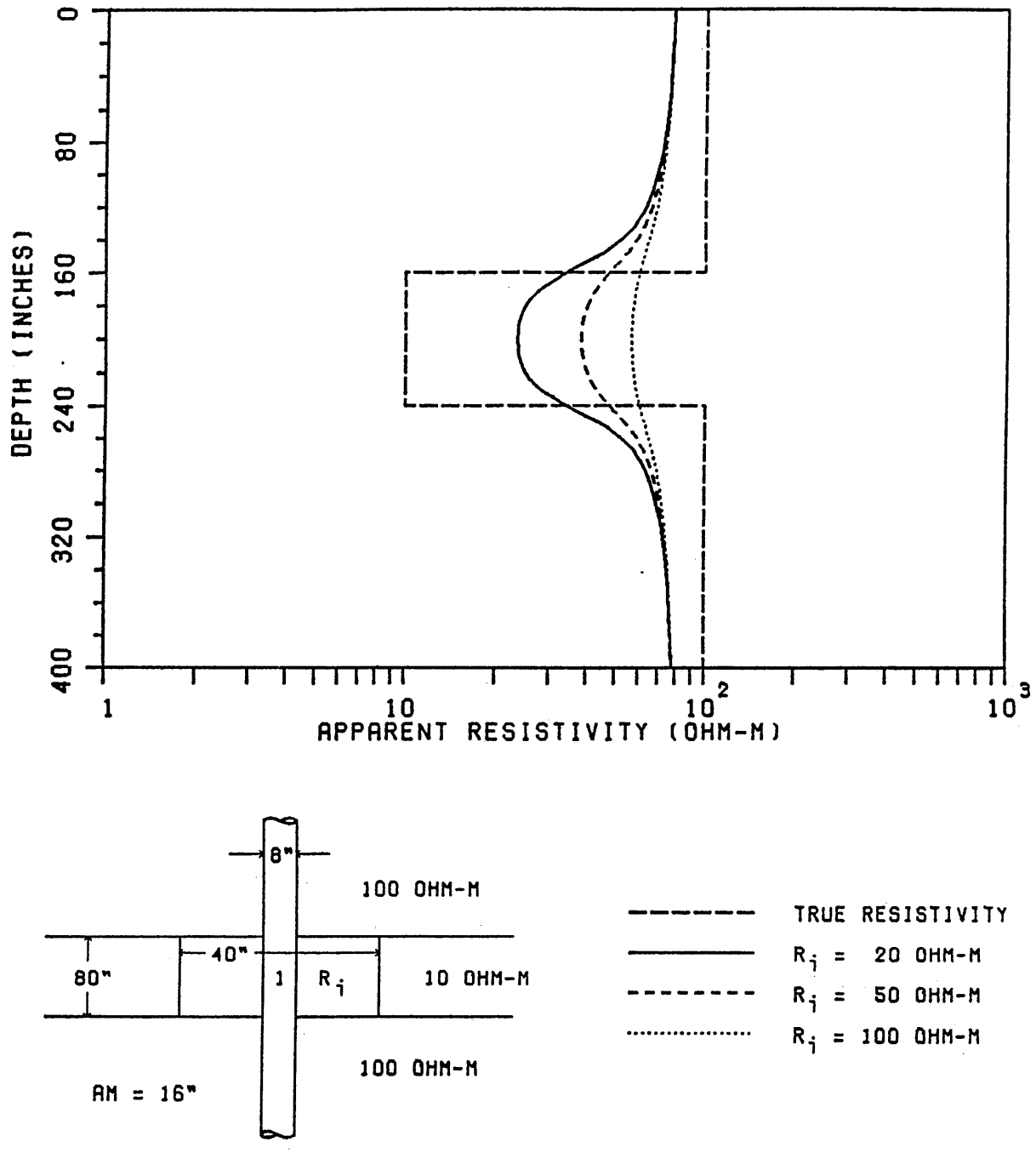

A-1.10 Variations in Ri (Normal-Thick-Conductive)

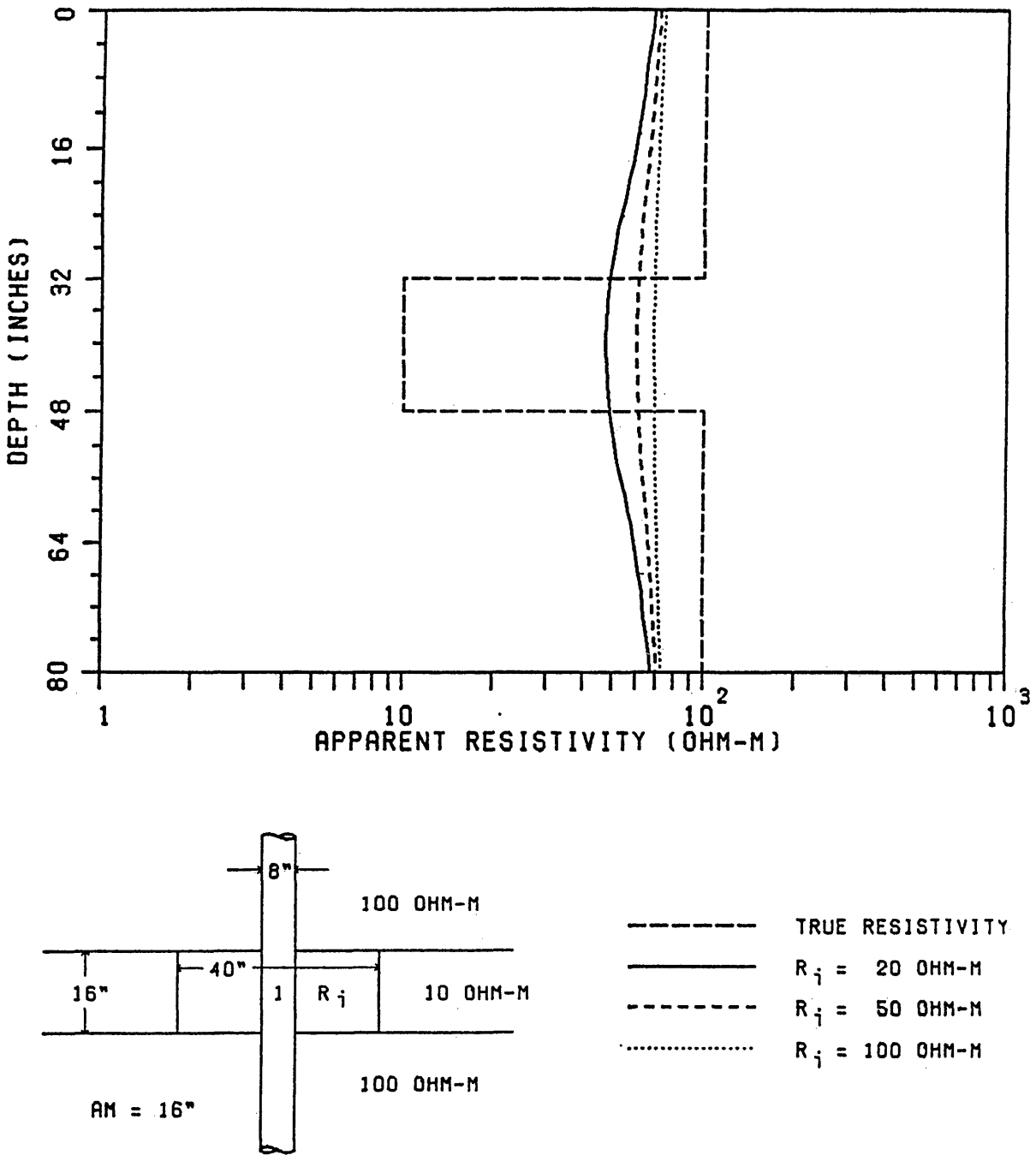

A-1.11 Variations in Ri (Normal-Critical-Conductice)

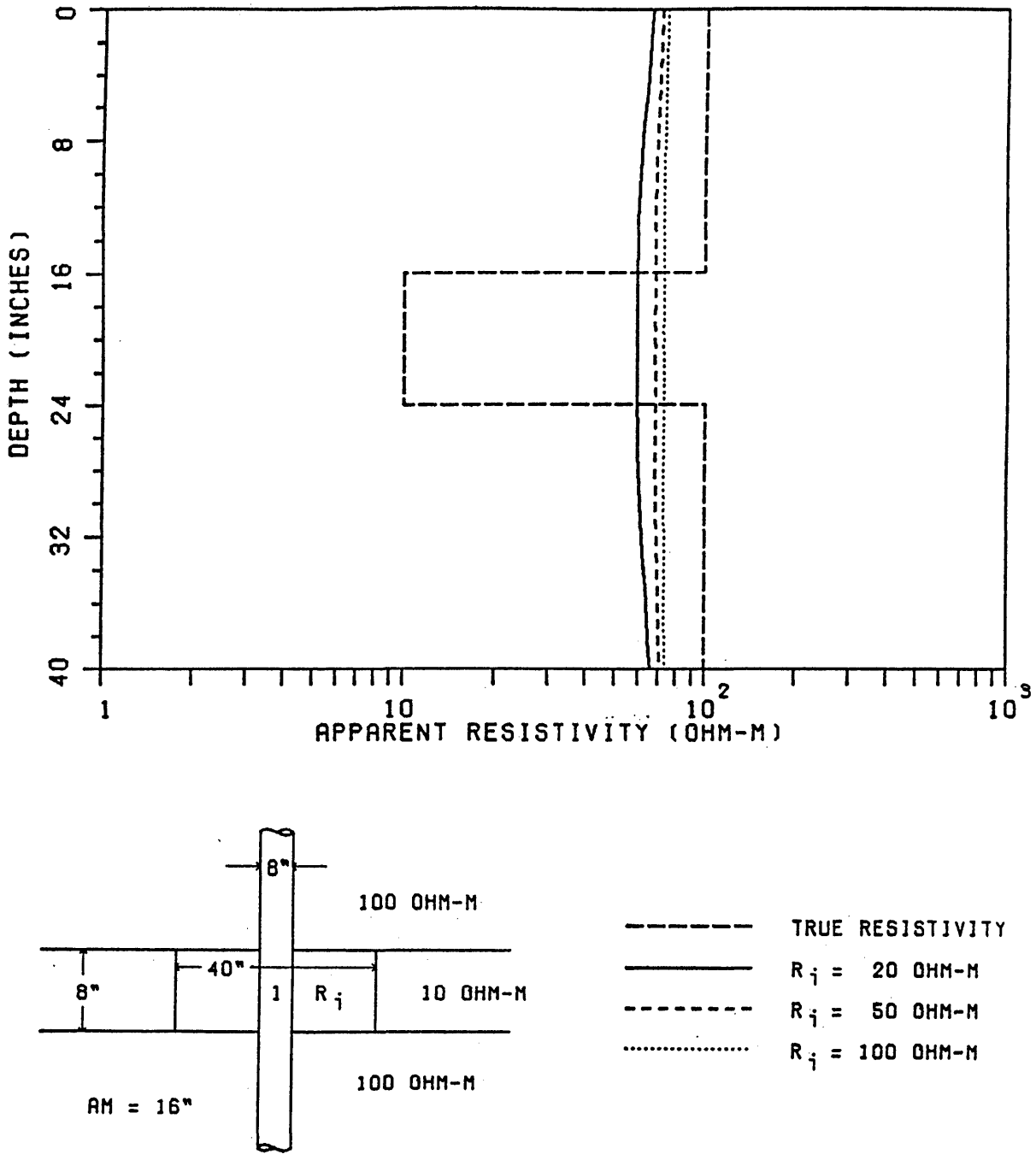

A-1.12 Variations in Ri (Normal-Thin-Conductive)

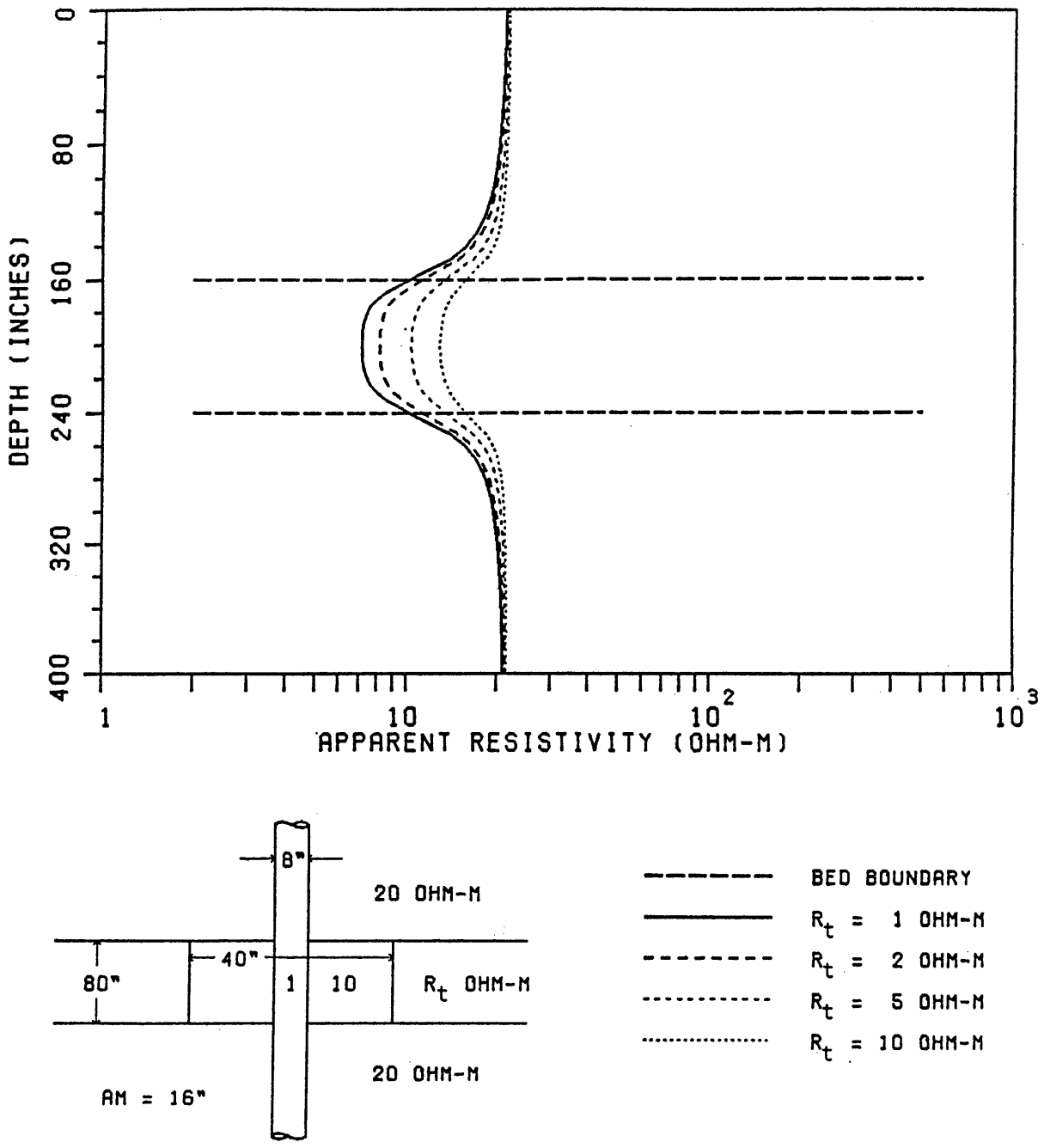

A-1.13 Variations in Rt (Normal-Thick-Conductive)

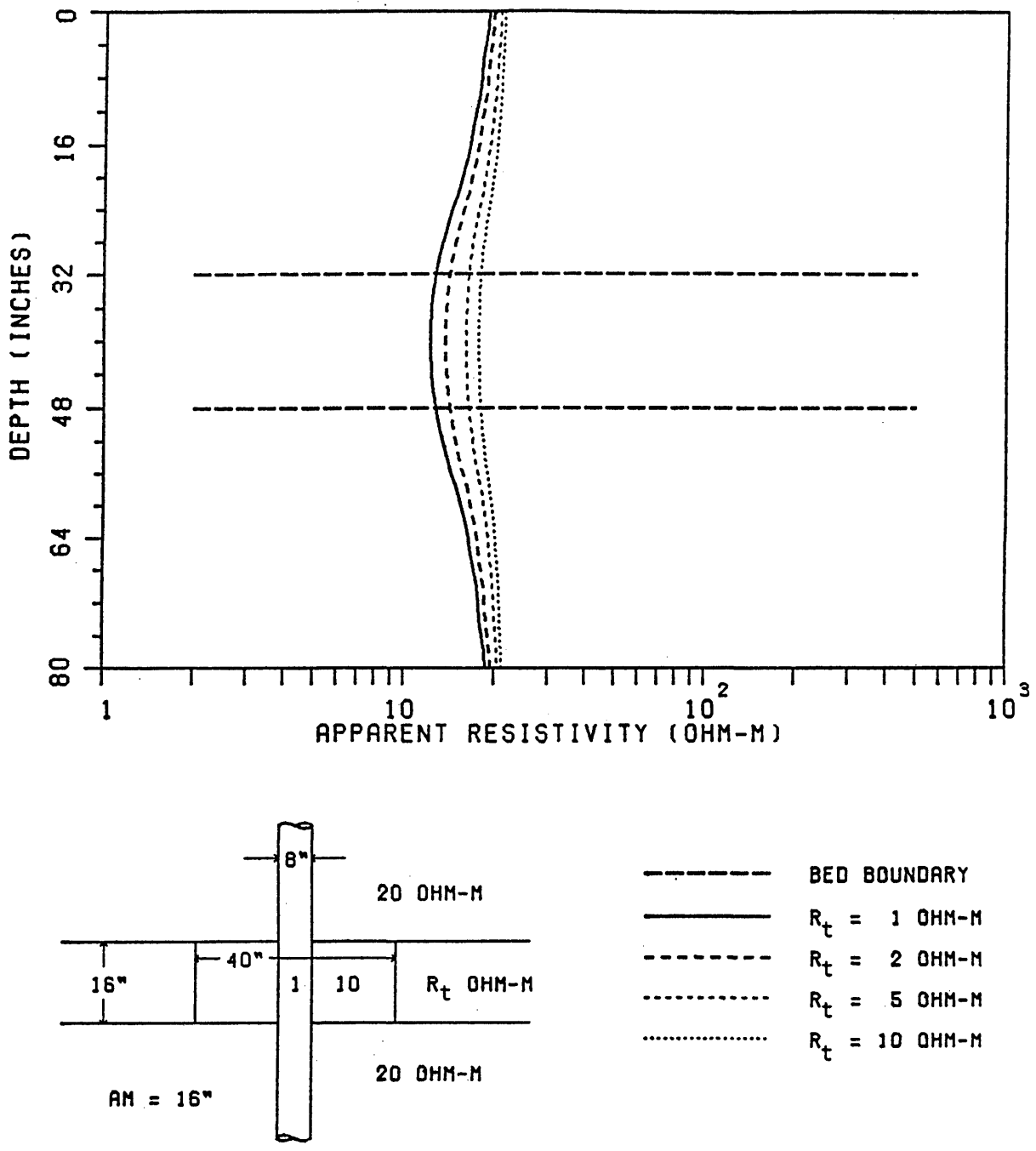

A-1.14 Variations in Rt (Normal-Critical-Conductive)

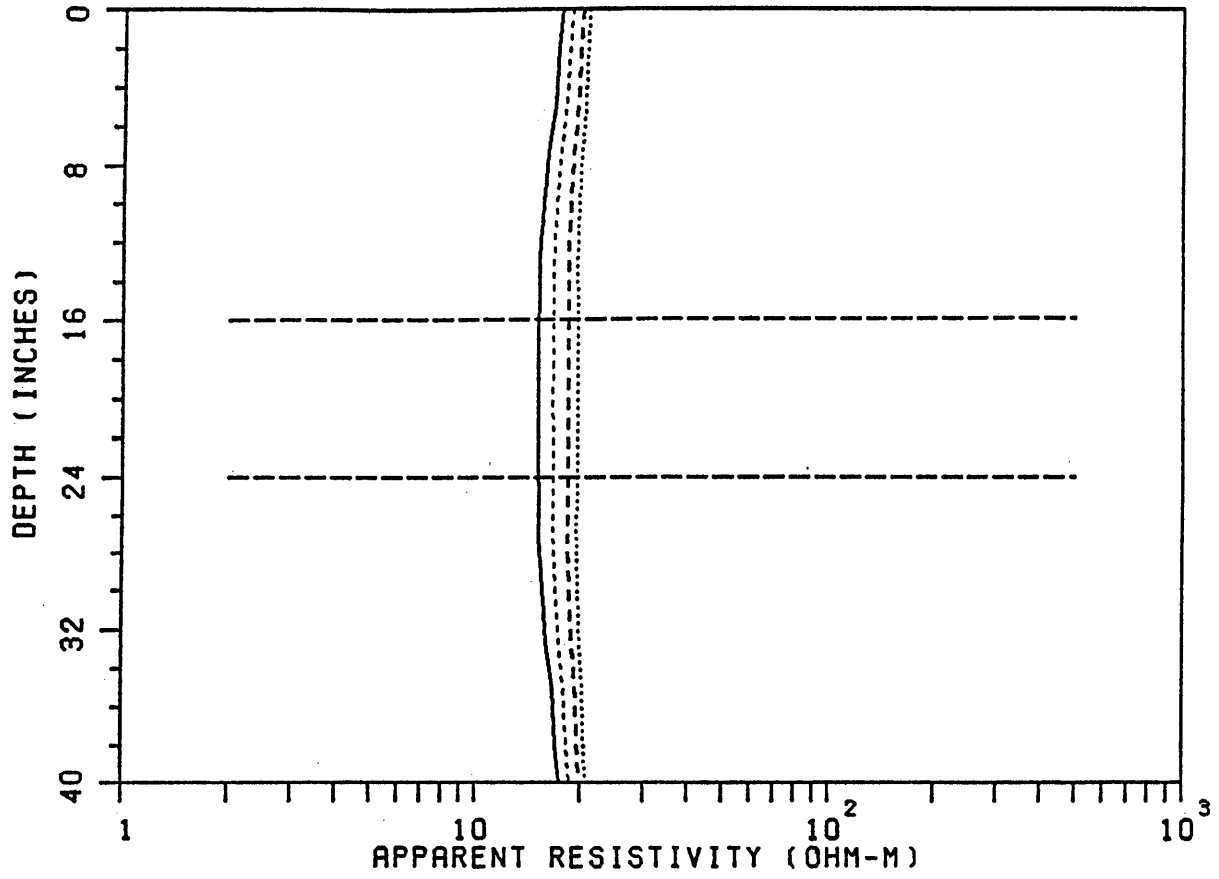

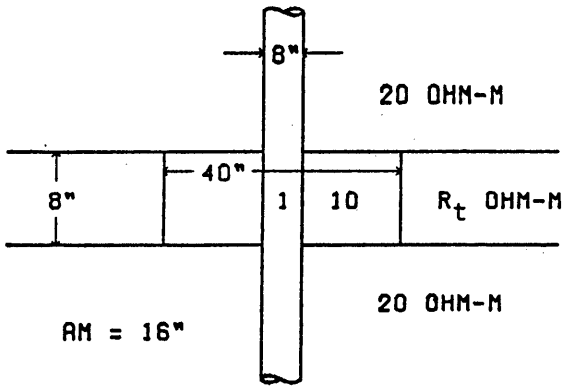

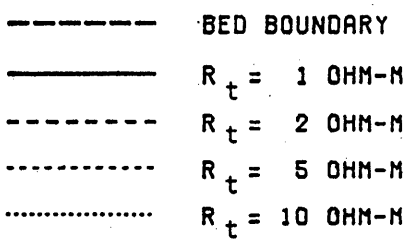

A-1.15 Variations in Rt (Normal-Thin-Conductive)

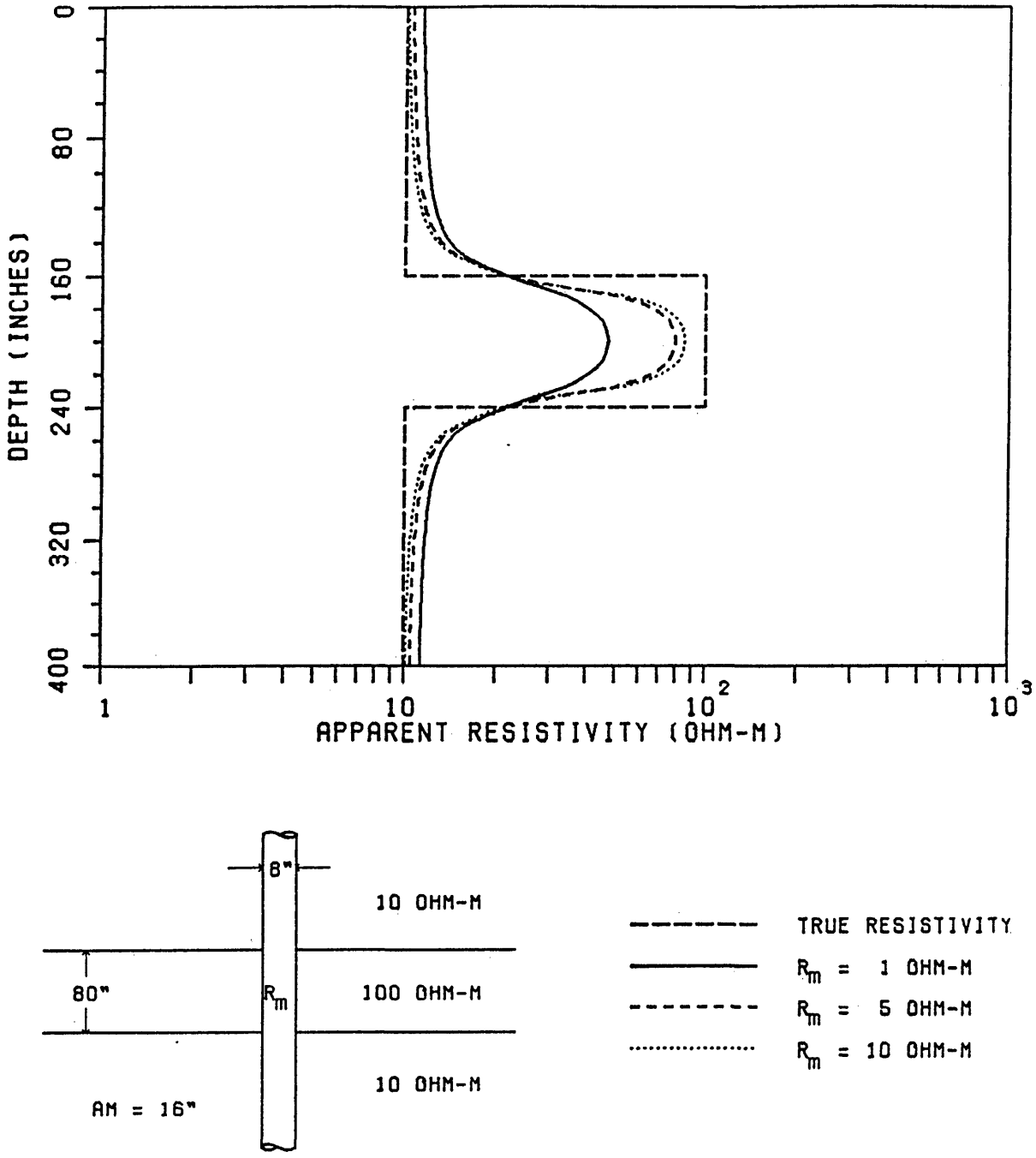

A-2.1 Variations in Rm (Normal-Thick-Resistive)

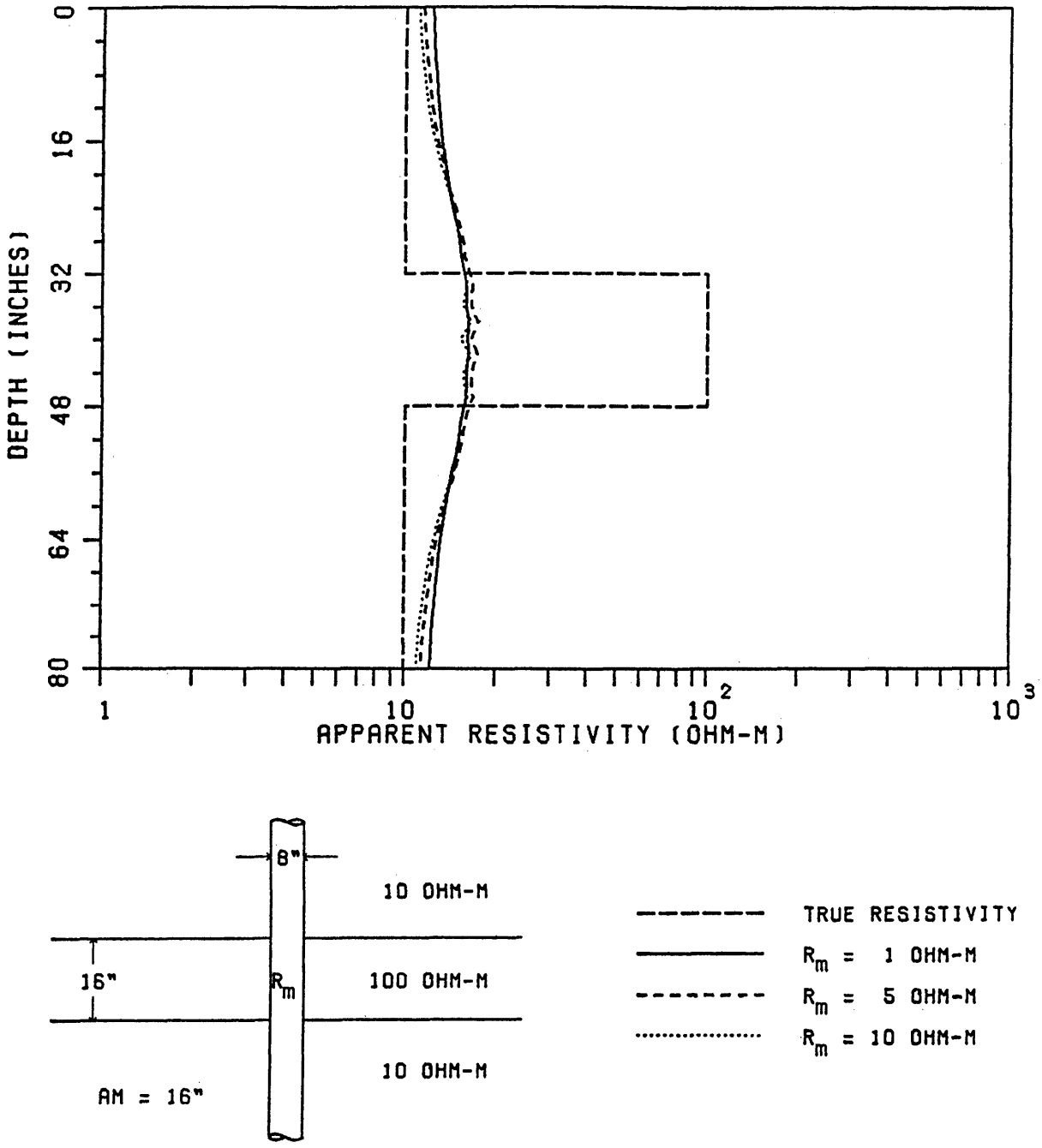

A-2.2 Variations in Rm (Normal-Critical-Resistive)

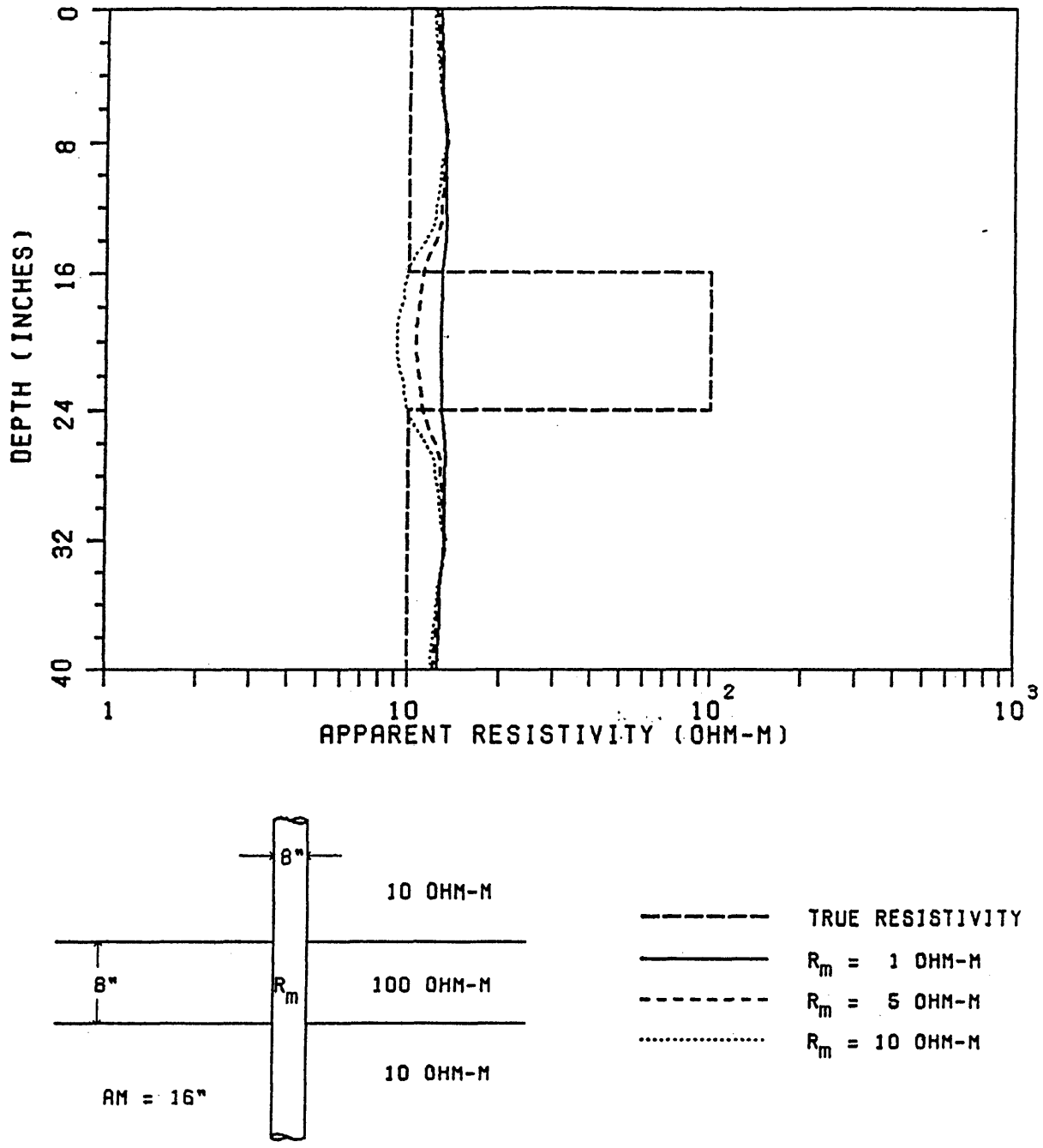

A-2.3 Variations in Rm (Normal-Thin-Resistive)

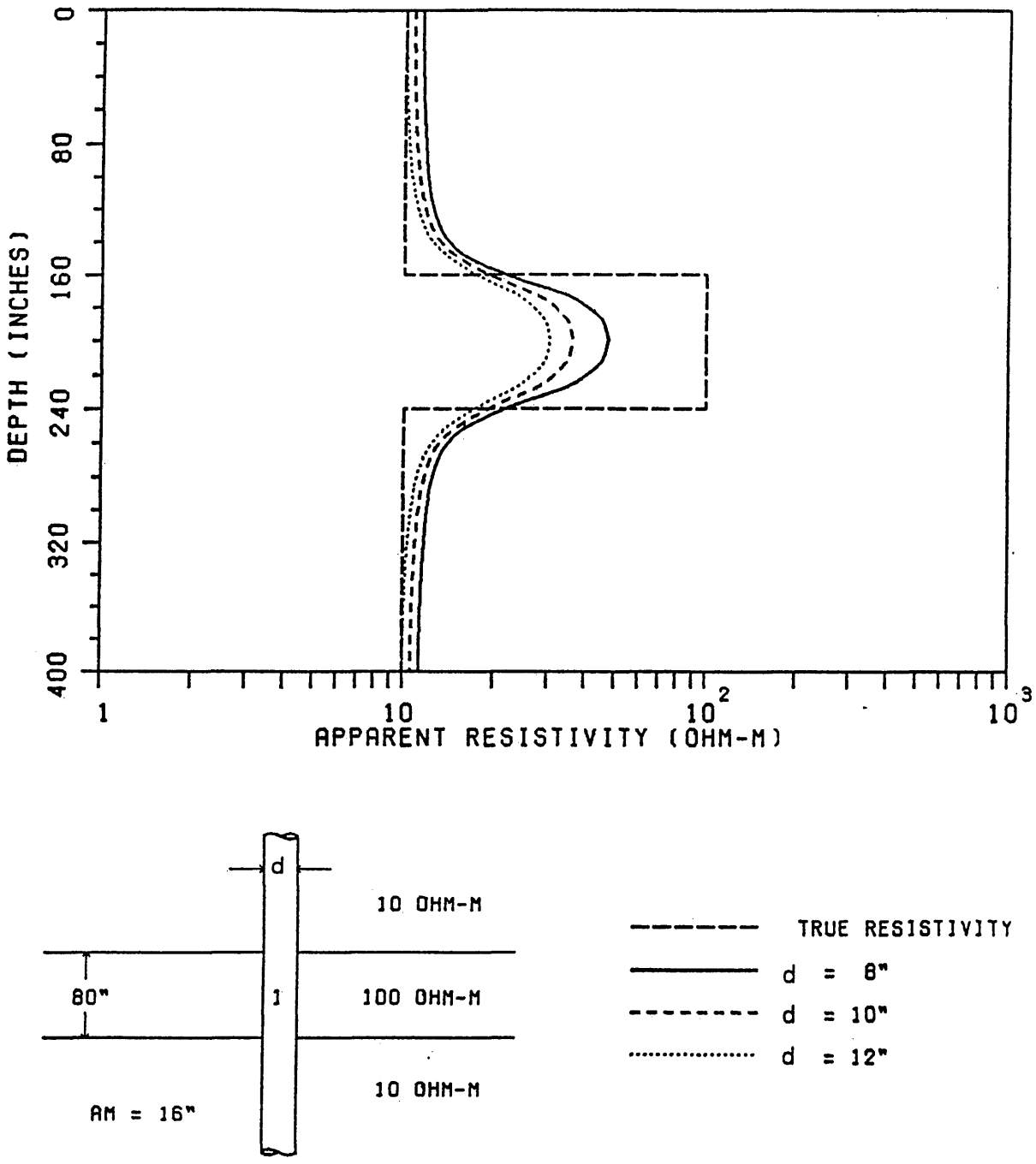

A-2.4 Variations in d (Normal-Thick-Resistive)

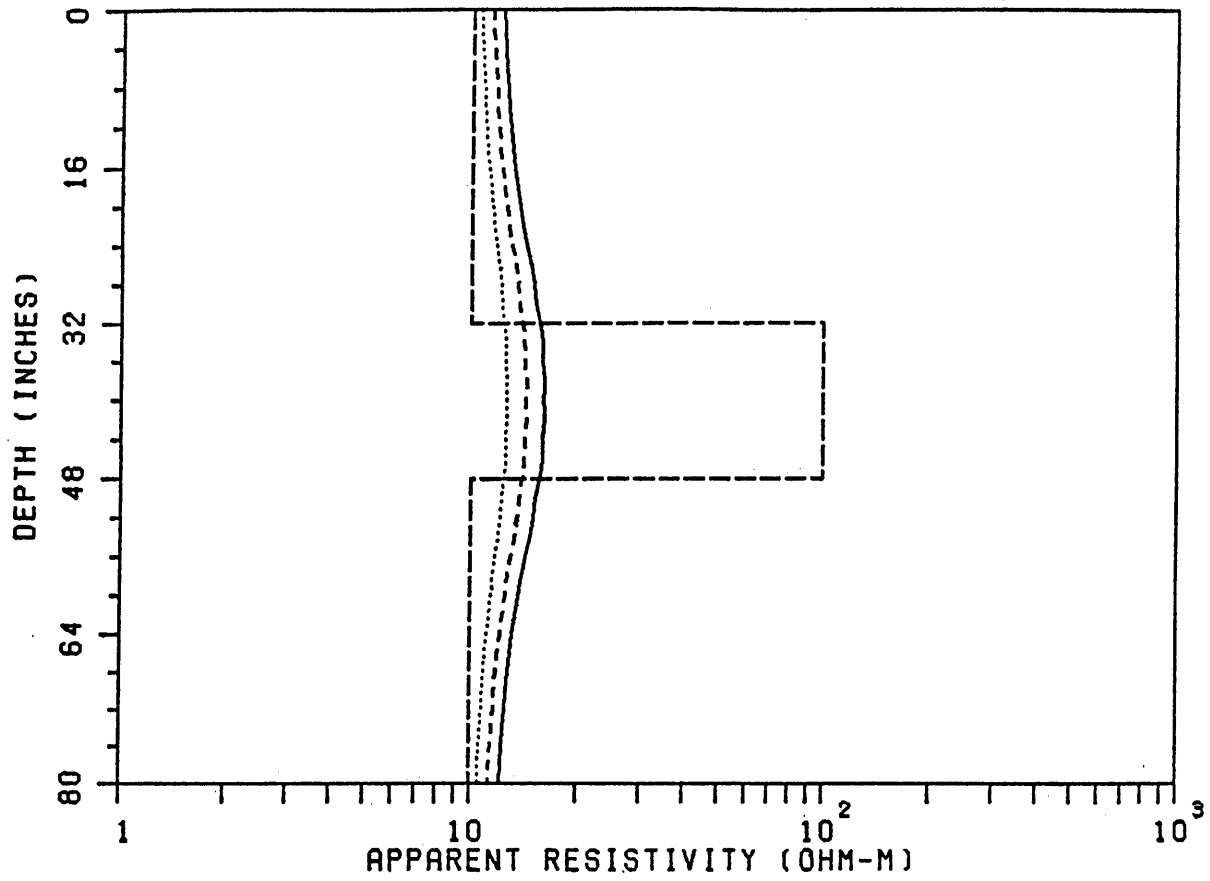

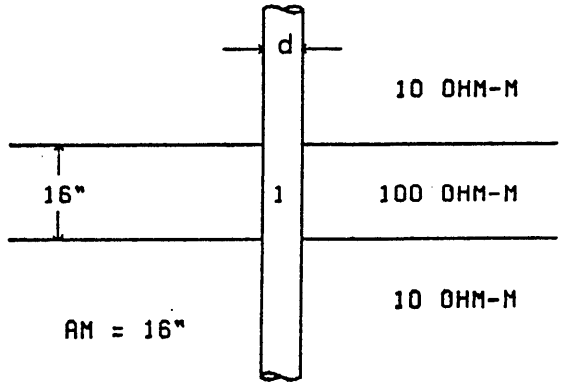

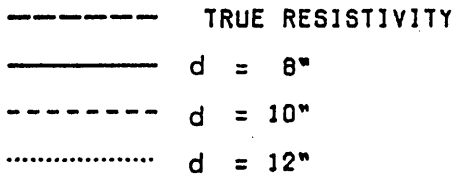

A-2.5 Variations in d (Normal-Critical-Resistive)

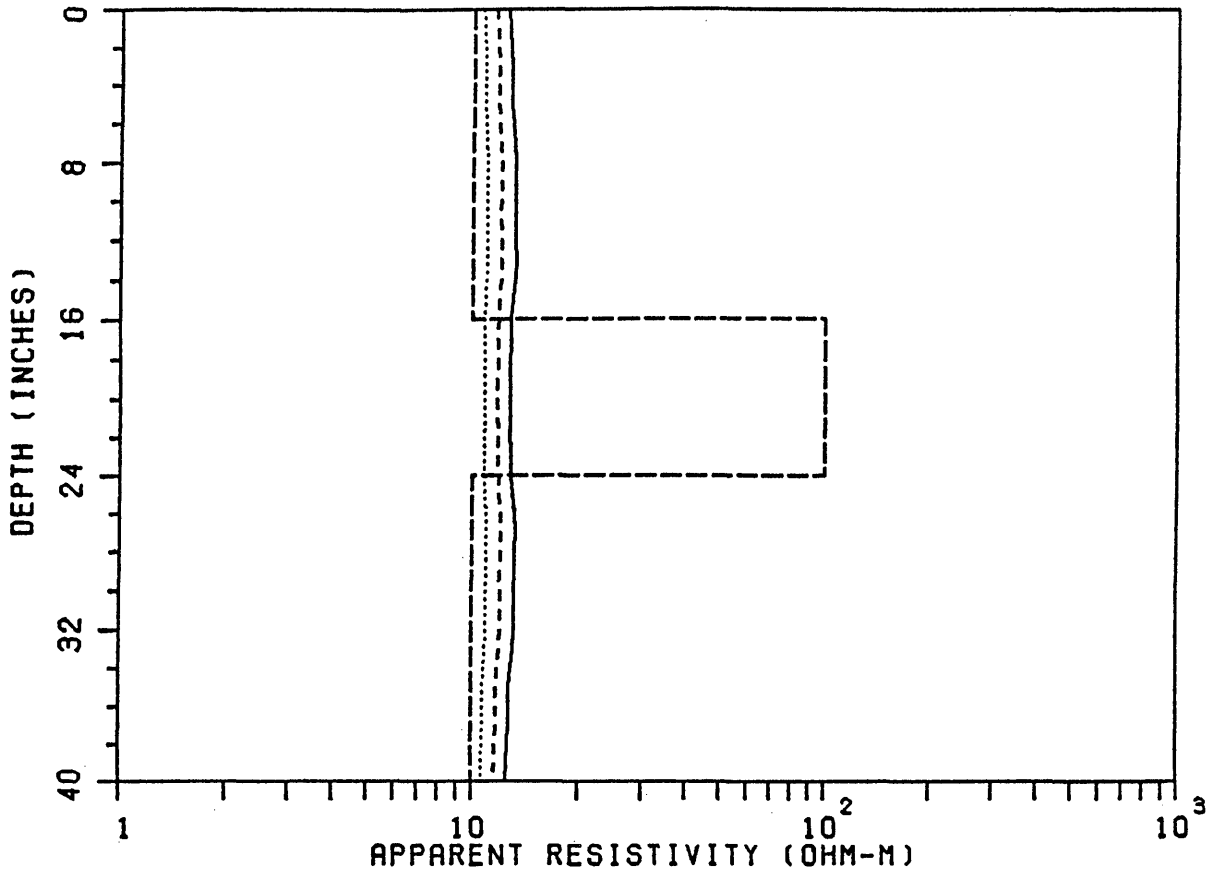

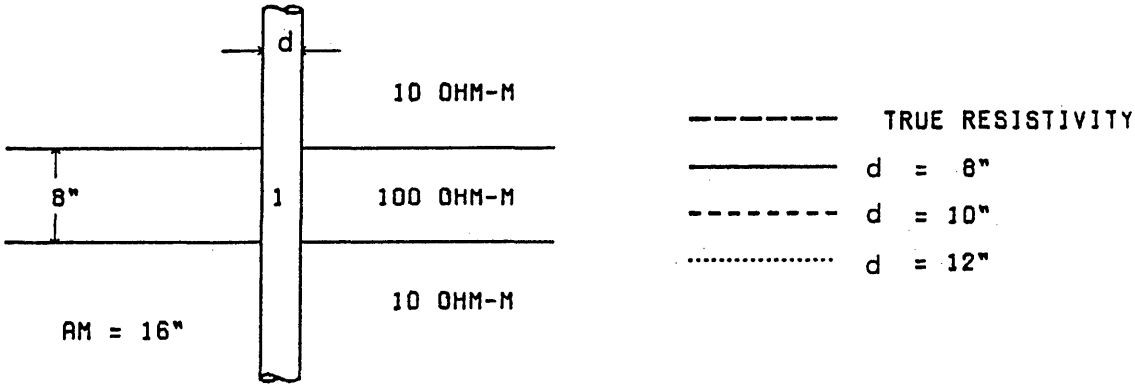

A-2.6 Variations in d (Normal-Thin-Resistive)

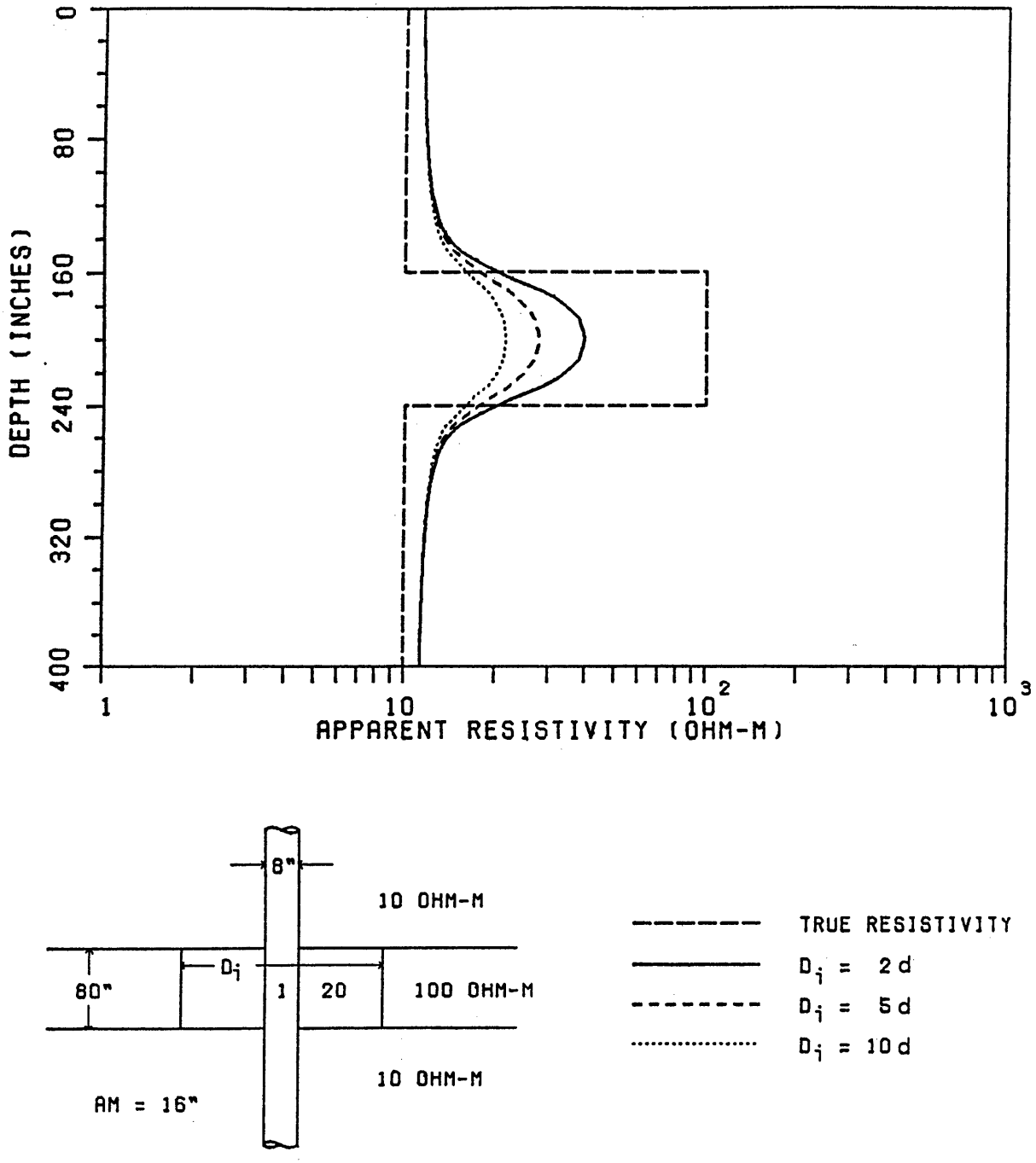

A-2.7 Variations in Di (Normal-Thick-Resistive)

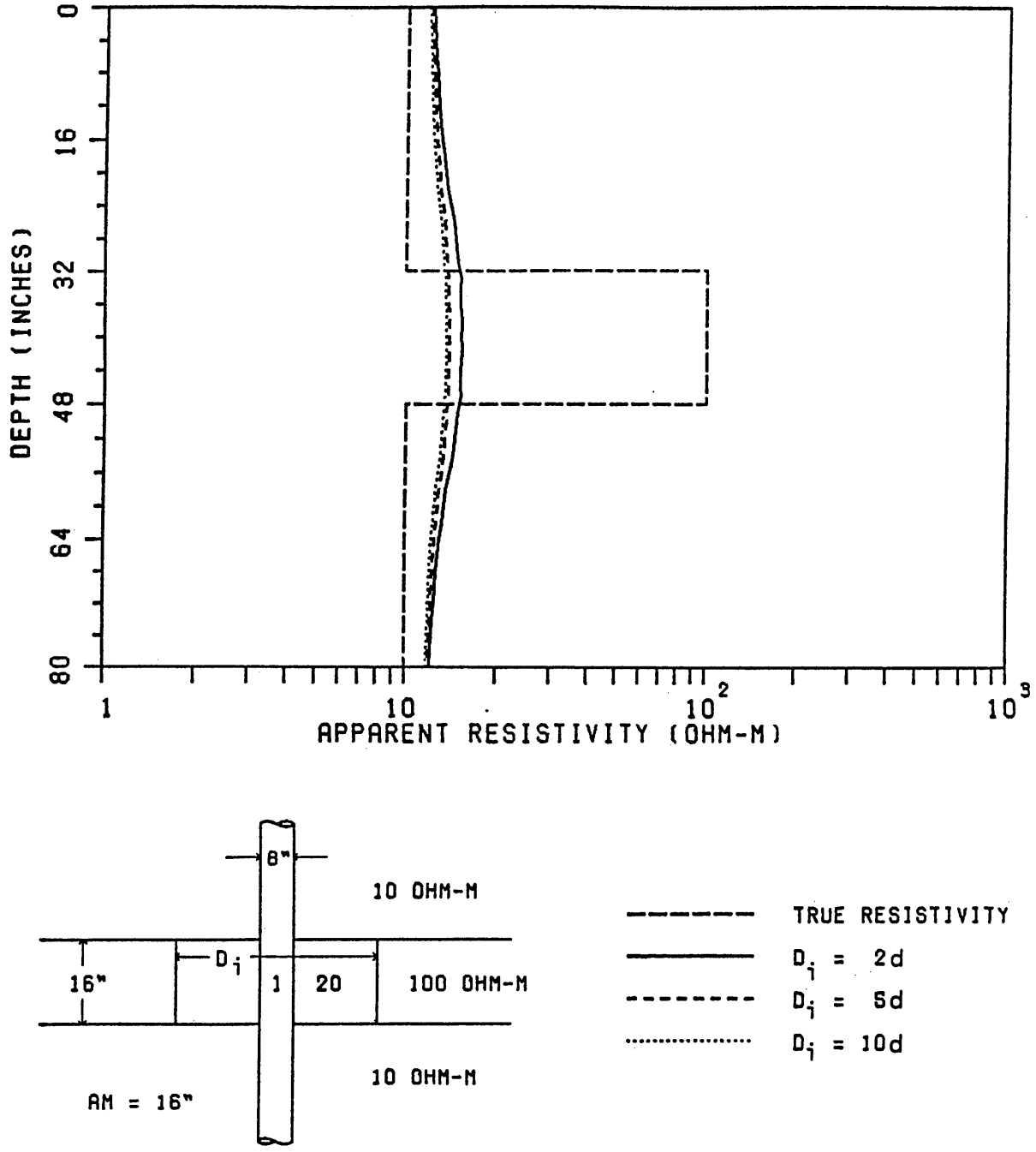

A-2.8 Variations in Di (Normal-Critical-Resistive)

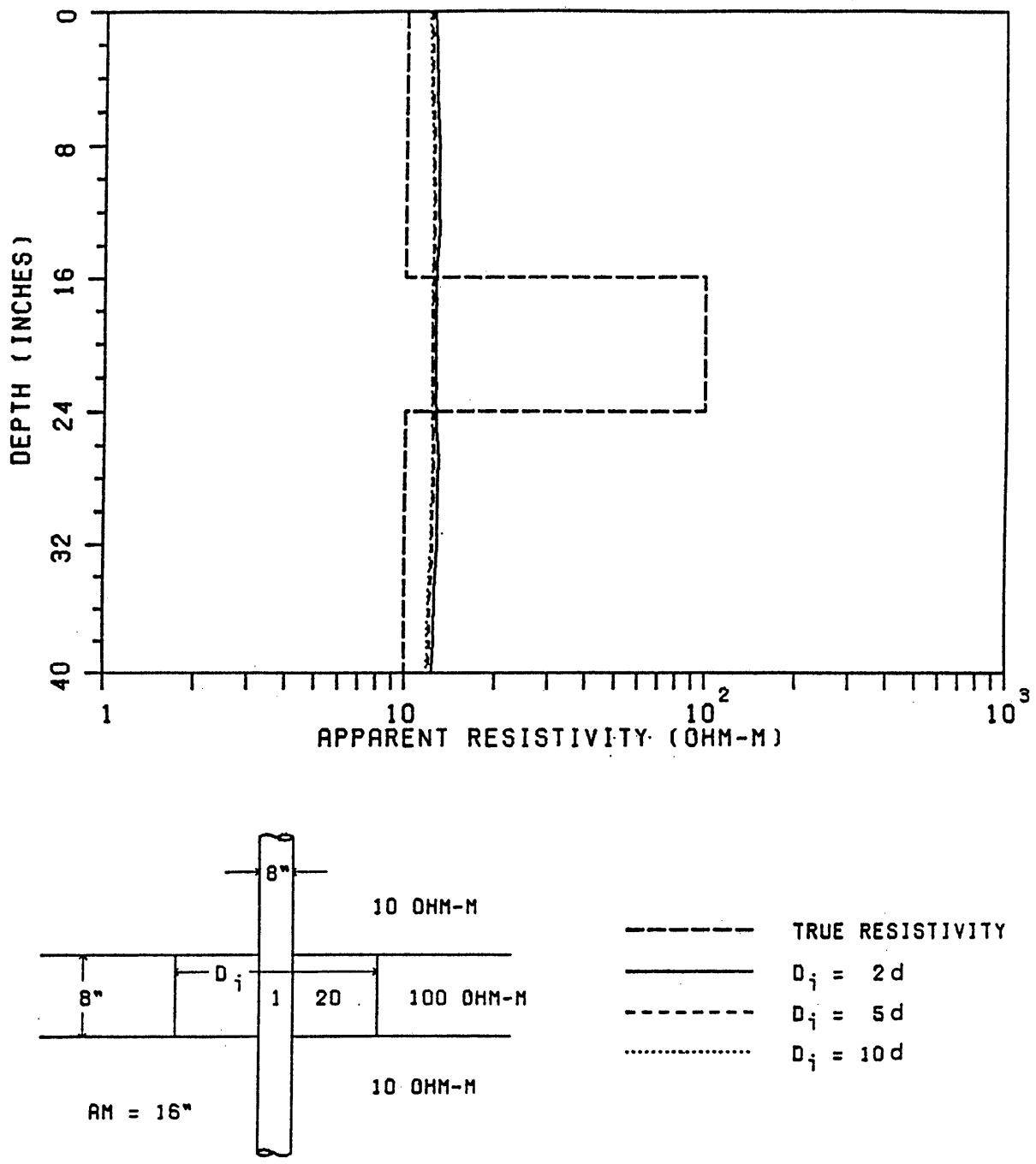

A-2.9 Variations in Di (Normal-Thin-Resistive)

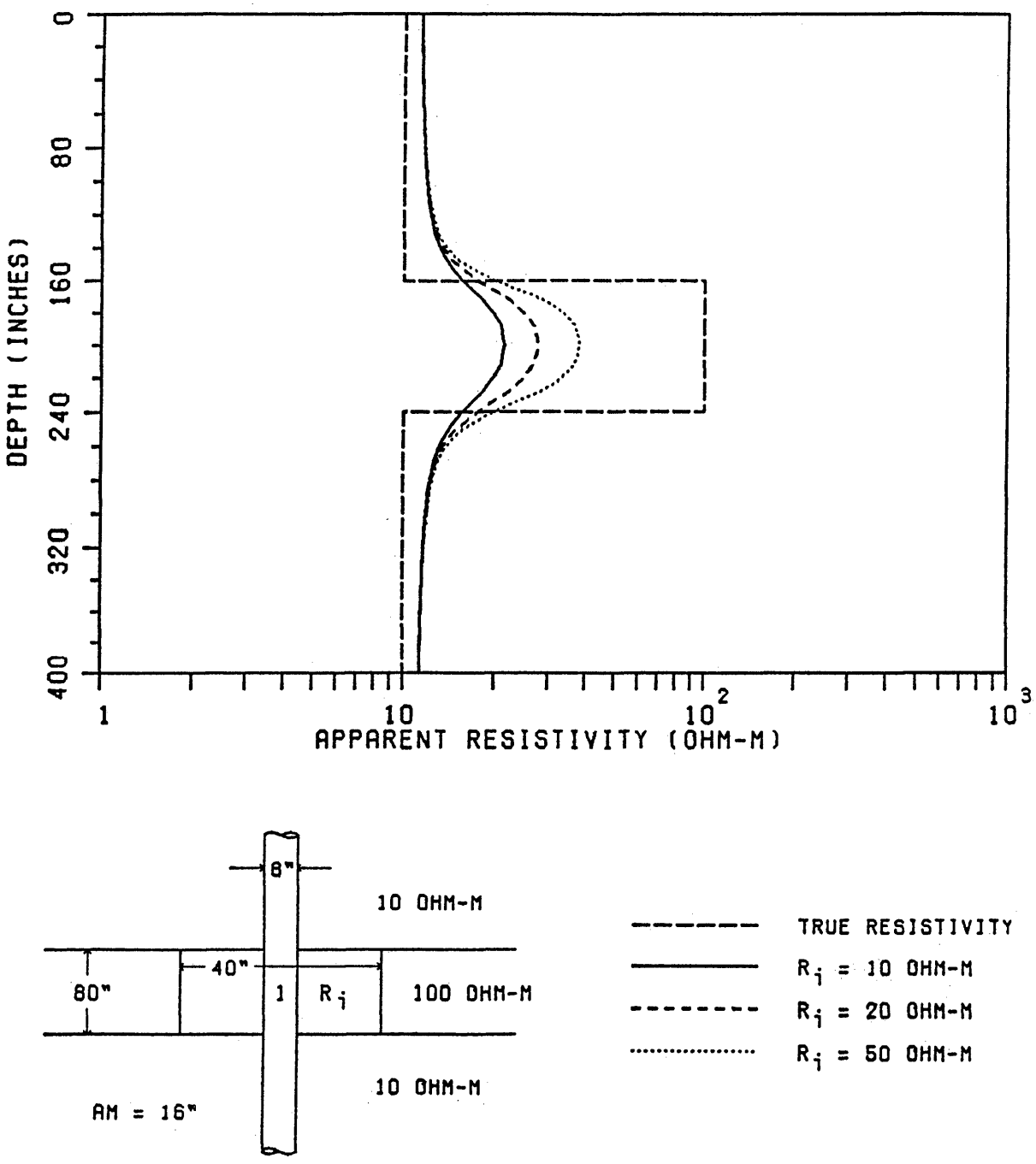

A-2.10 Variations in Ri (Normal-Thick-Resistive)

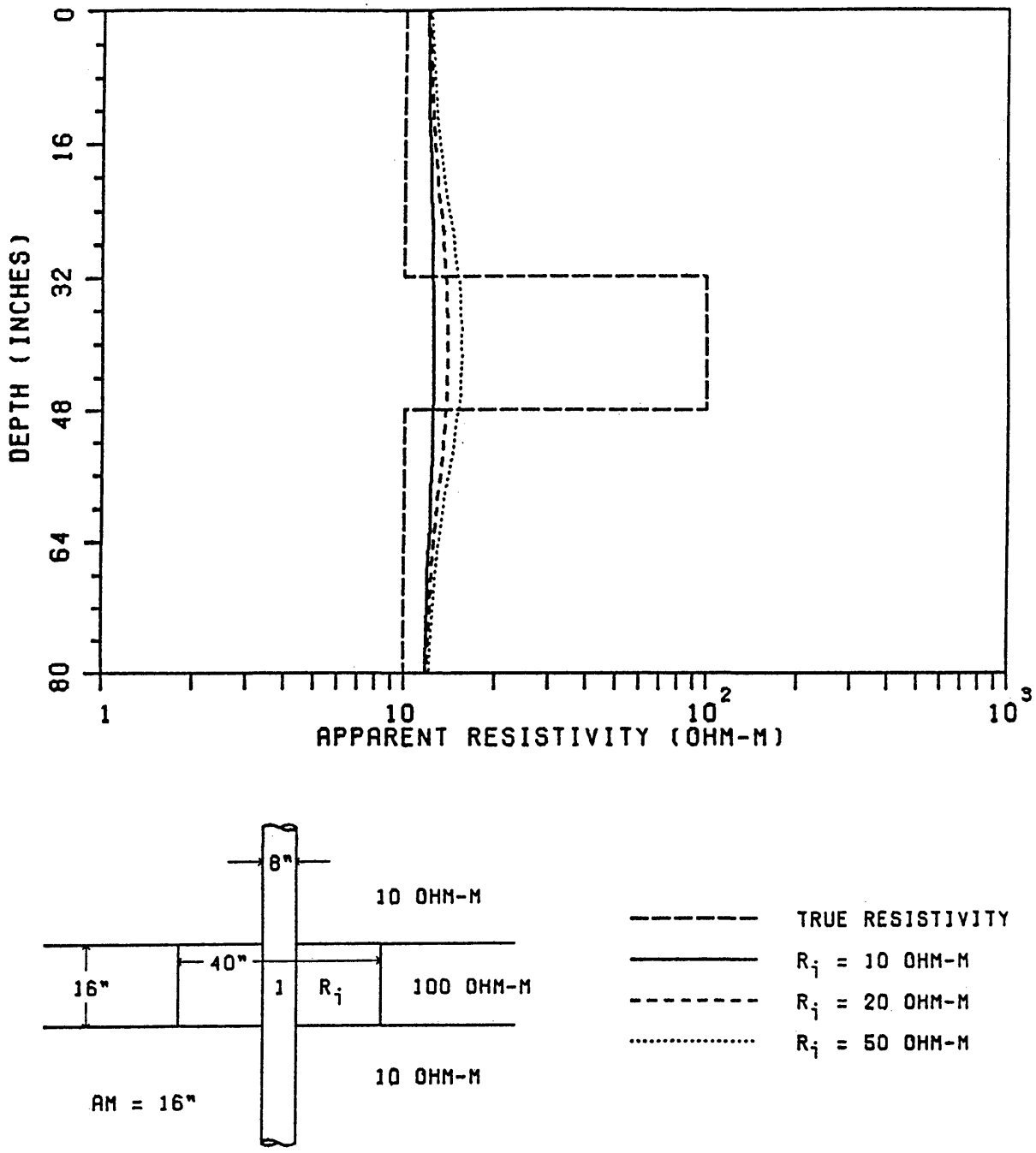

A-2.11 Variations in Ri (Normal-Critical-Resistive)

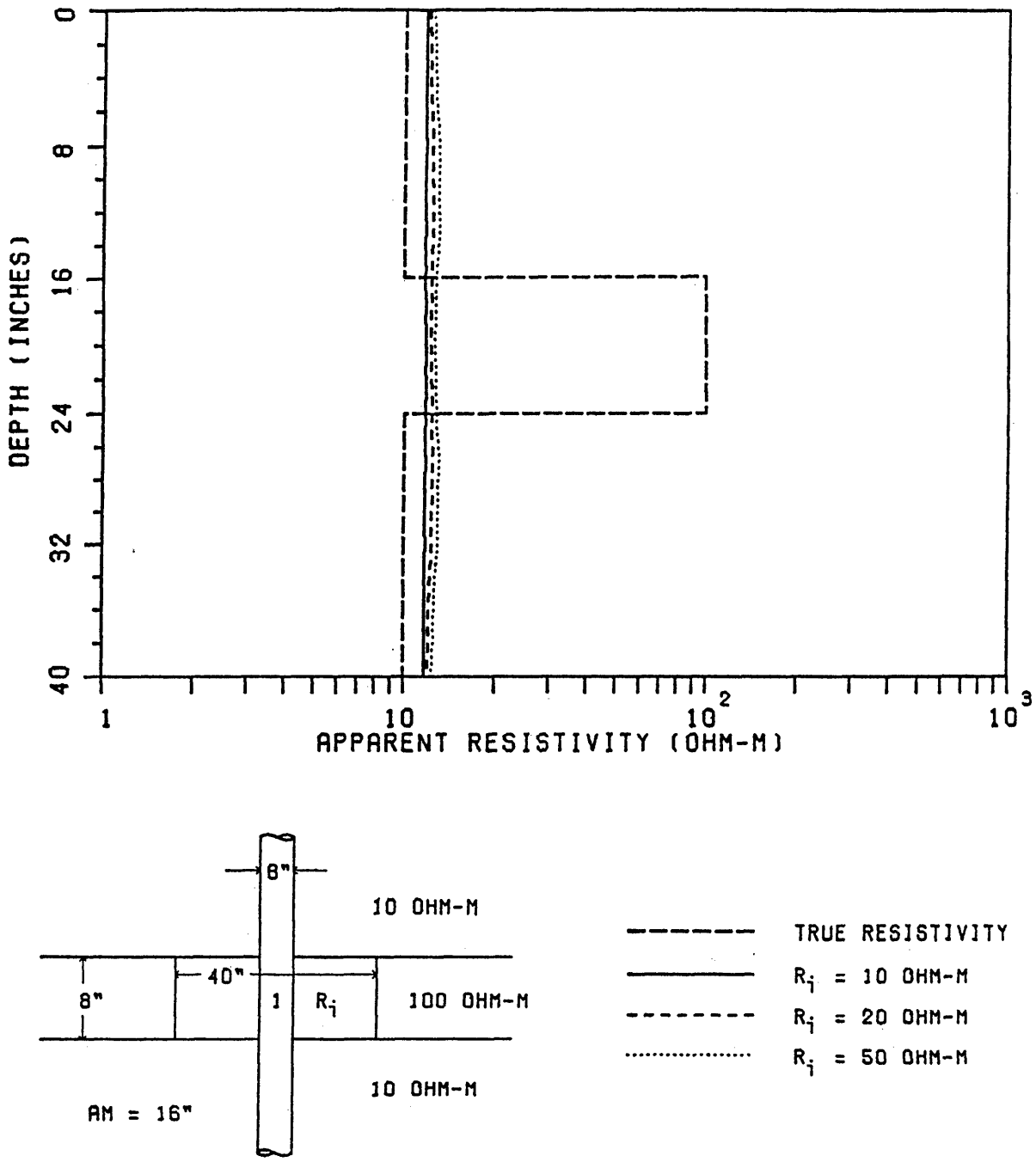

A-2.12 Variations in Ri (Normal-Thin-Resistive)

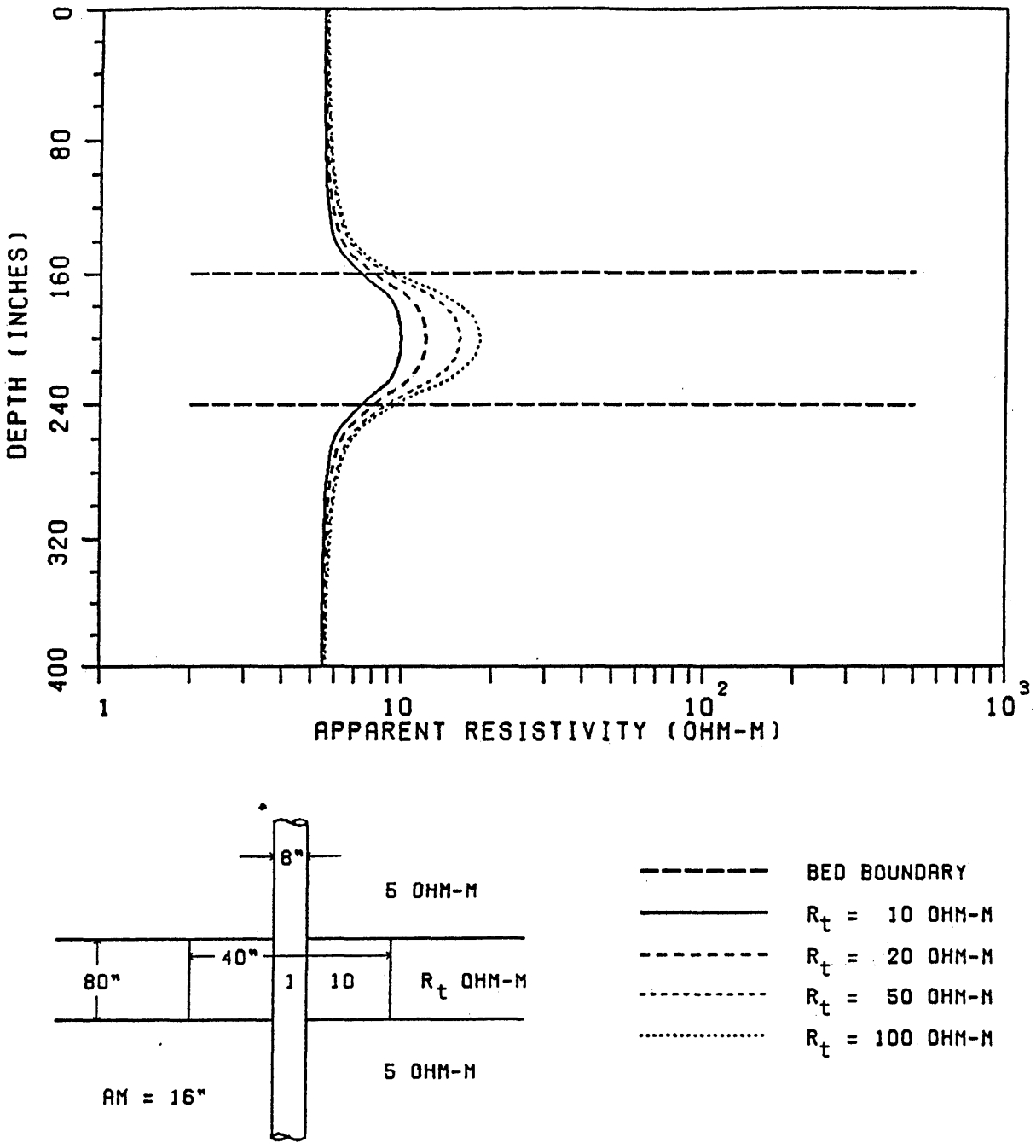

A-2.13 Variations in Rt (Normal-Thick-Resistive)

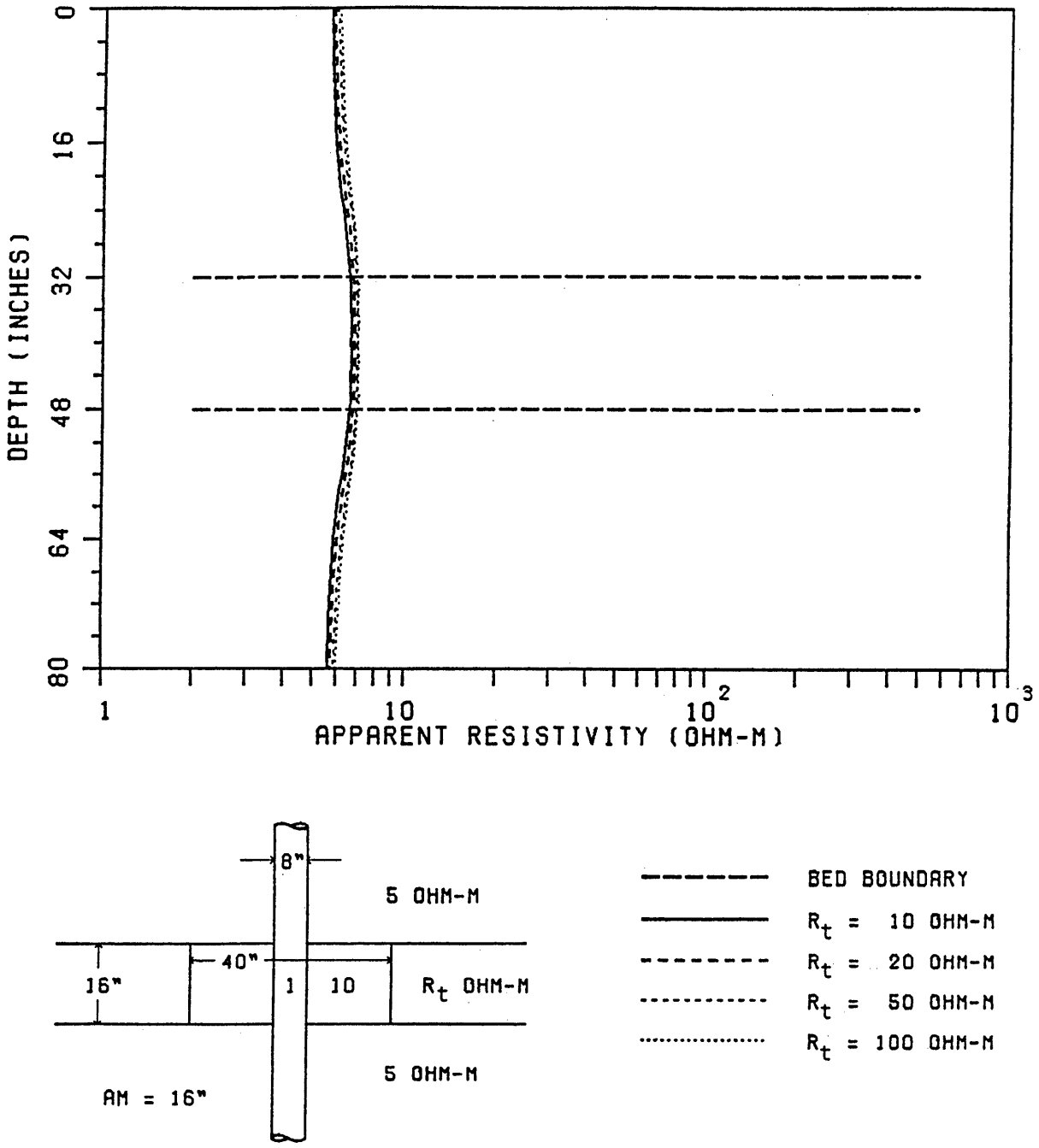

A-2.14 Variations in Rt (Normal-Critical-Resistive)

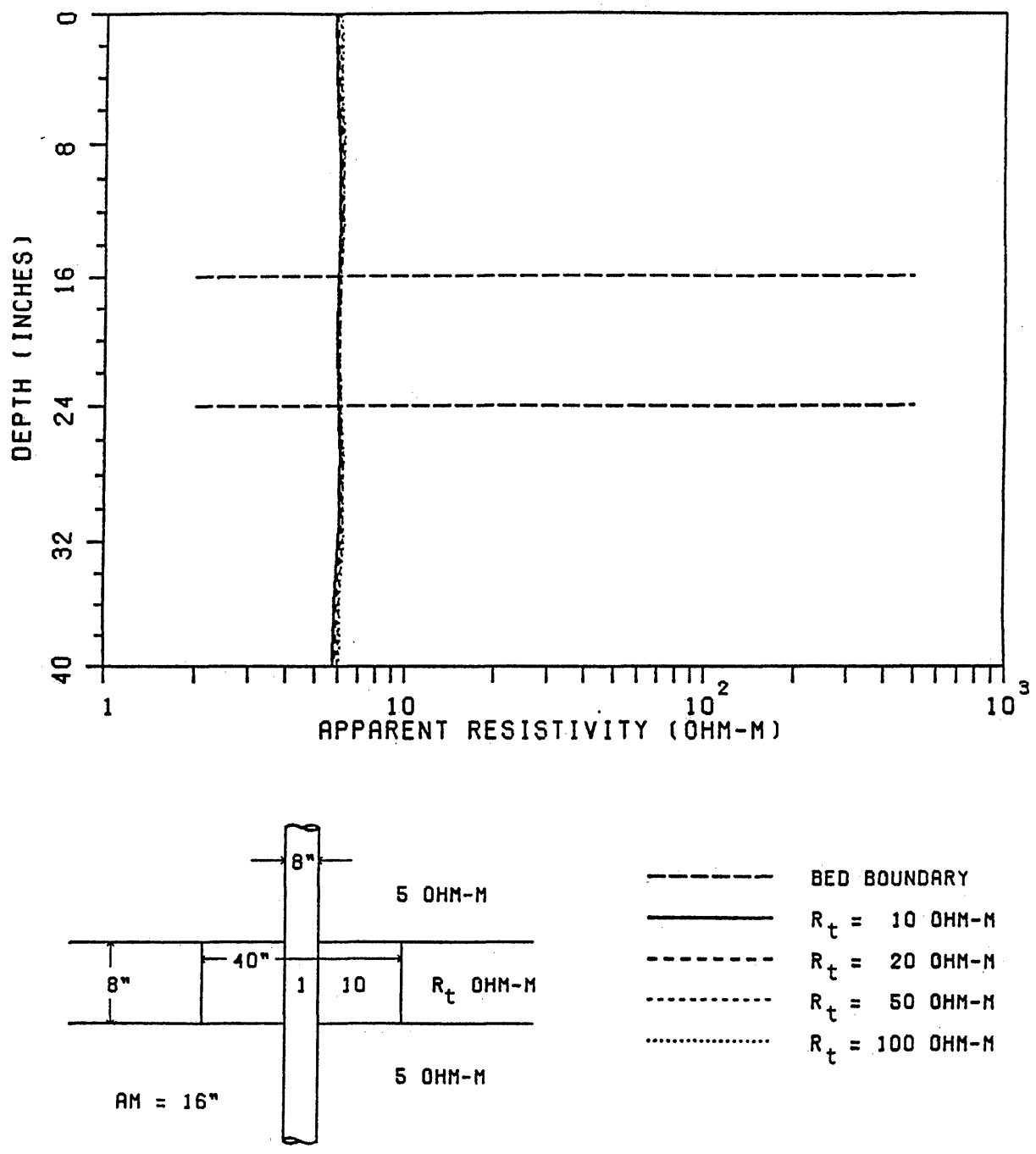

A-2.15 Variations in Rt (Normal-Thin-Resistive)

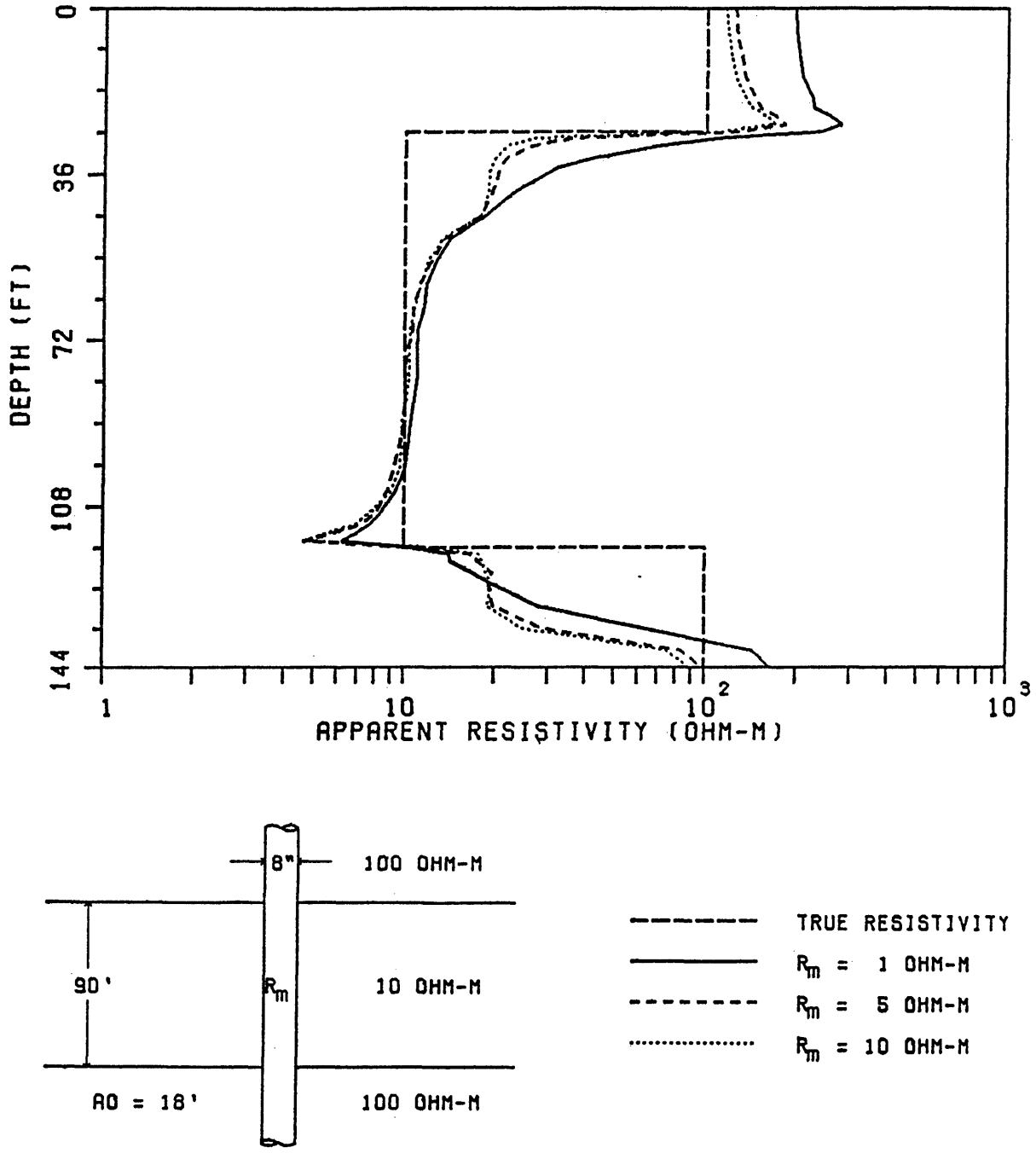

A-3.1 Variations in Rm (Lateral-Thick-Conductive)

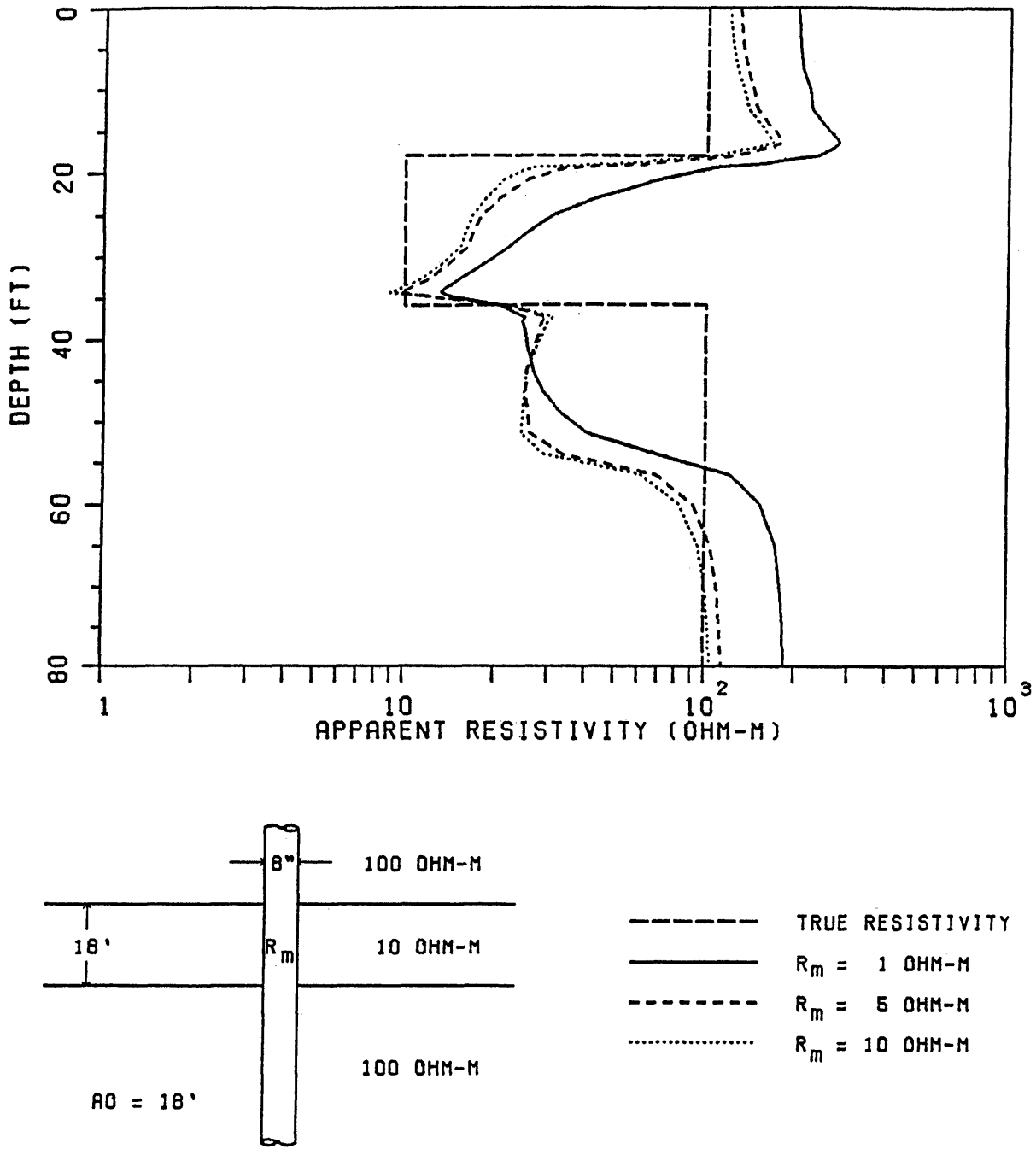

A-3.2 Variations in Rm (Lateral-Critical-Conductive)

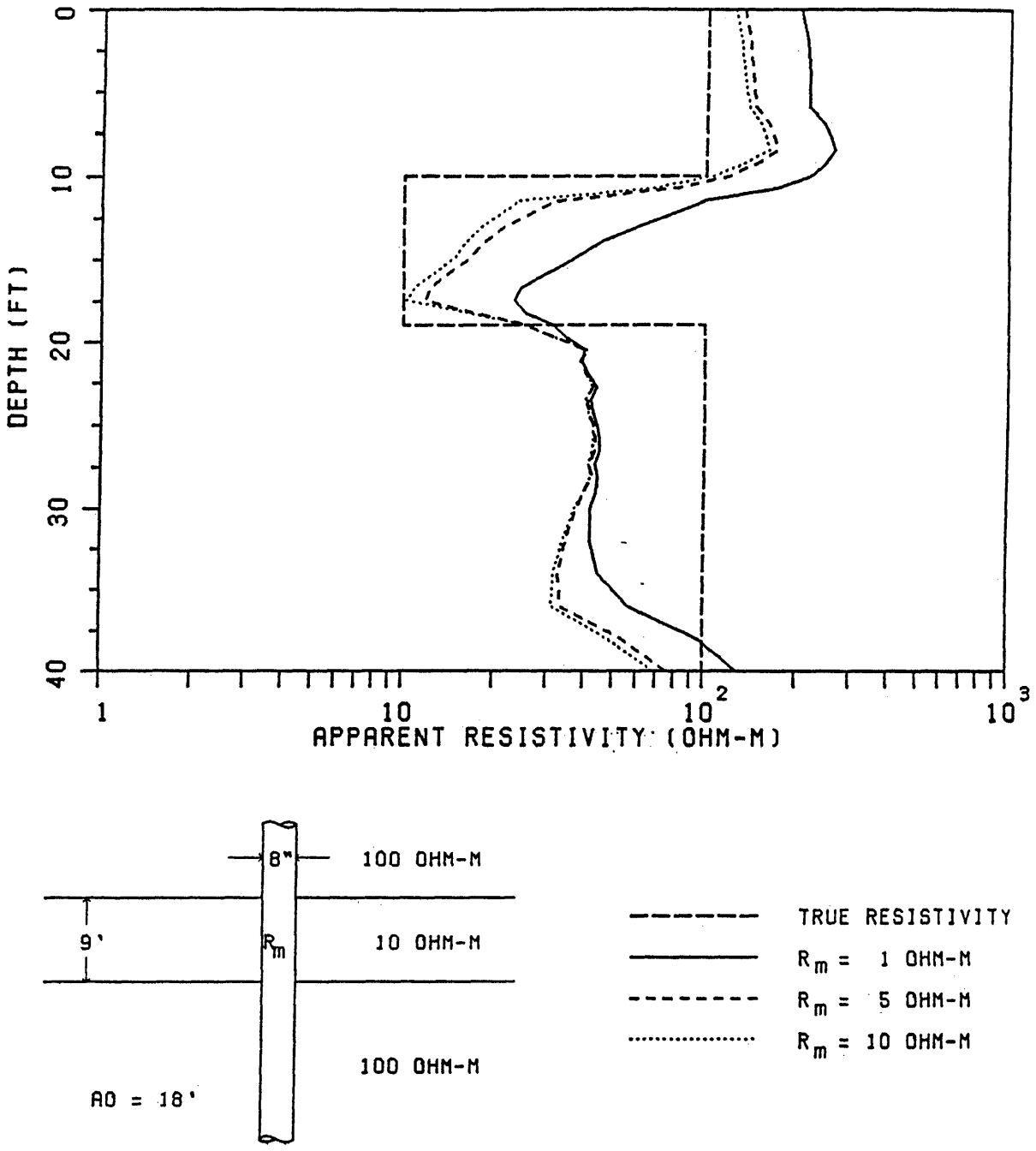

A-3.3 Variations in Rm (Lateral-Thin-Conductive)

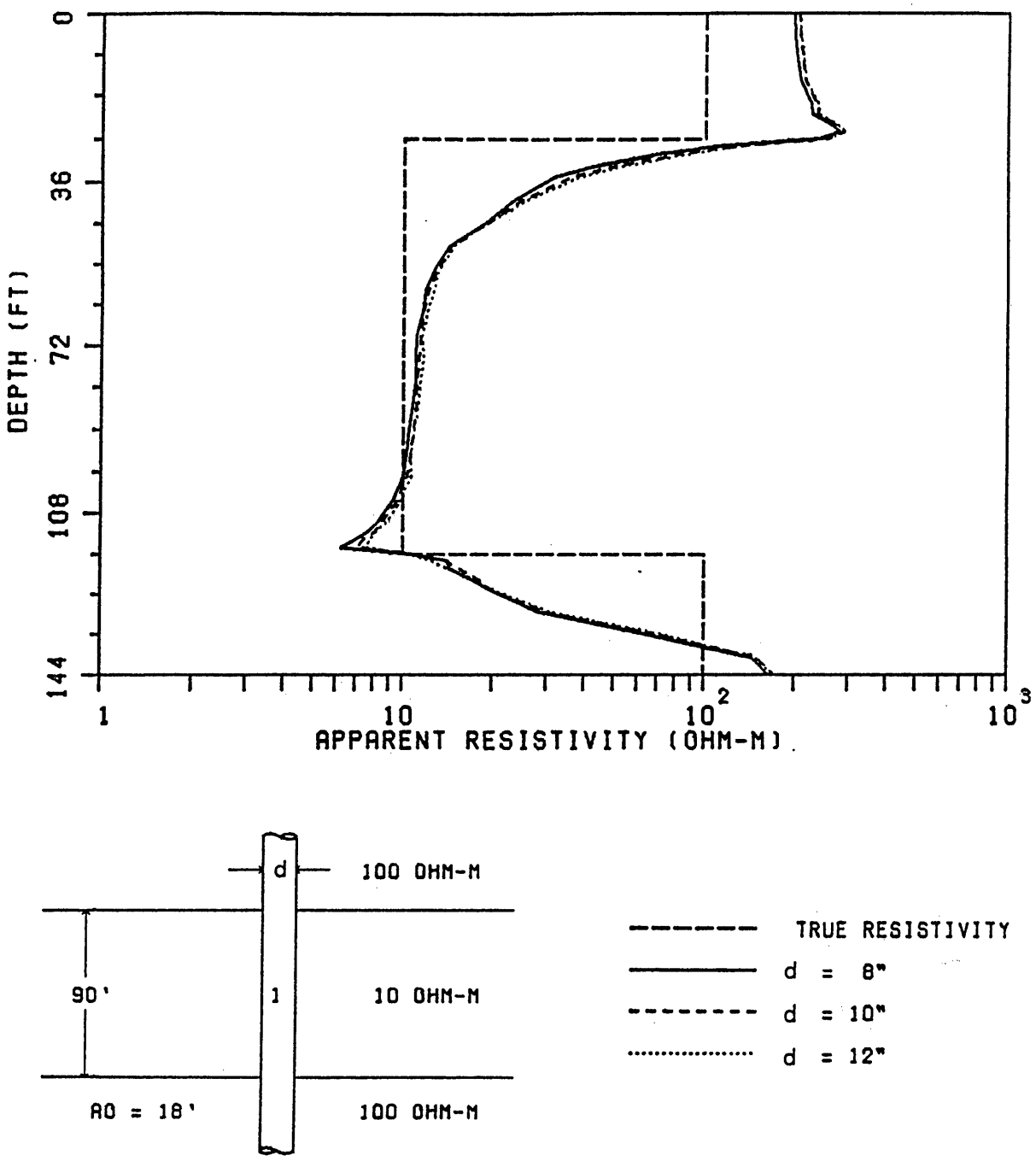

A-3.4 Variations in d (Lateral-Thick-Conductive)

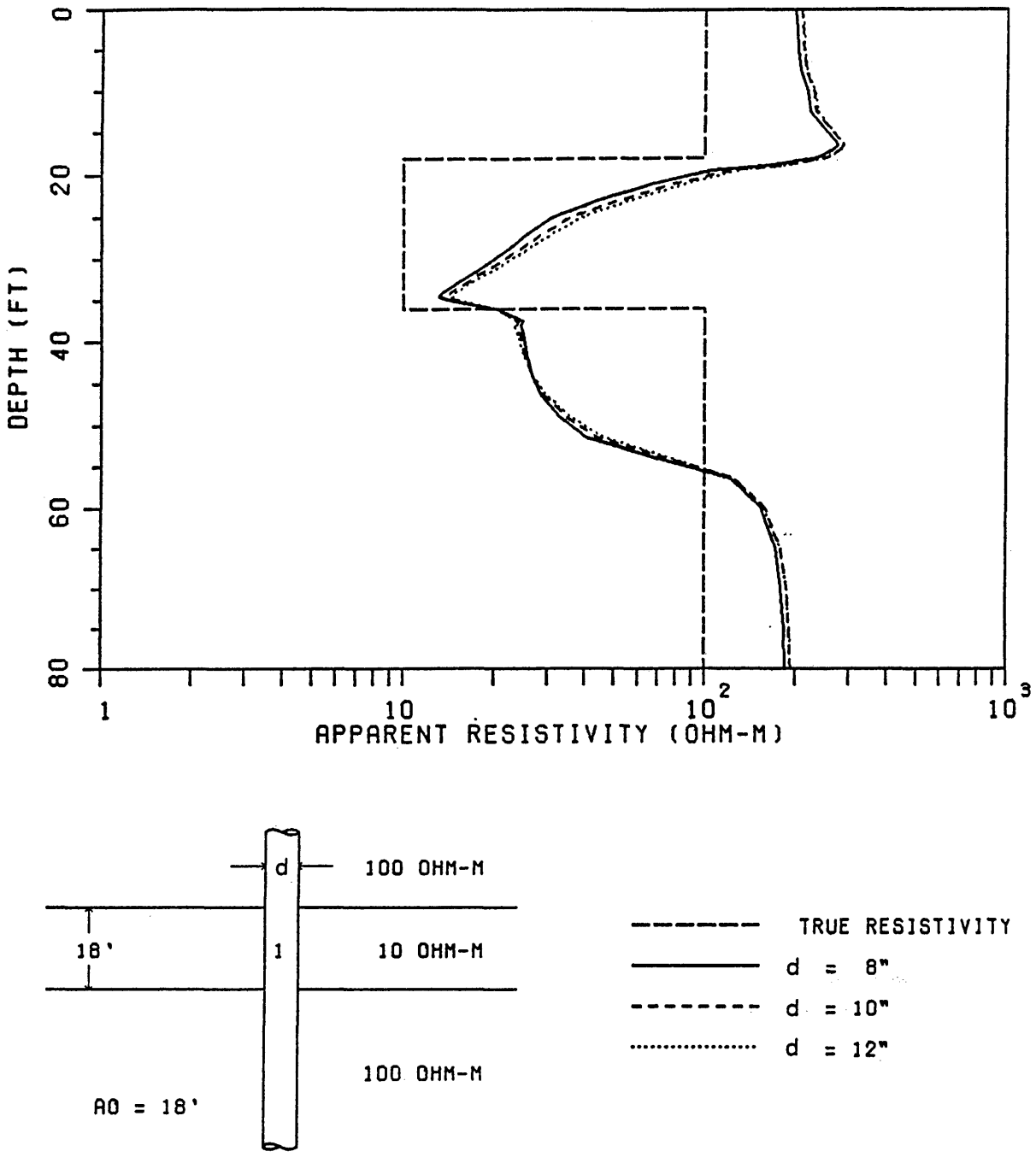

A-3.5 Variations in d (Lateral-Critical-Conductive)

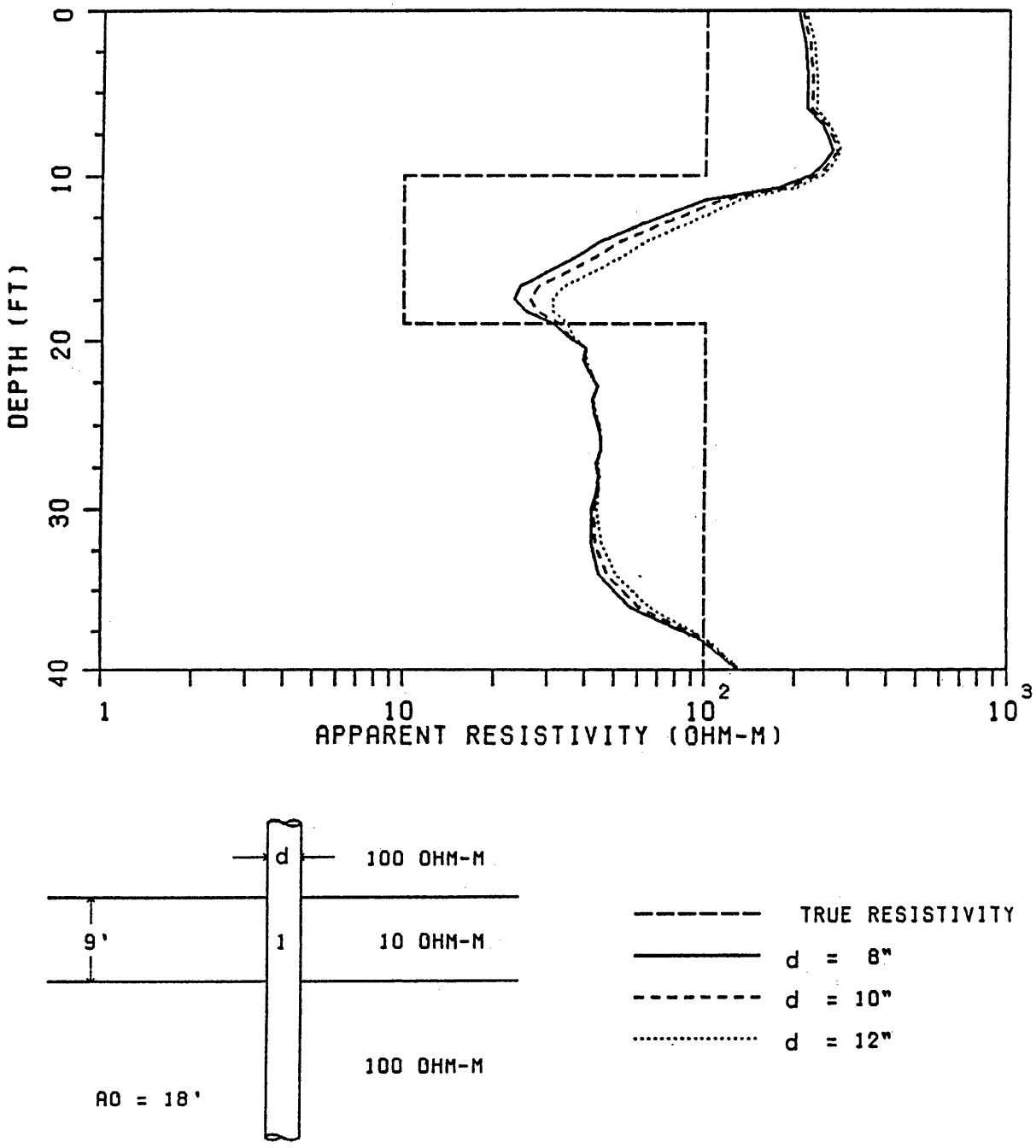

A-3.6 Variations in d (Lateral-Thin-Conductive)

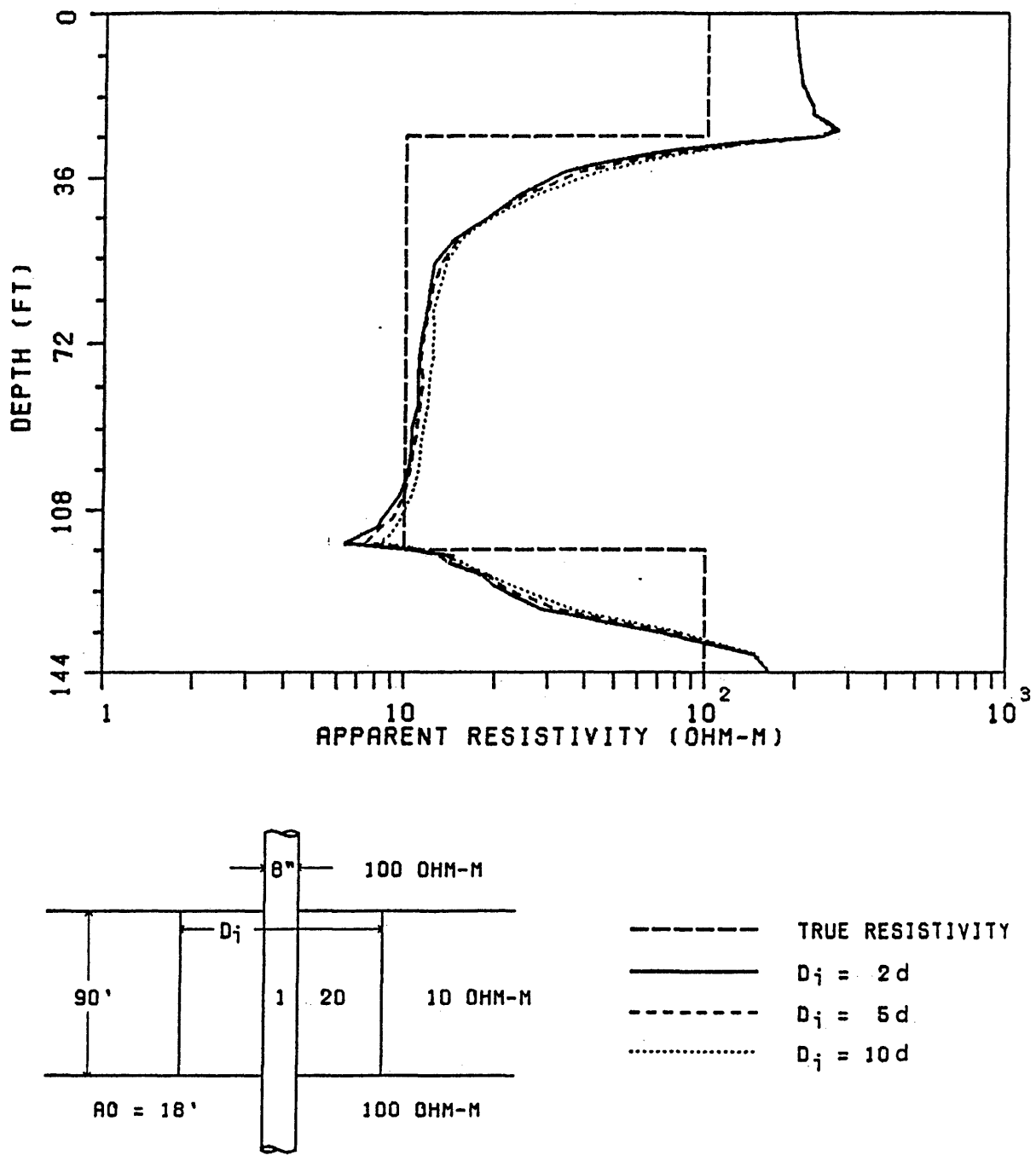

A-3.7 Variations in Di (Lateral-Thick-Conductive)

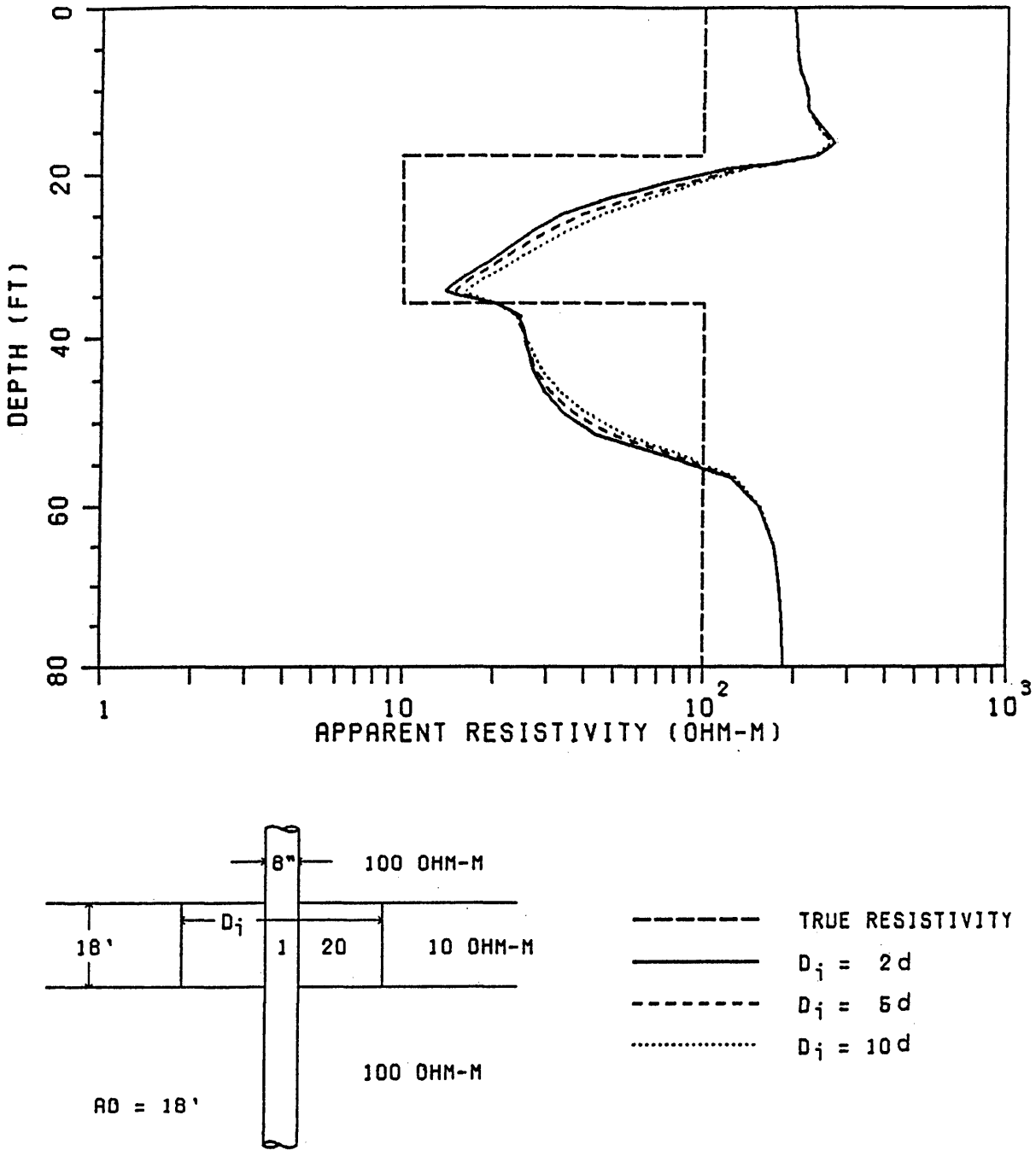

A-3.8 Variations in Di (Lateral-Critical-Conductive)

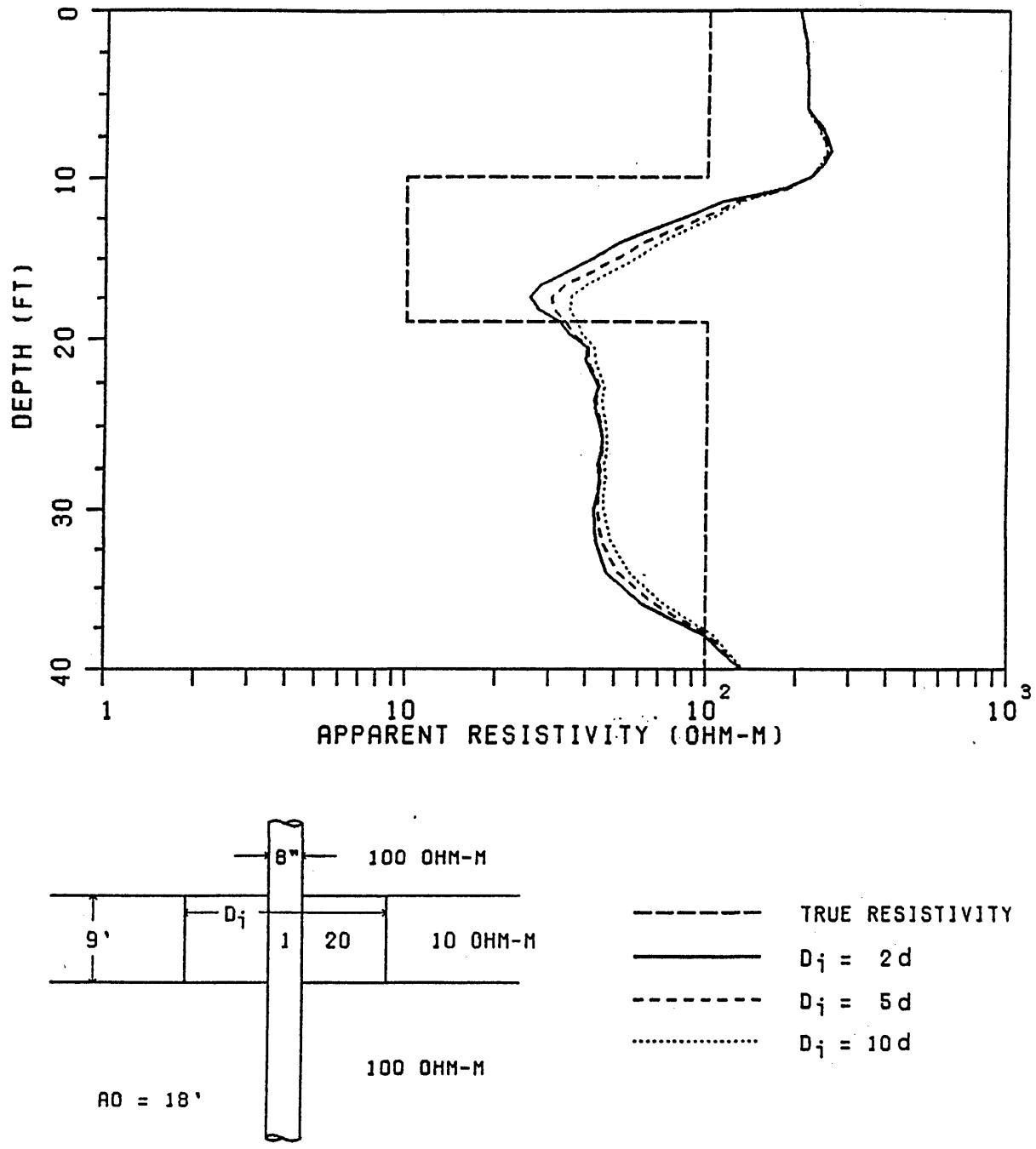

A-3.9 Variations in Di (Lateral-Thin-Conductive)

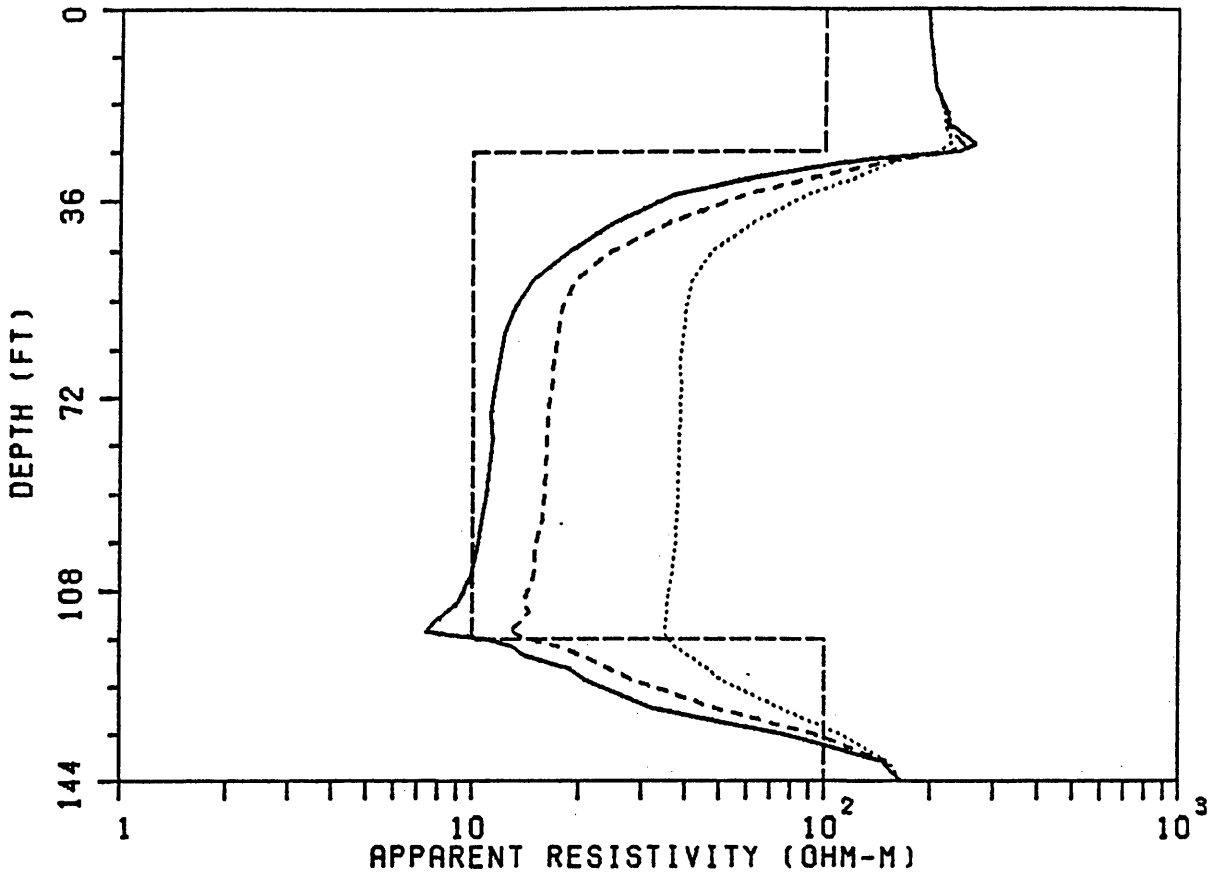

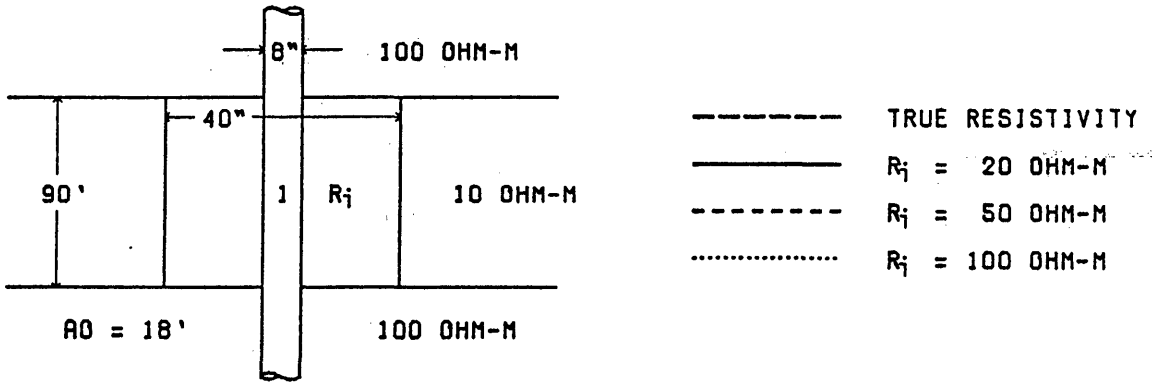

A-3.10 Variations in Ri (Lateral-Thick-Conductive)

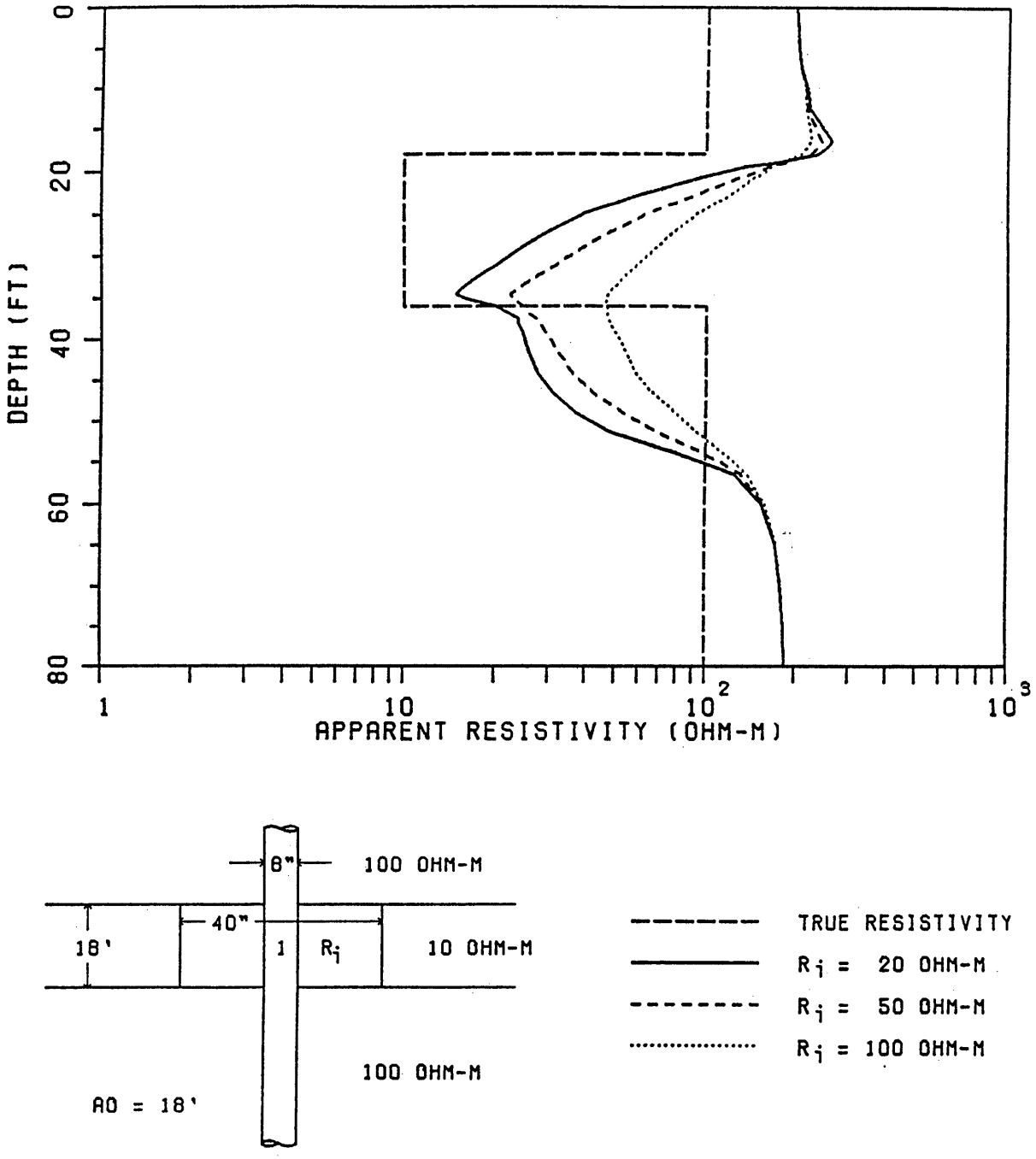

A-3.11 Variations in Ri (Lateral-Critical-Conductive)

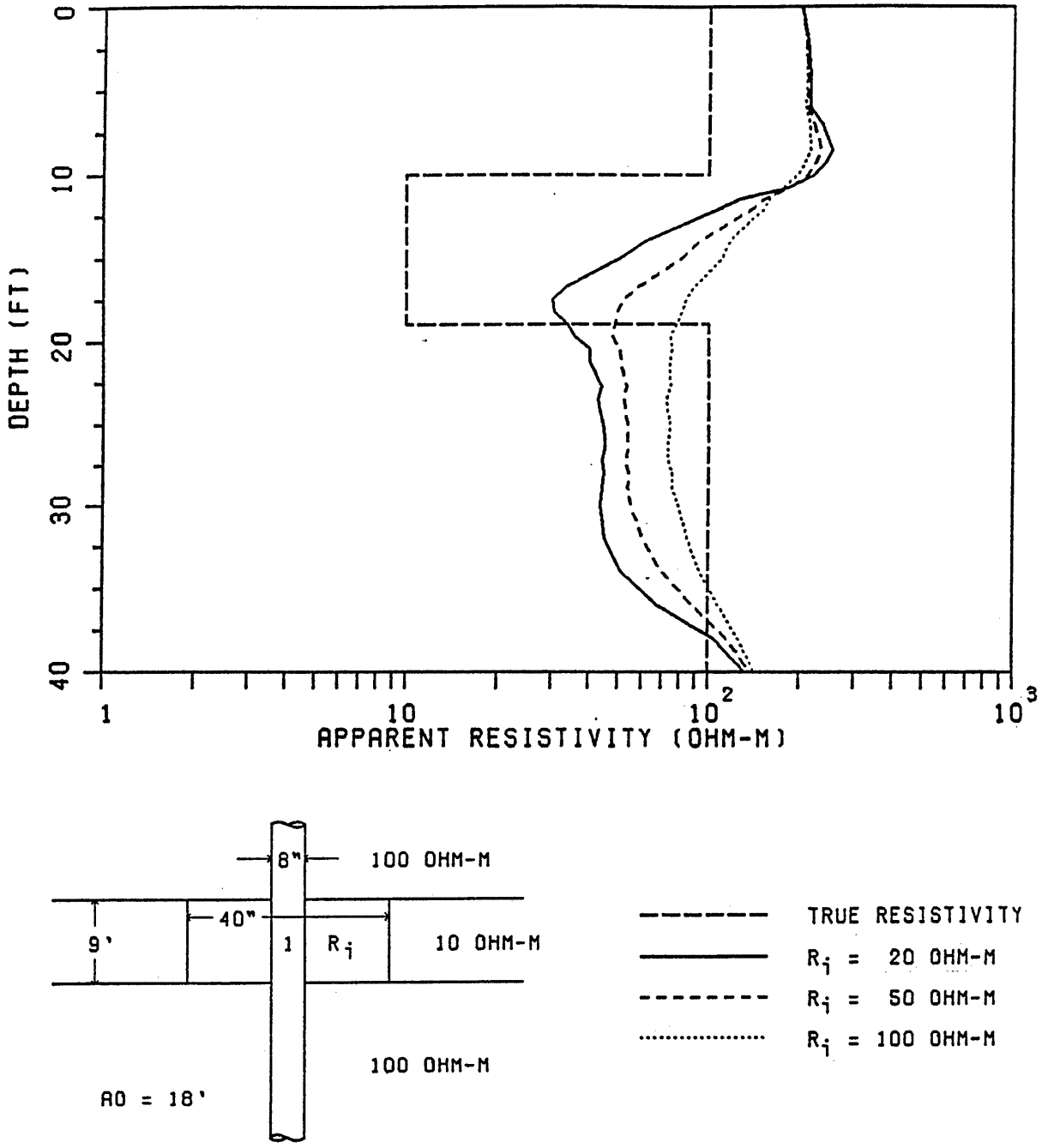

A-3.12 Variations in Ri (Lateral-Thin-Conductive)

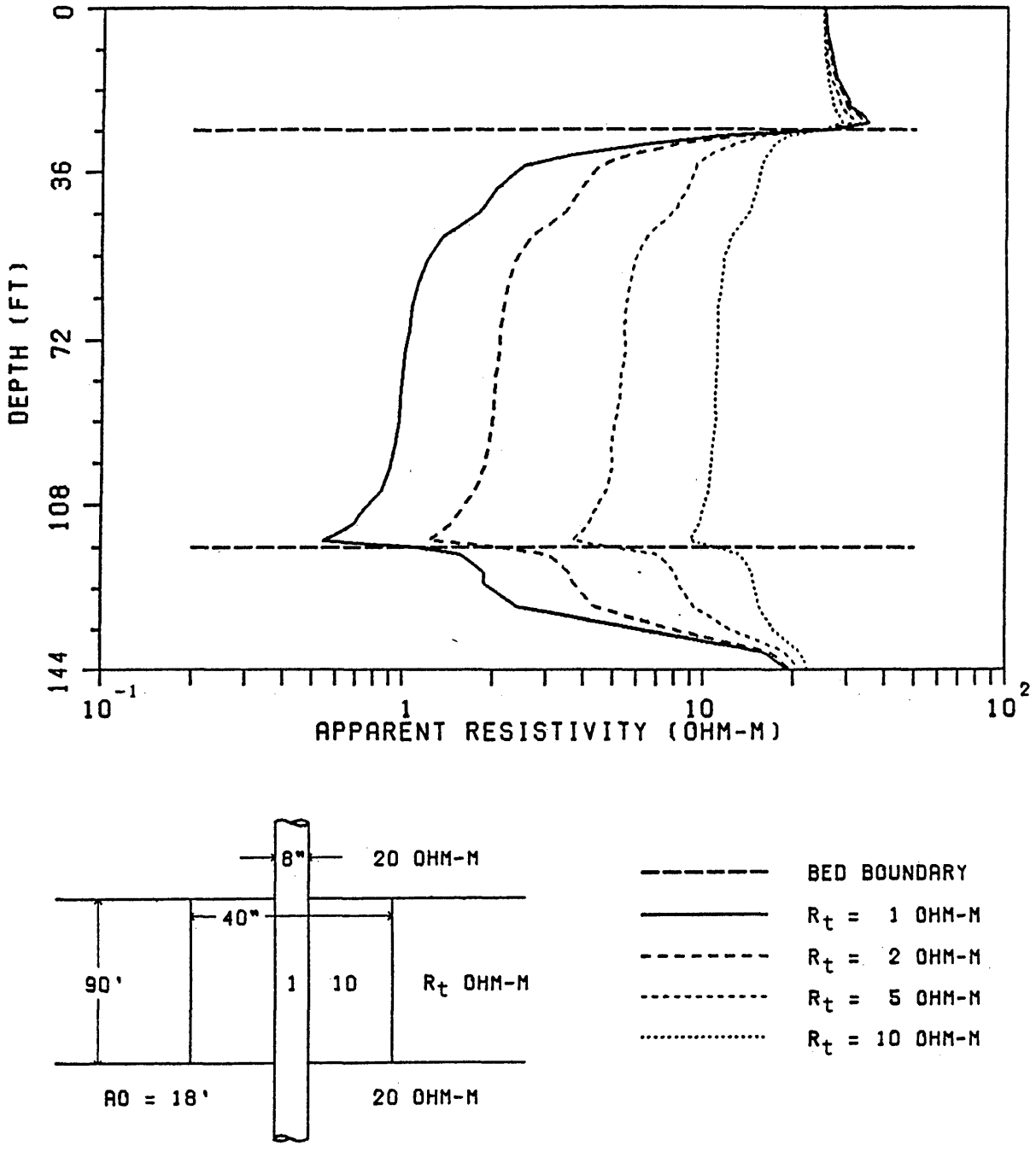

A-3.13 Variations in Rt (Lateral-Thick-Conductive)

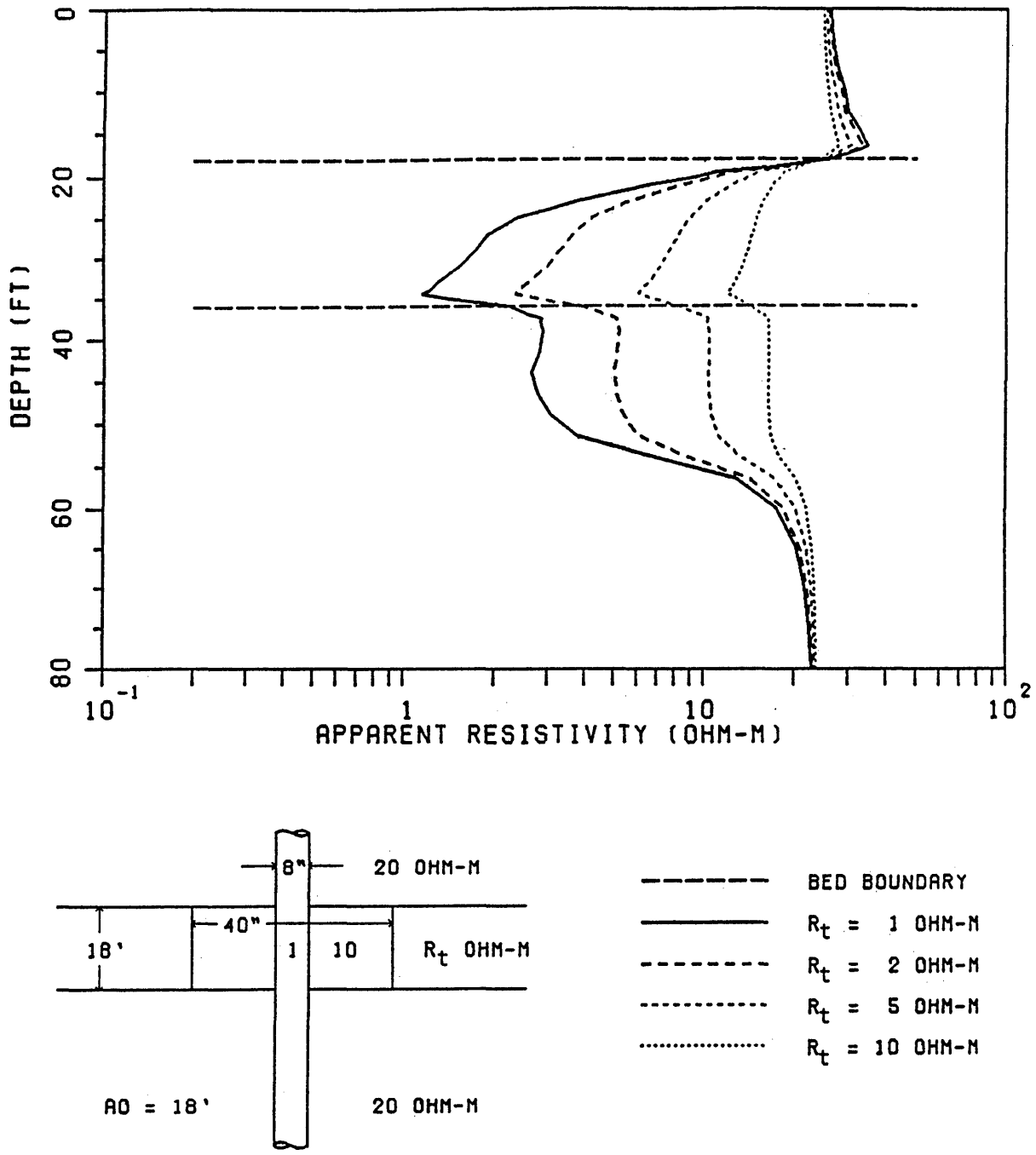

A-3.14 Variations in Rt (Lateral-Critical-Conductive)

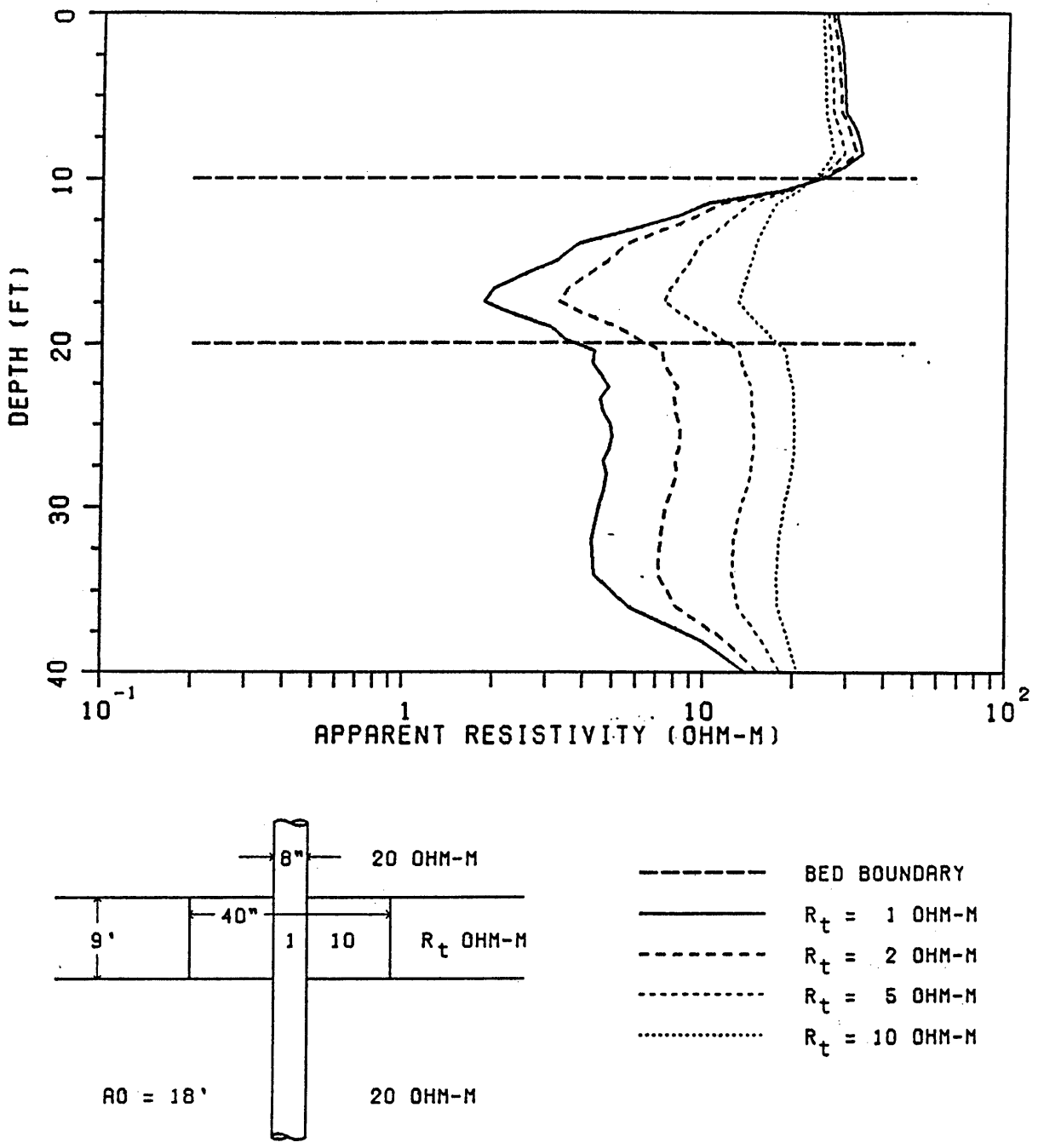

A-3.15 Variations in Rt (Lateral-Thin-Conductive)

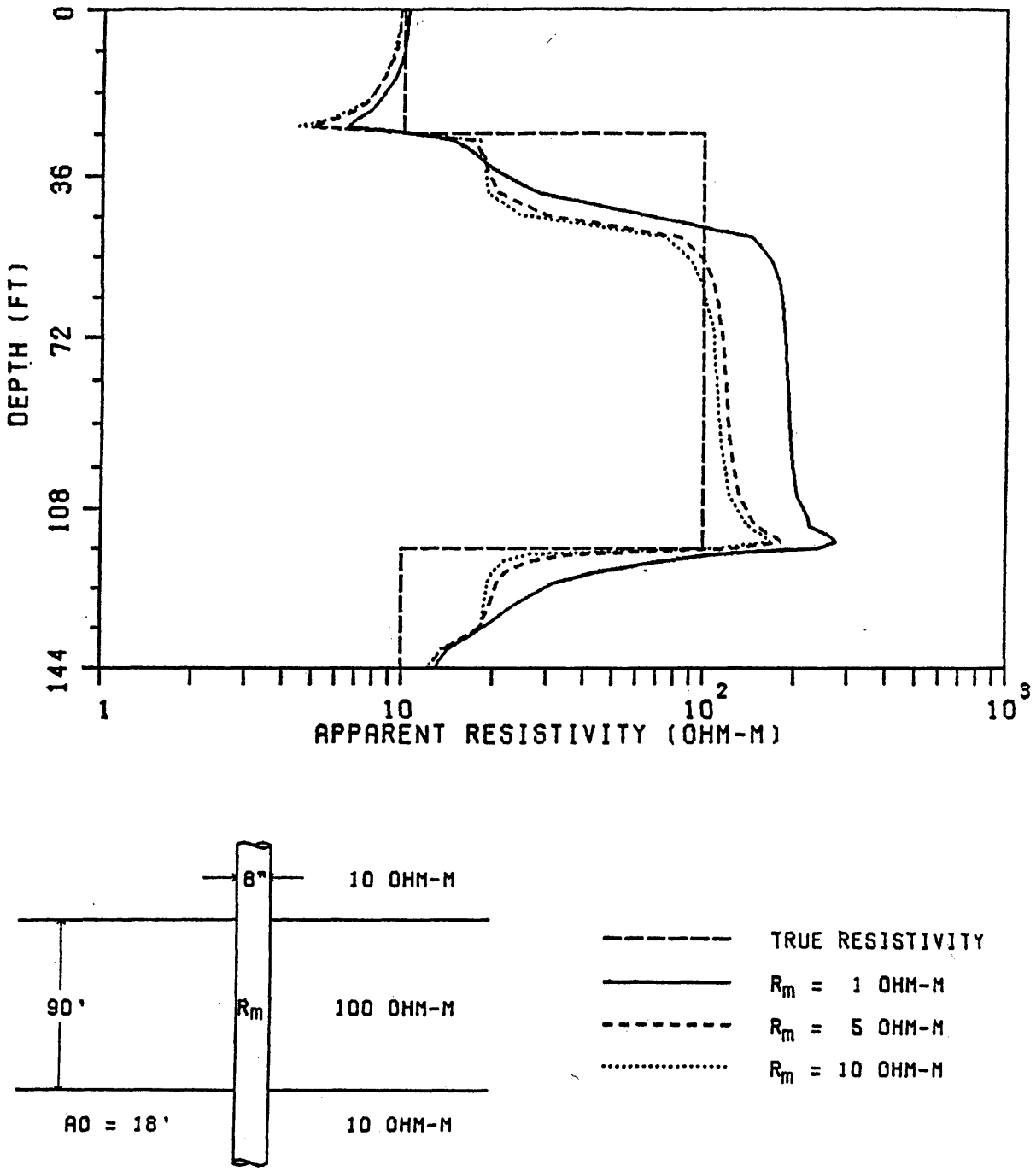

A-4.1 Variations in Rm (Lateral-Thick-Resistive)

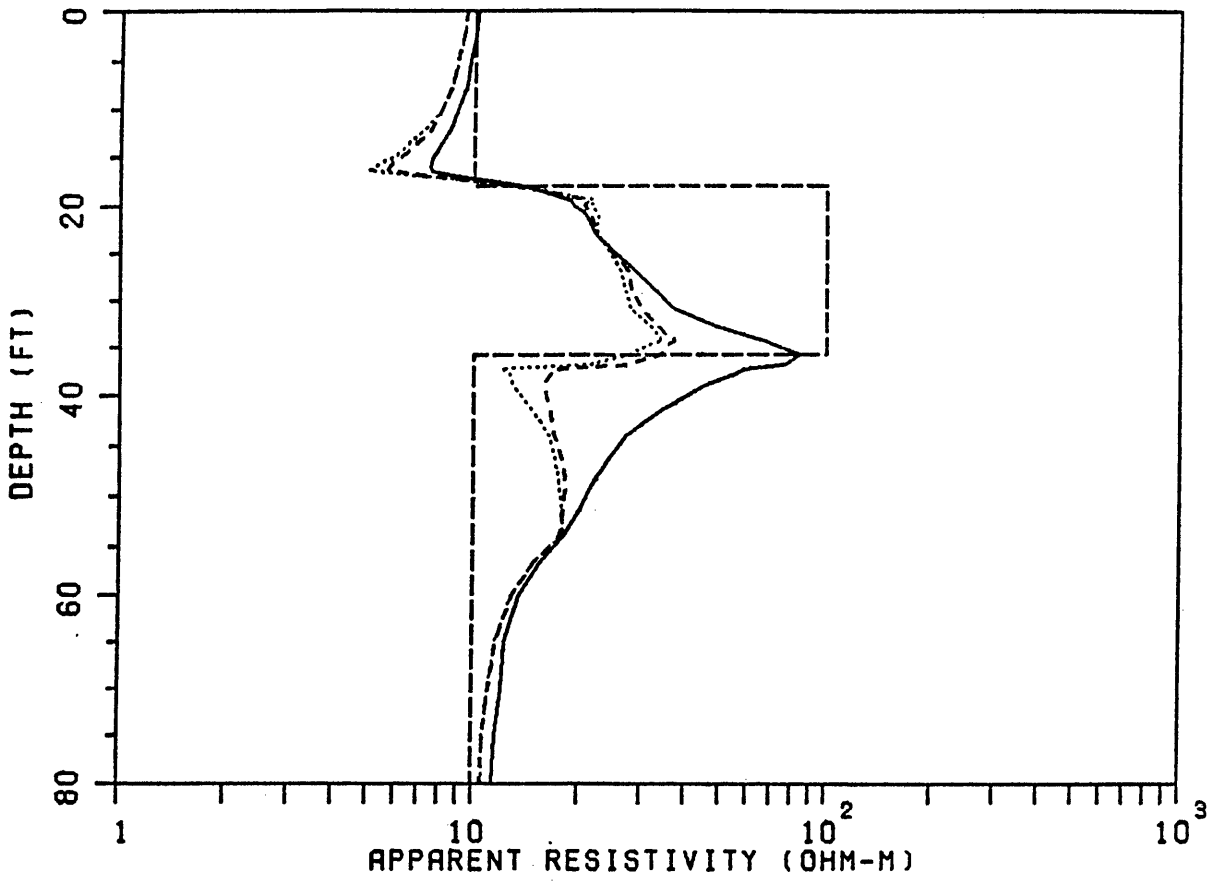

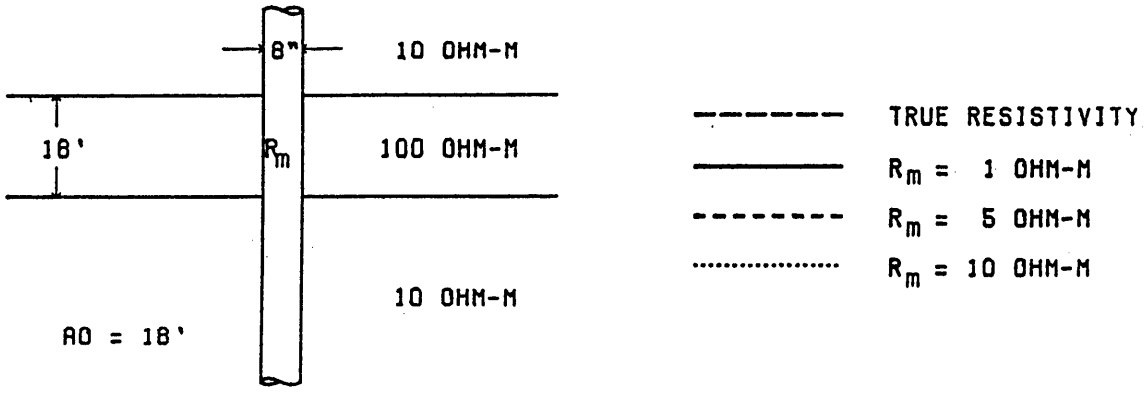

A-4.2 Variations in Rm (Lateral-Critical-Resistive)

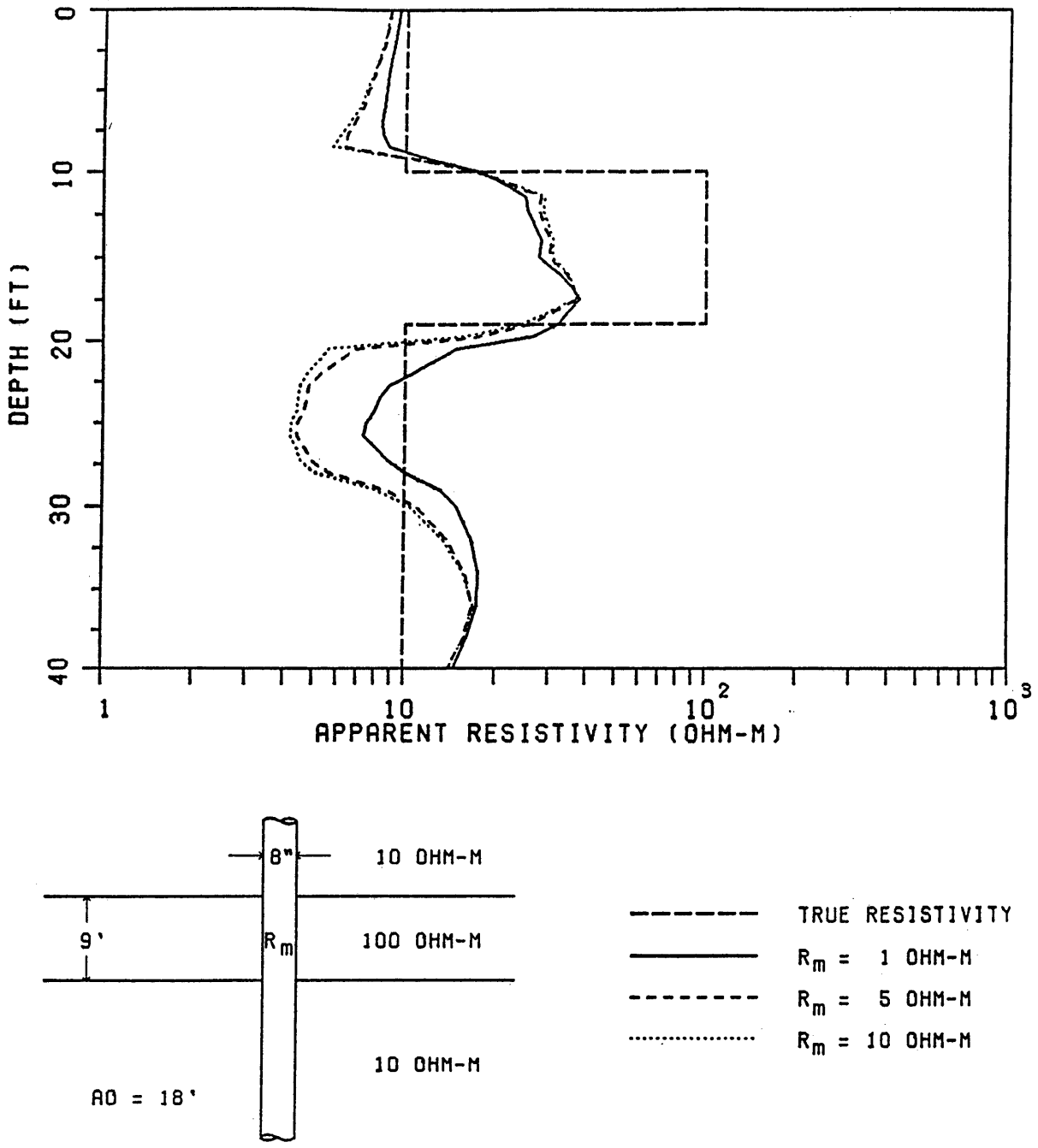

A-4.3 Variations in Rm (Lateral-Thin-Resistive)

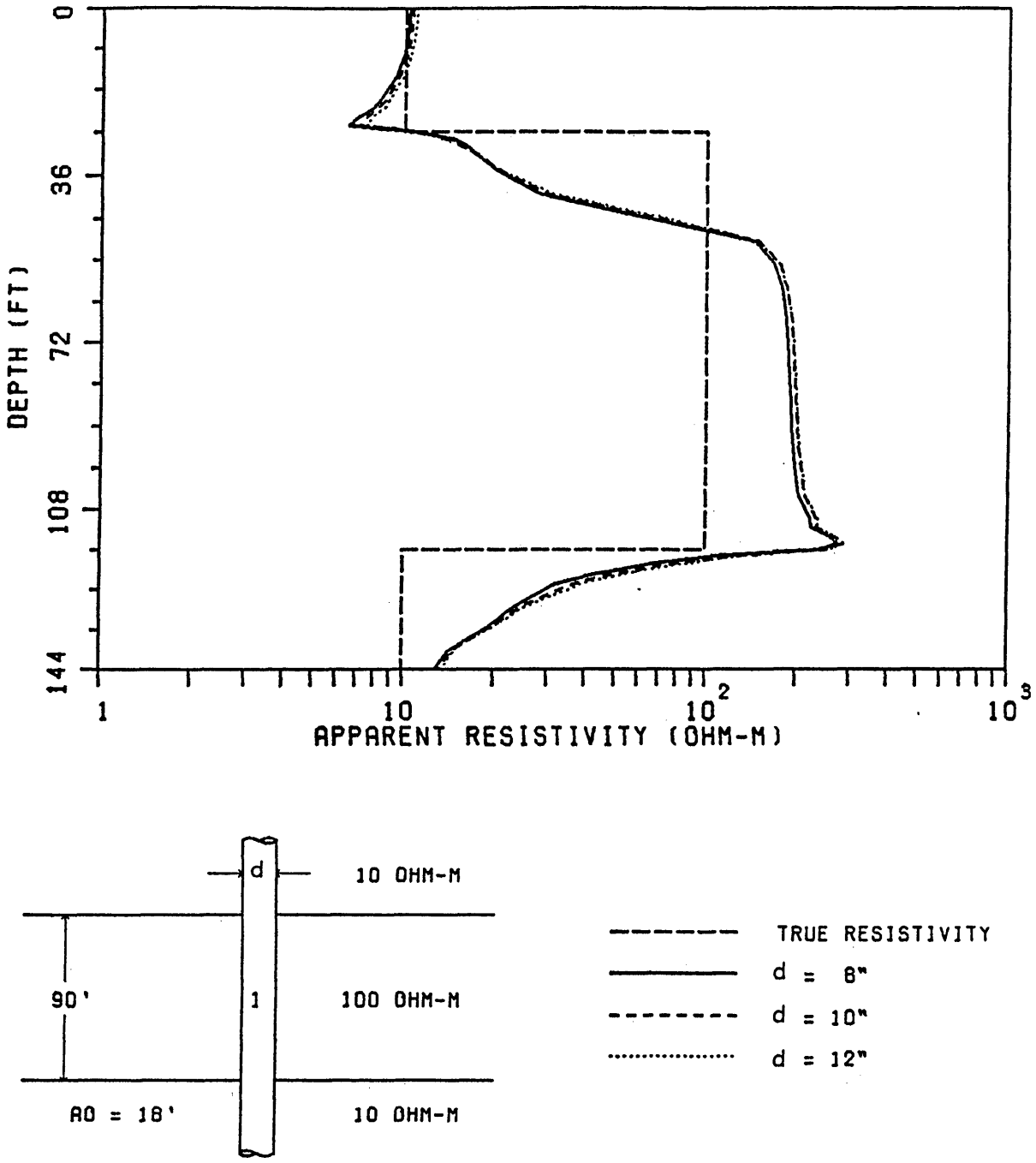

A-4.4 Variations in d (Lateral-Thick-Resistive)

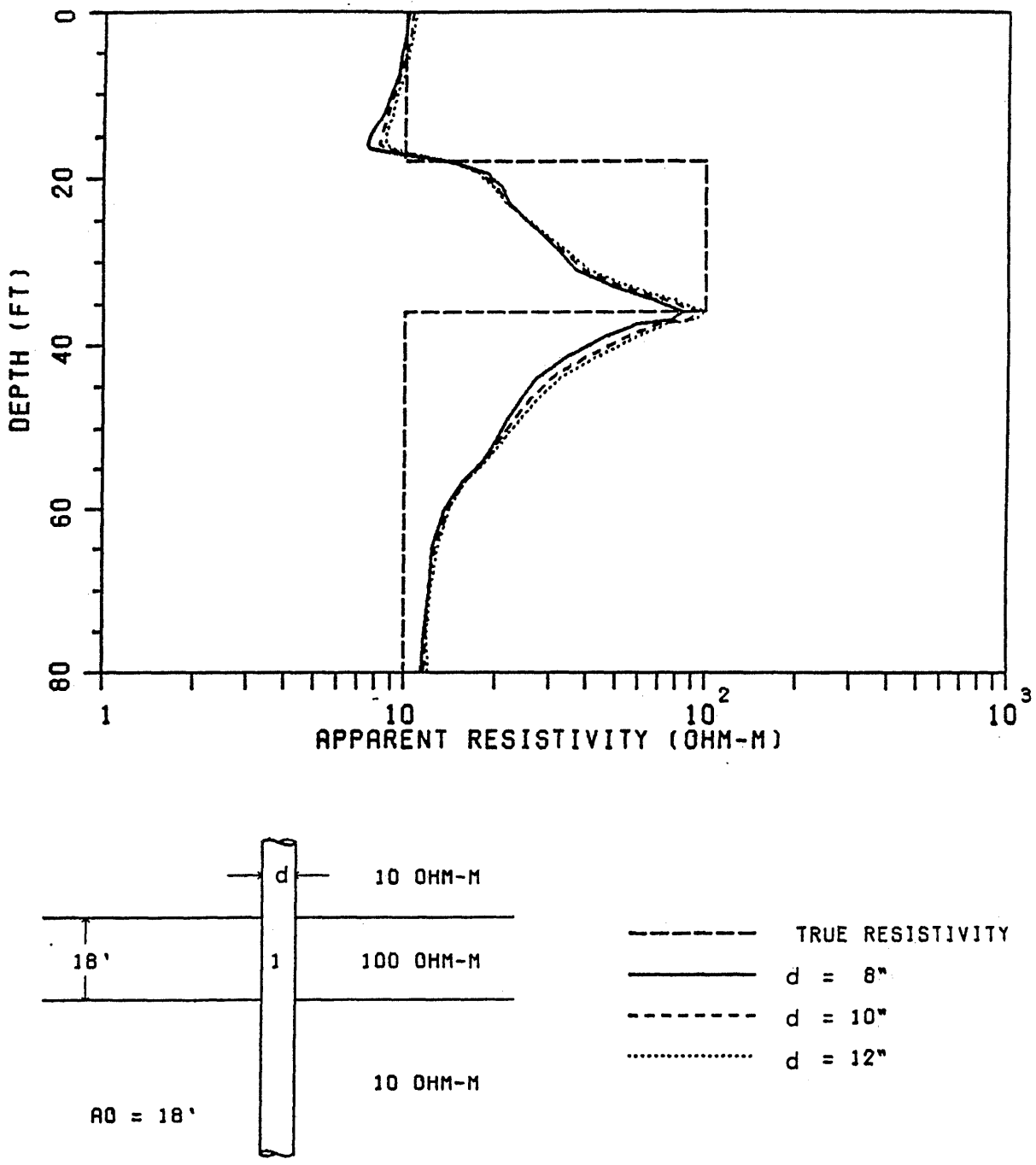

A-4.5 Variations in d (Lateral-Critical-Resistive)

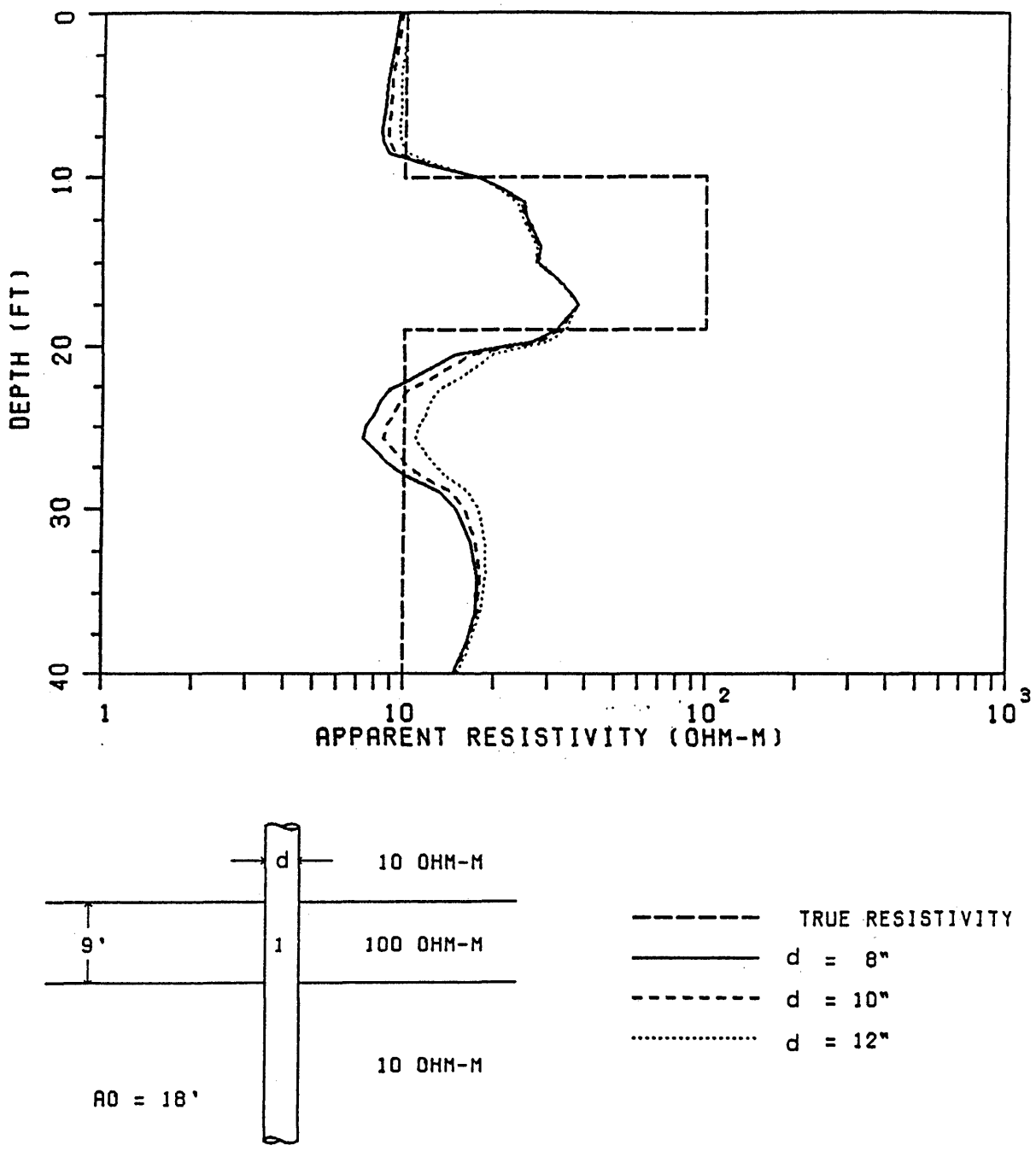

A-4.6 Variations in d (Lateral-Thin-Resistive)

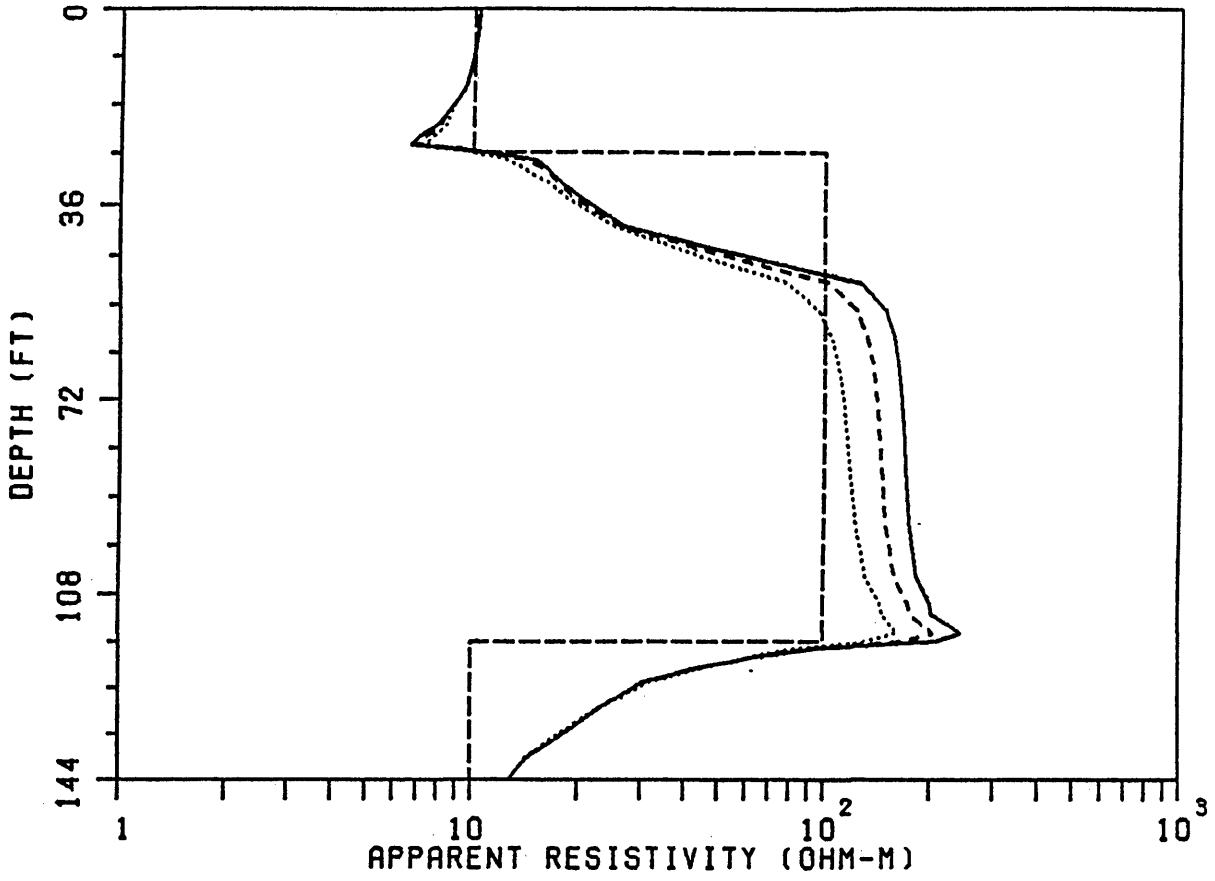

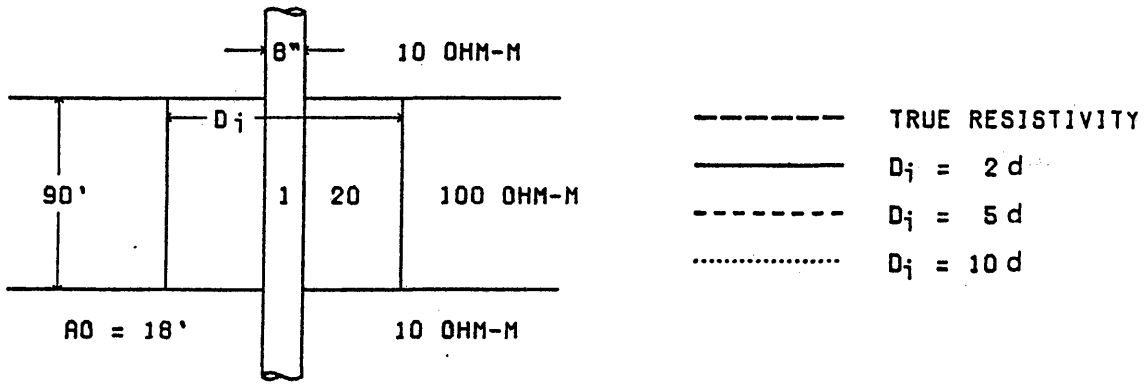

A-4.7 Variations in Di (Lateral-Thick-Resistive)

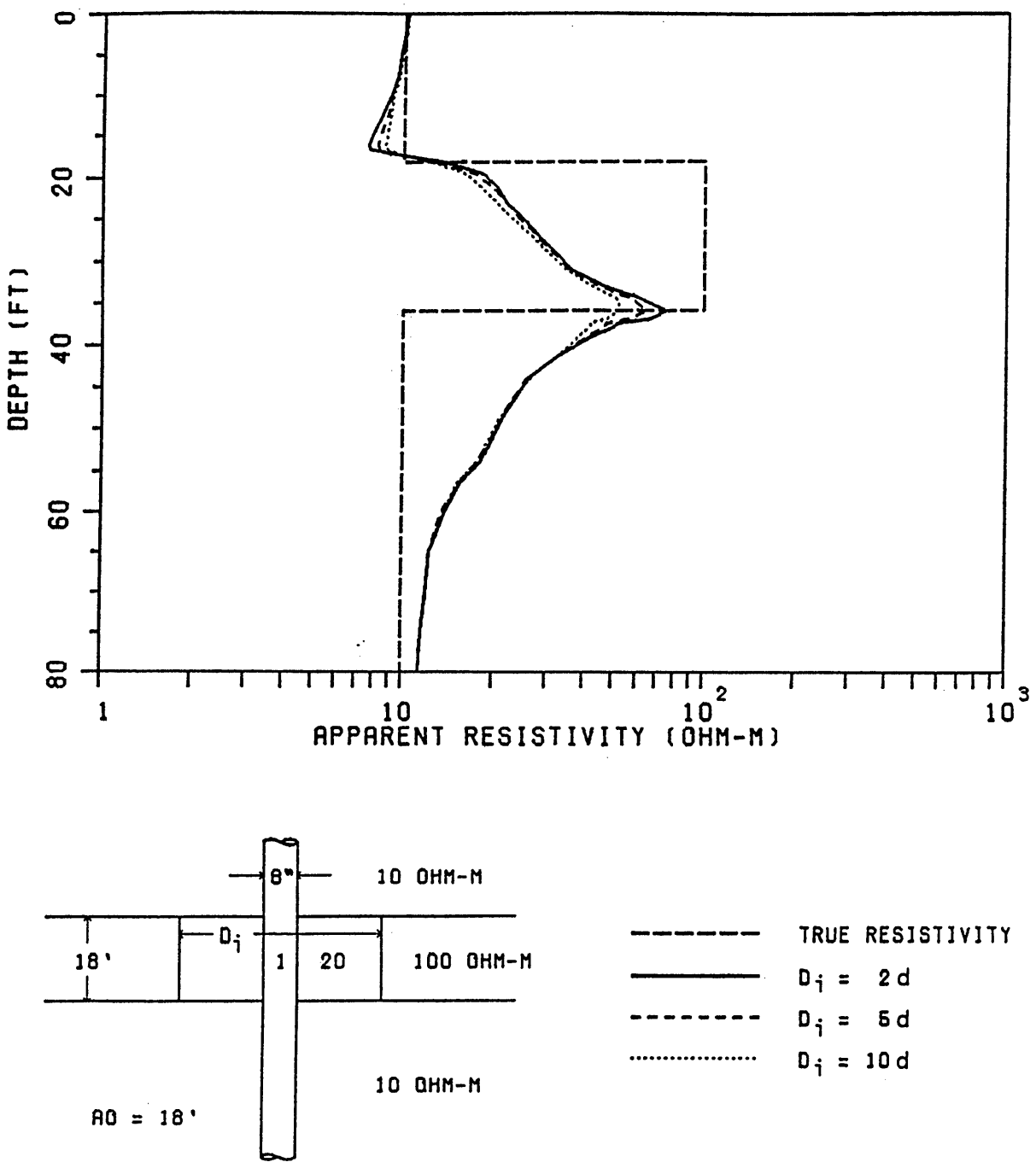

A-4.8 Variations in Di (Lateral-Critical-Resistive)

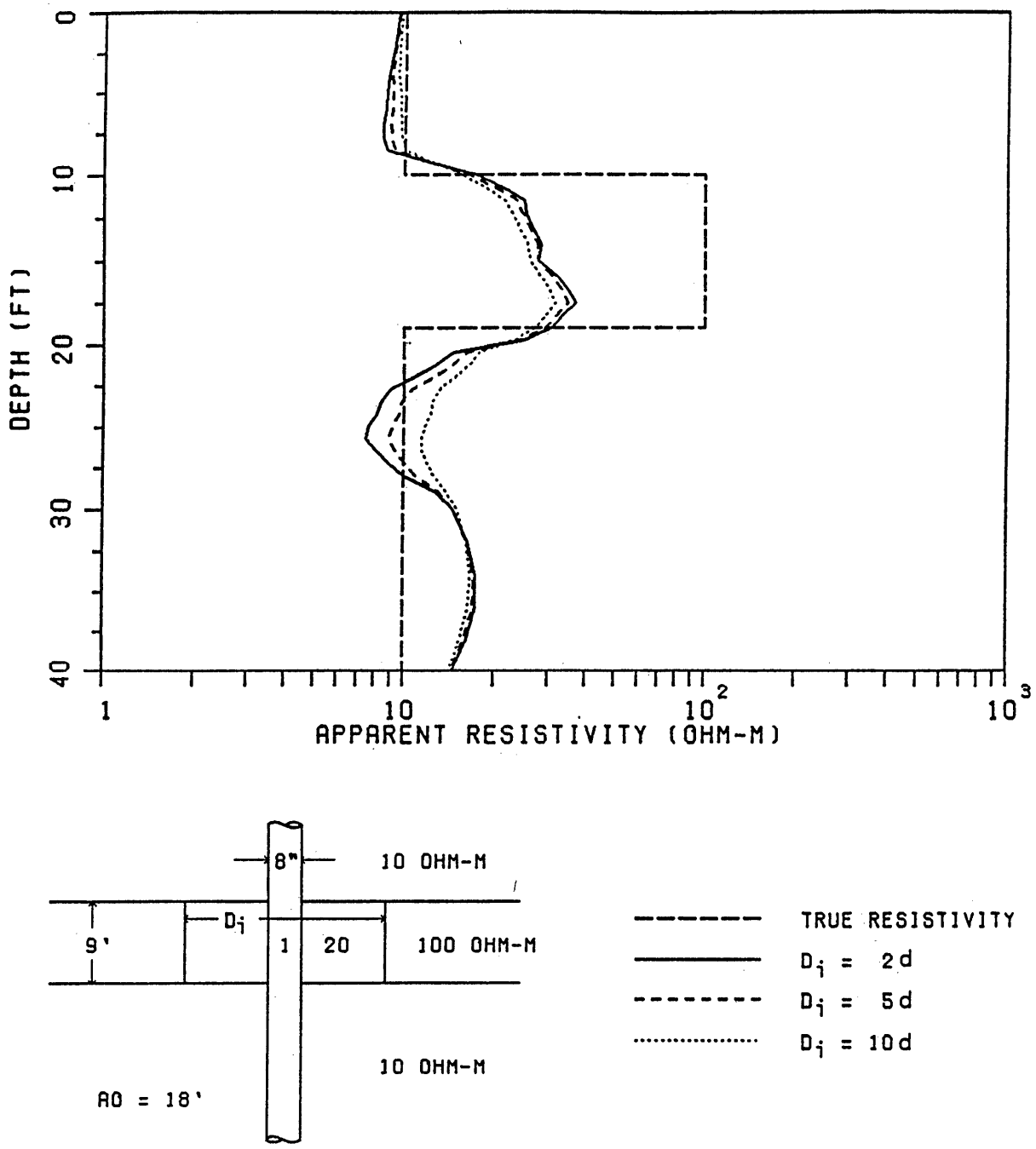

A-4.9 Variations in Di (Lateral-Thin-Resistive)

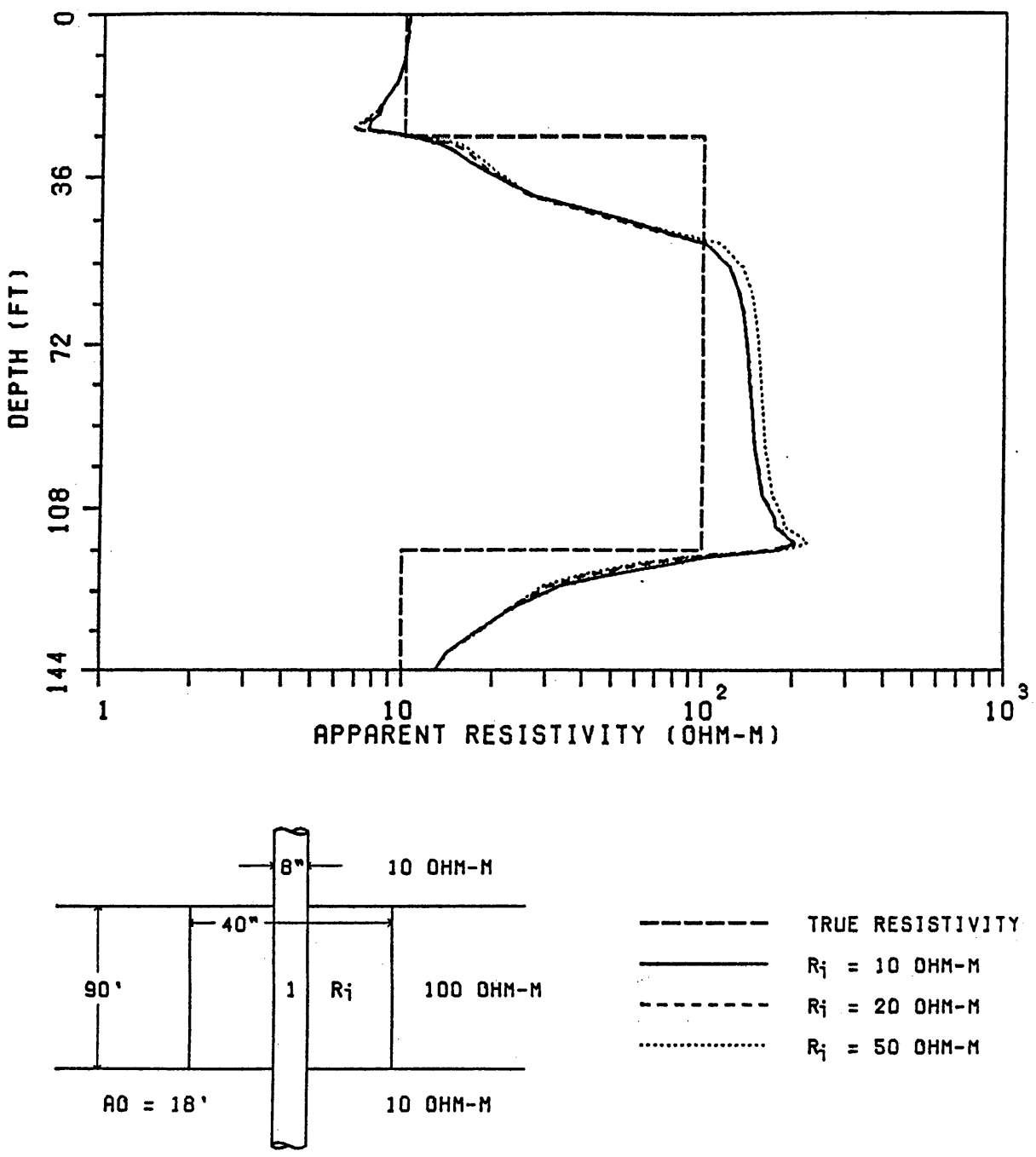

A-4.10 Variations in Ri (Lateral-Thick-Resistive)

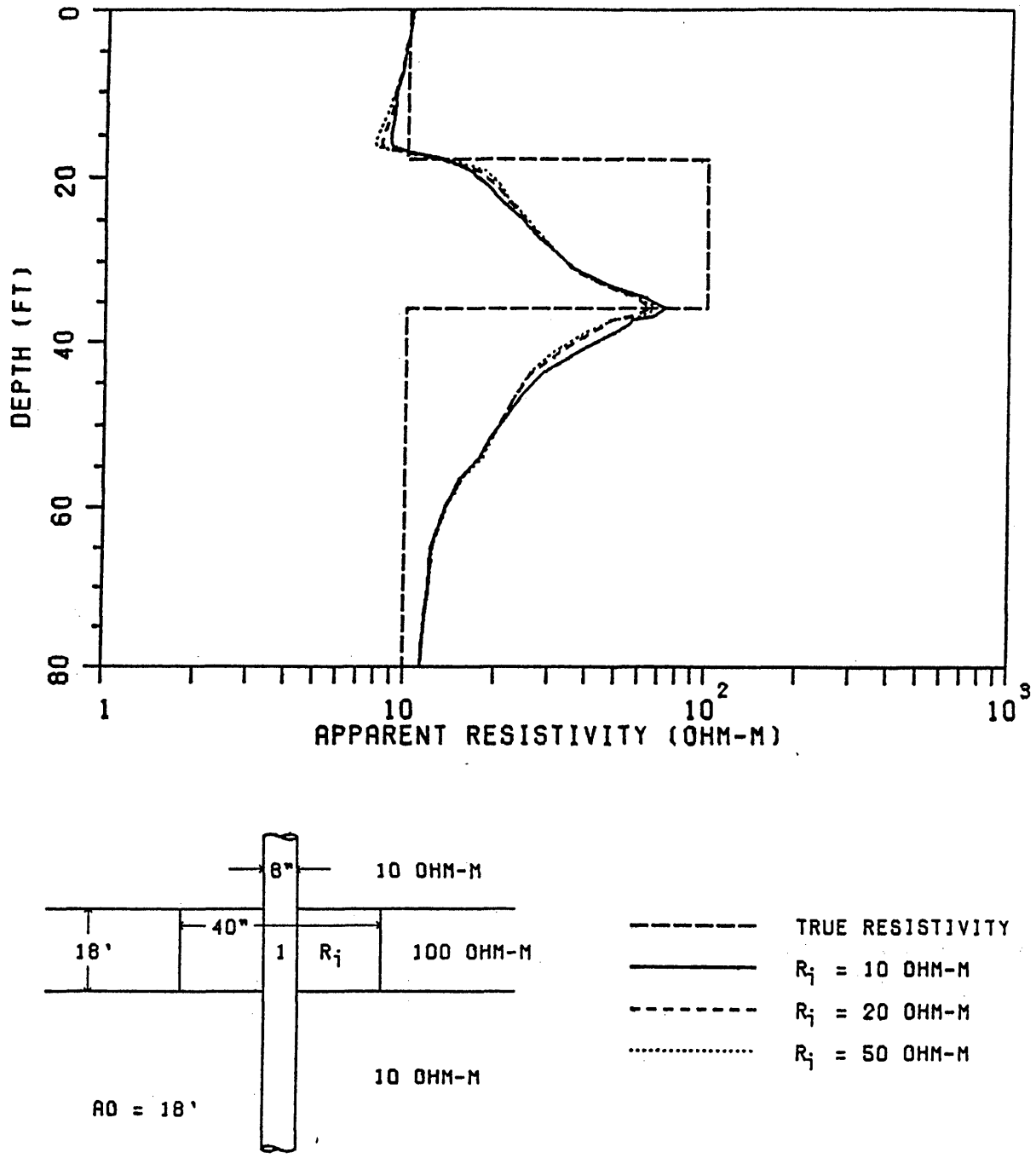

A-4.11 Variations in Ri (Lateral-Critical-Resistive)

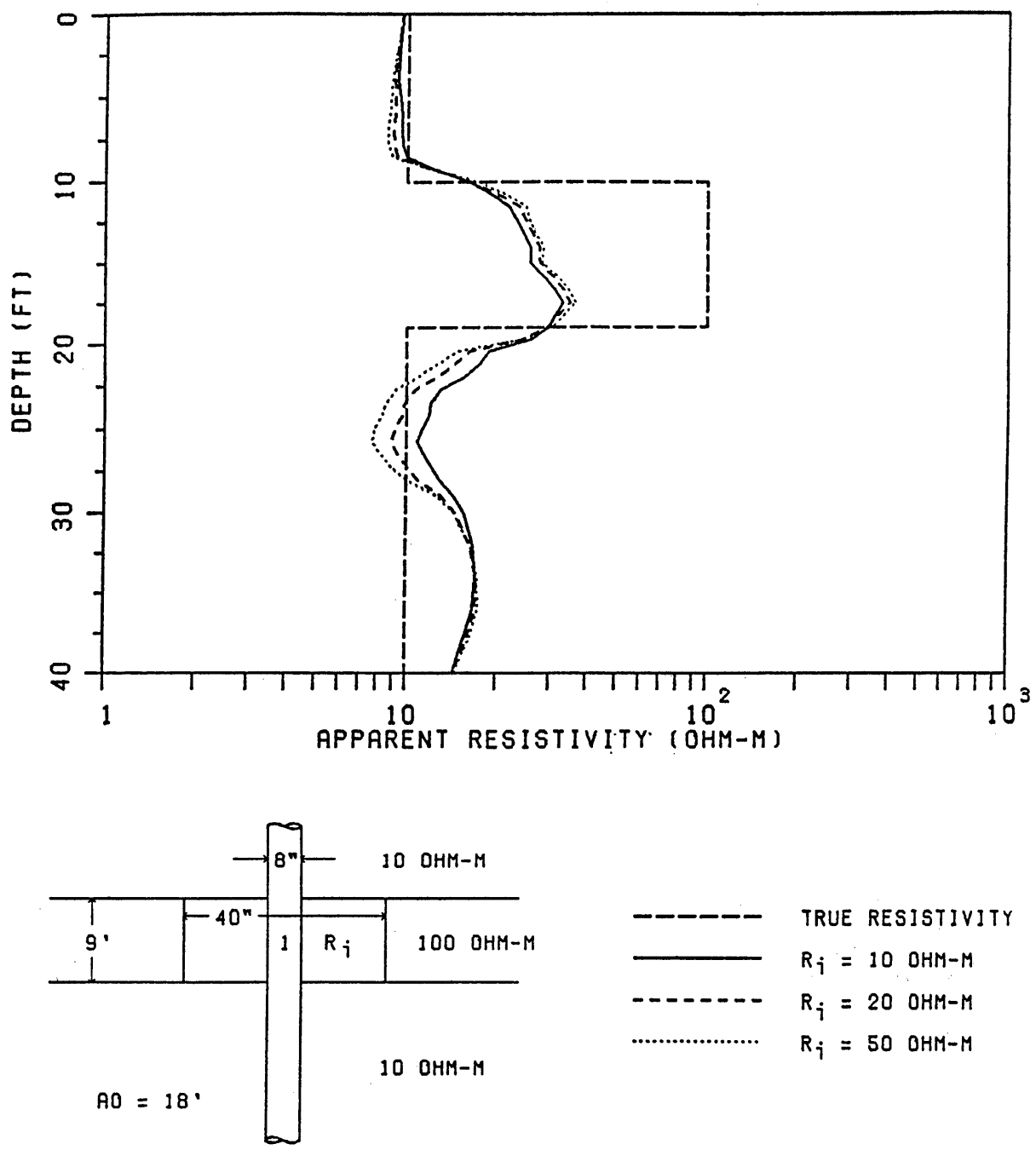

A-4.12 Variations in Ri (Lateral-Thin-Resistive)

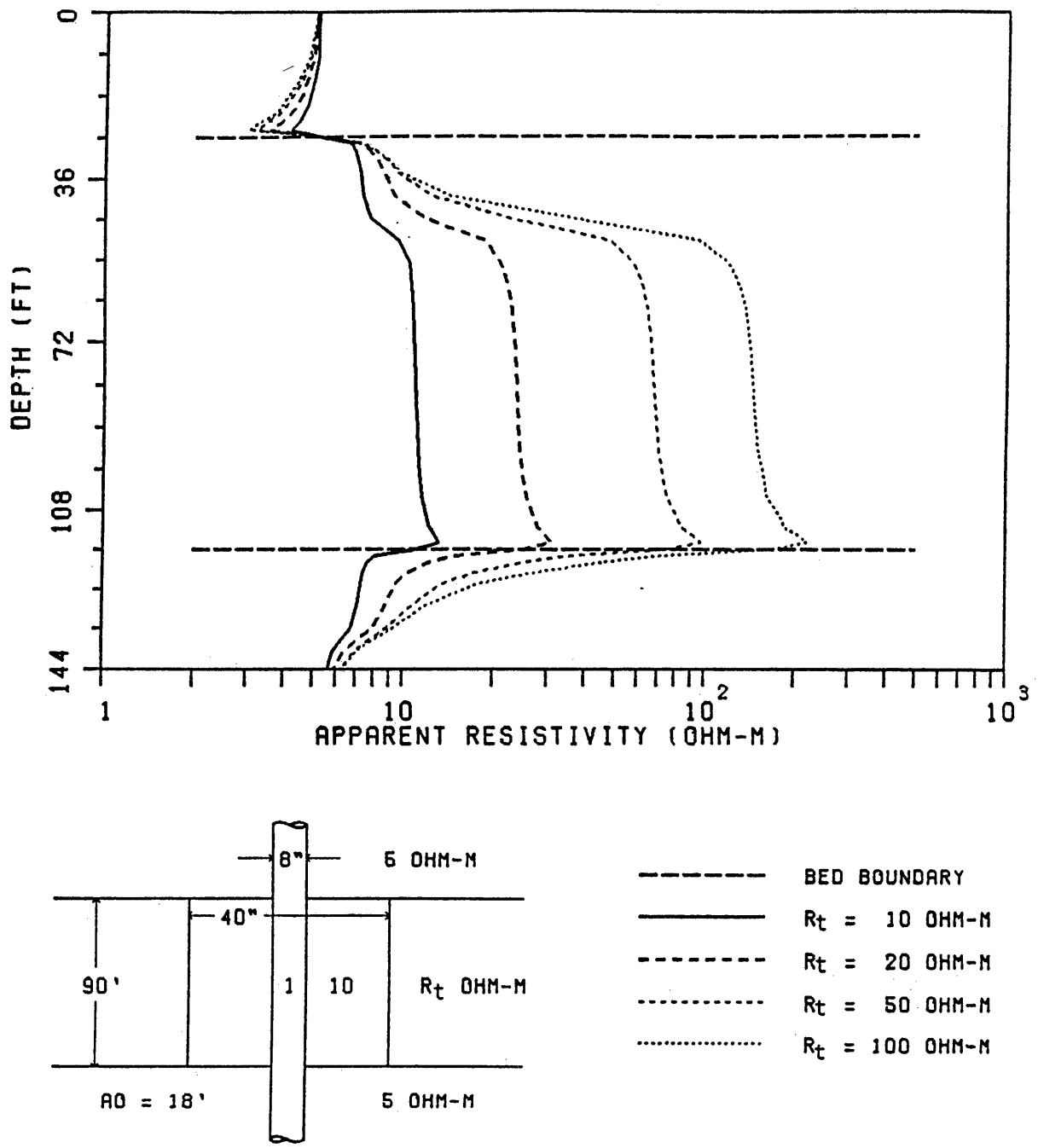

A-4.13 Variations in Rt (Lateral-Thick-Resistive)

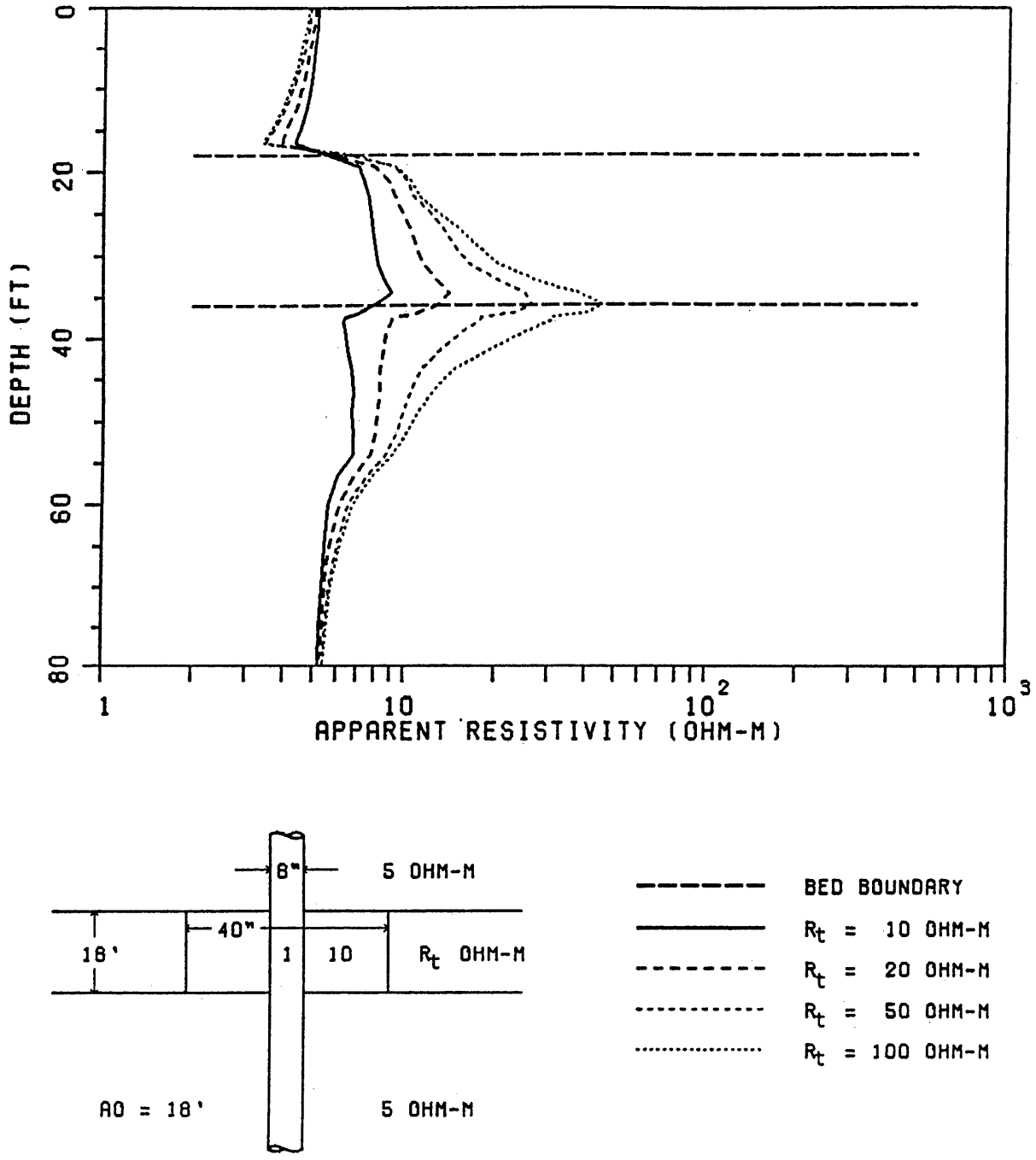

A-4.14 Variations in Rt (Lateral-Critical-Resistive)

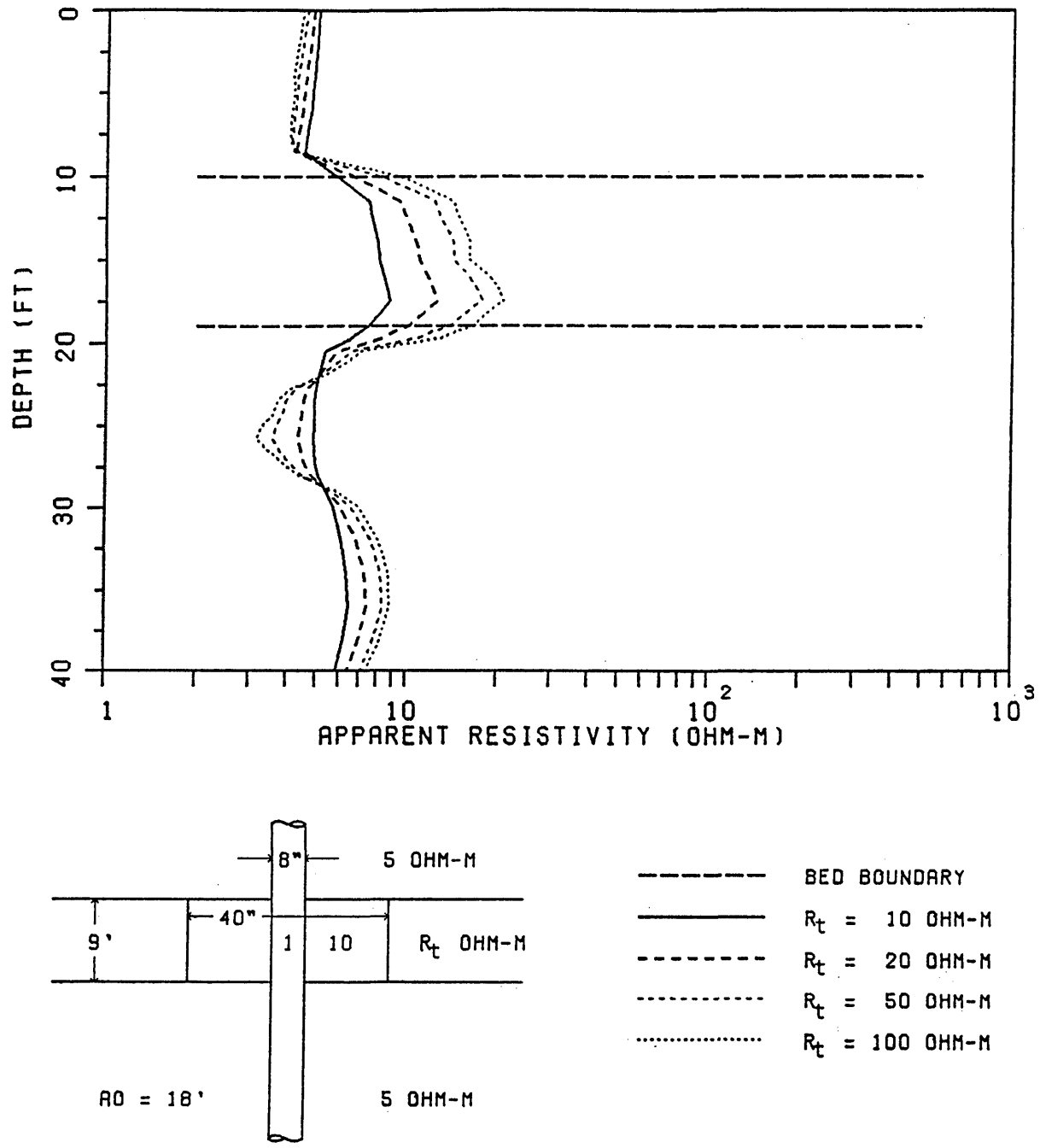

A-4.15 Variations in Rt (Lateral-Thin-Resistive)